Double-scale modelling of failure in rocks : influence of micro-cracks friction

Aleksandra Wrzesniak

UNIVERSITÉ DE GRENOBLE

THÈSE

Pour obtenir le grade de

DOCTEUR DE L'UNIVERSITÉ DE GRENOBLE

Spécialité : **Matériaux, Mécanique, Génie Civil, Électrochimie**

Arrêté ministériel : 7 août 2006

Présentée par

Aleksandra WRZESNIAK

Thèse dirigée par **Cristian DASCALU** et
codirigée par **Pierre BÉSUELLE**

préparée au sein du **Laboratoire 3SR**
dans **l'École Doctorale IMEP2**

Modélisation double-échelle de la rupture des roches: influence du frottement sur les micro-fissures

Thèse soutenue publiquement le **14 décembre 2012**,
devant le jury composé de :

Mme. Irini DJERAN-MAIGRE
Professeur, INSA Lyon (Président du jury)
M. André DRAGON
Directeur de recherche, CNRS Poitiers (Rapporteur)
M. Jian-Fu SHAO
Professeur, Université de Lille 1 (Rapporteur)
M. Darius SEYEDI
Chercheur, ANDRA (Examinateur)
M. Cristian DASCALU
Professeur, Université Pierre et Marie Curie (Directeur de thèse)
M. Pierre BÉSUELLE
Chercheur, CNRS Grenoble (Co-directeur de thèse)

Abstract

Double-scale modelling of failure in rocks: influence of micro-cracks friction

In continuum damage models, the degradation of the elastic moduli, as the results of microscopic crack growth, is represented through damage variables. The evolution of damage variable is generally postulated based on the results of the experimental observations. Many such phenomenological damage models have been proposed in the literature. The purpose of this contribution is to develop a new procedure in order to obtain macroscopic damage evolution laws, in which the damage evolution is completely deduced from micro-structural analysis. We use homogenization based on two-scale asymptotic developments to describe the overall behaviour starting from explicit description of elementary volumes with micro-cracks. We consider quasi-brittle (time independent) and sub-critical (time dependent) criteria for micro-cracks propagation. Additionally, frictional contact is assumed on the crack faces. An appropriate micro-mechanical energy analysis is proposed, leading to a damage evolution law that incorporates stiffness degradation, material softening, size effect, and unilaterality, different fracture behaviour in contact without and with friction. The information about micro-cracks is contained in the homogenized coefficients and in the damage evolution law. The homogenized coefficients describe the overall response in the presence of (possibly static) micro-cracks, as they are computed with the (quasi-) static microscopic solution. The damage law contains the information about the evolution of micro-cracks, as a result of the energy balance in time during the microscopic propagation. The homogenized law is obtained in the rate form. Effective coefficients are numerically computed for different crack lengths and orientations. This allows for the complete construction of the macroscopic laws. A first analysis concerns the local macroscopic behaviour, for complex loading paths, in order to understand the behaviour predicted by the two-scale model and the influence of micro structural parameters, like for example friction coefficient. Next, the FEM implementation of the macroscopic equations is performed and simulations for various compression tests are conducted. The results of the numerical simulations are compared with the experimental results obtained using a new true-triaxial apparatus recently developed at the Laboratory 3SR in Grenoble (France).

Keywords: *micro-cracks, asymptoptic homogenization, damage, unilateral contact, friction, geomaterials, quasi-brittle behaviour, sub-critic, time effects*

Résumé

Modélisation double-échelle de la rupture des roches : influence du frottement sur les micro-fissures

Dans les modèles des milieux continus, la dégradation des modules d'élasticité, résultats de la propagation des fissures microscopiques, est représentée par des variables d'endommagement. L'évolution de la variable d'endommagement est généralement formulée sur la base d'observations expérimentales. De nombreux modèles phénoménologiques d'endommagement ont été proposés dans la littérature. L'objet de cette thèse est de développer une nouvelle procédure pour obtenir des lois d'évolution macroscopique d'endommagement, dans lesquelles l'évolution de l'endommagement est entièrement déduite de l'analyse de la microstructure. Nous utilisons une homogénéisation basée sur des développements asymptotiques pour décrire le comportement global à partir de la description explicite d'un volume élémentaire microfissuré. Nous considérons d'une part un critère quasi-fragile (indépendant du temps) puis un critère sous-critique (dépendant du temps) pour décrire la propagation des microfissures. De plus, le frottement entre les lèvres des microfissures est pris en compte. Une analyse énergétique est proposée, conduisant à une loi d'évolution d'endommagement qui intègre une dégradation de la rigidité, un adoucissement du comportement du matériau, des effets de taille et d'unilatéralité, mettant en avant un comportement différent à la rupture en contact avec et sans frottement. L'information sur les micro-fissures est contenue dans les coefficients homogénéisés et dans la loi d'évolution de l'endommagement. Les coefficients homogénéisés décrivent la réponse globale en présence de micro-fissures (éventuellement statiques), tels qu'ils sont calculées avec la (quasi-) solution microscopique statique. La loi d'endommagement contient l'information sur l'évolution des micro-fissures, résultant de l'équilibre énergétique dans le temps pendant la propagation microscopique. La loi homogénéisée est formulée en incrément de contrainte. Les coefficients homogénéisés sont calculées numériquement pour des longueurs de fissures et des orientations différentes. Cela permet la construction complète des lois macroscopiques. Une première analyse concerne le comportement local macroscopique, pour des trajets de chargement complexes, afin de comprendre le comportement prédit par le modèle à deux échelles et l'influence des paramètres micro structuraux, comme par exemple le coefficient de frottement. Ensuite, la mise en œuvre en éléments finis des équations macroscopiques est effectuée et des simulations pour différents essais de compression sont réalisées. Les résultats des simulations numériques sont comparés avec les résultats expérimentaux obtenus en utilisant un nouvel appareil triaxial récemment mis au point au Laboratoire 3SR à Grenoble (France).

Mots clés : *micro-fissures, homogénéisation asymptotique, endommagement, contact unilatéral, frottement, géomatériaux, comportement quasi-fragile, propagation sous-critique, effet du temps*

Contents

List of Figures

List of Tables

Notations

E	Young modulus
ν	Poisson's ratio
λ,μ	Lamé constants
$\mathbf{x}$	macroscopic system of coordinates
$\mathbf{y}$	microscopic system of coordinates
ε	material's internal length represented by the size of a periodicity cell (elementary cell) and by the distance between centers of two neighboring micro-cracks
$\boldsymbol{\sigma}^{\varepsilon}$	stress tensor of the initial heterogeneous body, before homogenization
$\boldsymbol{u}^{\varepsilon}$	displacement fields of the initial heterogeneous body, before homogenization
$\mathbf{e}_x$	small strain tensor with respect to the macroscopic variable
Y	unit cell $Y = [0,1] \times [0,1]$ (microscopic level)
d^{ε}	length of a micro-crack in the elementary cell
d	length of the crack in the unit cell; it varies from 0 to 1, because it is defined as the projection of the crack on the horizontal axis
d_0	initial crack length in the unit cell
θ	crack orientation in the unit cell
$\mathbf{N}$	unit normal vector to the crack surface
$\mathbf{T}$	unit tangent vector to the crack surface
$\mathbb{N}$	normal component of the stress to the crack lip
$\mathbb{T}$	tangential component of the stress to the crack lip
$\mathbb{N}_{un}$	inelastic part of normal component of the stress to the crack lip
$\mathbb{T}_{un}$	inelastic part of tangential component of the stress to the crack lip
$\mathbf{L}$	left sense of sliding
$\mathbf{R}$	right sense of sliding

$\mathbf{E}^{pq}$	basic macroscopic deformation (frictionless case)
$\bar{\mathbf{E}}^{pq}$	basic macroscopic deformation (frictional case)
μ_f	microscopic Coulomb coefficient
μ_f^*	resultant macroscopic Coulomb coefficient
ϕ	friction angle
$[\cdot]$	jump across the crack faces
$\boldsymbol{\xi}(\mathbf{y})$	*characteristic functions* representing elementary deformation modes of the unit cell ($e_{xij}\left(\mathbf{u}^{(0)}\right) = E_{ij}^{pq}$)
$\boldsymbol{\eta}(\mathbf{y})$	*characteristic functions* representing elementary deformation modes of the unit cell ($e_{xij}\left(\mathbf{u}^{(0)}\right) = \bar{E}_{ij}^{pq}$)
$< \cdot >$	mean value operator
a_{ijkl}	elastic coefficients of the isotropic solid part
C_{ijkl}	homogenized (effective) elastic coefficients
I_{ijkl}	homogenized coefficients related with the dissipation of the energy due to frictional sliding
c_f	size of the fracture process zone around a crack tip (FPZ)
$\mathcal{G}^{\varepsilon}$	energy release rate at the crack tip
$\mathcal{G}_f$	critical fracture energy
$\mathcal{G}_{cr}$	maximum of $\mathcal{G}_f$
Y_d	macroscopic damage energy release rate
K_{IC}	fracture toughness ($K_{IC} = K_0$)
$K_{I,II}$	stress intensity factors
n	the subcritical crack growth index
v_0	crack velocity in subcritical crack growth at $K_I = K_0$

Chapter 1

General introduction

Contents

1.1 Context of the study

1.1.1 Radioactive waste disposal [2], [3], [4]

The production of radioactive waste started much earlier than the construction of the first nuclear power plants. In the 50s, for example, very small quantities of radium were used to fortify cattle feed or for serigrapht (screen-painting) purposes in the clock industry. However, it was in the medical field that use of radioelements was the most widely spread.

Nowadays, over and above the production of the electricity through nuclear energy, radioactivity has many other applications, especially for medical, research and industrial purposes. All those applications generate radioactive waste with various levels of radiotoxicity. It is therefore important to identify those levels and to implement relevant management means for every waste category. The radioactive waste have been classified as very-low-level waste, low- and intermediate-level short-lived waste, high-level and long-lived waste.

Created pursuant to the law of 30 December 1991, the French National Radioactive Waste Management Agency (*Agence nationale pour la gestion des dechets radioactifs* - ANDRA) is responsibile for managing all radioactive waste generated in France. It is placed under the supervision of the respective ministries for Industry, Research and Environment.

In the Aube district, Andra operates two surface disposal facilities, the first one for low- and intermediate-level short-lived waste (CSFMA) and the second one for very-low-level waste (CSTFA).

It also monitors a third facility (CSM), located in the Manche district, where no waste was received since 1994.

Lastly, ANDRA is in charge of the studies being conducted at the Meuse/Haute-Marne Underground Research Laboratory (MHM URL) on the feasibility of a deep geological repository for high-level and long-lived (HLLL) radioactive waste with a reversibility rationale.

HLLL waste results primarily from nuclear power-generating stations. On 31 December 2004, this waste represented 0.2% of total volume of waste being produced in France and 91.7% of total radioactivity. Currently, waste packages are stored on their production sites, pending a sustainable industrial management solution. The two main specificities of HLLL waste are the following: it produces heat and it contains HLLL radio-elements that may migrate out from the package over the long term. Those specificities must be taken into account in the design of any future deep geological repository.

Andra's research mission relies especially on the studies carried out in the Meuse/Haute-Marne Underground Research Laboratory (MHM URL), located at Bure (Meuse district). Designed as a comprehensive scientific tool, this underground laboratory contains no radioactive waste and will never be used for radioactive waste disposal. Scientists use the laboratory to study a 155-million-year-old clay-rock layer with a view to qualifying such a geological formation for the safe and reversible disposal of HLLL waste.

Andra's MHM URL does not form only a physical structure, located 500 m deep underground, but constitutes also as a scientific tool for which every phase represents a further step towards a better understanding of the rock, starting with the surface survey, continuing with the development of excavation methods and their actual application, up to rock instrumentation with data recording and interpretation.

In term of basic safety rules, the required criteria for siting and deep geological repository are as follow:

- No seismic risk over the long term;
- No significant water circulation within the repository;
- A suitable rock for structure excavation;
- Containment properties for radioactive substances;
- Located deep enough to protect the waste against various aggressions;

- No exceptional recoverable resources in the vicinity.

Several rock formations have the required properties to comply with this basic safety rule. After 10 years of investigations, Andra decided that the Callovo-Oxfordian formation of the Meuse/Haute-Marne site has favourable characteristics for the implementation of the deep geological repository for HLLL waste. The Callovo-Oxfordian is located under a 400-m layer of limestone and marly rock. The overburden pressure (exerted by the weight of those overlying formations) has compacted the rock and strongly reduced its porosity. Due to the resulting low quantity of water contained in the rock, the mechanical strength is enhanced in comparison to argillaceous rocks currently found on surface. The favourable characteristic of the Callovo-Oxfordian are:

- a stable geological environment with very low probability of seismic events;
- a regular, homogeneous and fault-free clay layer over a large area;
- the low permeability of the Callovo-Oxfordian formation with slow and very slight water circulations within the surrounding formations;
- the capability of the clay to trap and retain radioactive substances over long timescales (at least about 100,00 years);
- the capability of the rock to withstand various mine-excavation operations involving structures measuring several metres in diameter;
- the compatibility of the characteristic of the Callovo-Oxfordian formation with the reversibility rationale of the disposal;
- a very low impact of engineered materials (cement, concrete, metal, etc.) which is limited to the immediate vicinity of the structures. These materials contribute in part to the safety and the reverisibility of the disposal system;
- the possibilty to transpose the results achieved in the MHM URL to the neighbouring 250-km^2 zone;
- the absence of any exceptional recoverable natural resources (such as oil, water, ores, geothermics, etc.).

Andra has developed a large number of partnerships in France, like with the French Geological Survey (BRGM), the French Atomic Energy Commission (CEA), the National Scientific Research Center (CNRS) among others and approximately 100 laboratories of different fields, including Laboratory 3SR (Laboratoire Sols Solides Structures et Risques) in Grenoble. The present thesis was made in collaboration with Andra and was financially supported by Andra.

In such a complex projects, like deep geological repository for HLLL waste, many different aspects like geology, geomechanics, mineralogy and geochemistry, have to be considered. In the context of storage, the host rock will be submitted to various coupled perturbations such as mechanical loading, hydraulic flow, desaturation and resaturation, temperature variation and chemical reactions. All these features result in different research directions. Considering the complexity of such a multidisciplinary research project, the present work is devoted to the constitutive modeling of mechanical behavior of argillite and experimental testing on the Callovo-Oxfordian argillite using a new true-triaxial apparatus.

1.2 Motivation

Understanding and accurate modelling of the inelastic behaviour and failure of geomaterials are necessary considerations in many engineering applications. However, the geomaterials are difficult to model due to their complex micro-structure and their heterogeneities at certain scale. This heterogeneous nature has a significant influence on the observed macroscopic behaviour of the geomaterials. Various phenomenon occuring on the macroscopic level, such as inelastic non-linear stress-strain response, degradation of the elastic properties and induced anisotropy, material softening, hysteretic behaviour and irreversibile strain after unloading, originate from the physics and mechanics of the underlying microstructure. At the micro-scale, geomaterials contain various sources of heterogeneities such as cracks, pores, inclusions or grain boundaries and two basic physical mechanisms can be generally identified; propagation of micro-cracks and frictional sliding along closed crack surfaces. Determination of the macroscopic overall characteristics of heterogeneous media is an essential problem in many engineering applications. Studing the relation between microstructural phenomenon and the macroscopic behaviour allows to predict the behaviour of existing materials and make engineering design more efficient.

1.3 Introduction to homogenization techniques

Mathematical description of the physical process occuring in the real material obviously depends on the scale of observation. On the natural scale of observation, the specimen of the material may be seen as homogeneous, however on the microscopic scale it is heterogeneous. The description of such a material on the natural scale, in terms of continuum mechanics, is therefore some kind of approximation. In the case of heterogeneous media like soils and rocks, these two scales appear in natural manner: at the level of grains or fissures, the inhomogeneity is caused by the structure of the medium (different dimension of the grains, their shape, crack's distribution, interface), while on the natural scale of observation the medium can be seen as (almost) homogeneous, in the sense that the inhomogeneities statistically repeat in the space ($100g$ of the sand contain 10^7 grains, $100g$ of clay -10^{15} particles ([42])).

Heterogeneous media with a large number of heterogeneities cannot be described by considering each heterogeneity, that would yield to intractable boundary value problems. The way to overcome this limitation is to replace (if possible) the heterogeneous medium by an homogeneous one. The description of the equivalent homogeneous medium is valid at a very large scale (the macroscopic scale) with respect to the heterogeneity scale and should be independent from the macroscopic boundary conditions.

There are two main ways to derive a macroscopic description. The first one is directly macroscopic approach, which is often linked with the experiments and is called phenomenological approach. The second kind of continuous approach allows to deterime the macroscopic behaviour from the local description. This is an upscaling technique and the equivalent description at the macroscopic scale is called homogenized description.

When an upscaling technique is used, the macroscopic behaviour is obtained from the description at the heterogeneity scale that describes the physical process over Representative Elementary Volume (REV). The existance of such a volume is necessary for any continuous macroscopic representation of the physical system, and, as a consequence, is required for applying any upscaling method. By definition, the REV has to be sufficiently large for representing the heterogeneity scale and in the same time small enough compared to the macroscopic volume. The choice of the size of REV is the subject of various discussions (see for instance Dormieux [32]). As consequence of definition of REV, a condition of seperation of scales is required. This fundamental condition for homogenization methods can be expressed as:

$$\frac{l}{L} = \varepsilon \ll 1 \tag{1.1}$$

where l and L are characteristic lengths at the REV scale and at the macroscopic scale, respectively.

Most analytical or semi-analytical homogenization methods are based on the computation of the homogenized (effective) coefficents using various methods shortly summarized below:

- based on averaging theory. The computation of global properties of a heterogeneous material is obtained using averaging technique over each component, weighted with their volume fractions. This approach takes into account only one microstructural characteristic, the volume ratio of the heterogeneities, while the other aspects are abandoned. This method is used and/or enriched by different researches, such as Eshelby ([34]) or Mori and Tanaka ([65]). In this case, equivalent material properties are obtained from the analytical (or semi-analytical) solution of a boundary value problem for spherical or ellipsoidal inclusion of the material in an infinite matrix of another material.

- the self-consistent approach, which is an extension of the previous method, developed by Hill ([47]), and Christensen and Lo ([23]). The global properties of the material are obtained by embedding a particle of one phase into the effective material, whose properties are not known a priori.

- the method of multiscale asymptotic expansions introduced by Benssousan et al. ([14]), Sanchez-Palencia ([77]), Bakhvalov and Panasenko ([10]). This method is based on asymptotic developments of the displacement and stress fields with respect to a natural material length defined as the ratio between heterogeneities length and macroscopic characteristic length.

Besides analytical homogenization methods, an alternative approach has been developed i.e. multi-scale computational homogenization. The fundamentals of this approach have been presented in the papers by Suquet ([78]), Guedes and Kikuchi ([41]), Terada and Kikuchi ([82]), Ghosh et al. ([39]). The weak point of this method is the computational time as a consequence of computation of the stress-strain relationship at every point of interest of the macrocomponent by detailed modelling of the microstructure related to that point.

1.4 Two-scale damage model: asymptotic homogenization method

In this thesis, we consider a procedure to obtain micro-mechanical damage models for solids, in which the damage evolution laws are completely deduced from a micro-strutural analysis without any kind of phenomenological assumptions or idealization of the model. Our formulation remains in the context of classical continuum formulation, but introduces an internal length parameter through the damage evolution law, as a consequence of the microscopic balance of energy and Griffith-type propagation criterion for micro-cracks. The energy analysis is performed on a periodicity cell of finite size for arbitrary, a priori known, smooth trajectories of micro-cracks. The micro-mechanical damage models were obtained by using an upscaling procedure, which combines a periodic homogenization based on asymptotic developments and micro-fracture energy analysis. This procedure was initially developed by Dascalu and co-workers ([25, 29]) for time independent brittle type damage law. An extension to this model can be found in [31], where a wing-type micro-crack was introduced.

Further developments follow two directions: development of time independent and time dependent damage models. The extension of the time independent damage model is given by quasi-brittle damage law in both two- and three-dimensional space ([27, 28]). The second type of development is related to time dependent damage models with sub-critical criterion for micro-cracks . In the first step, it was considered that the propagation occurs in the fixed direction given by the orientation of the crack ([26, 27, 31]). In that case the local and global macroscopic computations were performed. The second step of this development concerns the equivalent rotating micro-crack. This complex two-scale time dependent damage model is capable to take into account both, a crack propagation and its change of orientation. Initially this model was proposed by François and Dascalu ([36]), but only the macroscopic local level was introduced. The implementation of this model at global macroscopic scale can be found in [31].

All these models summarized above, are formulated for quite general crack-face condition, taking into account only the crack opening or crack closing with frictionless contact. The present contribution to these models is to extend a crack-face conditions by taking into account the frictional contact. We consider a Coulomb friction criterion on the crack faces. Together with including frictional phenomenon, the model will be extended for quasi-brittle type damage law, leading to progressive propagation of micro-crack, which is more adequate to the rock's gradual fracture behaviour.

Additionaly, the new class of damage model will be introduced, i.e. time-dependent damage model for frictional micro-cracks, which will overcome some limitations occurring with the time independent type (macroscopic snap-back). The evolution of the micro-crack length is described through a sub-critical criterion governed by Charles's law ([21]).

For both time independent and time dependent class of damage models the energy analysis is performed on a periodicity cell of finite size containing a frictional micro-crack. An appropriate micro-mechanical energy analysis is proposed to formulate a damage evolution law which incorporates stiffness degradation, material softening, size effects, unilaterality, different fracture behaviour in contact with and without friction.

The different coefficients in the homogenized strain-stress law are obtained by finite element computations on the unit cell and special interpolation methods. These coefficients depend on the orientation of the crack, on the friction coefficient, on the sense of sliding and in consequence they lead to induced anisotropy and heterogeneity in the global response of the material.

Due to frictional phenomenon, different states of the crack are considered (stick, sliding and backsliding). This leads to different formulations of constitutive relation corresponding to different state of the crack. The macroscopic behaviour includes complex strain-stress response and irreversible strain after unloading. This particular behaviour can not be observed in the case of frictionless contact.

The geomechanical problems, in both types of the model, are solved for fixed direction of the propagation, which is determined by the orientation of the crack. Two orientations of the crack are considered.

1.5 Continuum damage/friction models

Nucleation and growth of microcracks are typical damage mechanisms in brittle and quasi-brittle solids like rocks, concrete, ceramics, iron and some class of composites. Due to their heterogeneous microstructure and dissipative phenomenon like micro-cracks growth and frictional sliding on crack faces, the macroscopic behaviour includes inelastic non-linear stress-strain response, degradation of elastic properties and induced anisotropy, hysteretic behaviour, unilateral effects related to cracks closure, and irreversible strain after unloading due to friction phenomenon.

Since the first introduction of the scalar damage concept by Kachanov (1958, [53]) and Rabotnov (1963, [76]) for creep of metals, continuum damage mechanics has become an emerging field of active research. Many researches adopted this theory to their problems. From the point of view of the construction procedure, one can classify the damage models in: macroscopic models (usually phenomenologically based) and micro-mechanical approach (two-scale and micromechanical models).

In the phenomenological approach, a model formulation may be based on micromechanically motivated mechanisms, or the damage tensor may be considered only as an internal state variable affecting the stress-strain response without a micromechanical background. Phenomenological models use internal variables to represent the density and orientation of microcracks, for instance, scalar variable for isotropic damage, second and fourth rank tensor to describe anisotropic damage. The constitutive equations are generally derived from the concept of effective stress or the formulation of a free energy potential. The damage evolution law is determined according to the principles of the irreversible thermodynamics. The main advantage of such models is that they provide macroscopic constitutive equations, which can be easily implemented and applied to engineering analyses. The main weakness is that some of the concepts and parameters involved in these models are not clearly related to physical mechanisms. Among various models found in the literature, let mention some, which deal with frictional sliding micro-cracks, like for instance Halm and Dragon ([46]), Dragon et al.([33]), Lawn and Marshall ([56]) , Bargellini et al. ([11]) and Poon et al. ([73]).

In the recent years, considerable efforts have been made to establish a link between microstructural fracture phenomenon and the corresponding macroscopic behaviour. Many researchers focused on the development of macroscopic modeling starting from considerations of micro-mechanical analysis of a cracked medium through homogenization procedures. In this way, the micro-mechanical arguments may lead to a better understanding of the phenomenon observed at the macroscopic level in the experiments. The homogenized models can be divided into micromechanical models and two-scale models.

Various micromechanical studies have been proposed in order to model evolving frictional micro-cracks like for instance Kachanov ([54]). This approach was further developed by many authors, such as Nemat-Nasser and Obata ([68]), Gambarotta and Lagomarsino ([38]) for noninteracting micro-cracks. For interacting and growing penny-shaped microcracks in the context of the self-consistent method we can refer to Lee and Ju ([57]). Moreover, these models are stress-based formulated and are limited to particular stress paths.

An interesting approach is proposed by Andrieux et al. ([5]). An important assumption made by these authors is that for local problem a fissure is rectilinear and small in comparison with dimensions of the basic cell. In this case an infinite medium approximation is allowable.

A three-dimensional strain-based micromechanical analysis (based on Andrieux et al. ([5])) of the brittle damage incorporating micro-crack closure and friction can be found in the work of Pensée et al. ([72]). This model shows a capability to predict several important aspects of brittle anisotropic damage (oriented mesocracks growth, unilateral effects) and hysteretic behaviour due to friction phenomenon.

A micromechanical modeling of closed frictional cracks as flat ellipsoidal inhomogeneities is proposed by Barthélémy et al. ([12]). Three interface friction laws were considered in this paper : von Mises, Coulomb and Drucker-Prager. The macroscopic behaviour of such a cracked medium was obtained by means of homogenization technique based on Eshelby's results.

The behaviour of closed frictional cracks is studied also in Zhu et al. ([84]) in context of Eshelby solution-based homogenization procedure. They consider a family of closed frictional microcracks obeying to the classical interface Coulomb law. In this paper three homogenized schemes are used: the dilute scheme, the Mori-Tanaka scheme (MT) and the Ponte Castaneda and Willis estimate (PCW). The damage evolution law and frictional sliding was determined using the standard thermodynamics framework.

In the context of asymptotic approach, Leguillon and Sanchez-Palencia ([58]) performed the homogenization of a two-dimensional linear elastic body in the presence of the Signorini's conditions with Coulomb's friction provided that fissures are rectilinear. The quasi-static problem was investigated.

Telega ([81]) proposed a model, which deals with the homogenization of a three-dimensional, geometrically linear hyperelastic solid weakened by periodically distributed microcracks in presence of the Signorini's condition and friction.

1.6 Scope and outline

The aim of this thesis is to develop, through homogenization technique, two-scale damage model based on explicit description of the micro-scale level including frictional phenomenon, which could describe the damage behaviour of the geomaterials.

The structure of the thesis, including this introductory chapter, is constructed as follow:

In the Chapter 2 the theoretical aspects concerning asymptotic homogenization and construction of the damage evolution law for frictional sliding micro-cracks are presented. The developments previously done are underlined. Numerical implementation of the microstructure is performed leading to the determination of different homogenized (effective) coefficients, different coefficients related to the dissipation of the energy due to frictional mechanism and components of the Coulomb friction law. Finally, the constitutive relations for each possible state of the crack, i.e. stick, sliding and backsliding are determined. These states are controlled by frictional law and by loading path.

In the Chapter 3 a quasi-brittle damage law is considered and results concerning the effective local (at a macroscopic point) behaviour are presented. The damage law is deduced from quasi-brittle propagation criteria for micro-cracks. The influence of friction on micro-cracks on the macroscopic behaviour is analyzed. In the first step a linear relation for R-curve is used, leading to a snap-back in overall response. In the second step, linear R-curve is extended, by adding a power function of d, to overcome the difficulties related to the snap-back. The comparison of the results obtained for these two resistance curves are presented. In the last part of this chapter the loading-unloading cycle is performed. The behaviour related to the frictional phenomenon like backsliding and stick case during unloading is obtained and analyzed.

Chapter 4 is dedicated to time-dependent damage model. In this chapter an alternative two-scale model, which is able to overcome the difficulties related to non-uniqueness and mesh-dependency, which were observed in the case of quasi-brittle damage model, is presented. This model is regularized by time dependency and is deduced by homogenization for micro-cracks that propagate subcritically. The evolution of the micro-crack length is described through a sub-critical criterion governed by Charles's law. The effective stress-strain and damage responses, depending on time, at macroscopic local point and on global macroscopic scale are numerically evaluated. In the local frame, the influence of the parameters involved in the model, such as crack velocity v_0, strain rate $\dot{e}$, subcritical growth coefficient n, internal length ε, under different compressive loadings and different friction coefficients are studied. Also the influence of friction coefficient and lateral stress is presented. In this chapter, also, the global macroscopic behaviour is discussed. The response of the material under different compressive loadings (uniaxial test and biaxial tests with lateral stresses) is analyzed. Geometry and boundary conditions are based on experimental tests, which were performed parallel to this studies. The effect of friction coefficient, lateral stress and their role in forming the damage localization zone is studied. In the last part of this chapter the influence of mesh size and element shape on the results is investigated.

The ability to characterize localized failure in rocks and, in particular, to follow the strain field evolution inside rock specimen during loading using new true-triaxial apparatus is

demonstrated in Chapter 5. The experimental device and characterization of the tests are presented. The effect of confinement on the process of failure and localization is studied. In the last part of Chapter 5, the numerical results are compared with experimental ones. The abilities of the two-scale time dependent damage model are discussed.

Finally, Chapter 6 gives a brief summary of the conclusions. Perspectives of future developments are shortly discussed.

Chapter 2

Multiscale modeling of damage

Contents

2.1 Introduction

In continuum damage models, micro-cracking is defined by the degradation of elastic moduli, through a damage variable. Generally, the damage evolution laws are postulated as results of phenomenological assumptions. A link between microstructural fracture phenomenon and the corresponding macroscopic behaviour becomes in the recent years a purpose of many researchers (see for instance Nemat-Nasser and Hori [69] for a review). The contributions to this topic are mainly based on non-evolving cracks, but for exception we can cite the researchers who considered the micro-crack evolution, like Andrieux et al.[5], Prat and Bazant [75], Caiazzo and Constanzo [19] or Pensée et al.[72].

An alternative approach is to determine a mechanically equivalent homogeneous material at the macrosopic scale, having relatively similar properties to the heterogeneous medium. The idea is to approximate the initial distribution of the micro-cracks with a periodic one.

A new procedure was proposed by Dascalu and co-workers ([17, 25, 29]). The micro-mechanical damage models were obtained by using an upscaling procedure, which combines a periodic homogenization based on asymptotic developments ([10]) and micro-fracture energy analysis. Damage evolution laws are completely deduced from microstructural analysis by homogenization, without phenomological assumptions. The microscopic

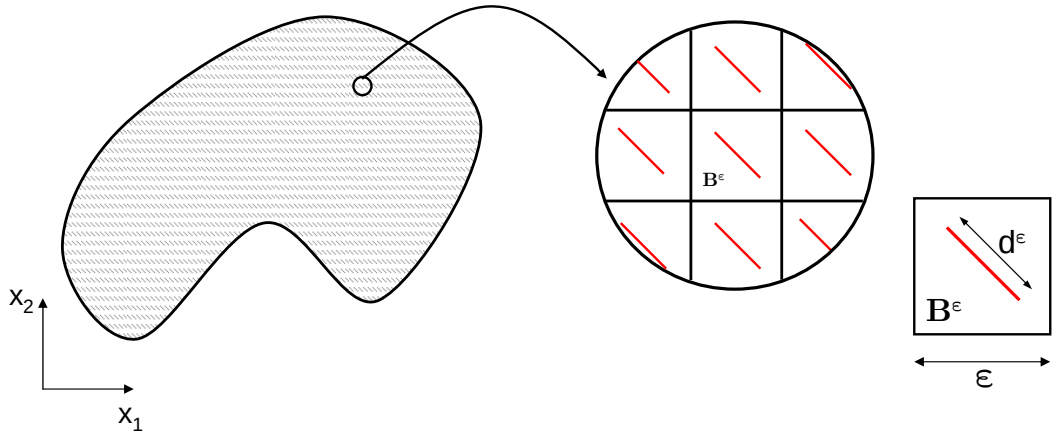

Figure 2.1: Fissured medium with locally periodic microstructure

energy analysis was performed on a periodicity cell of finite size which leads, through homogenization, to a macroscopic evolution equation for damage. In this equation the normalized micro-crack length appears as a damage variable and the cell size as a material length parameter. The resulting damage law naturally accounts for size-effects.

The initial model, developed by Dascalu et al.([25]), was formulated for quite general crack-face conditions and brittle-type criterion. However, it showed the ability to describe experimentally-observed damage behaviour for micro-cracks with frictionless contact. In this manuscript, the extension of crack-face condition will be made, including evolving frictional micro-cracks. In the literature we can find several contributions concerning asymptotic homogenization and frictional phenomenon on the crack lips, but only for non-evolving micro-cracks like for instance Leguillon and Sanchez-Palencia [58] or Telega [81]. On the other side there are other contributions for evolving frictional micro-cracks, which use different techniques like for instance Andrieux et al.[5], Halm and Dragon[46], Pensée et al.[72], Barthélémy et al.[12], Poon et al.[73] and Zhu et al.[84].

Together with including frictional phenomenon, the model will be extended for quasi-brittle type damage law, leading to progressive propagation of micro-crack, which are more adequate to the rock's gradual fracture behaviour. Additionaly, the new class of damage model will be introduced, i.e. time-dependent damage model for frictional micro-cracks, which will overcome some limitations occuring with the time independent type (macroscopic snap-back). The time-dependent damage model, which deals with friction-less contact and allows rotation of non-frictional micro-cracks, is developed by Dascalu and co-workers in [26, 27, 31, 36].

2.2 The model problem

We consider a two-dimensional isotropic elastic medium containing a large number of micro-cracks. A locally periodic distribution of micro-cracks is assumed, so as one can locally find a periodicity cell, of length ε, containing one crack (see Fig.2.1). The cracks are assumed to be smooth and of length d^ε, depending on time t. The length d^ε may differ from one crack to another, but varies smoothly almost everywhere in the elastic body.

Let $\mathcal{B}$ be a whole body, a bounded domain of $\mathcal{R}^2$ containing $\mathcal{N}$ micro-cracks $\mathcal{C}_\mathfrak{n}$, $n=1,...,\mathcal{N}$ and let's denote by $\mathcal{B}_\mathfrak{s} = {}^{B}/_{\mathcal{C}}$ the solid part, where $\mathtt{C} = \cup_{\mathfrak{n}=1}^{\mathtt{N}} \mathcal{C}_\mathfrak{n}$.

In the solid $\mathcal{B}_\mathfrak{s}$, we have the equilibrium equation (2.1)

$$\frac{\partial \sigma_{ij}^{\varepsilon}}{\partial x_j} = 0 \tag{2.1}$$

and the constituive relations for the linear elasticity

$$\sigma_{ij}^{\varepsilon} = a_{ijkl} e_{xkl}\left(\mathbf{u}^{\varepsilon}\right) \tag{2.2}$$

where $\mathbf{u}^{\varepsilon}$ and $\boldsymbol{\sigma}^{\varepsilon}$ are the displacement and the stress fields.

The small strain tensor e_{xij} is defined by

$$e_{xij} = \frac{1}{2}\left(\frac{\partial u_i}{\partial x_j} + \frac{\partial u_j}{\partial x_i}\right) \tag{2.3}$$

with respect to x variables and the elastic coefficients of the isotropic solid part a_{ijkl} are given by:

$$a_{ijkl} = \lambda \delta_{ij}\delta_{kl} + \mu\left(\delta_{ik}\delta_{jl} + \delta_{il}\delta_{jk}\right) \tag{2.4}$$

where λ and μ are Lamé constants.

On the crack faces, we can assume following cases :

- traction free opening

$$\boldsymbol{\sigma}^{\varepsilon}\mathbf{N} = 0;\ [\mathbf{u}^{\varepsilon}\cdot\mathbf{N}] > 0, \tag{2.5}$$

- nonfrictional contact

$$[\boldsymbol{\sigma}^{\varepsilon}\mathbf{N}] = 0;\ \mathbf{N}\boldsymbol{\sigma}^{\varepsilon}\mathbf{N} < 0;\ \mathbf{T}\boldsymbol{\sigma}^{\varepsilon}\mathbf{N} = 0;\ [\mathbf{u}^{\varepsilon}\cdot\mathbf{N}] = 0 \tag{2.6}$$

- frictional contact

$$[\boldsymbol{\sigma}^{\varepsilon}\mathbf{N}] = 0;\ \mathbf{N}\boldsymbol{\sigma}^{\varepsilon}\mathbf{N} < 0;\ [\mathbf{u}^{\varepsilon}\cdot\mathbf{N}] = 0 \tag{2.7}$$

  If

$$|\mathbf{T}\boldsymbol{\sigma}^{\varepsilon}\mathbf{N}| < -\mu_f \mathbf{N}\boldsymbol{\sigma}^{\varepsilon}\mathbf{N} \tag{2.8}$$

  the crack lips are stick.

  If

$$|\mathbf{T}\boldsymbol{\sigma}^{\varepsilon}\mathbf{N}| = -\mu_f \mathbf{N}\boldsymbol{\sigma}^{\varepsilon}\mathbf{N} \tag{2.9}$$

  the crack lips slide.

The first lines of nonfrictional and frictional case represent the contact conditions, which means that penetration between crack lips is avoided. The last two lines introduce frictional behaviour (stick and sliding). In the conditions above, $\mathbf{N}$ and $\mathbf{T}$ are the unit normal and tangent vectors to the crack surface, respectively. $[\cdot]$ represents the jump across the crack faces and μ_f is the Coulomb coefficient.

We assume that one of states, defined by conditions (2.5-2.9), holds in all the crack points, so each micro-crack can be completely open or close with and without friction. For small lengths of the crack this assumption seems reasonable. The way how to switch from one state to the other will be presented later, in terms of homogenized solution.

For the crack evolution we consider a Griffith-type energy criterion ([40]). This means that propagation can occur when the energy release rate at the crack tip $\mathcal{G}^\varepsilon$ reaches the critical energy threshold $\mathcal{G}_{cr}$:

$$\mathcal{G}^\varepsilon = \mathcal{G}_{cr} \tag{2.10}$$

where $\mathcal{G}_{cr}$ is a material parameter.

When

$$\mathcal{G}^\varepsilon < \mathcal{G}_{cr} \tag{2.11}$$

the evolution of the crack is not possible.

All the propagation equations can be summarized in the Kuhn-Tucker form:

$$\mathcal{G}^\varepsilon - \mathcal{G}_{cr} \leq 0; \qquad \dot{d} \geq 0; \qquad \dot{d}\,(\mathcal{G}^\varepsilon - \mathcal{G}_{cr}) = 0 \tag{2.12}$$

where $\dot{d} \geq 0$ expresses the irreversibility condition.

The energy release rate at each crack tip, for its smooth propagation, is given by the formula ([37]):

$$\mathcal{G}^\varepsilon = \lim_{r \to 0} \int_{\Gamma_r} \mathbf{e} \cdot \mathbf{b}\,(\mathbf{u}^\varepsilon)\,\mathbf{n}\,ds \tag{2.13}$$

where Γ_r is a circle of infinitesimal radius surrounding the crack tip, $\mathbf{e}$ is the unit vector in the propagation direction and $b_{ij}\,(\mathbf{u}^\varepsilon)$ is the Eshelby configurational stress tensor:

$$b_{ij}\,(\mathbf{u}^\varepsilon) = \frac{1}{2} a_{mnkl} e_{xkl}\,(\mathbf{u}^\varepsilon)\, e_{xmn}\,(\mathbf{u}^\varepsilon)\,\delta_{ij} - \sigma^\varepsilon_{jk} u^\varepsilon_{k,i} \tag{2.14}$$

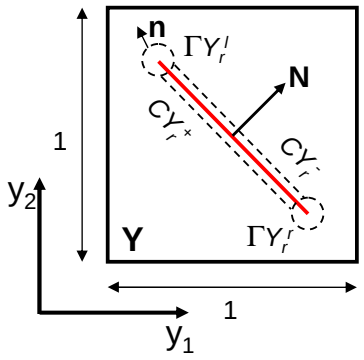

Figure 2.2: Crack geometry in the unit cell.

2.3 Homogenization by asymptotic developments

We consider the unit cell $Y = [0,1] \times [1,0]$ like in figure 2.2, which contains a crack CY of length $d = \frac{d^\varepsilon}{\varepsilon}$. The solid part of the unit cell is defined by $Y_s = {}^{Y}/_{CY}$. This damage variable can vary from 0 to 1, because it is defined as the projection of the crack on the cell axis.

The locally periodic microstructure is obtained by rescaling the unit cell by a small parameter ε (see Fig.2.3). In such a way the parameter ε becomes a natural microscopic length scale. The homogenization method requires the separation of the scales, and two different variables $\mathbf{x}$ and $\mathbf{y}$ must be introduced in order to formulate it mathematically. Variable $\mathbf{x}$ represents the macroscopic scale and variable $\mathbf{y}$ the microscopic one. The assumption that microstructural length is small enough with respect to a macroscopic characteristic length is necessary to proceed with the homogenization method. The macroscopic length is defined here as the characteristic dimension of the whole body. Therefore, the distinction between micro- and macroscopic variations is possible. These two variables are linked by the relation $\mathbf{y} = {}^{\mathbf{x}}/_{\varepsilon}$ so the total derivative with respect to $\mathbf{x}$ is:

$$\frac{d}{dx_i} = \frac{\partial}{\partial x_i} + \frac{1}{\varepsilon}\frac{\partial}{\partial y_i} \tag{2.15}$$

Following the homogenization by asymptotic developments we assume the expansions of $\mathbf{u}^\varepsilon$ and $\boldsymbol{\sigma}^\varepsilon$ in the form (e.g. Benssousan et al.,1978 [14], Bakhvalov and Panasenko,1989 [10]):

$$\mathbf{u}^\varepsilon(\mathbf{x},t) = \mathbf{u}^{(0)}(\mathbf{x},\mathbf{y},t) + \varepsilon\mathbf{u}^{(1)}(\mathbf{x},\mathbf{y},t) + \varepsilon^2\mathbf{u}^{(2)}(\mathbf{x},\mathbf{y},t) + \dots \tag{2.16}$$

$$\boldsymbol{\sigma}^\varepsilon(\mathbf{x},t) = \frac{1}{\varepsilon}\boldsymbol{\sigma}^{(-1)}(\mathbf{x},\mathbf{y},t) + \boldsymbol{\sigma}^{(0)}(\mathbf{x},\mathbf{y},t) + \varepsilon\boldsymbol{\sigma}^{(1)}(\mathbf{x},\mathbf{y},t) + \dots \tag{2.17}$$

where for $\mathbf{x} \in \mathcal{B}_\mathfrak{s}$, $\mathbf{y} \in Y$, $\mathbf{u}^{(i)}(\mathbf{x},\mathbf{y},t)$ and $\boldsymbol{\sigma}^{(i)}(\mathbf{x},\mathbf{y},t)$ are smooth functions and Y-periodic in $\mathbf{y}$.

Substituting the expansions of $\mathbf{u}^\varepsilon$ and $\boldsymbol{\sigma}^\varepsilon$ into the equilibruim equation (2.1) and grouping the terms corresponding to the same power of ε we obtain the following boundary problems:

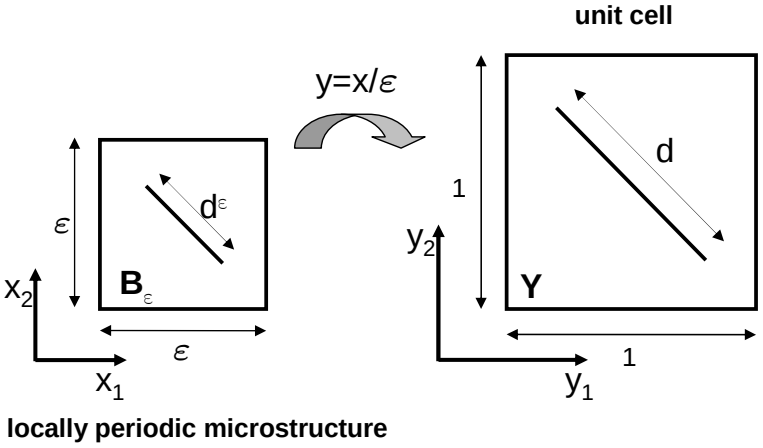

Figure 2.3: Rescaling of the unit cell to the microstructural period of the material.

$$\frac{\partial \sigma_{ij}^{(-1)}}{\partial y_j} = 0, \qquad \frac{\partial \sigma_{ij}^{(-1)}}{\partial x_j} + \frac{\partial \sigma_{ij}^{(0)}}{\partial y_j} = 0, \qquad \frac{\partial \sigma_{ij}^{(0)}}{\partial x_j} + \frac{\partial \sigma_{ij}^{(1)}}{\partial y_j} = 0 \tag{2.18}$$

Combining the constitutive relation (2.2) and the definition (2.3) throw Eqs.(2.16) and (2.17) we can get correspondingly:

$$\sigma_{ij}^{(-1)} = a_{ijkl} e_{ykl}\left(\mathbf{u}^{(0)}\right),$$

$$\sigma_{ij}^{(0)} = a_{ijkl}\left(e_{xkl}\left(\mathbf{u}^{(0)}\right) + e_{ykl}\left(\mathbf{u}^{(1)}\right)\right), \tag{2.19}$$

$$\sigma_{ij}^{(1)} = a_{ijkl}\left(e_{xkl}\left(\mathbf{u}^{(1)}\right) + e_{ykl}\left(\mathbf{u}^{(2)}\right)\right).$$

Concerning the boundary conditions on the crack face, for the open cracks we get:

$$\sigma_{ij}^{(-1)} N_j = 0,\ \sigma_{ij}^{(0)} N_j = 0,\ \sigma_{ij}^{(1)} N_j = 0, \text{ on } CY^{\pm} \tag{2.20}$$

and for nonfrictional closed cracks for different powers of ε ($m = -1, 0, 1$) we obtain:

$$\left[\sigma_{ij}^{(m)} N_j\right] = 0,\ N_i \sigma_{ij}^{(m)} N_j < 0,\ T_i \sigma_{ij}^{(m)} N_j = 0, \text{ on } CY^{\pm} \tag{2.21}$$

In the case of frictional closed cracks, the first two in (2.21) still hold:

$$\left[\sigma_{ij}^{(m)} N_j\right] = 0,\ N_i \sigma_{ij}^{(m)} N_j < 0, \text{ on } CY^{\pm} \tag{2.22}$$

and from the first relation in (2.22) we get:

$$\left[T_i \sigma_{ij}^{(m)} N_j\right] = 0, \text{ on } CY^{\pm} \tag{2.23}$$

Additionaly to the contact conditions, one of the two conditions holds:

$$\text{if} |T_i \sigma_{ij}^{(m)} N_j| < -\mu_f N_i \sigma_{ij}^{(m)} N_j, \text{ the crack lips are stick on } CY^{\pm} \tag{2.24}$$

$$\text{if} |T_i \sigma_{ij}^{(m)} N_j| = -\mu_f N_i \sigma_{ij}^{(m)} N_j, \text{ the crack lips are sliding on } CY^{\pm} \tag{2.25}$$

Taking into account all the conditions presented above, we can write boundary-value problems of different order in ε $(\mathbf{u}^{(0)}, \mathbf{u}^{(1)}, \mathbf{u}^{(2)})$. The boundary-value problem for $\mathbf{u}^{(0)}$ has a form :

$$\frac{\partial}{\partial y_j}\left(a_{ijkl} e_{ykl}\left(\mathbf{u}^{(0)}\right)\right) = 0 \text{ in } Y_s \tag{2.26}$$

$$\left(a_{ijkl} e_{ykl}\left(\mathbf{u}^{(0)}\right)\right) N_j = 0 \text{ on } CY^{\pm} \tag{2.27}$$

The first order boundary-value problem is determined by the terms of the first order in ε. The cell problems can be written for different states of the crack, knowing $\mathbf{u}^{(0)}(\mathbf{x}, t)$ and with periodic boundary condition on the external cell boundary.

For open cracks we have:

$$\frac{\partial}{\partial y_j}\left(a_{ijkl} e_{ykl}\left(\mathbf{u}^{(1)}\right)\right) = 0 \text{ in } Y_s \tag{2.28}$$

$$\left(a_{ijkl} e_{ykl}\left(\mathbf{u}^{(1)}\right)\right) N_j = -\left(a_{ijkl} e_{xkl}\left(\mathbf{u}^{(0)}\right)\right) N_j \text{ on } CY^{\pm} \tag{2.29}$$

For closed cracks (non-frictional and frictional) we have:

$$\frac{\partial}{\partial y_j}\left(a_{ijkl} e_{ykl}\left(\mathbf{u}^{(1)}\right)\right) = 0 \text{ in } Y_s \tag{2.30}$$

In the presence of non-frictional cracks:

$$\left[\left(a_{ijkl} e_{ykl}\left(\mathbf{u}^{(1)}\right)\right) N_j\right] = 0 \tag{2.31}$$

$$N_i a_{ijkl}\left(e_{ykl}\left(\mathbf{u}^{(1)}\right) + e_{xkl}\left(\mathbf{u}^{(0)}\right)\right) N_j < 0 \tag{2.32}$$

$$T_i a_{ijkl}\left(e_{ykl}\left(\mathbf{u}^{(1)}\right)+e_{xkl}\left(\mathbf{u}^{(0)}\right)\right)N_j=0 \tag{2.33}$$

In the presence of friction, together with (2.31) and (2.32), the additional boundary condition is introduced:

$$T_i a_{ijkl}\left(e_{ykl}\left(\mathbf{u}^{(1)}\right)+e_{xkl}\left(\mathbf{u}^{(0)}\right)\right)N_j =$$

$$-\mu_f N_i a_{ijkl}\left(e_{ykl}\left(\mathbf{u}^{(1)}\right)+e_{xkl}\left(\mathbf{u}^{(0)}\right)\right)N_j \text{ on } CY \tag{2.34}$$

The homogenization procedure adopted here is based on the first order of cell solution.

As mentioned before, the solution of the problem is determined by microscopic states of contact and opening. In order to distinguish between these states, the following approximation is proposed. On the crack faces of the unit cell, one has the condition (2.29), in which the microscopic solution appears within a force-type source term. The orientation of this force vector with respect to the crack line (i.e. the tendency of this force to open or close the crack) may be considered as an indicator of the opening or closing state. At the microscopic level, these two states induce a seperation of the space $\mathbf{R}$ of deformations $e_{x11}, e_{x12}, e_{x22}$ into two subregions $\mathbf{R}^{\pm}$ defined by ([25]):

$$\mathbf{R}^{\pm}=\left\{\mathbf{e_x} \mid N_i a_{ijkl} e_{xkl}\left(\mathbf{u}^{(0)}\right)N_j \gtrless 0\right\} \tag{2.35}$$

In case of frictional behaviour the subregion $\mathbf{R}^{-}$(corresponding to the closed cracks) is divided into three subregions, where cracks can slide in two different manners (lets say left and right) or the crack lips are stick. These regions are defined by:

$$\mathbf{D}^R=\{\mathbf{e_x} \mid N_i a_{ijkl} e_{xkl}\left(\mathbf{u}^{(0)}\right)N_j<0;\, T_i a_{ijkl} e_{xkl}\left(\mathbf{u}^{(0)}\right)N_j>0 \text{ and}$$
$$|T_i a_{ijkl} e_{xkl}\left(\mathbf{u}^{(0)}\right)N_j| \geq -\mu_f N_i a_{ijkl} e_{xkl}\left(\mathbf{u^{(0)}}\right)N_j\} \tag{2.36}$$

$$\mathbf{D}^L=\{\mathbf{e_x} \mid N_i a_{ijkl} e_{xkl}\left(\mathbf{u}^{(0)}\right)N_j<0;\, T_i a_{ijkl} e_{xkl}\left(\mathbf{u}^{(0)}\right)N_j<0 \text{ and}$$

$$|T_i a_{ijkl} e_{xkl}\left(\mathbf{u}^{(0)}\right)N_j| \geq -\mu_f N_i a_{ijkl} e_{xkl}\left(\mathbf{u}^{(0)}\right)N_j\} \tag{2.37}$$

$$\mathbf{S}=\{\mathbf{e_x} \mid N_i a_{ijkl} e_{xkl}\left(\mathbf{u}^{(0)}\right)N_j<0 \text{ and}$$

$$|T_i a_{ijkl} e_{xkl}\left(\mathbf{u}^{(0)}\right)N_j| < -\mu_f N_i a_{ijkl} e_{xkl}\left(\mathbf{u}^{(0)}\right)N_j\} \tag{2.38}$$

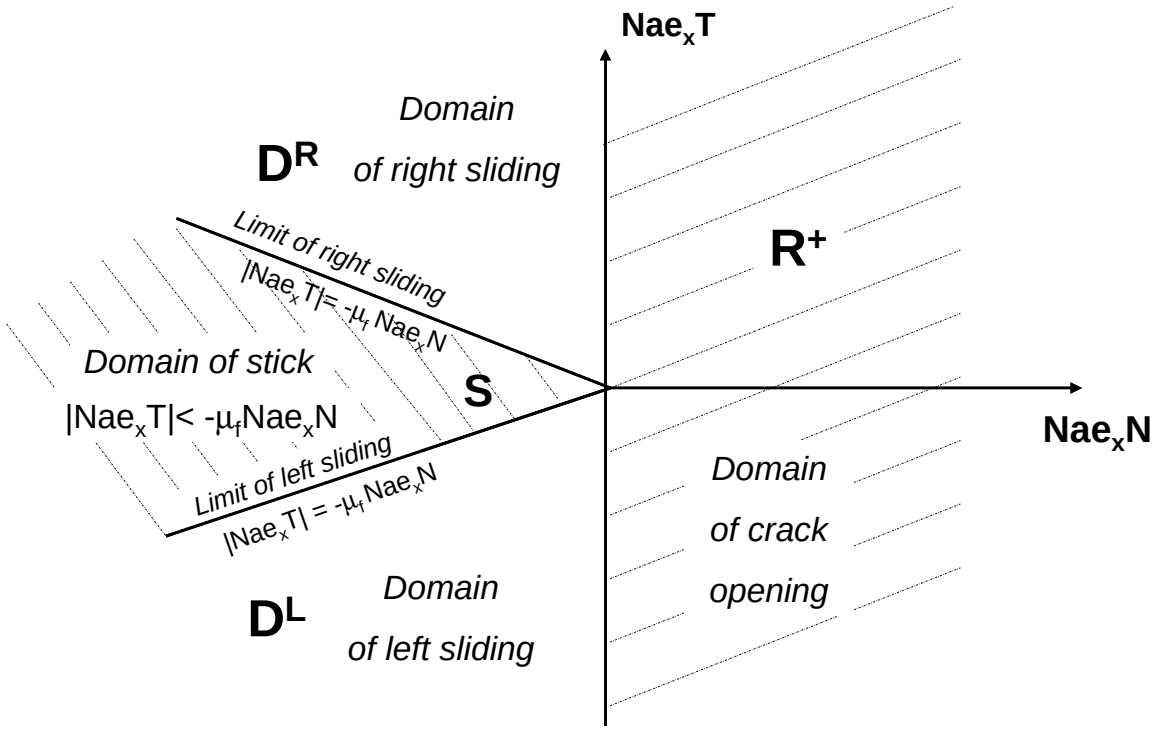

Figure 2.4: Domains of linearity in space $\mathbf{R}$ of deformations $e_{x11}, e_{x12}, e_{x22}$.

where $\mathbf{T}$ and $\mathbf{N}$ are tangent and normal unit vector, respectively. $\mathbf{D}^R$, $\mathbf{D}^L$ are the linear domains of right and left sliding, $\mathbf{S}$ is the domain of stick and μ_f is the friction coefficient. These different states are illustrated in figure 2.4.

In each regime the first order perturbation $\mathbf{u}^{(1)}$ can be written as linear function of $\mathbf{e_x}\left(\mathbf{u}^{(0)}\right)$.

Choosing a system of generators $\mathbf{E}^{pq}$ (for macroscopic deformations) in each domain such that $E_{ij}^{pq} = \delta_{ip}\delta_{jq}$ for $\mathbf{R}^+$and $E_{ij}^{pq} = -\delta_{ip}\delta_{jq}$ for $\mathbf{R}^-$, the macroscopic deformation $\mathbf{e_x}\left(\mathbf{u}^{(0)}\right)$ can be written as a linear combination of these elements, for instance in the case of $\mathbf{R}^+$:

$$e_{xij}\left(\mathbf{u}^{(0)}\right) = e_{x11}E_{ij}^{11} + e_{x12}E_{ij}^{12} + e_{x21}E_{ij}^{21} + e_{x22}E_{ij}^{22}$$

In each regime (opening or closure), the solution $\mathbf{u}^{(1)}$ can be written in the form

$$\mathbf{u}^{(1)}(\mathbf{x},\mathbf{y},t) = \boldsymbol{\xi}^{pq}(\mathbf{y})\, e_{xpq}\left(\mathbf{u}^{(0)}\right)(\mathbf{x},t) \tag{2.39}$$

where the characteristic funtions $\boldsymbol{\xi}^{pq}(\mathbf{y})$ are the elementary solutions of the cell problem (e.g. for openning case (2.28) and (2.29)), in which we took $e_{xij}\left(\mathbf{u}^{(0)}\right) = E_{ij}^{pq}$.

Basically, this approch is valid in case of opening and closing without friction. To take into account friction some more transformations have to be done. The reason comes from the fact that the region of closing is divided into subregions of sliding. For each domain of sliding, the system of generators $\bar{E}^{pq}$ has to be chosen to respect the sense of sliding

(left and right). In this case the macroscopic deformation $\mathbf{e_x}\left(\mathbf{u}^{(0)}\right)$ can be written as a linear combination of these elements :

$$e_{xij}\left(\mathbf{u}^{(0)}\right) = \alpha_{pq}\left(\mathbf{u}^{(0)}\right)\bar{E}_{ij}^{pq} = \alpha_{11}\bar{E}_{ij}^{11} + \alpha_{12}\bar{E}_{ij}^{12} + \alpha_{21}\bar{E}_{ij}^{21} + \alpha_{22}\bar{E}_{ij}^{22} \tag{2.40}$$

where α_{pq} are linear functions of $\mathbf{u}^{(0)}$ and $\bar{E}_{ij}^{pq}$ are different with respect to E_{ij}^{pq}.

Let the vector $\boldsymbol{\eta}^{pq}$ be a particular solution for $e_{xij}\left(\mathbf{u}^{(0)}\right) = \bar{E}_{ij}^{pq}$, the solution $\mathbf{u}^{(1)}$ can be written as:

$$\mathbf{u}^{(1)}(\mathbf{x},\mathbf{y},t) = \boldsymbol{\eta}^{pq}(\mathbf{y})\,\alpha_{pq}(\mathbf{x},t) \tag{2.41}$$

The objective of this work is to study the frictional behaviour, so the following developments will be focused on this case. The first order cell solution, equivalent to (2.30)-(2.34), can be now written in terms of $\boldsymbol{\eta}^{pq}$:

$$\frac{\partial}{\partial y_j}\left(a_{ijkl}e_{ykl}\left(\boldsymbol{\eta}^{pq}\right)\right) = 0 \text{ in } Y_s \tag{2.42}$$

$$\left[\left(a_{ijkl}e_{ykl}\left(\boldsymbol{\eta}^{pq}\right)\right)N_j\right] = -\left[a_{ijkl}\bar{E}_{kl}^{pq}N_j\right] \text{ on } CY \tag{2.43}$$

$$N_i a_{ijkl}\left(e_{ykl}\left(\boldsymbol{\eta}^{pq}\right) + \bar{E}_{kl}^{pq}\right)N_j < 0 \text{ on } CY \tag{2.44}$$

$$T_i a_{ijkl}\left(e_{ykl}\left(\boldsymbol{\eta}^{pq}\right) + \bar{E}_{kl}^{pq}\right)N_j = \pm\mu_f N_i a_{ijkl}\left(e_{ykl}\left(\boldsymbol{\eta}^{pq}\right) + \bar{E}_{kl}^{pq}\right)N_j \text{ on } CY \tag{2.45}$$

for sliding micro-cracks. The signs $\pm$ in the relation (2.45) are associated with the sense of sliding, "+" for $\bar{\mathbf{E}}^{pq} \in \mathbf{D}^R$ and "−" for $\bar{\mathbf{E}}^{pq} \in \mathbf{D}^L$.

Introducing the averaged value operator for $\sigma_{ij}^{(0)}$we get:

$$\frac{\partial}{\partial x_j} < \sigma_{ij}^{(0)} >= 0 \tag{2.46}$$

and

$$\Sigma_{ij}^{(0)} \equiv < \sigma_{ij}^{(0)} > \tag{2.47}$$

or

$$\Sigma_{ij}^{(0)} = \frac{1}{\mid Y \mid}\int_{Y_s}\left(a_{ijkl}e_{xkl}\left(\mathbf{u}^{(0)}\right) + a_{ijkl}e_{ykl}\left(\mathbf{u}^{(1)}\right)\right)dy \tag{2.48}$$

Using a general macroscopic deformation, in each domain of linearity (2.40) and the form (2.41) for solution $\mathbf{u}^{(1)}$ we get:

$$\Sigma_{ij}^{(0)} = \frac{1}{\mid Y \mid} \int_{Y_s} \left(a_{ijkl} \bar{E}_{kl}^{mn} + a_{ijkl} e_{ykl} \left(\boldsymbol{\eta}^{mn} \right) \right) dy \, \alpha_{mn} \left(\mathbf{u}^{(0)} \right) \tag{2.49}$$

which can be written as

$$\Sigma_{ij}^{(0)} = C_{ijmn}^{\alpha} \alpha_{mn} \left(\mathbf{u}^{(0)} \right) \tag{2.50}$$

where

$$C_{ijmn}^{\alpha} = \frac{1}{\mid Y \mid} \int_{Y_s} \left(a_{ijkl} \bar{E}_{kl}^{mn} + a_{ijkl} e_{ykl} \left(\boldsymbol{\eta}^{mn} \right) \right) dy \tag{2.51}$$

are the effective or homogenized coefficients. Since $\mid Y \mid = 1$, in what follows $\mid Y \mid$ will be omitted.

Therefore we can write:

$$\Sigma_{ij}^{(0)} = C_{ijmn} e_{xmn} \left(\mathbf{u}^{(0)} \right) \tag{2.52}$$

where C_{ijmn} are obtained as a combination of C_{ijmn}^{α}. The values of C_{ijmn} depend on domains $\mathbf{D}^R$ and $\mathbf{D}^L$ and they are not symmetric in each domain, because in the case of frictional crack the sliding domains have to be respected. The symmetry depends on the chosen system of generators. For nonfrictional contacting and open crack, the C_{ijmn} is symmetric ([17]) because the symmetric system of generators can be chosen. For frictional cracks, we retrieve the classical symmetry of the coefficients by comparing those corresponding to two senses of sliding. For instance : $C_{1111}^R = C_{2222}^L$.

All the developments presented until now are correct only for loading phase, when the cracks slide. For unloading phases, some additional developments and assumptions have to be made. Due to friction, during unloading the cracks stop to slide and they are under stick condition up to a certain point when cracks start to slide again in the opposite direction (back slide). In this case, the homogenized behaviour includes the permament slip, which is obtained under the condition:

$$\frac{d[\mathbf{u}^{\varepsilon} \mathbf{T}]}{dt} = 0 \tag{2.53}$$

The second term of the homogenized equation (2.48) can be written as:

$$\int_{Y_s} a_{ijkl} e_{ykl} \left(\mathbf{u}^{(1)} \right) dy = \frac{1}{2} a_{ijkl} \int_{Y_s} \left(\frac{\partial u_k^{(1)}}{\partial y_l} + \frac{\partial u_l^{(1)}}{\partial y_k} \right) dy \tag{2.54}$$

Using the divergence theorem we obtain:

$$\frac{1}{2}a_{ijkl}\int_{Y_s}\left(\frac{\partial u_k^{(1)}}{\partial y_l}+\frac{\partial u_l^{(1)}}{\partial y_k}\right)dy=\frac{1}{2}a_{ijkl}\int_{CY}\left(\left[u_k^{(1)}\right]N_l+\left[u_l^{(1)}\right]N_k\right)ds_y \tag{2.55}$$

Assuming that $\left[u_m^{(1)}N_m\right]$=0, the jump of displacement can be written in terms of only tangential component and it has following form: $\left[u_k^{(1)}\right]=\left[u_m^{(1)}T_m\right]T_k$. This implies the homogenized behaviour for the stick case in the form:

$$\Sigma_{ij}^{(0)}=a_{ijkl}\left(e_{xkl}\left(\mathbf{u}^{(0)}\right)+e_{kl}^{p}\left(\mathbf{u}^{(1)}\right)\right) \tag{2.56}$$

where $e_{kl}^{p}\left(\mathbf{u}^{(1)}\right)$ represents the inelastic part of deformation and it is formulated as follows:

$$e_{kl}^{p}=\frac{1}{2}\left(T_kN_l+T_lN_k\right)\int_{CY}\left[u_m^{(1)}T_m\right]ds_y \tag{2.57}$$

N and **T** are unit normal and tangential vectors to the crack line, respectively.

The equivalent form of (2.57) written in terms of $\boldsymbol{\eta}^{pq}$ is:

$$e_{kl}^{p}=\frac{1}{2}\left(T_kN_l+T_lN_k\right)\int_{CY}\left[\eta_m^{pq}T_m\right]ds_y \tag{2.58}$$

The Coulomb friction criterion (2.34) has to include also the inelastic terms, in order to satisfy the sliding and stick conditions during unloading. The switch between these different states should be done at the macroscopic level. At this level a good approximation is to integrate the formulations of tangential and normal components of the stress in (2.34) over the crack. We define:

$$\mathbb{T}\equiv T_ia_{ijkl}e_{xkl}\left(\mathbf{u}^{(0)}\right)N_j\int_{CY}ds_y+\int_{CY}\left(T_ia_{ijkl}e_{ykl}\left(\mathbf{u}^{(1)}\right)N_j\right)ds_y \tag{2.59}$$

$$\mathbb{N}\equiv N_ia_{ijkl}e_{xkl}\left(\mathbf{u}^{(0)}\right)N_j\int_{CY}ds_y+\int_{CY}\left(N_ia_{ijkl}e_{ykl}\left(\mathbf{u}^{(1)}\right)N_j\right)ds_y \tag{2.60}$$

They can be expressed with respect to characteristic functions using (2.40) and (2.41):

$$\mathbb{T}^{pq}\equiv T_ia_{ijkl}\bar{E}_{kl}^{pq}N_j\int_{CY}ds_y+\int_{CY}\left(T_ia_{ijkl}e_{ykl}\left(\boldsymbol{\eta}^{pq}\right)N_j\right)ds_y \tag{2.61}$$

$$\mathbb{N}^{pq}\equiv N_ia_{ijkl}\bar{E}_{kl}^{pq}N_j\int_{CY}ds_y+\int_{CY}\left(N_ia_{ijkl}e_{ykl}\left(\boldsymbol{\eta}^{pq}\right)N_j\right)ds_y \tag{2.62}$$

The condition defining the sliding regime can be formulated in general form as:

$$\mathbb{N}<0,\qquad \mid\mathbb{T}\mid=-\mu_f\mathbb{N} \tag{2.63}$$

and the condition defining stationary contact as:

$$\mathbb{N} < 0, \qquad |\,\mathbb{T}\,| < -\mu_f \mathbb{N} \tag{2.64}$$

In the stick regime, during unloading, the terms representing inelastic contribution can be deduced from the cell problem:

$$div_y\left(\mathbf{a}\mathbf{e}_{\mathbf{y}}\left(\mathbf{u}^{(1)}\right)\right) = 0 \tag{2.65}$$

$$\left[u_m^{(1)} N_m\right] = 0 \text{ on } CY \tag{2.66}$$

$$\left[u_m^{(1)} T_m\right] = f(\mathbf{y}) \text{ on } CY \tag{2.67}$$

$$\left[\boldsymbol{\sigma}^{(0)}\mathbf{N}\right] = 0 \text{ on } CY \tag{2.68}$$

Here, the $f(\mathbf{y})$ does not depend on t as in (2.53) and it corresponds to the last loading step before unloading.

During unloading, together with periodic boundary conditions on the external boundaries, the equilibrium equation (2.65) and boundary conditions like (2.66)-(2.68) do not depend on $\mathbf{e}_{\mathbf{x}}\left(\mathbf{u}^{(0)}\right)$, so that, the solution $u_m^{(1)}$ remains constant. We define inelastic terms as:

$$\mathbb{T}_{un} \equiv \int_{CY}\left(T_i a_{ijkl} e_{ykl}\left(\mathbf{u}^{(1)}\right) N_j\right) ds_y \tag{2.69}$$

$$\mathbb{N}_{un} \equiv \int_{CY}\left(N_i a_{ijkl} e_{ykl}\left(\mathbf{u}^{(1)}\right) N_j\right) ds_y \tag{2.70}$$

and their equivalent forms written with respect to characteristic functions are:

$$\mathbb{T}_{un}^{pq} \equiv \int_{CY}\left(T_i a_{ijkl} e_{ykl}\left(\boldsymbol{\eta}^{pq}\right) N_j\right) ds_y \tag{2.71}$$

$$\mathbb{N}_{un}^{pq} \equiv \int_{CY}\left(N_i a_{ijkl} e_{ykl}\left(\boldsymbol{\eta}^{pq}\right) N_j\right) ds_y \tag{2.72}$$

The condition defining the stick limit in unloading phase can be formulated in general form as:

$$\mathbb{N} < 0, \qquad |\,\mathbb{T}\,| < -\mu_f \mathbb{N} \tag{2.73}$$

with constant $\mathbb{T}_{un}$ and $\mathbb{N}_{un}$, computed for the last configuration of loading, the crack lips are stick.

When the relations in (2.73) are no more satisfied, under the same loading direction, the backsliding (*left or right*) starts and it is described by sliding conditions in the opposite direction.

2.4 Energy analysis

The damage law is deduced from the micromechanical energy balance on the unit cell containing one evolving micro-crack. The trajectory of the propagation is assumed to be smooth and known. The propapagation of the tips is symmetric with respect to its center and the micro-crack evolution is completly described by the change of its length. The energy analysis is done for general boundary conditions on the crack lips in the form:

$$\left[\boldsymbol{\sigma}^{(0)}\mathbf{N}\right] = 0 \tag{2.74}$$

For the energy balance on the unit cell the following results were proved in [25].

Proposition1: Under the continuity condition (2.74), the energy balance during the evolution of the micro-crack was proved in the form :

$$\frac{d}{dt}\int_{Y\,s}\frac{1}{2}a_{ijkl}e_{ykl}(\mathbf{u}^{(1)})e_{yij}\left(\mathbf{u}^{(1)}\right)dy + \mathcal{G}_y\dot{d} = \int_{CY}a_{ijkl}e_{ykl}\left(\mathbf{u}^{(1)}\right)N_j\left[\dot{u}_i^{(1)}\right]ds_y \tag{2.75}$$

with

$$\mathcal{G}_y = \lim_{r\to 0}\int_{\Gamma Y_r}\mathbf{e}\cdot\mathbf{b}\left(\mathbf{u}^{(1)}\right)\mathbf{n}\,ds_y$$

where

$$b_{ij}\left(\mathbf{u}^{(1)}\right) = U\left(\mathbf{u}^{(1)}\right)\delta_{ij} - \sigma_{ik}\left(\mathbf{u}^{(1)}\right)\frac{\partial u_k^{(1)}}{\partial y_j}$$

$$U\left(\mathbf{u}^{(1)}\right) = \frac{1}{2}a_{ijkl}e_{ykl}\left(\mathbf{u}^{(1)}\right)e_{ymn}\left(\mathbf{u}^{(1)}\right) \tag{2.76}$$

$$\sigma_{ik}\left(\mathbf{u}^{(1)}\right) = a_{iklm}e_{ylm}\left(\mathbf{u}^{(1)}\right)$$

Proposition 2: Under the condition $\left[\sigma_{ij}^{(0)}N_j = 0\right]$ on the crack lips of an evolving crack CY of length $d(t)$ in the unit cell it was proved that:

$$\frac{1}{2}\dot{d}\frac{dC_{ijkl}}{dd}e_{xkl}\left(\mathbf{u}^{(0)}\right)e_{xij}\left(\mathbf{u}^{(0)}\right) + \mathcal{G}_y\dot{d} + \frac{d}{dt}\int_{CY}\frac{1}{2}\sigma_{ij}^{(0)}N_j\left[u_i^{(1)}\right]ds_y - \int_{CY}\sigma_{ij}^{(0)}N_j\left[\dot{u}_i^{(1)}\right]ds_y = 0 \tag{2.77}$$

The proofs presented in [25] play an important role in the further developmnents of the damage evolution law.

2.5 Damage evolution law

To construct the damage evolution law for frictional sliding micro-cracks, we use the properties of homogenized solution and the scaling relation for energy release rate. We write the relation (2.77) in equivalent form:

$$\frac{1}{2}\frac{d}{dt}\int_{Y_s} a_{ijkl}e_{xkl}\left(\mathbf{u}^{(0)}\right)e_{yij}\left(\mathbf{u}^{(1)}\right)dy - \int_{Y_s} a_{ijkl}e_{xkl}\left(\dot{\mathbf{u}}^{(0)}\right)e_{yij}\left(\mathbf{u}^{(1)}\right)dy +$$

$$\frac{1}{2}\frac{d}{dt}\int_{CY}\left(a_{ijkl}e_{xkl}\left(\mathbf{u}^{(0)}\right)+a_{ijkl}e_{ykl}\left(\mathbf{u}^{(1)}\right)\right)N_j\left[u_i^{(1)}\right]ds_y -$$

$$\int_{CY}\left(a_{ijkl}e_{xkl}\left(\mathbf{u}^{(0)}\right)+a_{ijkl}e_{ykl}\left(\mathbf{u}^{(1)}\right)\right)N_j\left[\dot{u}_i^{(1)}\right]ds_y+\mathcal{G}_y\dot{d}=0 \tag{2.78}$$

In the following step, the integrals in (2.78) can be expressed in terms of characteristic functions $\boldsymbol{\eta}^{pq}$ using (2.40) and (2.41). The first two integrals can be written:

$$\frac{1}{2}\frac{d}{dt}\int_{Y_s} a_{ijkl}e_{xkl}\left(\mathbf{u}^{(0)}\right)e_{yij}\left(\mathbf{u}^{(1)}\right)dy - \int_{Y_s} a_{ijkl}e_{xkl}\left(\dot{\mathbf{u}}^{(0)}\right)e_{yij}\left(\mathbf{u}^{(1)}\right)dy =$$

$$\frac{1}{2}\frac{d}{dt}\int_{Y_s} a_{ijkl}\bar{E}_{kl}^{mn}e_{yij}\left(\boldsymbol{\eta}^{pq}\right)dy\,\alpha_{mn}\left(u^{(0)}\right)\alpha_{pq}\left(u^{(0)}\right) -$$

$$\frac{1}{2}\int_{Y_s} a_{ijkl}\bar{E}_{kl}^{mn}e_{yij}\left(\boldsymbol{\eta}^{pq}\right)dy\left(\alpha_{mn}\left(\dot{\mathbf{u}}^{(0)}\right)\alpha_{pq}\left(\mathbf{u}^{(0)}\right)-\alpha_{mn}\left(\mathbf{u}^{(0)}\right)\alpha_{pq}\left(\dot{\mathbf{u}}^{(0)}\right)\right) \tag{2.79}$$

Taking into account the symmetry of the elastic tensor a_{ijkl} and the relation (2.51), the integral $\int_{Y_s} a_{ijkl}e_{yij}\left(\boldsymbol{\eta}^{pq}\right)dy$, can be formulated as follows:

$$\int_{Y_s} a_{klij}e_{yij}\left(\boldsymbol{\eta}^{pq}\right)dy = C_{klpq}^{\alpha} - a_{klij}\bar{E}_{ij}^{pq} \tag{2.80}$$

Substituting (2.80) into the first integral of the right part of the relation (2.79) and using the fact that the only term depending on t is C_{klpq}^{α}, we can write:

$$\frac{1}{2}\frac{d}{dt}\int_{Y_s} a_{ijkl}\bar{E}_{kl}^{mn}e_{yij}\left(\boldsymbol{\eta}^{pq}\right)dy\alpha_{mn}\left(\mathbf{u}^{(0)}\right)\alpha_{pq}\left(\mathbf{u}^{(0)}\right)=\frac{1}{2}\frac{dC_{klpq}^{\alpha}}{dt}\bar{E}_{kl}^{mn}\alpha_{mn}\left(\mathbf{u}^{(0)}\right)\alpha_{pq}\left(\mathbf{u}^{(0)}\right) \tag{2.81}$$

The second integral in (2.78) can be transformed into the expression over crack lips. Using the symmetric properties of the elastic tensor a_{ijkl} and the periodic conditions on the external boundary of the cell we can write:

$$\int_{Y_s} a_{klij} e_{yij}\left(\boldsymbol{\eta}^{pq}\right) dy = \int_{CY} a_{ijkl}\left[\eta_i^{pq}\right] N_j ds_y \tag{2.82}$$

and finally we obtain:

$$\frac{1}{2}\int_{Y_s} a_{ijkl}\bar{E}_{kl}^{mn} e_{yij}\left(\boldsymbol{\eta}^{pq}\right) dy \left(\alpha_{mn}\left(\dot{\mathbf{u}}^{(0)}\right)\alpha_{pq}\left(\mathbf{u}^{(0)}\right) - \alpha_{mn}\left(\mathbf{u}^{(0)}\right)\alpha_{pq}\left(\dot{\mathbf{u}}^{(0)}\right)\right) =$$

$$\frac{1}{2}\int_{CY} a_{ijkl}\bar{E}_{kl}^{mn}\left[\eta_i^{pq}\right] N_j ds_y \left(\alpha_{mn}\left(\dot{\mathbf{u}}^{(0)}\right)\alpha_{pq}\left(\mathbf{u}^{(0)}\right) - \alpha_{mn}\left(\mathbf{u}^{(0)}\right)\alpha_{pq}\left(\dot{\mathbf{u}}^{(0)}\right)\right) \tag{2.83}$$

The third integral in (2.78) has the form:

$$\frac{1}{2}\frac{d}{dt}\int_{CY}\left(a_{ijkl}e_{xkl}\left(\mathbf{u}^{(0)}\right) + a_{ijkl}e_{ykl}\left(\mathbf{u}^{(1)}\right)\right) N_j\left[u_i^{(1)}\right] ds_y =$$

$$\frac{1}{2}\frac{d}{dt}\int_{CY}\left(a_{ijkl}\bar{E}_{kl}^{mn} + a_{ijkl}e_{ykl}\left(\boldsymbol{\eta}^{mn}\right)\right) N_j\left[\eta_i^{pq}\right] ds_y \alpha_{mn}\left(\mathbf{u}^{(0)}\right)\alpha_{pq}\left(\mathbf{u}^{(0)}\right) +$$

$$\frac{1}{2}\int_{CY}\left(a_{ijkl}\bar{E}_{kl}^{mn} + a_{ijkl}e_{ykl}\left(\boldsymbol{\eta}^{mn}\right)\right) N_j\left[\eta_i^{pq}\right] ds_y$$

$$\left(\alpha_{mn}\left(\dot{\mathbf{u}}^{(0)}\right)\alpha_{pq}\left(\mathbf{u}^{(0)}\right) + \alpha_{mn}\left(\mathbf{u}^{(0)}\right)\alpha_{pq}\left(\dot{\mathbf{u}}^{(0)}\right)\right) \tag{2.84}$$

The last term of the (2.78) can be transformed into:

$$\int_{CY}\left(a_{ijkl}e_{xkl}\left(\mathbf{u}^{(0)}\right) + a_{ijkl}e_{ykl}\left(\mathbf{u}^{(1)}\right)\right) N_j\left[\dot{u}_i^{(1)}\right] ds_y =$$

$$\int_{CY}\left(a_{ijkl}\bar{E}_{kl}^{mn} + a_{ijkl}e_{ykl}\left(\boldsymbol{\eta}^{mn}\right)\right) N_j\left[\dot{\eta}_i^{pq}\right] ds_y \alpha_{mn}\left(\mathbf{u}^{(0)}\right)\alpha_{pq}\left(\mathbf{u}^{(0)}\right) +$$

$$\int_{CY}\left(a_{ijkl}\bar{E}_{kl}^{mn} + a_{ijkl}e_{ykl}\left(\boldsymbol{\eta}^{mn}\right)\right) N_j\left[\eta_i^{pq}\right] ds_y \alpha_{mn}\left(\mathbf{u}^{(0)}\right)\alpha_{pq}\left(\dot{\mathbf{u}}^{(0)}\right) \tag{2.85}$$

Substituting the obtained expressions (2.81),(2.83),(2.84),(2.85) into (2.78) we get:

$$\left(\frac{1}{2}\frac{dC_{klpq}^{\alpha}}{dt}\bar{E}_{kl}^{mn} + I_{mnpq}^{\alpha}\right)\alpha_{mn}\left(\mathbf{u}^{(0)}\right)\alpha_{pq}\left(\mathbf{u}^{(0)}\right) +$$

$$S_{mnpq}^{\alpha}\left(\alpha_{mn}\left(\dot{\mathbf{u}}^{(0)}\right)\alpha_{pq}\left(\mathbf{u}^{(0)}\right) - \alpha_{mn}\left(\mathbf{u}^{(0)}\right)\alpha_{pq}\left(\dot{\mathbf{u}}^{(0)}\right)\right) + \mathcal{G}_y\dot{d} = 0 \tag{2.86}$$

where

$$I^{\alpha}_{mnpq} = \frac{1}{2}\frac{d}{dd}\int_{CY}\left(a_{ijkl}\bar{E}^{mn}_{kl} + a_{ijkl}e_{ykl}\left(\boldsymbol{\eta}^{mn}\right)\right)N_j\left[\eta^{pq}_i\right]ds_y -$$

$$\int_{CY}\left(a_{ijkl}\bar{E}^{mn}_{kl} + a_{ijkl}e_{ykl}\left(\boldsymbol{\eta}^{mn}\right)\right)N_j\left[\dot{\eta}^{pq}_i\right]ds_y \tag{2.87}$$

$$S^{\alpha}_{mnpq} = \frac{1}{2}\int_{CY} a_{ijkl}e_{ykl}\left(\boldsymbol{\eta}^{mn}\right)N_j\left[\eta^{pq}_i\right]ds_y \tag{2.88}$$

In [17] was proved that the tensor S^{α}_{mnpq} is symmetric. This implies that in the Eq.(2.86) this term is vanishing.

To complete the damage evolution law, we need to use the scaling relation for the energy-release rate [25]:

$$\mathcal{G}^{\varepsilon} = \varepsilon\mathcal{G}_y \tag{2.89}$$

This results as a consequence of the fact that expression (2.13) can be written using the two-scale development (2.16) of $\mathbf{u}^{\varepsilon}(\mathbf{x},t)$. Therefore, the relation (2.13) becomes:

$$\mathcal{G}^{\varepsilon} = \lim_{r\to 0}\int_{\Gamma_r} e_i\left(\frac{1}{2}a_{mnkl}\left(e_{xkl}\left(\mathbf{u}^{(0)}\right) + e_{ykl}\left(\mathbf{u}^{(1)}\right)\right)\left(e_{xmn}\left(\mathbf{u}^{(0)}\right) + e_{ymn}\left(\mathbf{u}^{(1)}\right)\right)\delta_{ij} - \right.$$
$$\left. + a_{ikmn}\left(e_{xmn}\left(\mathbf{u}^{(0)}\right) + e_{ymn}\left(\mathbf{u}^{(1)}\right)\right)\left(\frac{\partial u^{(0)}_k}{\partial x_j} + \frac{\partial u^{(1)}_k}{\partial y_j}\right)\right)n_j dS \tag{2.90}$$

By change of variables in the integral (2.90) with $dS = \varepsilon ds_y$ and taking into account the singularity of $\mathbf{u}^{(1)}$ at crack tips ([37]) we get:

$$\mathcal{G}^{\varepsilon} = \varepsilon\lim_{r\to 0}\int_{\Gamma Y_r} e_i\left(\frac{1}{2}a_{mnkl}e_{ykl}\left(\mathbf{u}^{(1)}\right)e_{ymn}\left(\mathbf{u}^{(1)}\right)\delta_{ij} - a_{ikmn}e_{ymn}\left(\mathbf{u}^{(1)}\right)\frac{\partial u^{(1)}_k}{\partial y_j}\right)n_j ds_y. \tag{2.91}$$

which proves the relation (2.89).

The relation (2.89) introduces the microstructural length parameter ε in the damage law, which together with the propagation criterion (2.10), finally gets the form:

$$\dot{d}\left(\left(\frac{1}{2}\frac{dC_{mnpq}}{dd} + I_{mnpq}\right)e_{xmn}\left(\mathbf{u}^{(0)}\right)e_{xpq}\left(\mathbf{u}^{(0)}\right) + \frac{\mathcal{G}_{cr}}{\varepsilon}\right) = 0 \tag{2.92}$$

where C_{mnpq} and I_{mnpq} are obtained correspondingly as a combination of C^{α}_{mnpq} and I^{α}_{mnpq}.

Summarizing the equations of the previous sections, for frictional micro-cracks, we can define the macroscopic problem to be solved in terms of:

- homogenized equilibrium equation

$$\frac{\partial}{\partial x_j}\left(C_{mnpq}\left(d\right)e_{xpq}\left(\mathbf{u}^{(0)}\right)\right)=0 \tag{2.93}$$

- energy balance

$$\dot{d}\left(\left(\frac{1}{2}\frac{dC_{mnpq}\left(d\right)}{dd}+I_{mnpq}\left(d\right)\right)e_{xmn}\left(\mathbf{u}^{(0)}\right)e_{xpq}\left(\mathbf{u}^{(0)}\right)+\frac{\mathcal{G}_{cr}}{\varepsilon}\right)=0 \tag{2.94}$$

- irreversibility condition

$$\frac{dd}{dt}\geq 0 \tag{2.95}$$

- damage criterion

$$\left(\frac{1}{2}\frac{dC_{mnpq}\left(d\right)}{dd}+I_{mnpq}\left(d\right)\right)e_{xmn}\left(\mathbf{u}^{(0)}\right)e_{xpq}\left(\mathbf{u}^{(0)}\right)+\frac{\mathcal{G}_{cr}}{\varepsilon}\geq 0 \tag{2.96}$$

The last three relations are macroscopic versions of the corresponding fracture law defined in (2.12).

2.6 Numerical implementation of the micro-structure

To determine the law of macroscopic behaviour it is necessary to compute homogenized coefficients C_{ijkl} and the coefficients in the terms representing the dissipation of energy due to friction on the crack lips, called here I_{ijkl}. For a length d of a given micro-crack, these coefficients depend only on the solution of the cell problem. The cell problems were solved for two orientations of the crack and for several length $d\in[0,1]$, different values of Coulomb coefficients and two senses of sliding (left and right) in order to compute C_{ijkl} and I_{ijkl}. Figure 2.5 illustrates the direction of sliding: left and right sense of sliding for the orientation of the crack fixed at 135°.

Let's analyse the example of the crack oriented at 135°. We are interested in the solution of compression case with two sliding types. To find the correct response of the unit cell, we have to choose the system of generators satisfying the conditions (2.36) or (2.37). First, we chose a system of generators such that ${}^{R}\bar{\mathbf{E}}^{kl}\in\mathbf{D}^{R}$ (which means that we consider right sliding type and conditions (2.36) are satisfied) and such that the macroscopic deformation, $\mathbf{e}_{\mathbf{x}}\left(\mathbf{u}^{(0)}\right)$ could be written as a linear combination of these elements (${}^{R}\bar{\mathbf{E}}^{kl}$). This system was chosen as:

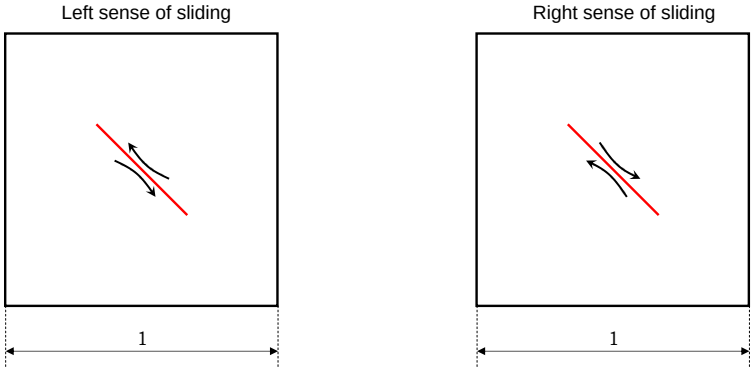

Figure 2.5: Sense of sliding for crack inclined at 135°: a) left sense of sliding, b) right sense of sliding.

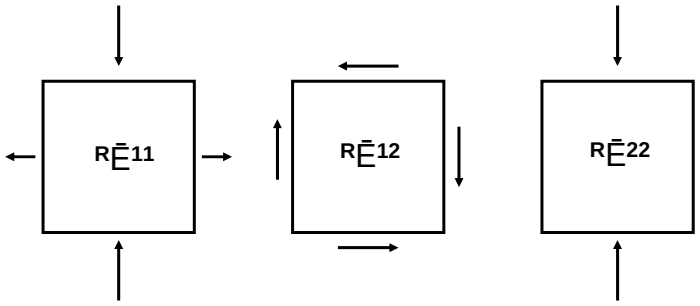

Figure 2.6: Application of the basic macroscopic deformation on the unit cell in the case of right sliding corresponding to 2.97.

$$\left\{ {}^{R}\bar{\mathbf{E}}^{11} = \begin{pmatrix} 1/4 & 0 \\ 0 & -1 \end{pmatrix}; {}^{R}\bar{\mathbf{E}}^{12} = {}^{R}\bar{\mathbf{E}}^{21} = \frac{1}{2}\begin{pmatrix} 0 & -1 \\ -1 & 0 \end{pmatrix}; {}^{R}\bar{\mathbf{E}}^{22} = \begin{pmatrix} 0 & 0 \\ 0 & -1 \end{pmatrix} \right\} \tag{2.97}$$

and the macroscopic deformation $\mathbf{e_x}\left(\mathbf{u}^{(0)}\right)$ has a form :

$$\mathbf{e_x}\left(\mathbf{u}^{(0)}\right) = {}^{R}\alpha_{kl}\,{}^{R}\bar{\mathbf{E}}^{kl} \tag{2.98}$$

with ${}^{R}\alpha_{11} = 4e_{x11}$; ${}^{R}\alpha_{12} = {}^{R}\alpha_{21} = -e_{x12}$; ${}^{R}\alpha_{22} = -4e_{x11} - e_{x22}$.

If ${}^{R}\boldsymbol{\eta}^{kl}$ are elementary solutions of the cell, obtained by appling ${}^{R}\bar{\mathbf{E}}^{kl}$, the solution $\mathbf{u}^{(1)}$ corresponding to $\mathbf{e_x}\left(\mathbf{u}^{(0)}\right)$ can be written as:

$$\mathbf{u}^{(1)} = {}^{R}\alpha_{kl}\,{}^{R}\boldsymbol{\eta}^{kl} \tag{2.99}$$

Now, let's assume that ${}^{L}\bar{\mathbf{E}}^{kl} \in \mathbf{D}^{L}$. It means that the type of left sliding is present and conditions (2.37) are satisfied. The procedure is analogous to the previous case and the following ${}^{L}\bar{\mathbf{E}}^{kl}$ were choosen:

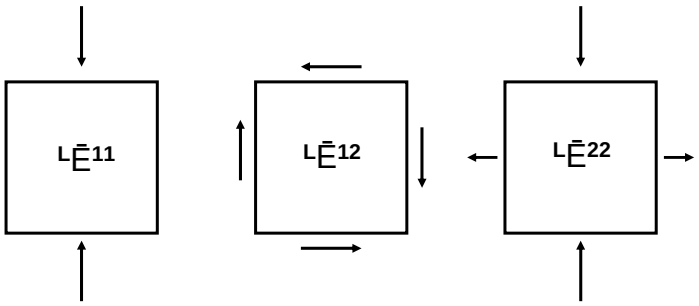

Figure 2.7: Application of the basic macroscopic deformation on the unit cell in the case of left sliding corresponding to 2.100.

$$\left\{ {}^{L}\bar{\mathbf{E}}^{11} = \begin{pmatrix} -1 & 0 \\ 0 & 0 \end{pmatrix}; {}^{L}\bar{\mathbf{E}}^{12} = {}^{L}\bar{\mathbf{E}}^{21} = \frac{1}{2}\begin{pmatrix} 0 & -1 \\ -1 & 0 \end{pmatrix}; {}^{L}\bar{\mathbf{E}}^{22} = \begin{pmatrix} -1 & 0 \\ 0 & 1/4 \end{pmatrix} \right\} \tag{2.100}$$

The macroscopic deformation for the left sliding is written:

$$\mathbf{e}_{\mathbf{x}}\left(\mathbf{u}^{(0)}\right) = {}^{L}\alpha_{kl}\,{}^{L}\bar{\mathbf{E}}^{kl} \tag{2.101}$$

with ${}^{L}\alpha_{11} = -e_{x11} - 4e_{x22}$; ${}^{L}\alpha_{12} = {}^{L}\alpha_{21} = -e_{x12}$; ${}^{L}\alpha_{22} = 4e_{x22}$

Applying the deformations ${}^{R}\bar{\mathbf{E}}^{kl}$ and ${}^{L}\bar{\mathbf{E}}^{kl}$ on the unit cell together with periodic boundary conditions we find solutions (${}^{R}\boldsymbol{\eta}^{11}$, ${}^{R}\boldsymbol{\eta}^{12} = {}^{R}\boldsymbol{\eta}^{21} = {}^{L}\boldsymbol{\eta}^{12} = {}^{L}\boldsymbol{\eta}^{21}$, ${}^{R}\boldsymbol{\eta}^{22}$,${}^{L}\boldsymbol{\eta}^{11}$ and ${}^{L}\boldsymbol{\eta}^{22}$) of 5 elementary problems. The periodic conditions for the external boundaries of the unit cell are written in a form [78]:

$$\left(\mathbf{v} - \bar{\mathbf{E}}^{kl}\mathbf{y}\right)^{+} = \left(\mathbf{v} - \bar{\mathbf{E}}^{kl}\mathbf{y}\right)^{-} \tag{2.102}$$

where $\mathbf{v}$ and $\mathbf{y}$ are displacement and initial position vectors respectively of the points on the external boundaries of the unit cell. The $\bar{\mathbf{E}}^{kl}$ are elementary deformations for left or right sliding. $\pm$ defines two opposite boundaries of the unit cell.

The computations of the unit cell were performed by using the finite element method implemented in COMSOL Multiphysics ([24]).

The Fig. 2.8 presents the different solutions (${}^{R}\boldsymbol{\eta}^{11}$,${}^{R}\boldsymbol{\eta}^{12}$,${}^{R}\boldsymbol{\eta}^{22}$) obtained on the unit cell by applying ${}^{R}\bar{\mathbf{E}}^{11}$, ${}^{R}\bar{\mathbf{E}}^{12}$ and ${}^{R}\bar{\mathbf{E}}^{22}$ for different friction coefficients ($\mu_f = 0.0, 0.1, 0.3, 0.5$) in terms of vertical displacement.

Based on the cell computation, the homogenized coefficients $C_{ijkl}(d)$ and integrals $I_{ijkl}(d)$ are determined. The analytical formulations of $C_{ijkl}(d)$ and $I_{ijkl}(d)$ are given by (2.51) and (2.87) respectively.

It is necessary to express the $C_{ijkl}(d)$ and $I_{ijkl}(d)$ as functions of damage variable, in order to know all effective coefficients for every values of $d \in [0,1]$ at each moment.

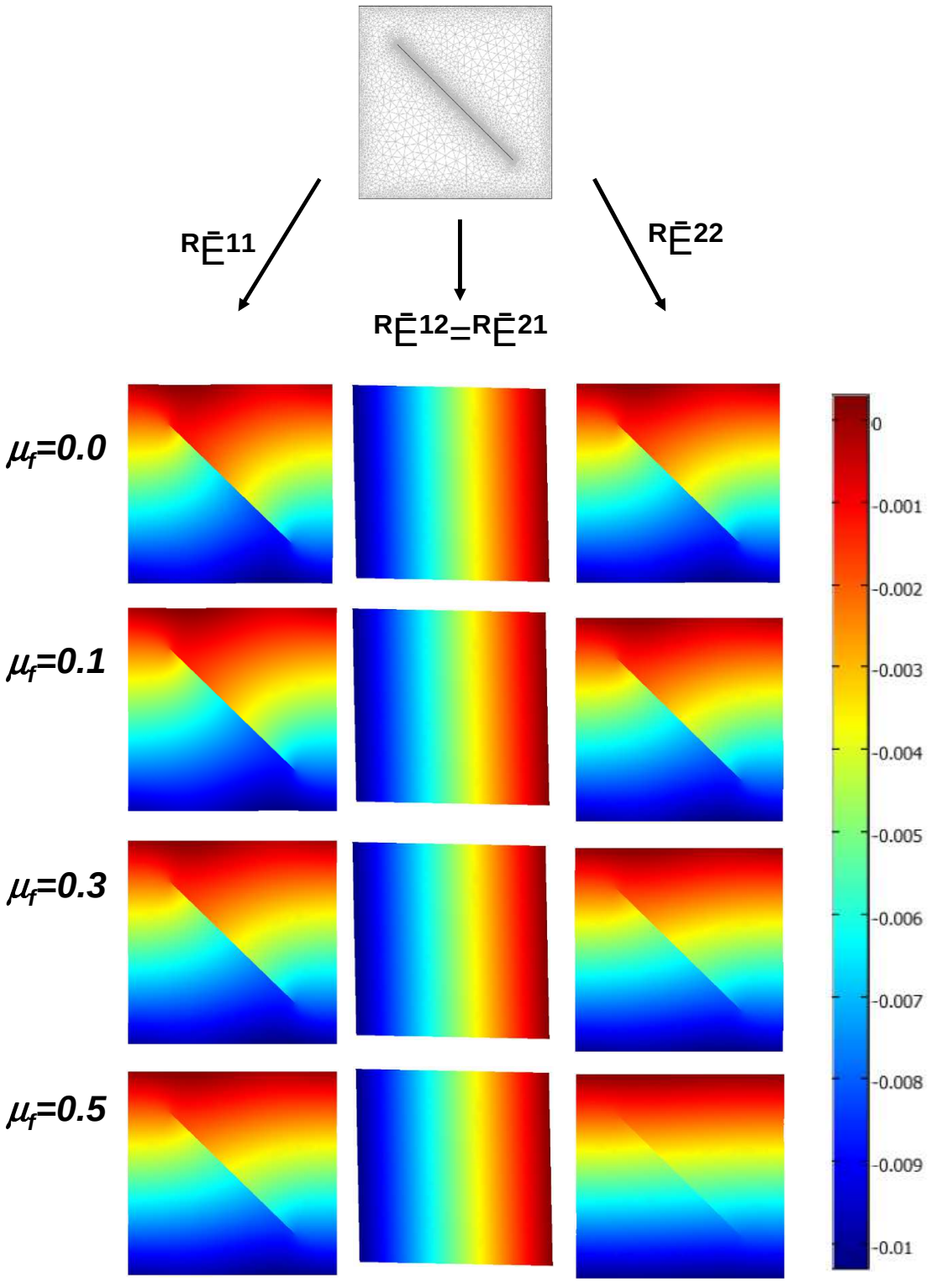

Figure 2.8: Set of the cells in the modes: ${}^R\boldsymbol{\eta}^{11}, {}^R\boldsymbol{\eta}^{12} = {}^R\boldsymbol{\eta}^{21}, {}^R\boldsymbol{\eta}^{22}$ with and without friction for a crack oriented at 135°.

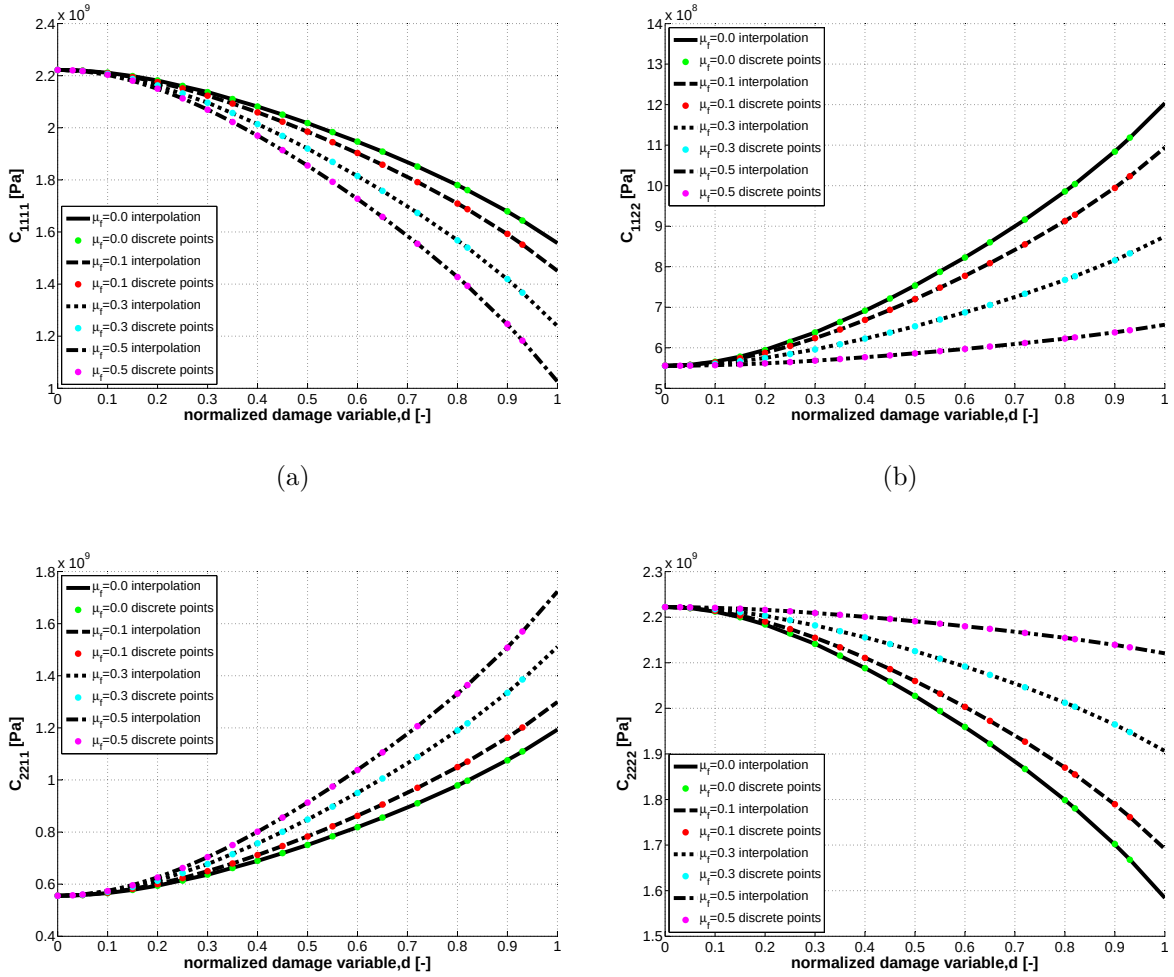

(a) (b)

(c) (d)

Figure 2.9: The homogenized coefficients versus damage variable for different friction coefficients $\mu_f = 0.0, 0.1, 0.3, 0.5$ for the crack oriented at 135° and right sense of sliding: a) C^R_{1111}, b) C^R_{1122}, c) C^R_{2211}, d) C^R_{2222}.

To perform the multi-scale damage computation we need to prepare a database, which includes the results of the interpolations of the $C_{ijkl}(d)$ and $I_{ijkl}(d)$ based on several discrete micro-cracks lengths, two different orientations of these cracks, two senses of sliding and different friction coefficients.

Figure 2.9 presents the effective (homogenized) coefficients for the crack oriented at 135°, for right sense of sliding and different friction coefficients $\mu_f = 0.0, 0.1, 0.3, 0.5$. Only degradated and non vanishing terms are plotted.

We remark that presence of micro-cracks leads to induced anisotropy in overall response.

Looking at the component C_{2222} in figure 2.9 we observe that the highest loss of stiffness takes place for non frictional material, whereas increasing the friction coefficient the loss is lower.

The periodicity conditions do not allow dilatation or contractions of the unit cell, and

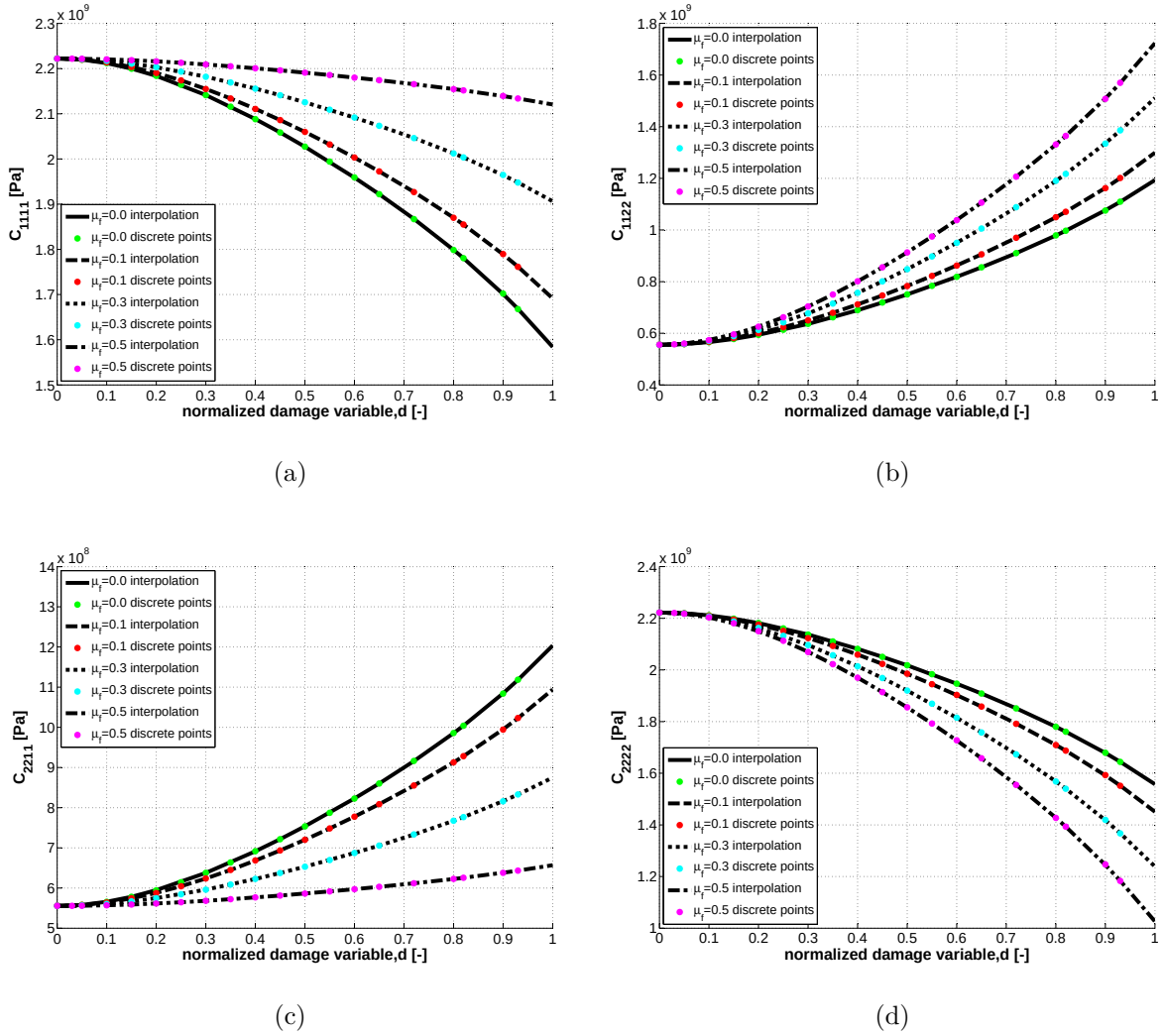

Figure 2.10: The homogenized coefficients versus damage variable for different friction coefficients $\mu_f = 0.0, 0.1, 0.3, 0.5$ for the crack oriented at 135° and left sense of sliding: a) C^L_{1111}, b) C^L_{1122}, c) C^L_{2211}, d) C^L_{2222}.

this can explain the increasing tendency of C_{1122}. For higher friction coefficients the rise in C_{1122} is less evident, and this comes from the fact that sliding is slowed down by the friction.

The components C_{1111} and C_{2211} are negative contributions, since they correspond to different sliding sense, acting against the considered sliding. This contribution amplifies with friction coefficient.

Under pure shear loading for the crack inclined at 135° and for any length, the body behaves like uncracked, which makes C_{1212} and C_{2121} be equal to the elastic quantities, a_{1212} and a_{2121}, respectively.

For $d = 0$ the homogenized coefficients are equal to elastic ones $C_{ijkl} = a_{ijkl}$.

Figure 2.10 presents the effective (homogenized) coefficients for the crack oriented at 135°, for left sense of sliding and different friction coefficients $\mu_f = 0.0, 0.1, 0.3, 0.5$. Only

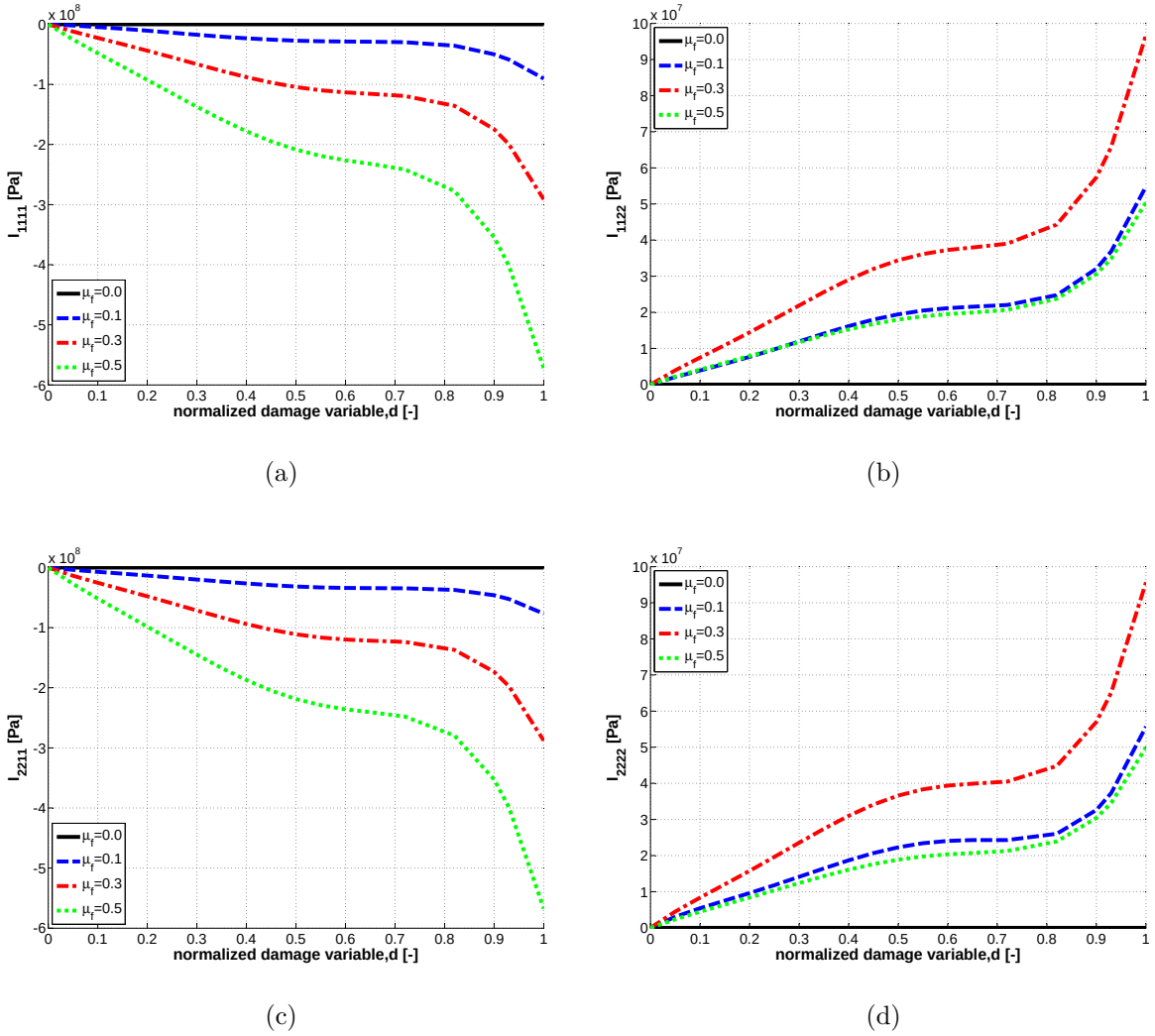

Figure 2.11: Integrals $I_{ijkl}(d)$ versus damage variable for different friction coefficients $\mu_f = 0.0, 0.1, 0.3, 0.5$ for the crack oriented at 135° and right sense of sliding: a) I^R_{1111}, b) I^R_{1122}, c) I^R_{2211}, d) I^R_{2222}.

degradated and non vanished terms are plotted. We retrive the classical symmetry of the coefficients by comparing those corresponding to two senses of sliding. For instance : $C^R_{1111} = C^L_{2222}$ (see Fig.2.9a and Fig.2.10d).

Next, we analyse the homogenized terms I_{ijkl}. The dissipation due to friction is computed as an integral on the crack lips using the (2.87) where $\left[\eta_i^{pq}\right]$ is the jump of the displacement across the crack lips and $\left[\frac{d\eta_i^{pq}}{dd}\right]$ is the jump across crack lips of the derivative of the displacement.

In order to compute these terms, the mesh for unit cell computations had to be constructed in such a way that each node on one side of the crack lip needs to have corresponding one on the other side (i.e. the coordinates of the considered nodes have to be the same). In this way the jump of the displacement was computed in each single node of the crack. The jump of the derivative was computed using the solution obtained from the computations of two lengths of the crack which difference is equal $\triangle d = 0.001$.

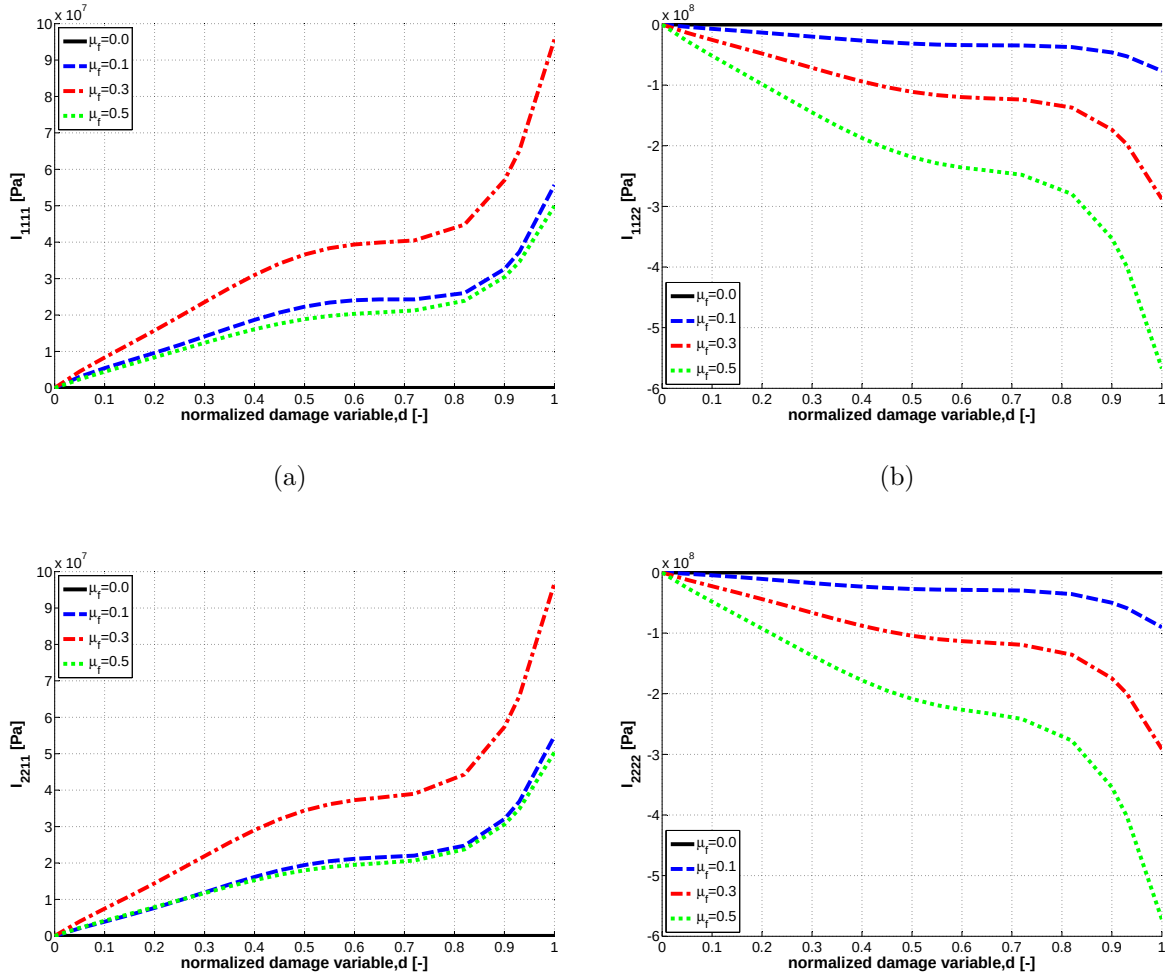

Figure 2.12: Integrals $I_{ijkl}(d)$ versus damage variable for different friction coefficients $\mu_f = 0.0, 0.1, 0.3, 0.5$ for the crack oriented at 135° and left sense of sliding: a) I^L_{1111}, b) I^L_{1122}, c) I^L_{2211}, d) I^L_{2222}.

In each computation the nodes were in the same position. The derivative of the displacement was computed using the finite-difference scheme:

$$\frac{\eta_i^{d1} - \eta_i^d}{\triangle d} \tag{2.103}$$

In such a way we obtained required quantities in each node which allowed us to compute numerically the integrals $I_{ijkl}(d)$ on the crack lips.

Figure 2.11 shows these integrals versus normalized damage variable for right sense of sliding, crack orientation 135° and for different friction coefficients $\mu_f = 0.0, 0.1, 0.3, 0.5$.

Under pure shear loading for the crack inclined at 135° and for any length, the body behaves like uncracked, making I_{1212} and I_{2121} be equal to zero. Because of the fact that these terms represent the dissipation due to friction, for frictionless contact they are equal to zero.

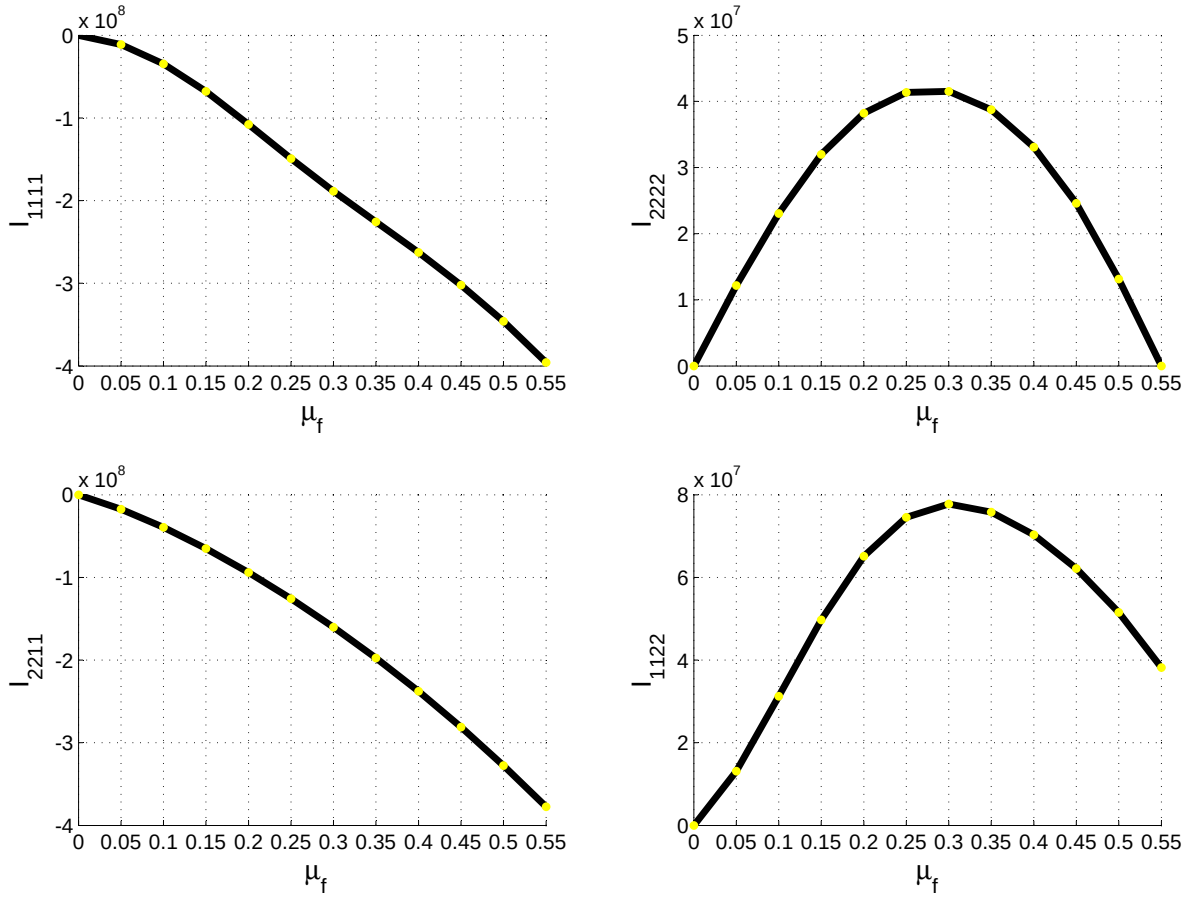

Figure 2.13: Integrals I_{1111}, I_{2222}, I_{1122} and I_{2211} *vs* various friction coefficients $\mu_f = 0.0 - 0.55$ for right sense of sliding and crack $d = 0.5$ oriented at 135°.

Figure 2.12 presents the evolution of dissipative terms I_{ijkl} versus damage variable for left sense of sliding.

The evolution of dissipative terms I_{ijkl} versus various friction coefficient ($\mu_f = 0.0 - 0.55$) for right sense of sliding is shown in the figure 2.13. As mentioned before, when $\mu_f = 0.0$ the dissipative terms are equal to zero.

The integral I_{2222} was obtained by applying a macroscopic deformation e_{x22} on the unit cell, which lets the crack slide in the proper sense for that case. We observe that the function $(I_{2222} - \mu_f)$ is not monotonic and it has absolute maximum at $\mu_f = 0.3$ (see fig.2.13). It can be explained by the fact that the stick case is reached for higher values of friction coefficient, so the jump of the displacement across crack lips goes to zero.

The integral I_{1111} is linked to the opposite sense of sliding. This is why the obtained function is monotonically decreasing with increase of friction coefficient, i.e. the resistance of the sliding reduces with the friction.

The interpolation procedure of discrete points of C_{ijkl} and I_{ijkl} has an important influence on the further macroscopic computations, because the macroscopic damage equation is solved based on these polynomials. As interpolation method we used Least Square Method with additional restriction.

We imposed that the derivatives of C_{ijkl} are smooth and monotonically decreasing or increasing.

To interpolate I_{ijkl} we request that the $I_{ijkl}(d=0)=0$ as a consequence of undamaged properties of the material, i.e. when there is no crack, there is no dissipation.

In such a way we minimized the errors which could come from the basic interpolations. Figures 2.9 and 2.10 show the discrete points of C_{ijkl} and their interpolation with 5 degree polynomials.

The homogenized coefficients and dissipative terms for the crack oriented at 45° were determined in the analogous way, respecting the linear domains of sliding and friction law (2.36-2.38).

For each orientation of the crack (in this case 45° and 135°) by applying presented scheme, we obtain the homogenized coefficients C_{ijkl} and dissipative terms I_{ijkl} for left and right sense of sliding, and for different friction coefficients $\mu_f = 0.0, 0.1, 0.3, 0.5$.

Based on this data we construct the input database for solving the damage equation under different types of loading and friction coefficients.

In order to use correct input in the macroscopic computations (e.g. left and right sliding, stick state, backsliding) we introduce the additional terms representing tangential and normal components of the stress to the crack line. The relations between them and corresponding states of the crack are illustrated in figure 2.14. In the case of progressive loading, the previous assumptions (2.36)-(2.38) are still valid and they are able to follow a correct state of the crack. The situation is more complex for unloading phase, especially in presence of friction. Under unloading conditions the cracks become stick until some point when sliding occurs again (like in [5, 46, 56, 72, 84]). The tangential $\mathbb{T}$ and normal $\mathbb{N}$ components of the stress are good indicators to archive these states and they are defined by the formulas (2.61) and (2.62). They also enter the database as results of the interpolation of the discrete points computed on the crack face in the unit cell for several crack lengths.

A hypothetical loading and unloading cycle of a rock containing a single closed crack under uniaxial compression is shown in Fig.2.15 ([48]).

Initial loading along OA occurs with an effective modulus $E^d < E^{un}$. E^d is an effective modulus for damaged material and E^{un} is modulus of the uncracked material. Unloading phase (path AB) first occurs with the modulus E^{un} up to point B where reverse sliding begins on the crack. The rock specimen continues to deform along BO with the modulus E^{drev}, which is the modulus of damaged material for opposite sense of sliding than during loading.

Following this theoretical scheme, the homogenized stress-strain relations for each state of loading can be defined.

Figure 2.16 shows the idealized example, adopted in our case, of stress-strain curve with all states of the crack which have to be considered.

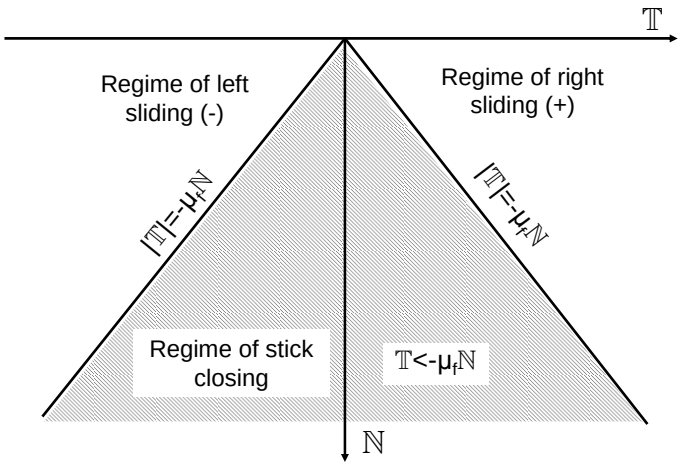

Figure 2.14: The crack states determined by Coulomb law in terms of normal and tangential component of the stress ($\mathbb{T}$ and $\mathbb{N}$).

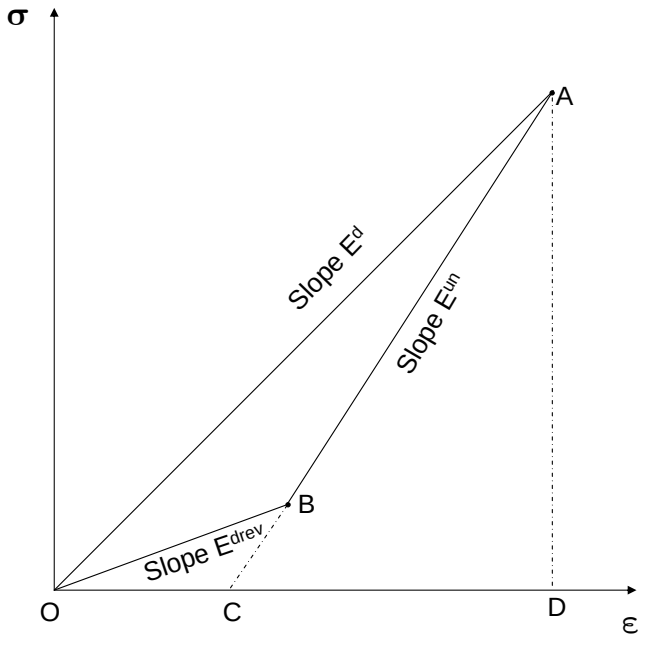

Figure 2.15: Uniaxial stress-strain diagram of a rock containing a single closed crack, loaded and unloaded along path OABO [48].

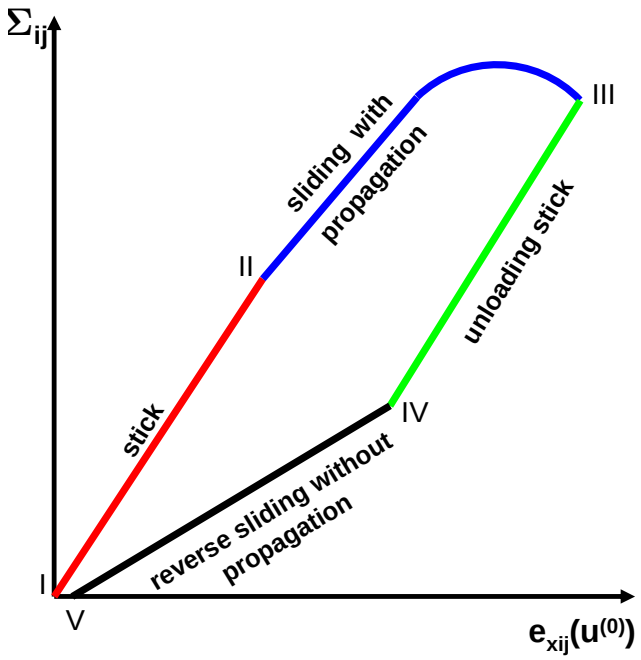

Figure 2.16: Idealized example of the stress-strain curve.

The first state $(I-II)$ represents the stick case, when eq.(2.38) is satisfied. In this situation, with or without existing crack in the body, we consider the material as being homogeneous. The stress is expressed by the rate type formulation:

$$\dot{\Sigma}_{ij}^{(0)} = a_{ijkl}\dot{e}_{xkl}\left(\mathbf{u}^{(0)}\right) \tag{2.104}$$

where tensor a_{ijkl} is an elastic tensor of the uncracked body.

During progressive loading, the path $(II-III)$ occurs when one of the conditions (2.36) or (2.37) is verified. In this regime crack evolves and slides. The formulation for stress is as follows:

$$\dot{\Sigma}_{ij}^{(0)} = A_{ijkl}\left(d\right)\dot{e}_{xkl}\left(\mathbf{u}^{(0)}\right) \tag{2.105}$$

where $A_{ijkl}\left(d\right)$ are the homogenized tangent moduli computed using the damage law.

When unloading phase $(III-IV)$ takes place the stress in computed by using the elastic tensor a_{ijkl} and it has a form:

$$\dot{\Sigma}_{ij}^{(0)} = a_{ijkl}\dot{e}_{xkl}\left(\mathbf{u}^{(0)}\right) \tag{2.106}$$

In this case the condition (2.73) is satisfied, indicating that crack lips are stick. The components of friction law ($\mathbb{N}$ and $\mathbb{T}$) are computed from (2.60) and (2.59) with constant value of (2.70) and (2.69), respectively.

The last regime $(IV-V)$ is related to the regime in which the reverse sliding occurs. The stick condition (2.73) does no longer hold, and the constitutive relation is expressed by:

$$\dot{\Sigma}_{ij}^{(0)} = C_{ijkl}^{rev}(d)\,\dot{e}_{xkl}\left(\mathbf{u}^{(0)}\right) \tag{2.107}$$

where $C_{ijkl}^{rev}(d)$ are homogenized coefficients. In the last formulation (2.107) the homogenized coefficients of the opposite sense of sliding are used, i.e. if during loading phase the crack slides in one sense, then in the regime $(IV-V)$ it will slide in the opposite one. The components of friction law ($\mathbb{N}$ and $\mathbb{T}$) are computed from (2.60) and (2.59), respectively, using the values of reverse sliding. We assume that in this regime the crack does not evolve.

In what follows, we regroup (2.104)-(2.107) under the general relation:

$$\dot{\Sigma}_{ij}^{(0)} = A_{ijkl}(d)\,\dot{e}_{xkl}\left(\mathbf{u}^{(0)}\right) \tag{2.108}$$

where $A_{ijkl}(d)$ takes different forms depending on the state of sliding or stick.

2.7 Conclusions

In this chapter we presented the theoretical aspects concerning asymptotic homogenization and damage law. The asymptotic homogenization technique was employed to deduce the overall response of the micro-fractured elastic body. A damage evolution equation has been completly obtained from the microscopic energy balance for evolving microcracks. Since the microstructural length, which is the size of the periodic cell, enters the homogenized damage law, the model is able to describe size effects.

The numerical implementation of the micro-structure was presented and it was a necessary step to determine the law of macroscopic behaviour. The homogenized coefficients C_{ijkl} and the terms representing the dissipation of energy due to friction on the crack lips I_{ijkl} were computed as results of the elastic problem for the characteristic functions $\boldsymbol{\eta}^{pq}(\mathbf{y})$ in the unit cell for various normalized lengths of the crack. These different coefficients depend on the sense of sliding, on friction coefficients and on the orientation of the crack, whose inflences were studied in this chapter.

Finally, we determined the constitutive relation for each possible state of the crack, i.e. stick, sliding and backsliding. These states are controlled by frictional law and by loading path.

Chapter 3

Time independent damage models

Contents

3.1 Introduction

In this chapter the main goal is to construct micro-mechanical damage models to describe failure of clay rocks. We use periodic homogenization based on two-scale asymptotic developments to describe the overall damage behaviour starting from an explicit description of elementary volumes with micro-cracks [10, 25, 58]. For the crack evolution we consider a Griffith-type energy criterion. The friction problem is treated using Coulomb's law [17, 58]. An appropriate micro-mechanical energy analysis is proposed to formulate a damage evolution law which incorporates stiffness degradation, material softening, size effects, unilaterality, different fracture behaviour in contact with and without friction.

The detailed theoretical aspects concerning homogenization method, energy analysis and damage evolution law were presented in the Chapter *2*. In this chapter, we consider a quasi-brittle damage law and we give results concerning the effective local (in a macroscopic point) behaviour.

The influence of friction on micro-cracks is analyzed. The damage law is deduced from quasi-brittle propagation criteria for micro-cracks. The different coefficients in the homogenized strain-stress law are obtained by finite element computations on the unit cell and special interpolation methods. A specific numerical procedure was developed in order to overcome difficulties related to periodic boundary conditions, unilateral contact on micro-cracks and friction boundary conditions. The analysis of the effective constitutive behaviour is a necessary step for macroscopic simulations of damage.

3.2 Quasi-brittle damage model

In the previous papers ([25, 27]) a 2D brittle damage model obtained through homogenization was developed. The Griffith fracture criterion ([40]) was assumed for micro-cracks. The critical fracture energy was considered to be constant, i.e. $\mathcal{G}_f = \mathcal{G}_{cr}$. In that case, for an initially undamaged material, the response predicted by the damage model is elastic up to a threshold of damage initiation, when complete failure ($d = 1$) instantaneously occurs.

Such a model is adequate for truly brittle material, however the experimental observations indicate that rocks show more gradual fracture behaviour, i.e. a quasi-brittle response. In this section we describe an alternative two-scale model in which, as a crack grows, the resistance of material increases until a maximum value is achieved. Such a behaviour arises due to development of the fracture process zone ahead of the crack tip. The maximum value of $\mathcal{G}_f$ is reached when this process zone is fully developed. The curve describing the increase in $\mathcal{G}_f$ with d is often referred as the R-curve and it is called resistance curve.

The fracture process zone (FPZ) in rocks is an area affected by micro-cracks and frictional slip surrounding the visible crack tip. The size of the FPZ is given by the distance between the defect tip and the farthest micro-crack from this tip ([66]). We denote by c_f the size of the process zone. To specify a particular material we have to give particular values for these parameters.

We consider the damage model corresponding to a quasi-brittle micro-fracture criterion in the form:

$$\left(\frac{1}{2}\frac{dC_{ijkl}(d)}{dd}e_{xkl}\left(\mathbf{u}^{(0)}\right)e_{xij}\left(\mathbf{u}^{(0)}\right)+\frac{\mathcal{G}^{\varepsilon}}{\varepsilon}+I_{mnpq}e_{xmn}\left(\mathbf{u}^{(0)}\right)e_{xpq}\left(\mathbf{u}^{(0)}\right)\right)\dot{d}=0 \qquad (3.1)$$

where

$$\mathcal{G}^{\varepsilon}=\mathcal{G}_{cr}(d,\varepsilon,c_f) \qquad (3.2)$$

is the R-curve we use in damage law, which can be a linear function in d. A simple example of R-curve that we consider in this chapter is the linear R-curve proposed by Bazant and Planas in [13]:

$$\mathcal{G}^{\varepsilon}\left(d^{\varepsilon}\right)=\frac{2\mathcal{G}_{cr}\left(d^{\varepsilon}-d_0^{\varepsilon}\right)}{c_f} \tag{3.3}$$

where c_f characterizes the size of the process zone at the crack tips of micro-cracks. When written in terms of the damage parameter $d^{\varepsilon}=\sqrt{2}d\varepsilon$ and considering that $d_0^{\varepsilon}=0$, the relation (3.3) leads to:

$$\frac{\mathcal{G}^{\varepsilon}\left(d\right)}{\varepsilon}=\frac{2\sqrt{2}\mathcal{G}_{cr}d}{c_f} \tag{3.4}$$

We note that microstructural length c_f takes the place of ε in the damage law.

The first term in the equation (3.1) is the negative of the damage energy release rate on a cell, the second one represents the dissipation due to micro fracture and the last one accounts the dissipation due to friction between crack lips. When the energy potentially released by elastic body becomes equal to the necessary energy for fracture, the micro-cracks are propagating.

The dissipation due to friction is computed as an integral on the crack lips using the following formula:

$$I^{\alpha}_{mnpq}=\frac{1}{2}\frac{d}{dd}\int_{CY}\left(a_{ijkl}\bar{E}^{mn}_{kl}+a_{ijkl}e_{ykl}\left(\boldsymbol{\eta}^{mn}\right)\right)N_j\left[\eta_i^{pq}\right]ds_y+$$

$$-\int_{CY}\left(a_{ijkl}\bar{E}^{mn}_{kl}+a_{ijkl}e_{ykl}\left(\boldsymbol{\eta}^{pq}\right)\right)N_j\left[\frac{d\eta_i^{pq}}{dd}\right]ds_y \tag{3.5}$$

where $\left[\eta_i^{pq}\right]$is a jump and $\left[\frac{d\eta_i^{pq}}{dd}\right]$is a jump of the displacement derivative across the crack lips.

To solve the damage equation (3.1) we have to use the computed $I_{ijkl}\left(d\right)$ and $C_{ijkl}\left(d\right)$ in the elementary cell of the length ε. The detailed procedure of these computations was presented in the Chapter 2.

3.3 Formulation of the damage problem

Summarizing, the homogenized quasi-brittle damage problem is formulated as follows:

- **Homogenized equilibrium**

$$\frac{\partial}{\partial x_j}\Sigma^{(0)}_{ij}=0$$

- **Macroscopic Coulomb law and effective stress-strain laws**

1. loading ($\dot{d} > 0$)
   - during stationary contact

$$| \mathbb{T} | < -\mu_f \mathbb{N}$$

$$\Sigma_{ij}^{(0)} = a_{ijkl}(E, \nu)\, e_{xkl}\left(\mathbf{u}^{(0)}\right)$$

   - during sliding

$$| \mathbb{T} | = -\mu_f \mathbb{N}$$

$$\Sigma_{ij}^{(0)} = C_{ijkl}\left(E, \nu, d, \mu_f, \theta\right) e_{xkl}\left(\mathbf{u}^{(0)}\right)$$

   where:

$$\mathbb{N} \equiv N_i a_{ijkl} e_{xkl}\left(\mathbf{u}^{(0)}\right) N_j \int_{CY} ds_y + \int_{CY} \left(N_i a_{ijkl} e_{ykl}\left(\mathbf{u}^{(1)}\right) N_j\right) ds_y$$

$$\mathbb{T} \equiv T_i a_{ijkl} e_{xkl}\left(\mathbf{u}^{(0)}\right) N_j \int_{CY} ds_y + \int_{CY} \left(T_i a_{ijkl} e_{ykl}\left(\mathbf{u}^{(1)}\right) N_j\right) ds_y$$

2. unloading ($\dot{d} = 0$)

   - during stationary contact

$$| \mathbb{T} | < -\mu_f \mathbb{N}$$

$$\Sigma_{ij}^{(0)} = a_{ijkl}(E, \nu)\left(e_{xkl}\left(\mathbf{u}^{(0)}\right) + e_{kl}^{p}\left(\mathbf{u}^{(1)}\right)\right)$$

$$\text{where } e_{kl}^{p}\left(\mathbf{u}^{(1)}\right) = \tfrac{1}{2}\left(T_k N_l + T_l N_k\right) \int_{CY} \left[u_m^{(1)} T_m\right] ds_y \text{ (eqs.2.53-2.57)}$$

   - during back sliding

$$| \mathbb{T} | = -\mu_f \mathbb{N}$$

$$\Sigma_{ij}^{(0)} = C_{ijkl}\left(E, \nu, d, \mu_f, \theta\right) e_{xkl}\left(\mathbf{u}^{(0)}\right)$$

   where during stationary contact

$$\mathbb{N} \equiv N_i a_{ijkl} e_{xkl}\left(\mathbf{u}^{(0)}\right) N_j \int_{CY} ds_y + \int_{CY} \left(N_i a_{ijkl} e_{ykl}\left(\mathbf{u}^{(1)}\right) N_j\right) ds_y$$

$$\mathbb{T} \equiv T_i a_{ijkl} e_{xkl}\left(\mathbf{u}^{(0)}\right) N_j \int_{CY} ds_y + \int_{CY} \left(T_i a_{ijkl} e_{ykl}\left(\mathbf{u}^{(1)}\right) N_j\right) ds_y$$

   with the constant $\int_{CY} \left(N_i a_{ijkl} e_{ykl}\left(\mathbf{u}^{(1)}\right) N_j\right)$ and $\int_{CY} \left(T_i a_{ijkl} e_{ykl}\left(\mathbf{u}^{(1)}\right) N_j\right) ds_y$, corresponding to the last configuration of loading.

   and where during back sliding

$$\mathbb{N} \equiv N_i a_{ijkl} e_{xkl}\left(\mathbf{u}^{(0)}\right) N_j \int_{CY} ds_y + \int_{CY} \left(N_i a_{ijkl} e_{ykl}\left(\mathbf{u}^{(1)}\right) N_j\right) ds_y$$

$$\mathbb{T} \equiv T_i a_{ijkl} e_{xkl}\left(\mathbf{u}^{(0)}\right) N_j \int_{CY} ds_y + \int_{CY} \left(T_i a_{ijkl} e_{ykl}\left(\mathbf{u}^{(1)}\right) N_j\right) ds_y$$

- **Damage evolution equations - Kuhn-Tucker form**

$$Y_d \leq \tfrac{\mathcal{G}_f}{\varepsilon}; \qquad \dot{d} \geq 0; \qquad \dot{d}\left(Y_d - \tfrac{\mathcal{G}_f}{\varepsilon}\right) = 0$$

$$\text{where } Y_d = -\tfrac{1}{2} \tfrac{dC_{ijkl}(d)}{dd} e_{xkl}\left(\mathbf{u}^{(0)}\right) e_{xij}\left(\mathbf{u}^{(0)}\right) + I_{mnpq}(d)\, e_{xmn}\left(\mathbf{u}^{(0)}\right) e_{xpq}\left(\mathbf{u}^{(0)}\right)$$

3.4 Numerical results

At the local macroscopic level we study the macroscopic behaviour in compression including contact and friction for one orientation of the crack and right sense of sliding, different Coulomb's coefficients and different lateral stresses. The numerical tests, such as uniaxial and biaxial compressions, are based on following parameters: the orientation of the crack is 135°, the material is non damaged isotropic elastic with Young's modulus $E = 2\,GPa$, Poisson's ratio $\nu = 0.2$, the critical fracture energy $\mathcal{G}_{cr} = 20\,J/m^2$ and the microstructural length $c_f = 10^{-3}\,m$.

We will present the inflence of friction coefficient ($\mu_f = 0.0, 0.1, 0.3$ and 0.5) under uniaxial compression. The effects of the lateral stresses ($\Sigma_{11} = 0\,Pa, -2\times10^6\,Pa$, $-6\times10^6\,Pa$ and $-12\times10^6\,Pa$) will be performed on the material defined by friction coefficient $\mu_f = 0.3$.

3.4.1 Numerical integration method

For the analysis of the homogenized response in a macroscopic point, the input of the system are the macroscopic strain $e_{xkl}\left(\mathbf{u}^{(0)}\right)$ and/or stress $\Sigma_{ij}^{(0)}$, depending on the physical problem to be studied. For each step, the problem is solved in local point by an iterative procedure as follows:

1. Initialization (determination of the sense of sliding using macroscopic deformation $e_{xkl}\left(\mathbf{u}^{(0)}\right)$ and elastic moduli a_{ijkl})

   - prediction of macroscopic strain (calculation of the unknown components of $\mathbf{e_x}$) :
     $e_{xkl,n} = a^{-1}_{ijkl}\Sigma^{(0)}_{ij}$

   - determination of crack state (closure, sense of sliding using system (2.36), (2.37), (2.38))

2. Construction of homogenized response

   (a) if loading:

   - step $n = 1$, iteration $i+1$
   - prediction of macroscopic strain using homogenized coefficients for correct sense of sliding (calculation of the unknown components of $\mathbf{e_x}$):
     $e^i_{xkl,n} = C^{-1}_{ijkl}\left(d^i_{n-1}\right)\Sigma^{(0)}_{ij}$

   - computation of $\mathbb{N}$ (2.62) and $\mathbb{T}$ (2.61) for correct sense of sliding
   - verification of Coulomb friction law for sliding (2.63) and stationary contact (2.64)

- determination of the homogenized coefficients:
  $C_{ijkl} = C_{ijkl}\left(d^i_{n-1}\right)$

- determination of the dissipative terms:
  $I_{ijkl} = I_{ijkl}(d^i_{n-1})$

- solve the damage equation (3.1) using bisection method (see Appendix A)
- update the damage variable d^{i+1}_n
- update the homogenized coefficients:
  $C_{ijkl} = C_{ijkl}\left(d^{i+1}_n\right)$

- update the dissipative terms:
  $I_{ijkl} = I_{ijkl}(d^{i+1}_n)$

- calculation of updated strain:
  $e^{i+1}_{xkl,n} = C^{-1}_{ijkl}\left(d^{i+1}_n\right)\Sigma^{(0)}_{ij}$

(b) if unloading

- step $n = 1$, iteration $i+1$
- prediction of macroscopic strain using homogenized coefficients for last sense of sliding:
  $e^i_{xkl,n} = C^{-1}_{ijkl}\left(d^i_{n-1}\right)\Sigma^{(0)}_{ij}$

- computation of $\mathbb{N}$ (2.62) and $\mathbb{T}$ (2.61) using $\mathbb{N}_{un}$ (2.72) and $\mathbb{T}_{un}$ (2.71) for unloading phase
- verification of Coulomb friction law for backsliding (2.63) and stationary contact (2.64)
- if backsliding compute $\mathbb{N}$ (2.62) and $\mathbb{T}$ (2.61)

- update the damage variable d^{i+1}_n
- update the homogenized coefficients:
  $C_{ijkl} = C_{ijkl}\left(d^{i+1}_n\right)$

- update the dissipative terms:
  $I_{ijkl} = I_{ijkl}(d^{i+1}_n)$

- calculation of updated strain:
  $e^{i+1}_{xkl,n} = C^{-1}_{ijkl}\left(d^{i+1}_n\right)\Sigma^{(0)}_{ij}$

3. the test of convergence of the solution $CONV = \frac{\|e^{i+1}_n - e^i_n\|^2}{\|e^{i+1}_n\|^2}$

(a) if $CONV \leq Tol$ return with new step $(n = n+1)$

(b) if $CONV > Tol$ return with new iteration $(i = i+1)$

4. Calculation of the macroscopic incremental stress-strain law:

   - $\dot{\Sigma}_{ij,n}^{i+1} = A_{ijkl}\left(d_n^{i+1}\right)\dot{e}_{xkl,n}^{i+1}$ where A_{ijkl} takes different forms depending on the state of sliding or stick.

Similar algorithm can be used for different types of loading.

3.4.2 Linear R-curve

In the first step we used linear relation for R-curve as used by Z. Bazant and J. Planas [13] and we analyzed the macroscopic response of the model in the local frame.

The R-curve has a form:

$$\mathcal{G}^{\varepsilon}\left(d^{\varepsilon}\right) = \frac{\mathcal{G}_{cr} 2 d^{\varepsilon}}{c_f} \tag{3.6}$$

3.4.2.1 Uniaxial compression: linear R-curve

To determine unit cell response (see Fig. 3.1a) we imposed a vertical deformation $e_{x22} < 0$ and we left horizontal direction free of stress. In this way we performed an uniaxial test for different friction coefficients ($\mu_f = 0.0, 0.1, 0.3$ and 0.5). For a fully developed damage zone, the damage parameter should be equal to 1.

We observe that the only way to achieve this state is to use the load–unload phase, since the effective stress-strain curves involve snap-back. We load until the state when damage parameter does not progress, and we continue with a reverse loading procedure.

Under reverse loading the maximum damage is achieved, and as a conseqence we obtain a snap-back behaviour in the overall response. During the snap-back steps (for a positive rate of deformation), we distinguish between the loading process in which, independently of the sense of loading, the damage increase and the unloading, which corresponds to constant damage. As we can observe in figures 3.1a and 3.1b the solution jumps between inelastic unload when the crack propagates, and elastic one when crack does not evolve. This shows that the two solutions (loading and unloading) coexist and our numerical scheme chooses one or the other in an uncontrollable manner. This is considered as a problem of control of the computation due to a non-uniqueness of solutions, the numerical solutions switch from one to an other.

For this quasi-brittle model, after a progressive loading and reverse loading we get the strain-stress response. The presence of friction delays the maximum damage, so the friction between crack lips causes the increase of material strength. Due to friction, we can observe the change in the shape of stress-strain curves between different friction coefficients. Together with increase of the friction coefficient we observe that snap-back

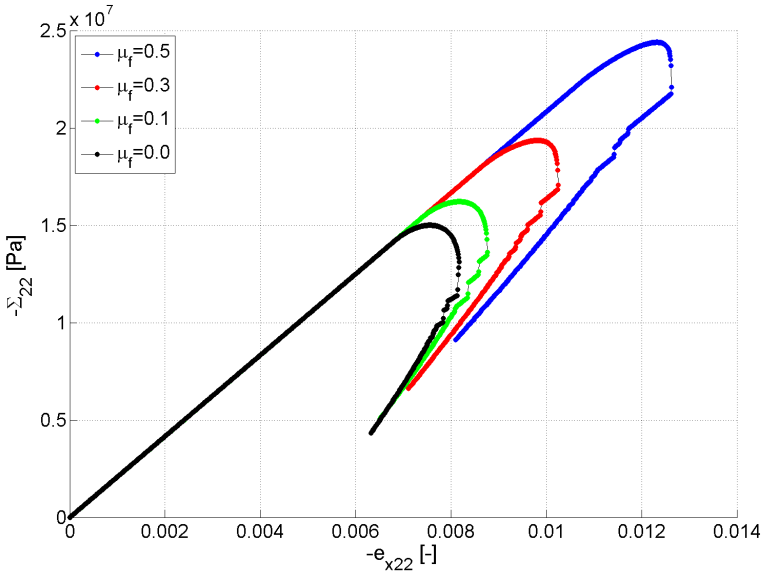

(a)

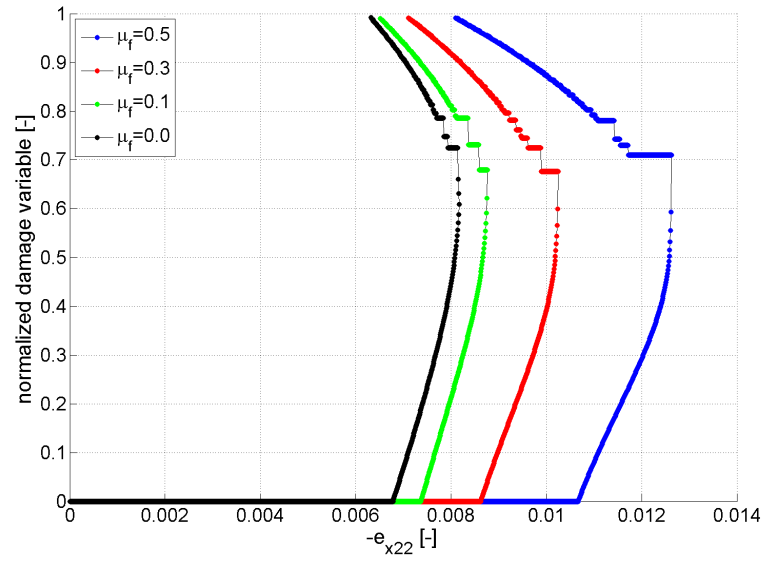

(b)

Figure 3.1: Uniaxial compression: numerical tests for different values of friction coefficients ($\mu_f = 0.0, 0.1, 0.3$ and 0.5) and linear R-curve: a) stress-strain ($\Sigma_{22} - e_{x22}$) curves, b) evolution of the damage variable (normalized crack length).

regime increases. This underlines that the friction coefficients has an important influence on the material behaviour during uniaxial test.

The evolution of the damage variable with the loading, corresponding to the Fig.3.1a, is presented in Fig.3.1b. The difference between the considered materials is visible along all phase of this evolution. For frictionless material, the evolution of damage demonstrates more rapid progress than for the frictional ones.

Following the increase of friction coefficients we can observe that damage evolution becomes slower. To reach the state of complete damage, higher deformation has to be applied on the frictional material, and it follows that the complete failure is delayed.

3.4.2.2 Biaxial compression with constant lateral stress: linear R-curve

Tests under different confining conditions were performed. We considered four loading paths with lateral stresses $\Sigma_{11} = 0\,Pa$, $-2\times10^6\,Pa$, $-6\times10^6\,Pa$ and $\Sigma_{11} = -12\times10^6\,Pa$. The tests start from the isotropic loading state ($\Sigma_{11} = \Sigma_{22}$).

We present the stress-strain curves for four different initial stresses. The results, for the case with friction ($\mu_f = 0.3$) and different values of confining pressures, are shown in Fig.3.2a. The non-monotonic loading path is needed to get fully damaged state for all tests. This shows that the snap-back is present in all macroscopic responses.

In order to have a clear view on the influence of the friction, the plot is made in terms of deformation $e_{x22} - e_{x22}^{isotropic}$ (where $e_{x22}^{isotropic}$ is initial deformation necessary for isotropic state) and $\Sigma_{22} - \Sigma_{11}$ (where Σ_{11} is lateral stress $\Sigma_{11} = 0\,Pa$, $-2\times10^6\,Pa$, $-6\times10^6\,Pa$, $-12\times10^6\,Pa$).

In this way we obtain the actual influence of the presence of friction, which is confirmed by the fact that the stress peak increases with the value of lateral stress. In case of nonfrictional material these curves would be coincided. The snap-back in the post-peak regime is also affected by lateral stress and softening amplitude is reduced with its increase.

Evolution of damage, which corresponds to those stress-strain curves, is presented in figure 3.2b. We observe that the damage evolution with respect to the axial strain at the begining of propagation slightly slows down when the lateral stress increases.

Figure 3.3 shows the stress path for four different initial stresses and friction coefficient $\mu_f = 0.3$. The presence of slope (see Figure 3.3) confirms that testing material is frictional and enables to determine the macroscopic friction angle and the friction coefficient. Friction angle and friction coefficient can be obtained by using the Mohr's circle and Coulomb's line.

Figure 3.4 shows the graphic interpretation of the peak stress state for several initial lateral stresses. The Coulomb's line crosses the vertical axis and that corresponds to a cohesion equal to $7.69\,MPa$. The angle of the Coulomb's line corresponds to the friction angle, which is equal to $\phi = 14.1°$. Using the value of friction angle we can get the value of friction coefficient from the relation

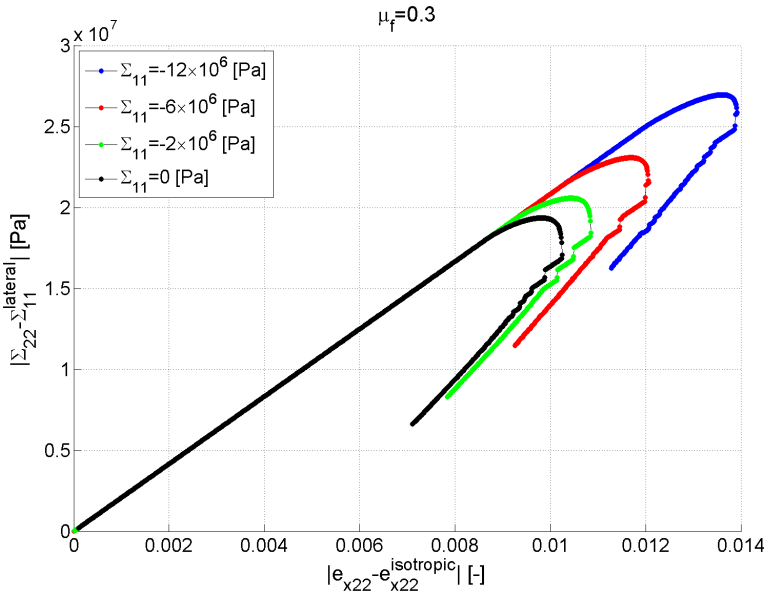

(a)

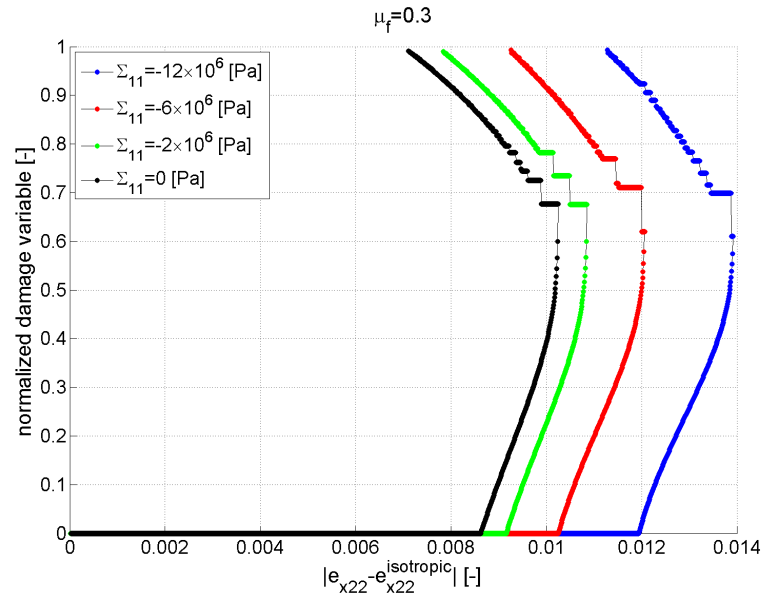

(b)

Figure 3.2: Biaxial compression: numerical tests for different values of confined pressures, friction coefficient equal $\mu_f = 0.3$ and linear R-curve: a) stress-strain ($\Sigma_{22} - e_{x22}$) curves, b) evolution of the damage variable (normalized crack length).

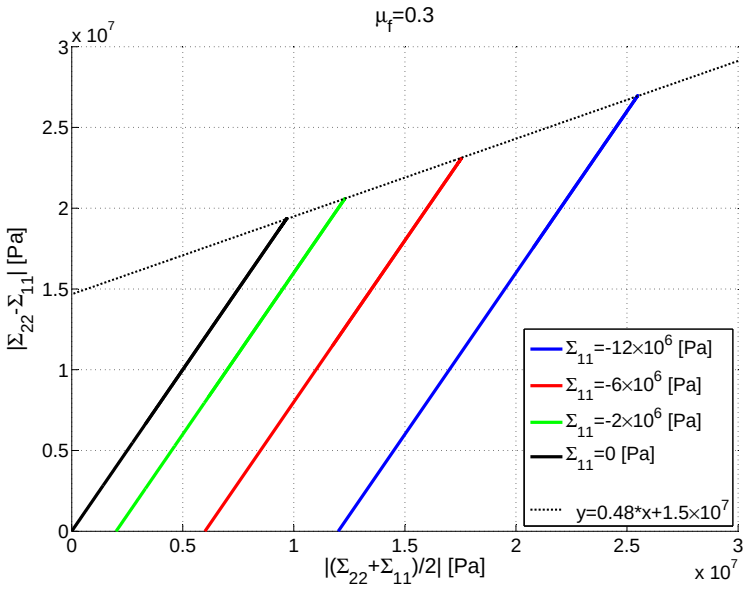

Figure 3.3: Stress path curves for different values of lateral stresses ($\Sigma_{11} = 0\,Pa$, $-2 \times 10^6\,Pa$, $-6 \times 10^6\,Pa$, $-12 \times 10^6\,Pa$) and friction coefficient equal $\mu_f = 0.3$.

microscopic friction coeffient $\mu_f[-]$	0.0	0.1	0.3	0.5
slope in the deviatoric and mean stress frame$[-]$	0.0	0.15	0.48	0.85
friction angle $\phi[^\circ]$	0.0	5.0	14.1	25.0
macroscopic friction coefficient $\mu_f^*[-]$	0.0	0.087	0.25	0.47

Table 3.1: The values of slope in the deviatoric and mean stress frame, friction angle ϕ and macroscopic friction coefficient μ_f^*.

$$\mu_f^* = tan\,(\phi) \tag{3.7}$$

Based on obtained results, the macroscopic friction coefficient is equal $\mu_f^* = 0.25$ while the corresponding microscopic friction coefficient is $\mu_f = 0.3$.

Figure 3.5 shows a comparison between different stress paths depending on friction coefficents $\mu_f = 0.0, 0.1, 0.3$ and 0.5. It can be observed that the slope of the peak stress paths changes according to the increase of friction coefficient. The slope is equal to zero for non frictional material and it is higher with the increase of friction. The slope values are summarized in the table 3.1.

The Mohr's circles and Coulomb's lines in case of different friction coefficients $\mu_f = 0.0, 0.1, 0.3$ and 0.5 are plotted in figure 3.6. We can observe that the angle ϕ grows together with the frictional properties of the material. Summary of obtained values can be found in table 3.1.

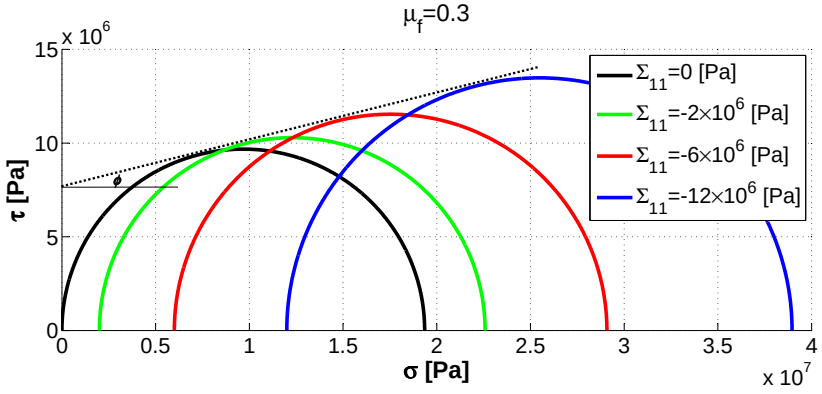

Figure 3.4: Mohr's circles and Coulomb's line for several initial lateral stresses ($\Sigma_{11} = 0\,Pa, -2\times10^6\,Pa, -6\times10^6\,Pa, -12\times10^6\,Pa$) and friction coefficient equal $\mu_f = 0.3$.

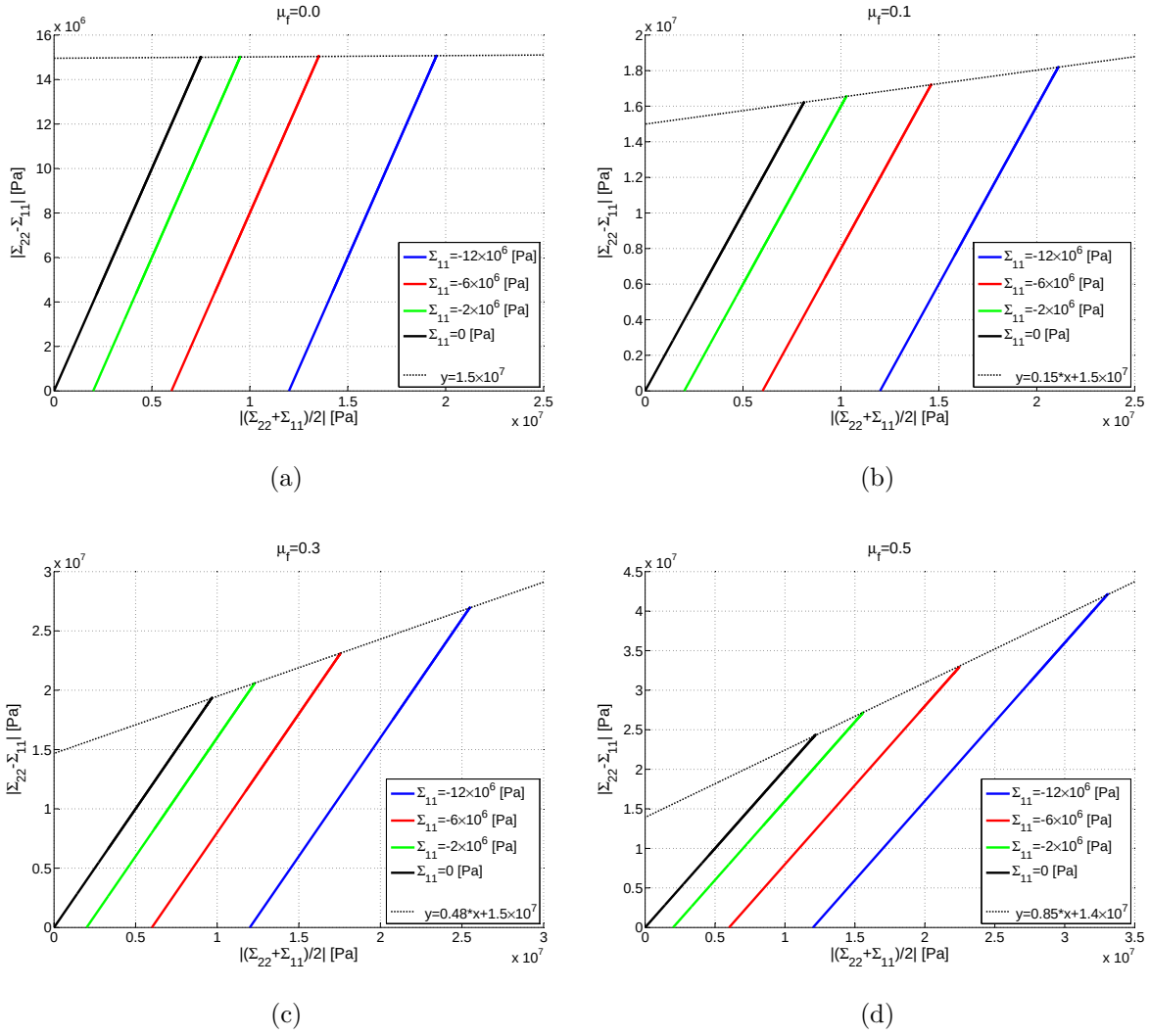

(a) (b)

(c) (d)

Figure 3.5: Stress paths curves for different friction coefficients and different lateral stresses ($\Sigma_{11} = 0\,Pa, -2\times10^6\,Pa, -6\times10^6\,Pa, -12\times10^6\,Pa$): a) $\mu_f = 0.0$, b) $\mu_f = 0.1$, c) $\mu_f = 0.3$, d) $\mu_f = 0.5$

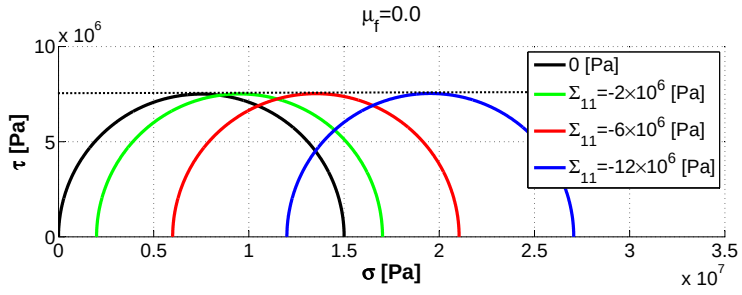

(a)

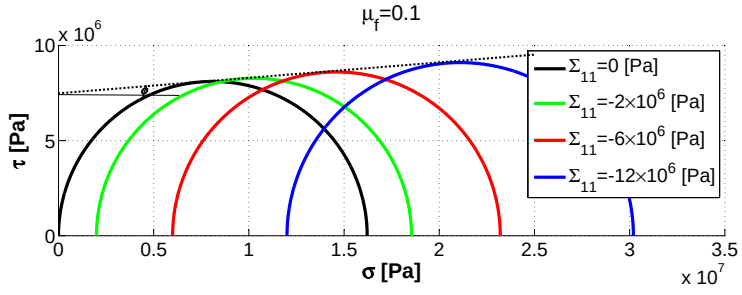

(b)

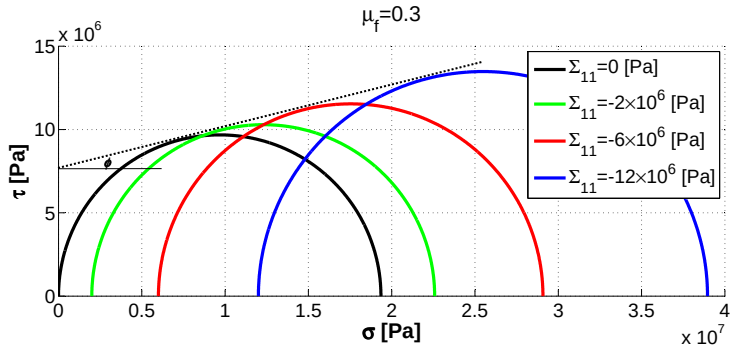

(c)

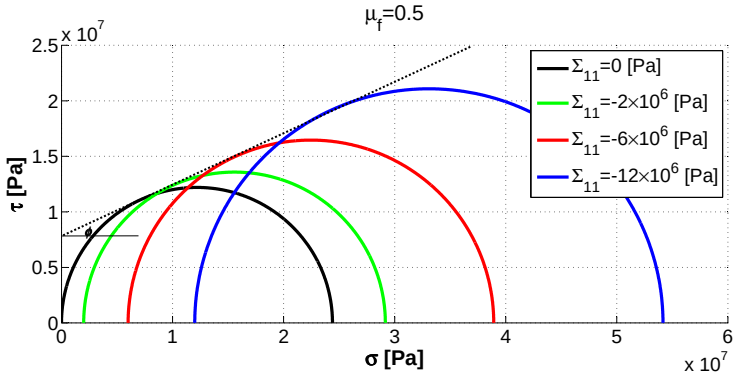

(d)

Figure 3.6: Mohr's circles and Coulomb's line for different friction coefficients under different lateral stresses ($\Sigma_{11} = 0\,Pa$, $-2\times10^6\,Pa$, $-6\times10^6\,Pa$, $-12\times10^6\,Pa$): a) $\mu_f = 0.0$, b) $\mu_f = 0.1$, c) $\mu_f = 0.3$, d) $\mu_f = 0.5$.

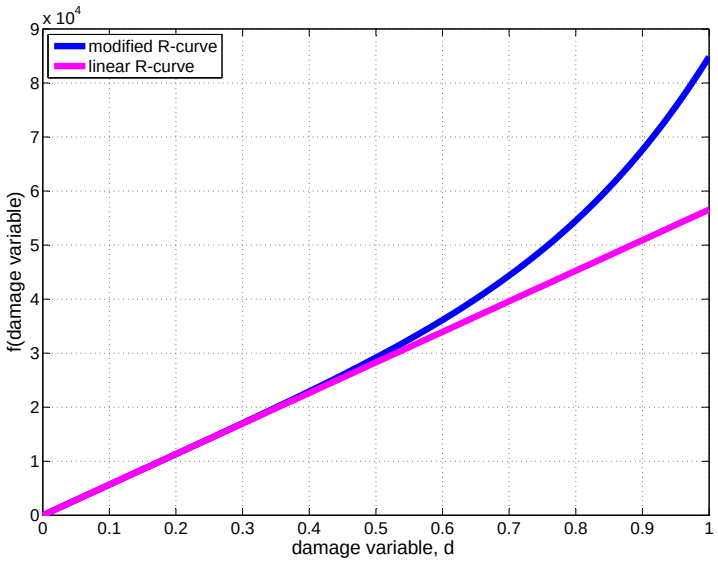

Figure 3.7: The linear R-curve (3.4) and the modified R-curve (3.9) versus damage variable d.

3.4.3 Modified R-curve

We consider that snap-back is not physical for constitutive relations and moreover is problematic in terms of numerical aspects. The snap-back is an example of strongly unstable structural behaviour. In order to avoid these difficulties, we look for an additional term in the R-curve function. We extend the previous linear relation (3.6) by adding a power function of d. The parametrical study shows that the power 5 is the smallest value which gives the response without snap-back. The R-curve which is used in this section has a following form:

$$\mathcal{G}^{\varepsilon}\left(d^{\varepsilon}\right)=\frac{\mathcal{G}_{cr}}{c_f^{\varepsilon}}2d^{\varepsilon}\left(1+\frac{1}{2}\left(\frac{d^{\varepsilon}}{\varepsilon}\right)^4\right) \tag{3.8}$$

When written in terms of the damage parameter $d^{\varepsilon}=\sqrt{2}d\varepsilon$ and $c_f^{\varepsilon}=c_f\varepsilon$ it leads to:

$$\frac{\mathcal{G}^{\varepsilon}\left(d\right)}{\varepsilon}=\frac{\mathcal{G}_{cr}}{c_f}\left(2\sqrt{2}d+\left(\sqrt{2}d\right)^5\right) \tag{3.9}$$

Figure 3.7 presents the linear and the modified R-curves.

Using the modified R-curve we performed the same tests as in previous section, in order to make a comparison and to study what is the influence of the R-curves on the macroscopic response.

3.4.3.1 Uniaxial compression: modified R-curve

The first test which was done is an uniaxial test for different values of friction coefficients $\mu_f = 0.0, 0.1, 0.3$ and 0.5 . In vertical direction we applied a deformation $e_{x22} < 0$ while horizontal direction is free of stress. Figure 3.8a shows the macroscopic response in terms of vertical stress and axial strain for different friction coefficients. The evolution of normalized damage variable with applied deformation, which corresponds to the figure 3.8a, is presented in the figure 3.8b. Concerning the influence of friction coefficient, we can observe that the strength of material increases together with it. The presence of friction is visible also in the shape of the evolution of damage variable (see Fig.3.8b). Generally, the presence of friction between crack lips slows down the process of propagation. The slope of the curve, *d vs* e_{x22}, at the begining of damage decreases with friction coefficient while at the end of loading the slope increases with friction coefficient.

As we can observe, the total damage occurs only after increasing loading, without snap-back. In such a way we are able to control the post-peak phase, which was difficult before. The responses, in case of linear and modified R-curve, show that until a certain point the solutions approach to each other. This fact can be deduced from the figure 3.7 where the used functions are plotted.

The functions overlap until the point where damage variable is close to 0.6, and above this value we can observe the influence of additional term. The presence of this term tends to have a less brittle behaviour and allows us to continue the loading and get total damage without snap-back.

3.4.3.2 Biaxial compression with constant lateral stress : modified R-curve

The modified R-curve has been used in the case of biaxial tests. The full damage was obtained only by loading procedure, what gives us a response without snap-back.

In order to study the frictional properties of the material the following computations were made. For one value of friction coefficient $\mu_f = 0.3$ the biaxial tests with different constant lateral stresses ($\Sigma_{11} = 0\,Pa$, $-2\times10^6\,Pa$, $-6\times10^6\,Pa$, $-12\times10^6\,Pa$) were performed. The tests were controlled by the macroscopic deformation e_{x22}, under constant lateral stress Σ_{11} . For each lateral stress the initial deformation was determined in order to perform isotropic state at the initial level. Figure 3.9a shows the macroscopic response in the terms of the strain $e_{x22} - e_{x22}^{isotropic}$ (where $e_{x22}^{isotropic}$is the initial macroscopic deformation) and $\Sigma_{22} - \Sigma_{11}$(where Σ_{11} is the constant lateral stress). In this way we obtained the actual influence of the presence of friction, which is underlined by the fact that the absolute value of the peak stress increases with the value of the lateral stresses (see Fig. 3.9a).

The evolution of the damage variable, which is linked to the previous plot (see Fig. 3.9a) is presented in the figure 3.9b. This evolution becomes slower and more controlled together with the increase of lateral stress. This plot corresponds also to the Fig.3.10 where stress paths for different values of lateral stresses are presented.

Based on the slope which appears in the figure 3.10 we can confirm that tested material is frictional. The macroscopic friction coefficient can be deduced from the graphical

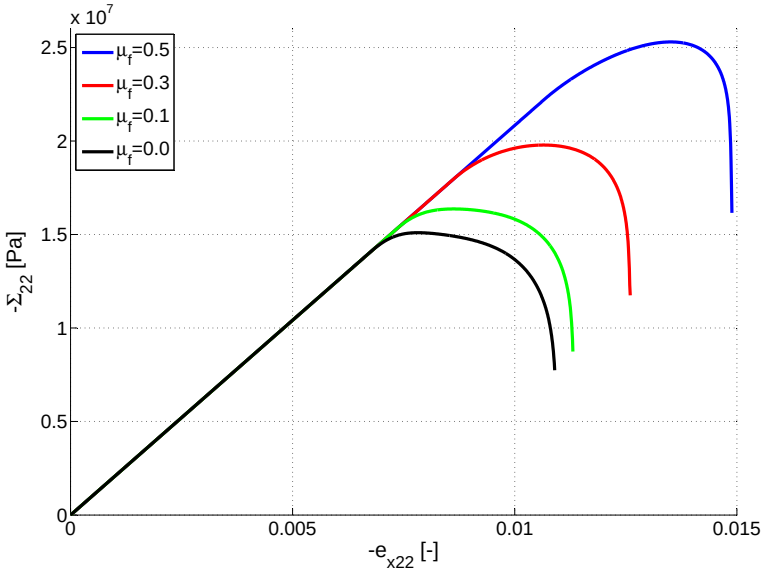

(a)

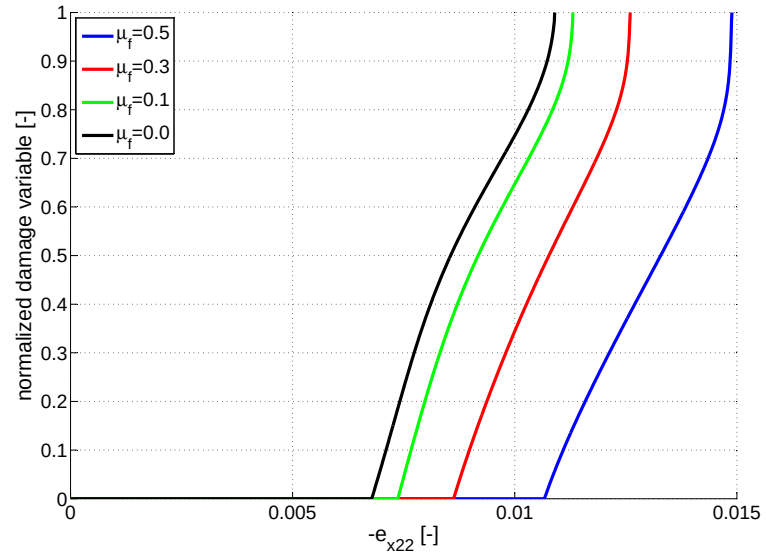

(b)

Figure 3.8: Uniaxial compression: numerical tests for different friction coefficients $\mu_f = 0.0, 0.1, 0.3, 0.5$ and modified R-curve: a) stress-strain ($\Sigma_{22} - e_{x22}$) curves, b) evolution of the damage variable (normalized crack length).

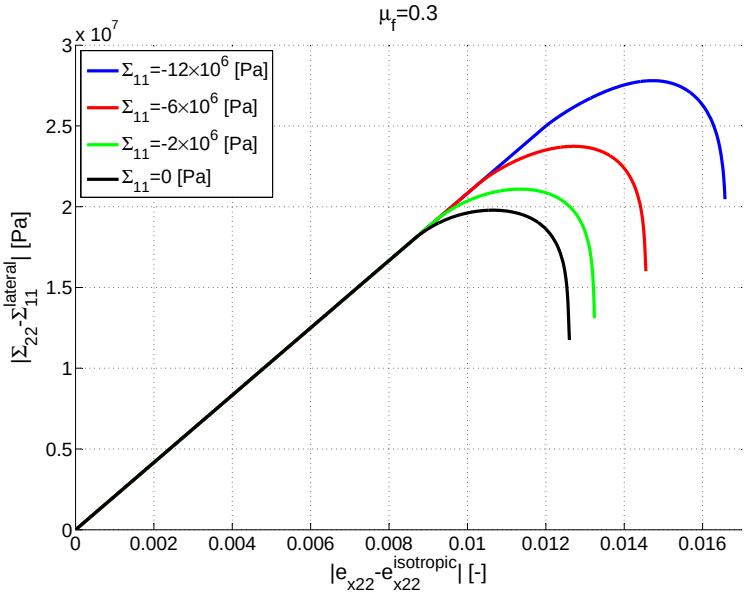

(a)

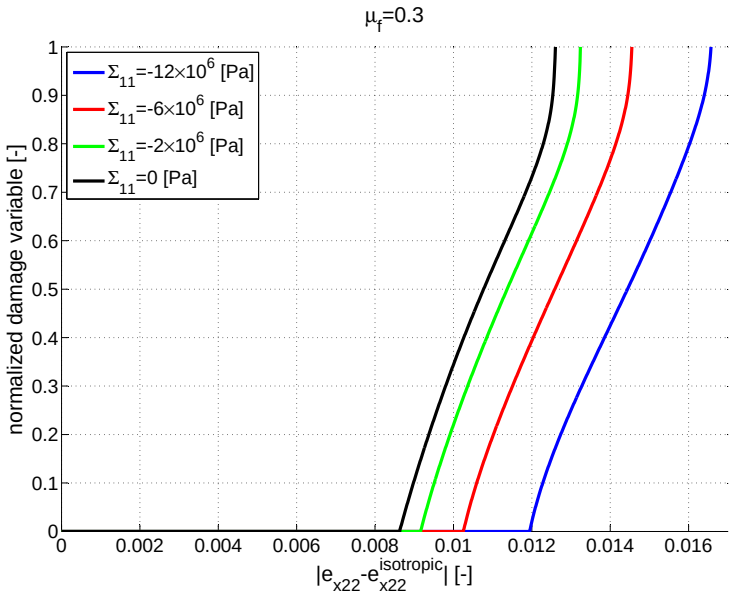

(b)

Figure 3.9: Biaxial compression: numerical tests for different constant lateral stresses ($\Sigma_{11} = 0\,Pa, -2 \times 10^6\,Pa, -6 \times 10^6\,Pa, -12 \times 10^6\,Pa$), friction coefficient $\mu_f = 0.3$ and modified R-curve: a) stress-strain ($\Sigma_{22} - e_{x22}$) curves, b) evolution of the damage variable (normalized crack length).

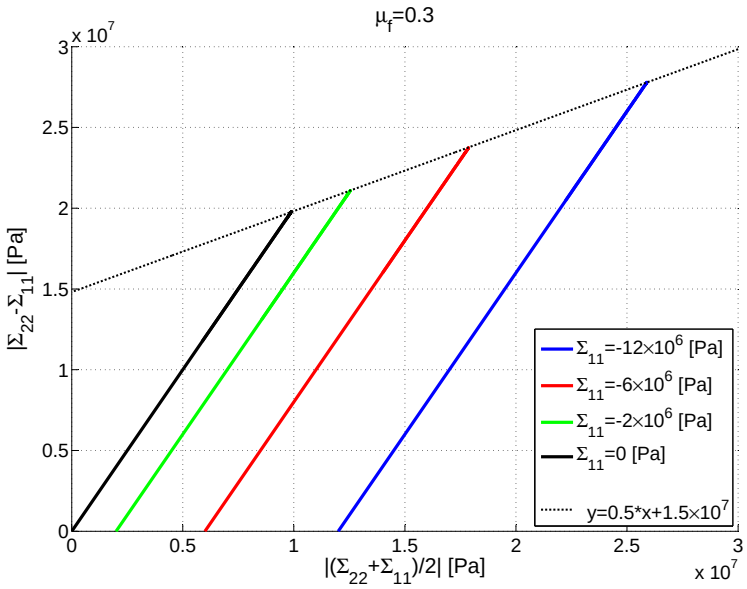

Figure 3.10: Stress path curves for different values of lateral stresses ($\Sigma_{11} = 0\,Pa$, $-2 \times 10^6\,Pa$, $-6 \times 10^6\,Pa$, $-12 \times 10^6\,Pa$) and friction coefficient $\mu_f = 0.3$

interpretation of Mohr's circles and Coulomb's line, which is presented in figure 3.11. The Coulomb's line, which is tangential to the Mohr's circle, gives us a friction angle $\phi = 14.5°$. From this angle the friction coefficient can be computed using the relation (3.7), where μ_f^* represents the macroscopic friction coefficient. As a result we obtain $\mu_f^* = 0.26$, while the microscopic friction coefficient used in the computations of the unit cell is equal to $\mu_f = 0.3$. According to the figure 3.11 another material parameter can be deduced. The Coulomb's line crosses the vertical axe in the point corresponding to the value of the cohesion and its obtained value is $c = 7.79\,MPa$.

Figure 3.12 shows the influence of the friction coefficient on stress path curves. The plots are made for different friction coefficients and at the same time for different constant lateral stresses. It can be observed that the slope of the peak stress paths changes according to the increase of the friction coefficient. The slope is equal to zero for non frictional material and it is higher for material with higher friction coefficient.

Figure 3.13 shows the influence of friction on the peak stress state. We can observe that the angle ϕ determined by Coulomb's line grows together with the frictional properties of the material.

Table 3.2 summarizes the values for micro- and macroscopic friction coefficient, friction angle, and slope in deviatoric and mean stress frame. The microscopic friction coefficient is a coefficient which was used in the computation on the unit cell and the macroscopic one is obtained based on the macroscopic results in the local frame. The values of the macroscopic friction coefficients are slightly reduced compared to microscopic one.

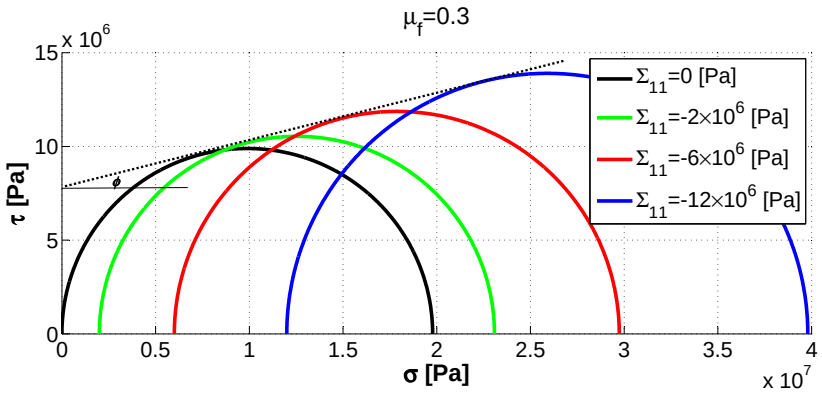

Figure 3.11: Mohr's circles and Coulomb's line (peak stress state) for several initial lateral stresses ($\Sigma_{11} = 0\,Pa$, $-2\times10^6\,Pa$, $-6\times10^6\,Pa$, $-12\times10^6\,Pa$) and friction coefficient $\mu_f = 0.3$

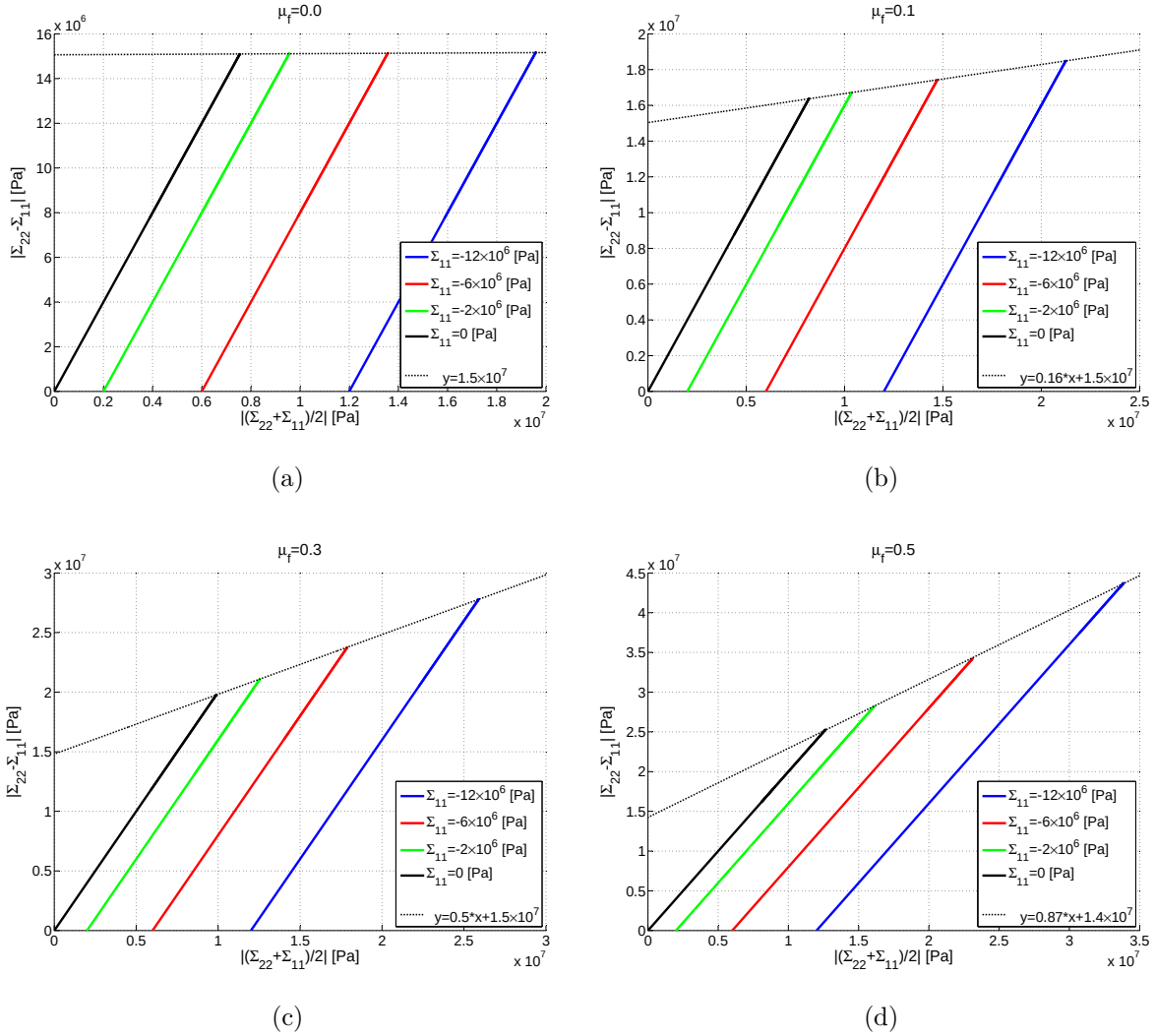

Figure 3.12: Stress path curves for different values of lateral stresses ($\Sigma_{11} = 0\,Pa$, $-2\times10^6\,Pa$, $-6\times10^6\,Pa$, $-12\times10^6\,Pa$) and friction coefficients: a) $\mu_f = 0.0$, b) $\mu_f = 0.1$, c) $\mu_f = 0.3$, d) $\mu_f = 0.5$.

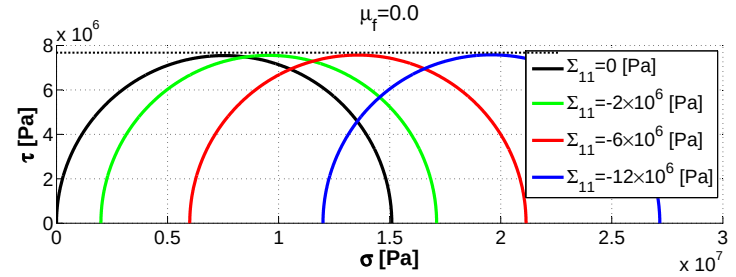

(a)

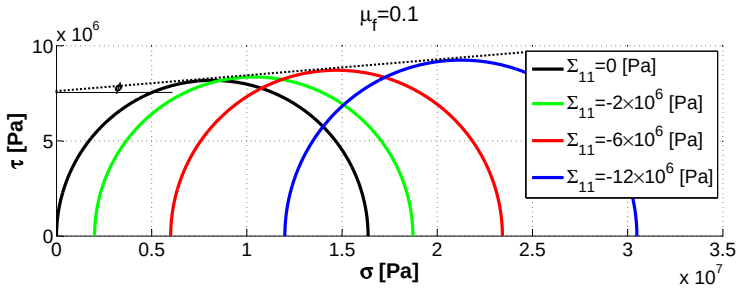

(b)

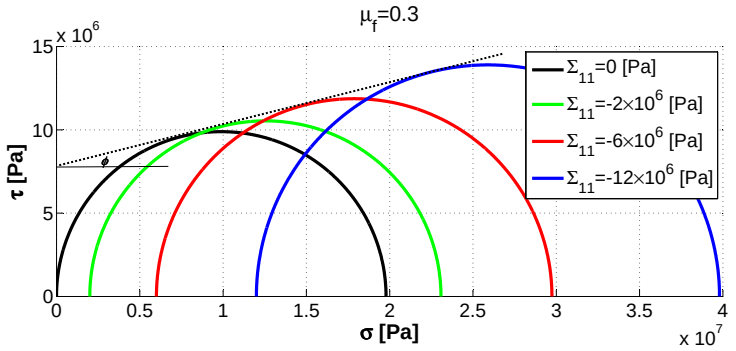

(c)

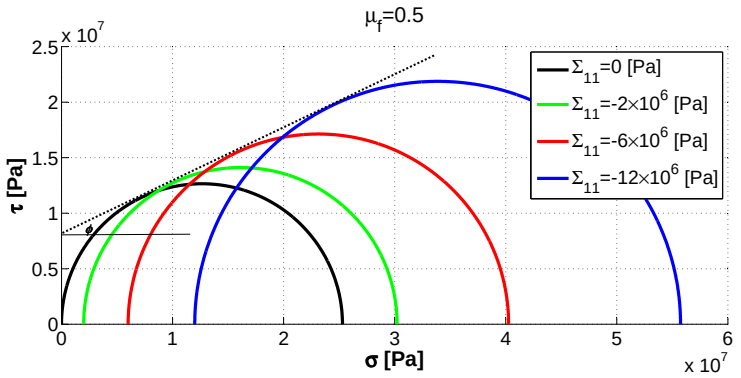

(d)

Figure 3.13: Mohr's circles and Coulomb's line for different friction under different lateral stresses ($\Sigma_{11} = 0\,Pa, -2\times10^6\,Pa, -6\times10^6\,Pa, -12\times10^6\,Pa$): a) $\mu_f = 0.0$, b) $\mu_f = 0.1$, c) $\mu_f = 0.3$, d) $\mu_f = 0.5$.

microscopic friction coeffient $\mu_f[-]$	0.0	0.1	0.3	0.5
slope in the deviatoric and mean stress frame[−]	0.0	0.16	0.5	0.87
friction angle $\phi[^\circ]$	0.0	5.0	14.5	25.5
macroscopic friction coefficient $\mu_f^*[-]$	0.0	0.087	0.26	0.48

Table 3.2: Summary of obtained slopes in deviatoric and mean stress frame, friction angles ϕ and macroscopic friction coefficients μ_f^* *vs* microscopic friction coefficients μ_f.

	Linear R-curve	Modified R-curve
slope in the deviatoric and mean stress frame[-]	0.48	0.5
friction angle ϕ [°]	14.1	14.5
macroscopic friction coefficient μ_f^*[-]	0.25	0.26
cohesion c [MPa]	7.69	7.79

Table 3.3: Influence of the linear and modified R-curve on the material parameters for microscopic friction coefficient $\mu_f = 0.3$

3.4.4 Comparison between linear and modified R-curves

The influence of the R-curve on the material parameters is presented in the table 3.3, which sums up the results obtained by using linear and modified resistance curve for microscopic friction coefficient $\mu_f = 0.3$. The additional term, which was used in the R-curve, doesn't have a strong influence on friction angle, friction coefficient, cohesion and stress paths. This modification allowed us to avoid a snap-back behaviour and to control the post-peak phase without significative interruption on the material parameters.

3.4.5 Loading - unloading cycle for modified R-curve

In this subsection we will perform uniaxial and biaxial tests with unloading regimes. In the models which couple the damage and friction, the response in the unloading phase contains unelastic behaviour, which can not be observed for nonfrictional materials. Due to frictional sliding micro-cracks, we can distinguish several states of crack, which are controlled by classical Coulomb law in the general form:

$$| \mathbb{T} | < -\mu_f \mathbb{N} \tag{3.10}$$

during stationary contact (i.e. crack lips are stick) and

$$| \mathbb{T} | = -\mu_f \mathbb{N} \tag{3.11}$$

during slip (i.e. the crack lips are sliding).

$\mathbb{N}$ and $\mathbb{T}$ are normal and tangential components of the stress to crack lip and they were deduced in the form:

$$\mathbb{N}^{pq} \equiv N_i a_{ijkl} \bar{E}^{pq}_{kl} N_j \int_{CY} ds_y + \int_{CY} \left(N_i a_{ijkl} e_{ykl} \left(\boldsymbol{\eta}^{pq} \right) N_j \right) ds_y \tag{3.12}$$

$$\mathbb{T}^{pq} \equiv T_i a_{ijkl} \bar{E}^{pq}_{kl} N_j \int_{CY} ds_y + \int_{CY} \left(T_i a_{ijkl} e_{ykl} \left(\boldsymbol{\eta}^{pq} \right) N_j \right) ds_y \tag{3.13}$$

These quantities come from the unit cell computations and they are stored as the polynomial functions in d .

Following many authors ([5, 46, 56, 72, 84]), who observed that during initial phase of unloading the crack faces remain stationary until the reverse sliding occurs, we rewrite the formulation for $\mathbb{N}$ (3.12) and $\mathbb{T}$ (3.13) for unloading phase by extracting an inelastic terms. These terms remain constant during unloading and they have following forms:

$$\mathbb{N}^{pq}_{un} = \int_{CY} \left(N_i a_{ijkl} e_{ykl} \left(\boldsymbol{\eta}^{pq} \right) N_j \right) ds_y \tag{3.14}$$

$$\mathbb{T}^{pq}_{un} = \int_{CY} \left(T_i a_{ijkl} e_{ykl} \left(\boldsymbol{\eta}^{pq} \right) N_j \right) ds_y \tag{3.15}$$

The terms (3.14) and (3.15) are computed for the last configuration of loading phase and are kept constant during unloading until the backsliding occurs. In the following tests we will not focus only on the material response under compressive loadings but also on the evolution and relations of the particular components of the Coulomb law (Eqs.3.10 and 3.11).

$E\,[Pa]$	$\nu\,[-]$	$c_f\,[m]$	$d_0\,[-]$	$\mathcal{G}_{cr}\left[\frac{J}{m^2}\right]$	$\theta\,[^\circ]$	$-\Sigma_{11}\,[Pa]$
2×10^9	0.2	10^{-3}	10^{-6}	20.0	135	0.0

Table 3.4: Parameters used in the simulations of uniaxial test at local macroscopic scale for quasi-brittle model.

3.4.5.1 Uniaxial compression: loading-unloading cycle

The first test in which we will study the influence of friction is uniaxial compression. We performed the loading-unloading path for different friction coefficients $\mu_f = 0.0, 0.1, 0.3$ and 0.5. The moment of unloading was fixed when the damage variable is equal to $d = 0.7$, in order to compare the responses in terms of stick case, appearance and duration of backsliding. The material parameters used in the simulations are listed in the table 3.4.

Figure 3.14 shows the stress-strain curves under uniaxial compression for different friction coefficients ($\mu_f = 0.0, 0.1, 0.3$ and 0.5). As previously observed, the presence of friction increases the strength of the material.

In the initial part of the unloading regime the micro-cracks are locked and in consequence the material is considered as undamaged (the curve is characterized by the effective modulus, E^{un}, which corresponds to the modulus of the uncracked material). This locking state extends with the friction coefficient.

In case of non frictional material, the stick phase can not occur, as can be seen in figure 3.14 (see the black curve) where unloading phase indicates an elastic behaviour.

As we can observe in Fig.3.14, the earliest reverse sliding appears for the material with friction coefficient equal to $\mu_f = 0.1$ and latest one for $\mu_f = 0.5$. During this backsliding the crack is unlocked and slides again, but in the opposite sense. The slope of the curve, in this regime, is determined by the effective modulus of damaged material for the sense of sliding opposite to the sense during loading. Due to frictional mechanism we obtained irreversible strain, which value grows together with increase of friction coefficient. This tendency is caused by the fact that for higher friction coefficients the stick case is extended and in consequence the higher values of inelastic deformation are stored by the system.

Figure 3.15 shows the evolution of damage variable during loading-unloading phase for different friction coefficients $\mu_f = 0.0, 0.1, 0.3$ and 0.5 under uniaxial compression. We load until damage variable reaches the value $d = 0.7$ and then we start the unloading procedure, in which the propagation is not present and in consequence the snap-back behaviour does not occur. The points indicating the begining of back sliding for different friction coefficients are shown in figure 3.15.

All these mechanisms, which appeared during loading-unloading test (i.e. sliding, stick and back sliding), are controlled by the $\mathbb{N}$ and $\mathbb{T}$ via Coulomb friction law (3.10 and 3.11).

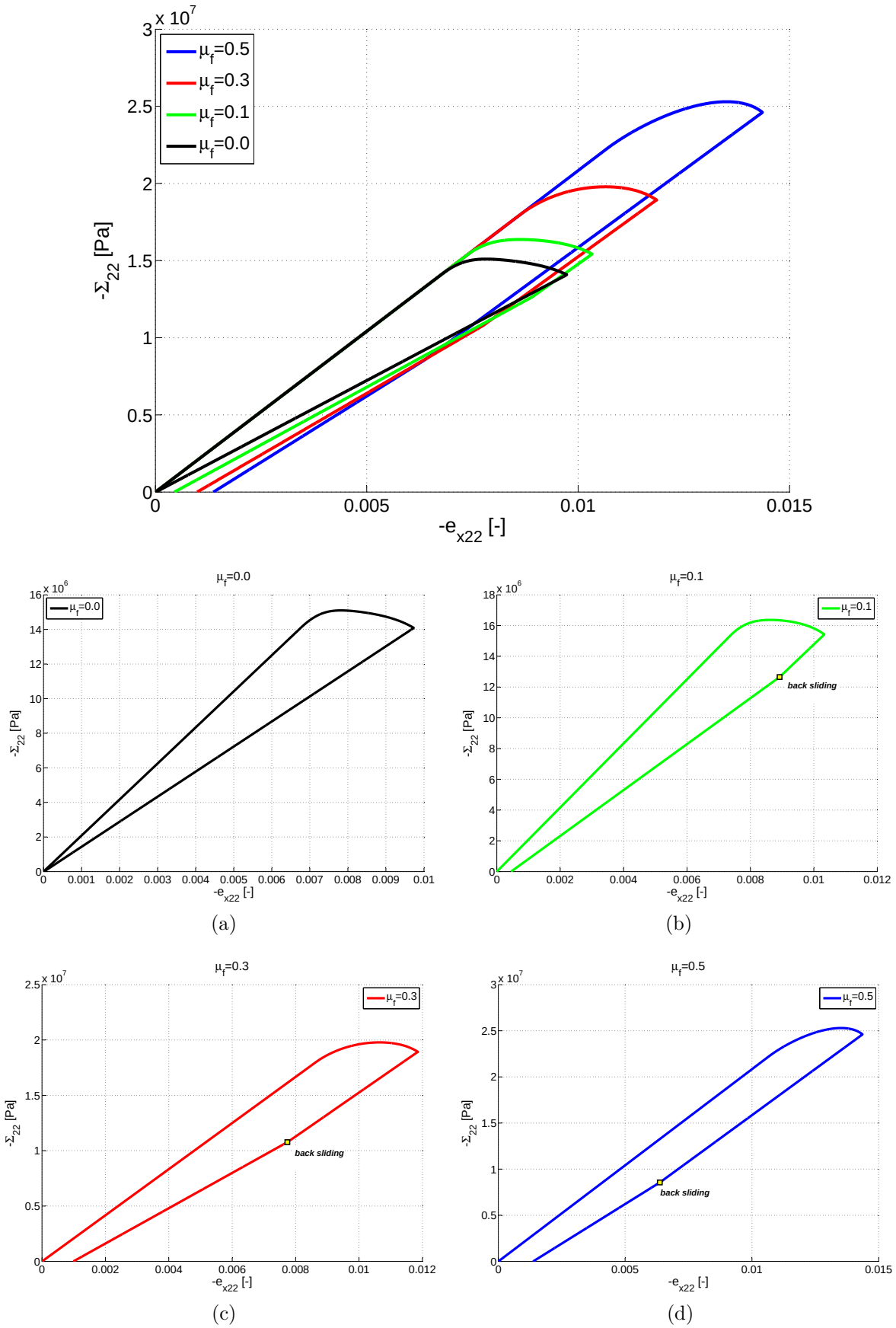

Figure 3.14: Stress-strain curves for uniaxial test for different friction coefficients during loading-unloading phase with focus on cases: a) $\mu_f = 0.0$, b) $\mu_f = 0.1$, c) $\mu_f = 0.3$, d) $\mu_f = 0.5$.

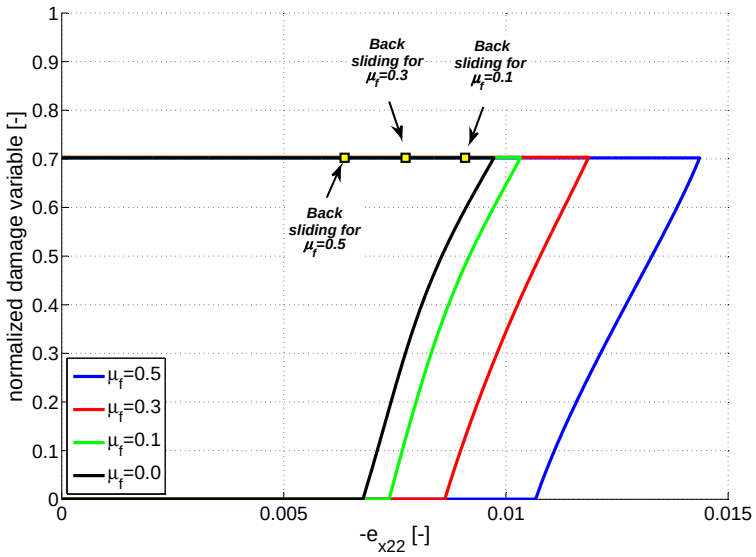

Figure 3.15: Evolution of the crack length for the uniaxial test for different friction coefficients $\mu_f = 0.0, 0.1, 0.3$ and 0.5 during loading-unloading phase.

Figure 3.16 shows the evolution of tangential components of the stress $\mathbb{T}$ during computations (loading-unloading) for different friction coefficients $\mu_f = 0.1, 0.3$ and 0.5. The arrows visible in the Fig. 3.16 indicate the direction of the evolution. $\mathbb{T}$ during loading is underlined in green and during unloading in red. The two dashed lines are theoretical limits for sliding (left and right).

Initially, $d_0 = 10^{-6}$ so that $\mathbb{T}$ is negligible. This changes when propagation starts.

When $\mathbb{T}$ takes positive values the right sliding is present, and it happens in this example during loading. A reverse sliding (left sliding) may occur only if the sign of $\mathbb{T}$ will change into negative one and Eq.3.11 is satisfied. The Eq.3.11 is satisfied when the value of $\mathbb{T}$ intersects the theoretical limit of left sliding for $d = 0.7$ (the last value of d during loading). The behaviour between the beginning of unloading and reverse sliding is controllled by the Eq.3.10. This regime represents two states when the sliding is blocked. The first one with still positive $\mathbb{T}$, and the second one with negative $\mathbb{T}$, still not sufficient to cause the sliding process.

Figure 3.17 presents the evolution of the normal component of stress $\mathbb{N}$, along the computation for different friction coefficients $\mu_f = 0.1, 0.3$ and 0.5. The sign of $\mathbb{N}$ is always negative during the loading-unloading phase due to compressive character of the test.

According to the friction Coulomb law defined by Eqs. 3.10 and 3.11, the ratio of tangential to normal component of the stress will oscillate between $-\mu_f$ and μ_f (or reverse, depending on the sense of sliding). Inside this interval there is no sliding but only on its boundaries.

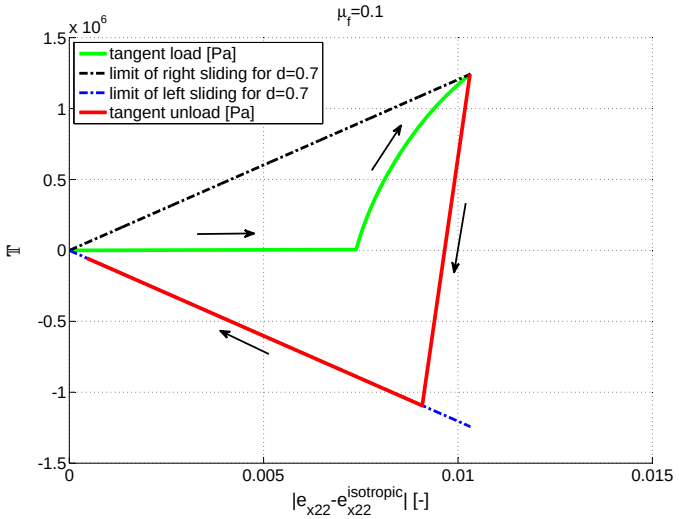

(a)

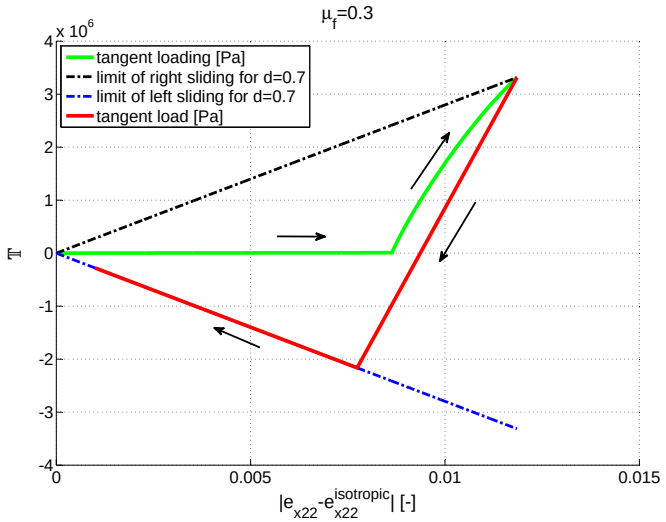

(b)

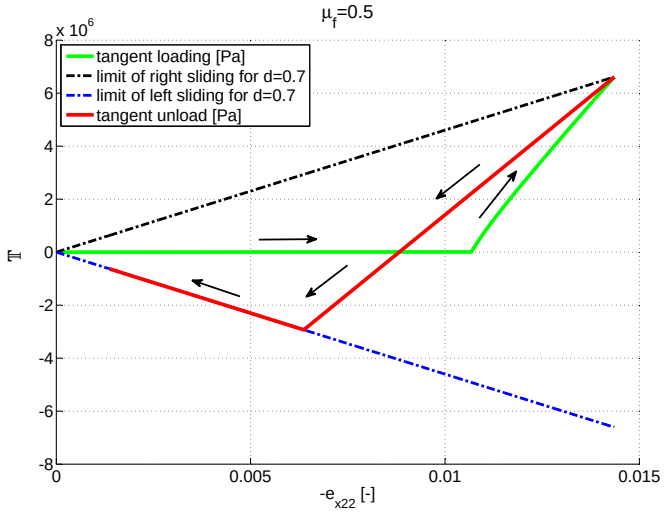

(c)

Figure 3.16: Evolution of the tangential component of the stress for the uniaxial test for different friction coefficients during loading-unloading phase and $d_0 = 10^{-6}$: a) $\mu_f = 0.1$, b) $\mu_f = 0.3$, c) $\mu_f = 0.5$.

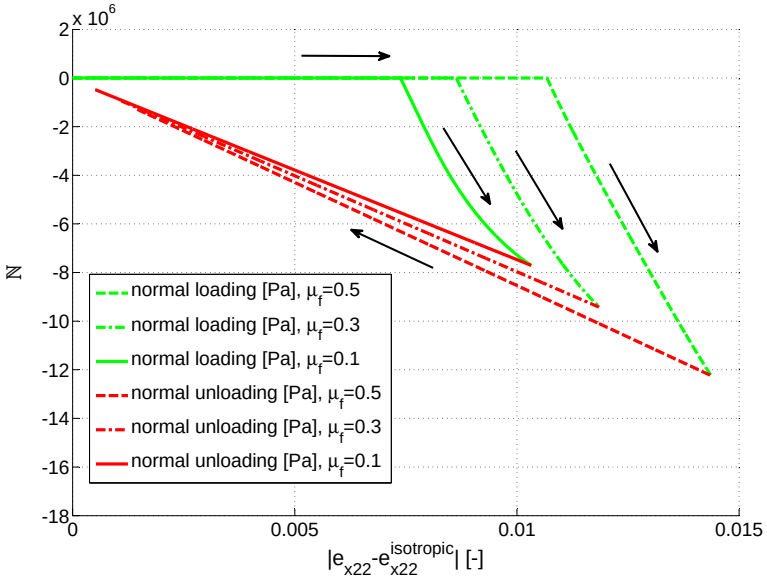

Figure 3.17: Evolution of the normal component of the stress for the uniaxial test for different friction coefficients $\mu_f = 0.1, 0.3$ and 0.5 during loading-unloading phase.

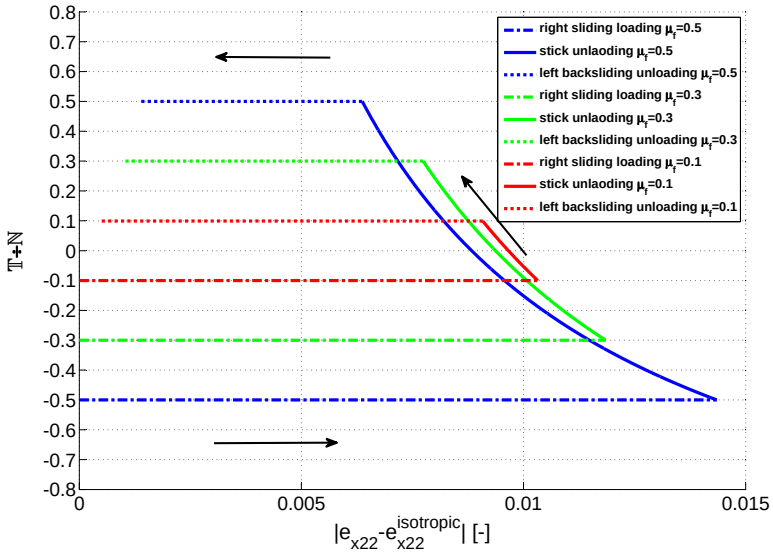

Figure 3.18: Evolution of the ratio of tangential to normal component of the stress ($\mathbb{T} \div \mathbb{N}$) for the uniaxial test for different friction coefficients $\mu_f = 0.1, 0.3$ and 0.5 during loading-unloading phase.

Figure 3.18 shows the evolution of the ratio of $\mathbb{T}$ to $\mathbb{N}$ during loading-unloading phase for different friction coefficients $\mu_f = 0.1, 0.3$ and 0.5. Depending on frictional properties of the material, the intervals are -0.1 to 0.1 for $\mu_f = 0.1$, -0.3 to 0.3 and -0.5 to 0.5 for $\mu_f = 0.3$ and $\mu_f = 0.5$ respectively. Figure 3.18 is directly related to macroscopic response of the material (see Fig.3.14), explaining the behaviour at each step of the computation (i.e. sliding right, stick and backsliding).

Figure 3.19 shows the stress-strain curve and the evolution of the damage variable under uniaxial compression for friction coefficient $\mu_f = 0.5$. The steps determined by the points A, B, C, D, E, F correspond to different macroscopic behaviour. These different states are controlled by Coulomb law through the relations of its components $\mathbb{T}$, $\mathbb{N}$ and μ_f. The evolution of these components is plotted in the figure 3.20. The steps are as it follows:

- in step AB, the damage does not progress and is equal to initial damage $d_0 = 10^{-6}$, so that the stress-strain relation is linear. $\mathbb{T}$ and $\mathbb{N}$ are negligible and the ratio $\mathbb{T} \div \mathbb{N}$ is established at $-\mu_f = 0.5$.
- between B and C, the slope of the stress-strain curve decreases due to crack propagation. $\mathbb{T}$ and $\mathbb{N}$ increase, but their ratio $\mathbb{T} \div \mathbb{N}$ is still equal to $-\mu_f = 0.5$.
- the unloading starts with the phase CD, in which no sliding occurs, and in consequence the propagation is blocked. $\mathbb{T}$ and $\mathbb{N}$ decrease and the ratio $\mathbb{T} \div \mathbb{N}$ changes inside the interval between $-\mu_f$ and μ_f (-0.5 and 0.5).
- the back sliding regime is determined by the step DEF :
  - in the step DE crack is still locked due to friction. $\mathbb{T}$ changes his sign and, like $\mathbb{N}$, it still decreases. The ratio $\mathbb{T} \div \mathbb{N}$ is still inside the interval between $-\mu_f$ and μ_f (-0.5 and 0.5).
  - in the step EF the sliding in the reverse direction occurs and the slope of the stress-strain curve decreases. $\mathbb{T}$ increases, following the limit of reverse sliding and $\mathbb{N}$ decrease. The ratio $\mathbb{T} \div \mathbb{N}$ is established at $\mu_f = 0.5$ due to the sliding in the reverse sense.
- point F indicates the irreversible strain stored by the system.

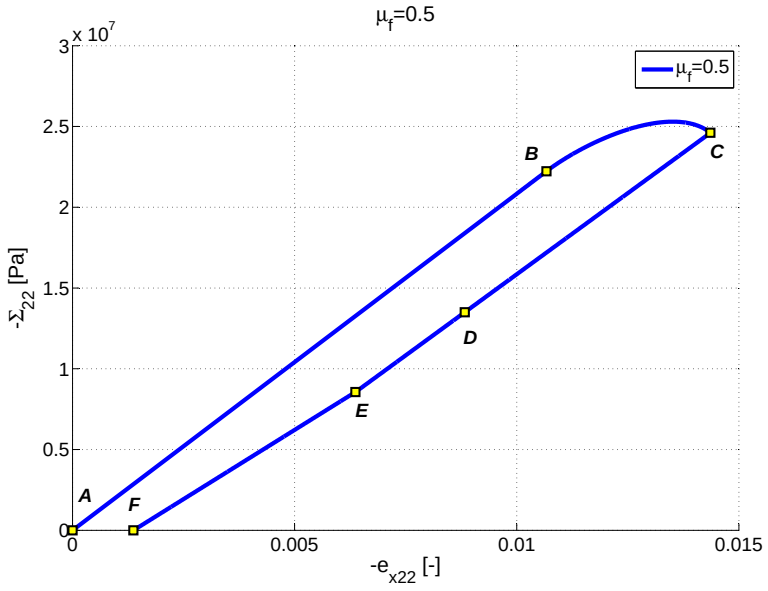

(a)

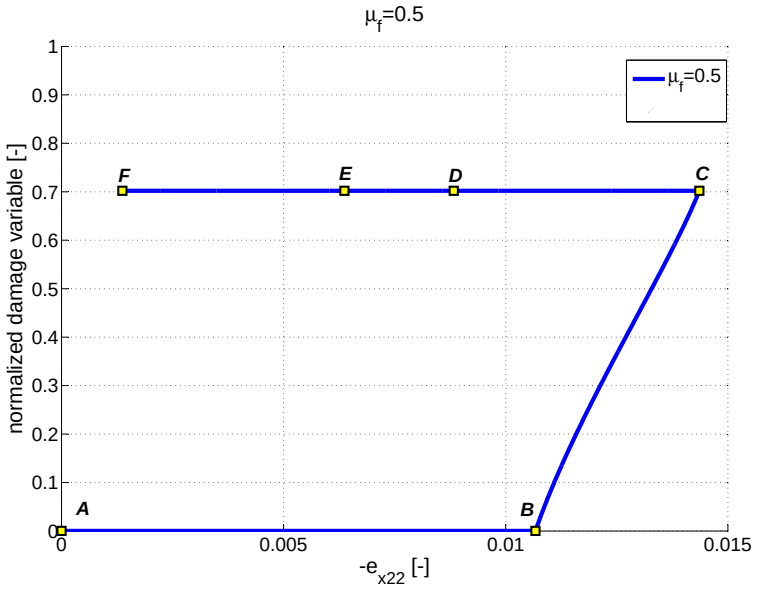

(b)

Figure 3.19: Uniaxial compression for friction coefficient $\mu_f = 0.5$: a) stress-strain curve, b) damage variable evolution.

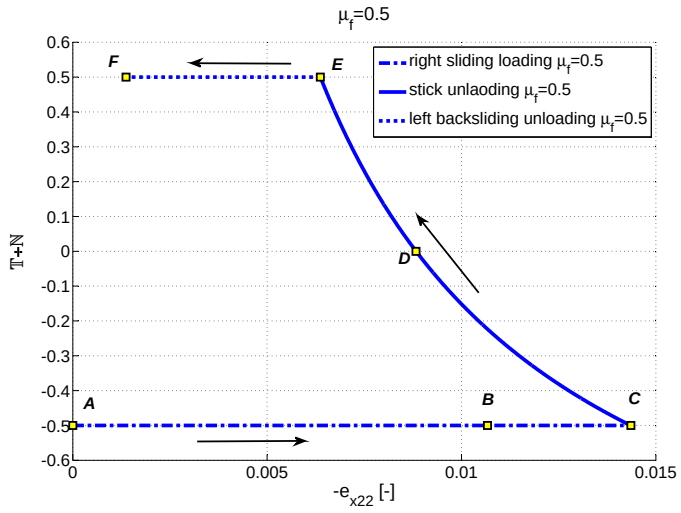

(a)

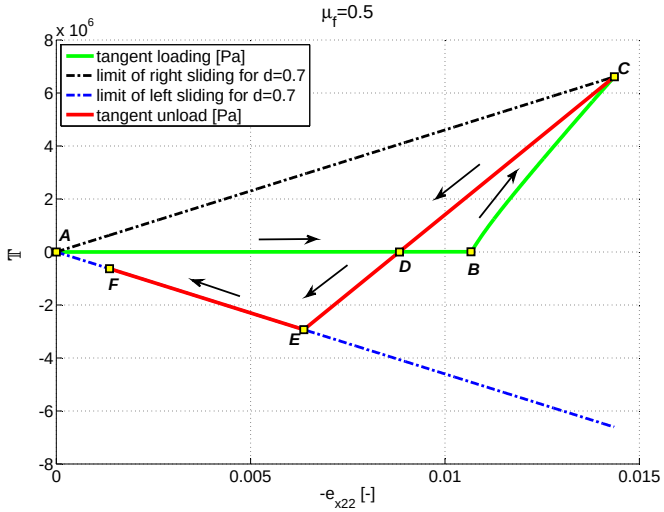

(b)

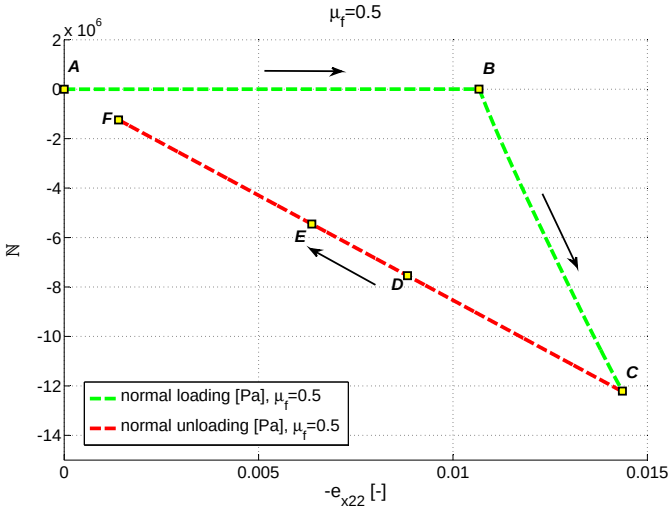

(c)

Figure 3.20: Uniaxial compression for friction coefficient $\mu_f = 0.5$: a) ratio $\mathbb{T} \div \mathbb{N}$, b) evolution of $\mathbb{T}$, c) evolution of $\mathbb{N}$.

$E\,[Pa]$	$\nu\,[-]$	$c_f\,[m]$	$d_0\,[-]$	$\mathcal{G}_{cr}\left[\frac{J}{m^2}\right]$	$\theta\,[^\circ]$	$\mu_f\,[-]$
2×10^9	0.2	10^{-3}	10^{-6}	20.0	135	0.3

Table 3.5: Parameters used in the simulations of biaxial test at local macroscopic scale for quasi-brittle model.

3.4.5.2 Biaxial compression with constant lateral stress: loading-unloading cycle

The second type of test is related to the influence of lateral stress on the macroscopic response of the material and on the components of Coulomb law ($\mathbb{T}$ and $\mathbb{N}$), under biaxial compression during loading-unloading phase. The biaxial tests were performed for different values of lateral stress ($\Sigma_{11} = 0\,Pa$, $-2\times10^6\,Pa$, $-6\times10^6\,Pa$, $-12\times10^6\,Pa$), one friction coefficient $\mu_f = 0.3$ and parameters listed in the table 3.5.

The macroscopic stress-strain curves are shown in figure 3.21. We can observe the influence of lateral stress on the strength of the material (it grows with its increase), on stick unloading phase and on backsliding regime. For higher lateral stress, the stick unloading phase is extended and in consequence the backsliding regime is reduced. Finally an irreversible strain is obtained with slightly higher values for higher lateral stresses. The evolution of the damage variable, corresponding to the previous plot (see Fig. 3.21) is shown in figure 3.22, where the points indicate the begining of back sliding for different lateral stresses. During the reverse loading, the damage does not evolve and the snap-back behaviour is not present.

The macroscopic behaviour is strictly related to the frictional mechanism defined by Coulomb law. Due to this law, the slip is possible only if the ratio of $\mathbb{T}$ to $\mathbb{N}$ will be equal to μ_f or to $-\mu_f$ (the sign depends on the sense of sliding). On the contrary, the stationary contact takes place inside this interval.

Linking the macroscopic response in figure 3.21 and the evolution of the ratio ($\mathbb{T} \div \mathbb{N}$) presented in figure 3.23, we can explain the obtained behaviour. At the beginning of loading, the crack may be locked due to applied load and friction law. In the case of uniaxial compression the crack slides from the beginning, while for the rest the sliding occurs when the ratio ($\mathbb{T} \div \mathbb{N}$) reaches the value of friction coefficient $-\mu_f = 0.3$. The minus comes from the right sense of sliding. Before this state, crack lips are locked. This stick regime extends while increasing the value of lateral stress. At the beginning of unloading phase, the ratio ($\mathbb{T} \div \mathbb{N}$) takes values from inside of the interval ($-\mu_f$ to μ_f) and in conseqence the crack lips are stick again. The back sliding will occur when the ratio ($\mathbb{T} \div \mathbb{N}$) will reach the value of friction coefficient for reverse sliding $\mu_f = 0.3$ (in this case left sliding). The back sliding occurs as first for the case of uniaxial compression ($\Sigma_{11} = 0\,Pa$) and as last for the compression with highest lateral stress ($\Sigma_{11} = -12\times10^6\,Pa$).

Figures 3.24 and 3.25 show the evolution of tangential and normal component of the stress to the crack lips during loading-unloading cycle for different lateral stresses ($\Sigma_{11} = 0\,Pa$, $-2\times10^6\,Pa$, $-6\times10^6\,Pa$, $-12\times10^6\,Pa$). The arrows, visible on graphs, indicate

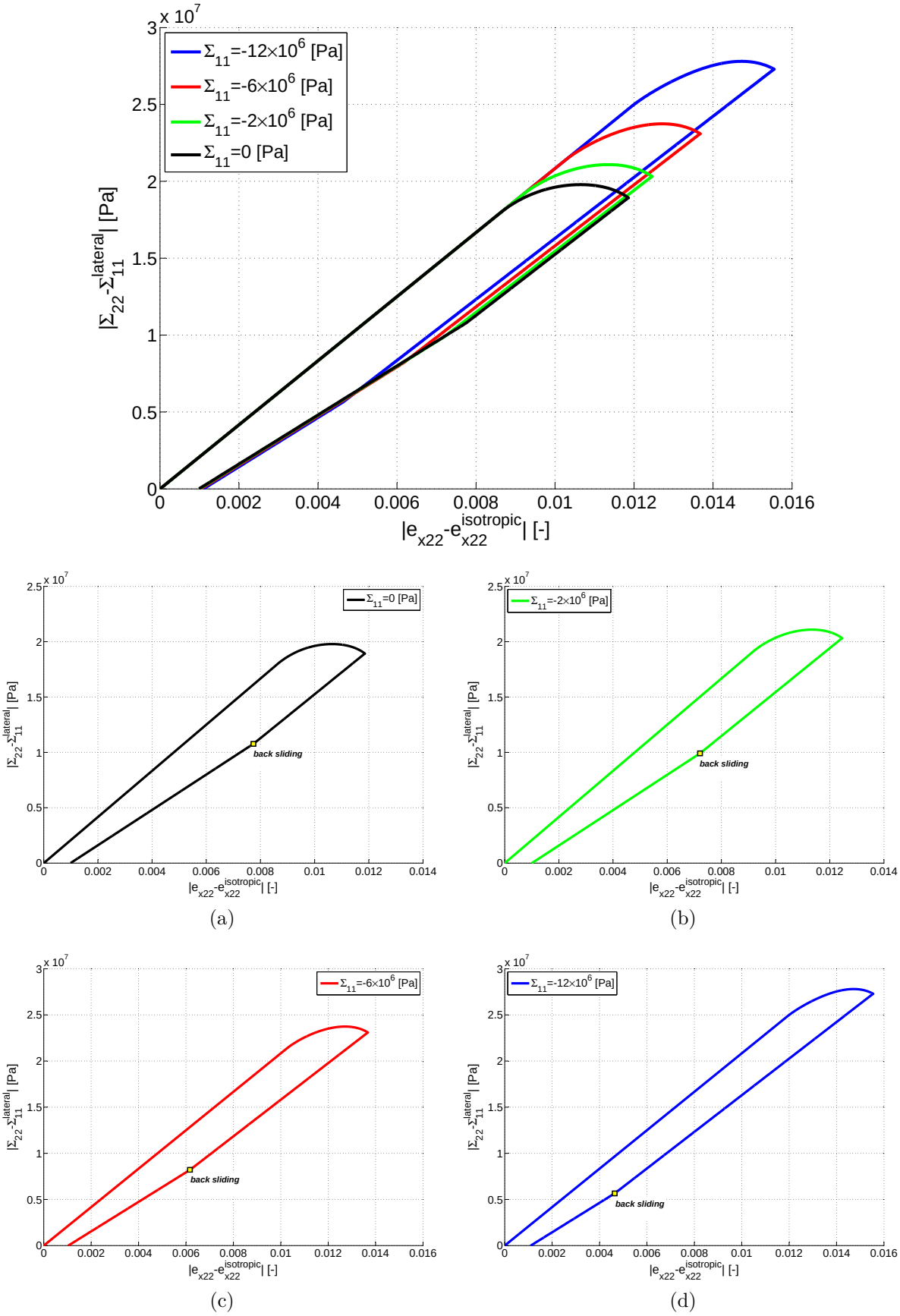

Figure 3.21: Stress-strain curves for friction coefficient $\mu_f = 0.3$ and different lateral stresses during loading-unloading phase with focus on cases: a) $\Sigma_{11} = 0\,Pa$, b) $\Sigma_{11} = -2 \times 10^6\,Pa$, c) $\Sigma_{11} = -6 \times 10^6\,Pa$, d) $\Sigma_{11} = -12 \times 10^6\,Pa$.

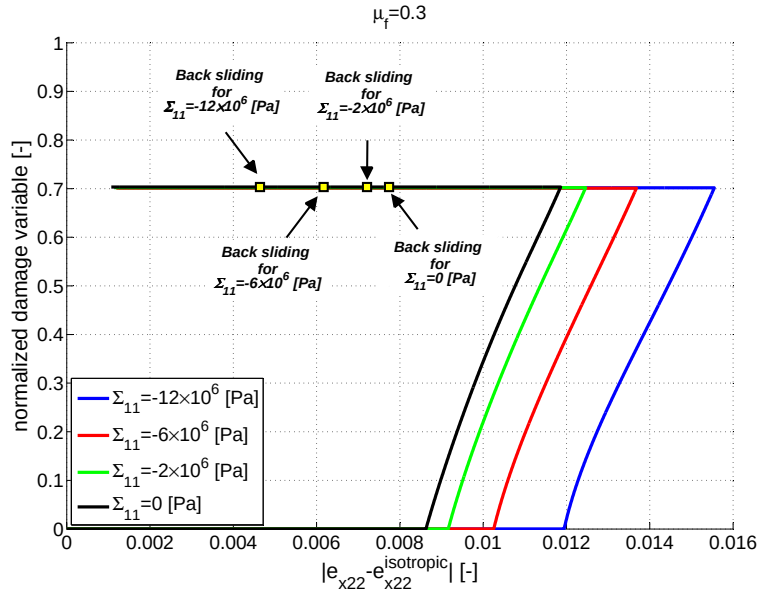

Figure 3.22: Evolution of the damage variable for different lateral stresses ($\Sigma_{11} = 0\,Pa, -2\times10^6\,Pa, -6\times10^6\,Pa, -12\times10^6\,Pa$) and friction coefficient $\mu_f = 0.3$ during loading-unloading phase.

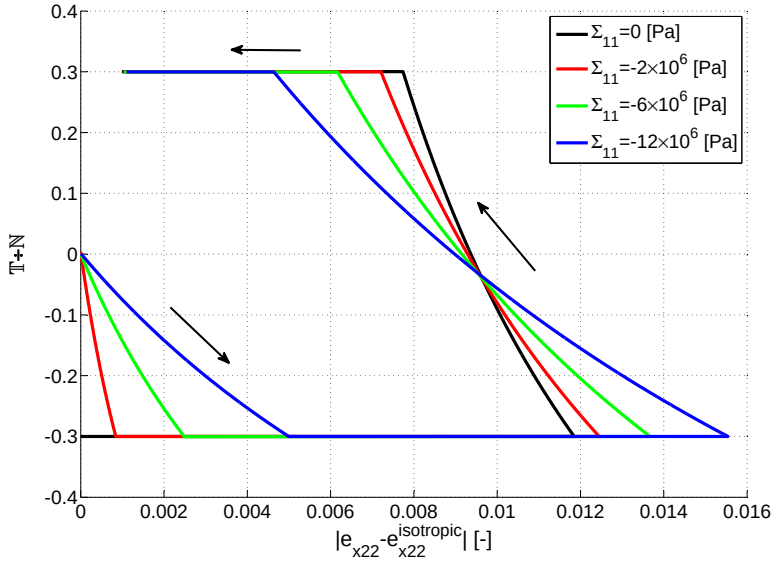

Figure 3.23: Evolution of the ratio between tangential and normal component of the stress for different constant lateral stresses ($\Sigma_{11} = 0\,Pa, -2\times10^6\,Pa, -6\times10^6\,Pa, -12\times10^6\,Pa$) and friction coefficient $\mu_f = 0.3$ during loading-unloading phase.

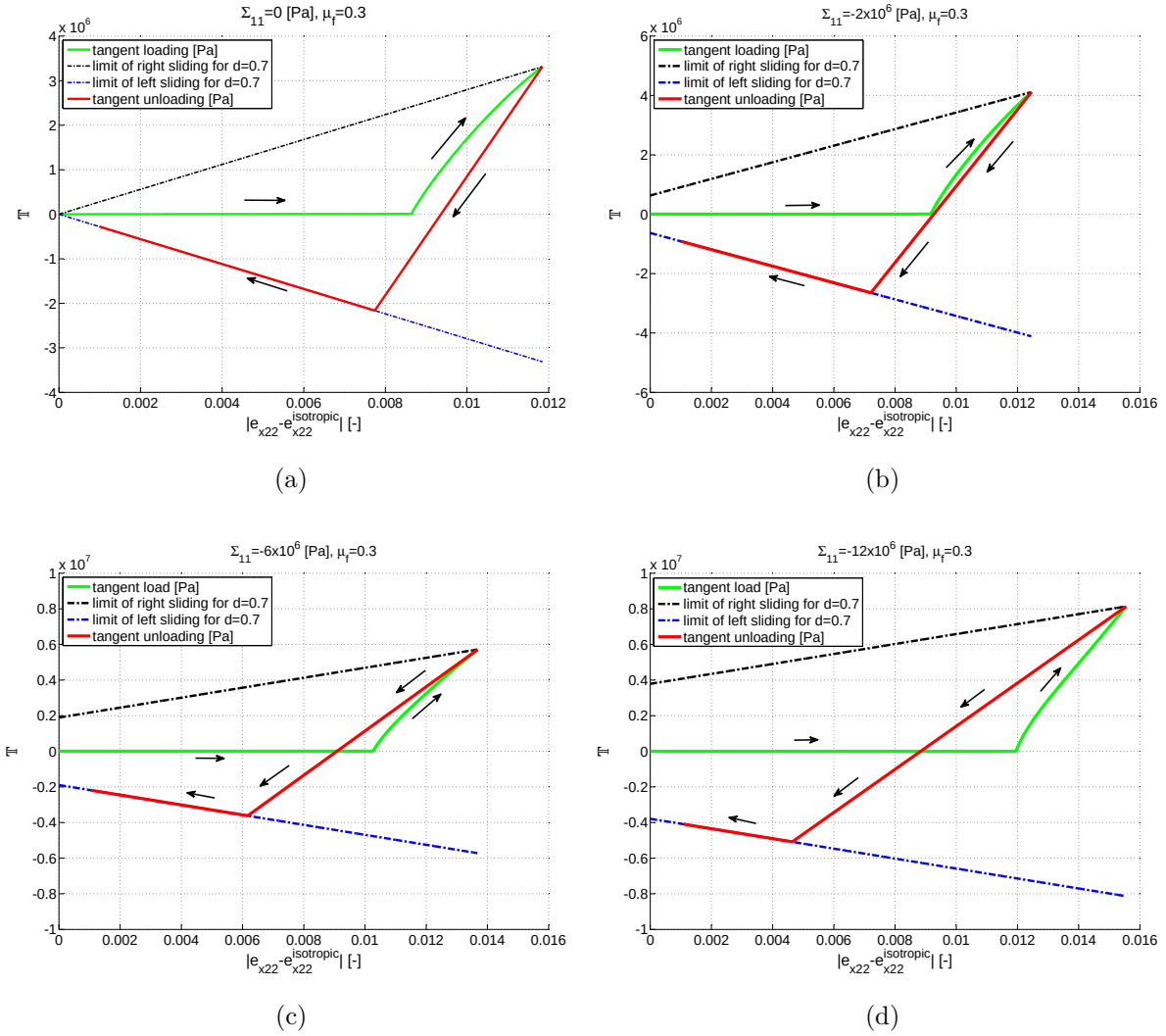

Figure 3.24: Evolution of the tangential component of the stress for friction coefficient $\mu_f = 0.3$ and different lateral stresses during loading-unloading phase a) $\Sigma_{11} = 0\,Pa$, b) $\Sigma_{11} = -2 \times 10^6\,Pa$, c) $\Sigma_{11} = -6 \times 10^6\,Pa$, d) $\Sigma_{11} = -12 \times 10^6\,Pa$.

the direction of loading and the corresponding evolution of tangential and normal component of the stress. During loading, $\mathbb{T}$ (determined by green curve and Eq.3.13) increases together with the propagation of the crack until d reaches the established value of $d = 0.7$. Then the unloading procedure starts, in which $\mathbb{T}$ (defined by red curve and Eqs.3.13 and 3.15) decreases until it intersects the line of the theoretical limit of the reverse sliding for $d = 0.7$ (the last d during loading). In the following regime the sliding Coulomb law (Eq.3.11) is satified and $\mathbb{T}$ is computed from Eq.3.13 using the data for sense of sliding opposite to loading one.

In the loading phase, $\mathbb{N}$ increases together with the growth of the damage variable and monotonically decreases during unloading. The sign of $\mathbb{N}$ is always negative due to compressive character of the test.

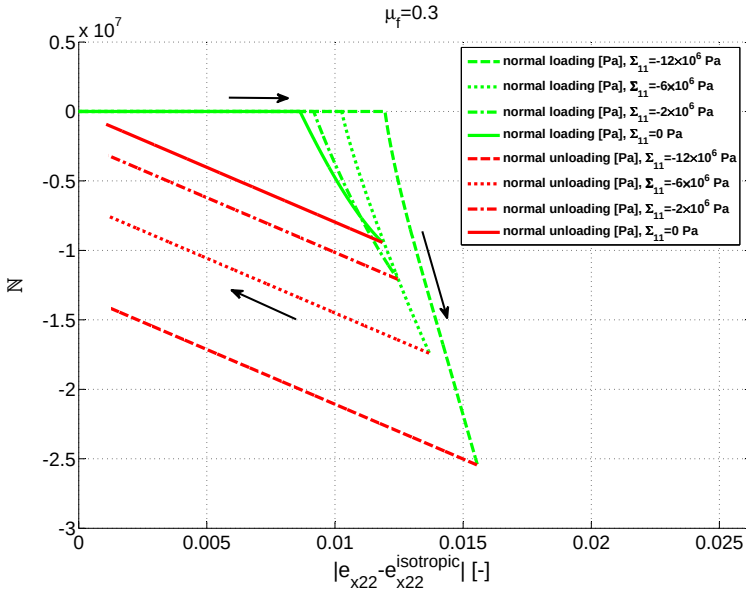

Figure 3.25: Evolution of the normal component of the stress for different lateral stresses ($\Sigma_{11} = 0\,Pa$, $-2\times10^6\,Pa$, $-6\times10^6\,Pa$, $-12\times10^6\,Pa$) and friction coefficient $\mu_f = 0.3$ during loading-unloading phase.

3.5 Conclusions

In this section, an alternative two-scale damage model is considered. In this model, as the crack grows, the resistance of the material increases until a maximum value is achieved. We considered a special fracture criterion for a crack in the elastic material to replace the effect of the process zone ([13]). The size of FPZ (fracture process zone) enters into the quasi-brittle type damage law through the variable c_f.

A damage evolution equation has been obtained from the microscopic energy balance for evolving micro-cracks and it links micro fracture with macro damage. The presented model includes friction, anisotropy and contact.

In the present chapter, we showed the results concerning the effective behaviour which results from homogenization. In the presented model, linear resistant curve leaded to snap-back behaviour in overall response. In order to avoid this phenomenon we looked for an additional term in the resistance curve. We studied the influence of this term in the R-curve and we compared them to the results obtained by using the linear resistance curve like in [13]. We observed that this change allowed us to avoid a snap-back and control the post-peak phase with light drift of material properties.

In the same time the influence of the friction was studied. The presence of the friction causes the increase of the material strength and changes the crack propagation characteristics. For non frictional material the crack propagation is faster while for the frictional material the process of the propagation slows down.

We studied also the influence of the lateral stress on the macroscopic response. The corresponding peak-stress value grows with response, confirming the presence of frictional

phenomenon. The increment of damage variable *vs* applied deformation decreases due to growth of lateral stress. The post-peak regime indicates slightly more brittle behaviour for the lower values of lateral stress while for higher values it is slightly more ductile.

In the aim to obtain a more ductile behaviour without snap-back, we modified the R-curve with an additional term as a power function of damage. Thanks to this additional term in the resistance curve, the loading-unloading cycle was possible to perform. We could study the behaviour related to frictional mechanisms like backsliding and stick case during unloading. All these mechanisms are controlled by Coulomb friction law.

We studied the evolution of the components of the friction law ($\mathbb{N}$ and $\mathbb{T}$) and their influence on the macroscopic behaviour. In the first phase of unloading the crack is locked due to friction, and this phase extends together with increase of friction coefficient and lateral stress. After this phase, the crack is unlocked and starts to slide in reverse sense, and consequently the backsliding regime is reduced.

Concerning the global computations, at the level of macro-structure, the deduced model needs regularization (like adding gradient terms), in order to avoid mesh-dependency and non-physical representation of the localization phenomenon. Such pathological behaviour is linked to the non-uniqueness of the solution of the boundary-value problems for the damage model involving softening effects.

In the next chapter a regularized two-scale model will be proposed.

Chapter 4

Time-dependent damage model

Contents

4.1 Introduction

In this chapter we present a two-scale model which is able to overcome the difficulties related to non-uniqueness and mesh-dependency, observed in the case of quasi-brittle damage model. The present model is regularized by time dependency. This model is deduced by homogenization for micro-cracks which propagate subcritically.

In classical fracture mechanics an isolated crack in a linear elastic body will propagate under tensile loading once the critical mode I stress intensity factor K_{IC} is reached or exceeded, while for lower values of K_I the propagation is not possible. The subcritical

criterion does not ignore the time effect and the crack propagation may occur for energy lower than the critical limit of fracture ([6]). One popular formulation describing the relation between subcritical crack growth and stress intensity factor in mode I, K_I, is Charles power law ([21]) which has the form:

$$\frac{dl}{dt} = v_0 \left(\frac{K_I}{K_0}\right)^n \tag{4.1}$$

where K_I is stress intensity factor for the tensile mode of rupture (Mode I), v_0 is referential velocity of the crack propagation and n is subcritical growth coefficient. K_0 is a particular stress intensity factor for which the velocity of the crack propagation is equal to v_0. K_0, v_0 and n are material parameters. K_I depends on stress state, internal length ε and geometry of the micro-crack.

Even if Charles formulation is mainly used in mode I problem, some authors proposed similar laws for mode II problems ([7, 49, 50]). Since our problem includes friction, the Charles power law has to be written in the mode II and has the form:

$$\frac{dl}{dt} = v_0 \left(\frac{K_{II}}{K_0}\right)^n \tag{4.2}$$

where K_{II} is mode II stress intensity factor.

In this chapter we will present a homogenized model of damage for micro-cracks obeying to the law (4.2). Results of local and global computations will be presented for uniaxial and biaxial compression tests. All numerical tests are performed for different friction coefficients or different lateral stresses. In the local frame we studied the influence of the model parameters (such as velocity v_0, strain rate $\dot{e}_{xkl}$, time t, subcritical growth coefficient n, internal length ε) in order to set the correct values for global macroscopic computations.

The verification of parameters was based on the experimental results which were performed parallel to this numerical developments. We indentified the model parameters in order to fit the time to failure, the strength and the deformation level.

At the global level, we studied the influence of the friction coefficient and the effects of different lateral stresses on the macroscopic response of the material .

The intention of this study is to determine the influence of the friction, therefore only two crack orientations are considered. Once the crack orientation is determined, it is set as an input and it is kept until the end of computation. There are two possible states of crack for each orientation, left sliding and right sliding. These states depend on the applied deformation.

4.2 Subcritical growth of micro-cracks and damage law

As was mentioned before, the evolution of the sliding micro-crack length is formulated through a subcritical criterion based on Charles law ([21]), used by many authors ([36, 51, 60, 63], among others):

$$\frac{dd^{\varepsilon}}{dt} = v_0 \left(\frac{K_{II}}{K_0}\right)^n \tag{4.3}$$

where v_0 is referential velocity of the crack propagation, n is subcritical growth coefficient, d^{ε} is a physical micro-crack length, K_0 is a particular stress intensity factor for which the velocity of the crack propagation is equal to v_0 and K_{II} is stress intensity factor for sliding mode (Mode II). Formulation of K_{II} will be presented in the following parts of this chapter.

The first step to formulate the damage evolution law with subcritical criterion of propagation is to link the energy release rate at the crack tips $\mathcal{G}^{\varepsilon}$ and stress intensity factors K_I and K_{II}, which leads to the following relationship between them for plane strain configuration [1]:

$$\mathcal{G}^{\varepsilon} = \frac{1-\nu^2}{E}\left[K_I^2 + K_{II}^2\right] \tag{4.4}$$

K_I and K_{II} are stress intensity factors for mode I and mode II, respectively. For the single mode of crack loading, exclusively mode I or mode II, the non-null stress intensity factor will appear in (4.4).

In case of mixed mode of loading, all stress intensity factors have to be taken into account. Since in this model the direction of the crack is fixed under pure mode II loading (sliding mode), the non vanishing stress intensity factor is K_{II}. Finally the relation (4.4) takes a form:

$$\mathcal{G}^{\varepsilon} = \frac{1-\nu^2}{E}\left[K_{II}^2\right] \tag{4.5}$$

It was proved in Dascalu et al.([25]), that for evolving microcracks, we have

$$\frac{\mathcal{G}^{\varepsilon}}{\varepsilon} = Y_d \equiv \left(-\frac{1}{2}\frac{dC_{ijkl}(d)}{dd} + I_{ijkl}(d) \right) e_{xkl}\left(\mathbf{u}^{(0)}\right) e_{xij}\left(\mathbf{u}^{(0)}\right) \tag{4.6}$$

where Y_d is a macroscopic damage energy release rate, C_{ijkl} are homogenized coefficients and I_{ijkl} are the coefficients linked with dissipation of the energy due to friction.

This relation has been employed in Dascalu et al.([26]) to obtain a two-scale time-dependent damage model for straight propagation of opening or frictionless micro-cracks. Now, the model is extended by including frictional micro-cracks. Combination of (4.5) and (4.6) yields to the expression of the stress intensity factor in mode II :

$$K_{II} = \sqrt{\frac{E\varepsilon}{1-\nu^2}\left(\left(-\frac{1}{2}\frac{dC_{ijkl}(d)}{dd} + I_{ijkl}(d) \right) e_{xkl}\left(\mathbf{u}^{(0)}\right) e_{xij}\left(\mathbf{u}^{(0)}\right) \right)} \tag{4.7}$$

However, if the mixed modes of crack loading are considered, the stress intensity factors can not be deduced from the energy-release rate and a different approch has to be used. This kind of approach was studied and developed in [31] and [36].

Currently, the aim is to study the influence of friction and in the future this model can be extended to mixed modes.

Substituting K_{II} of (4.7) in the subcritical law (4.3) and considering the definition of damage variable $d = \frac{d^{\varepsilon}}{\sqrt{2}\varepsilon}$, we can define a macroscopic time-dependent damage law in the form:

$$\dot{d} = \frac{v_0}{\sqrt{2}\varepsilon}\left(\frac{\sqrt{\frac{E\varepsilon}{1-\nu^2}\left(\left(-\frac{1}{2}\frac{dC_{ijkl}(d)}{dd} + I_{ijkl}(d) \right) e_{xkl}\left(\mathbf{u}^{(0)}\right) e_{xij}\left(\mathbf{u}^{(0)}\right) \right)}}{K_0} \right)^n \tag{4.8}$$

The damage equation (4.8) accounts not only for the rate effect but also for the size effect and friction phenomenon. According to (4.7), the stress intensity factor in damage equation (4.8) depends on the size of periodic structure ε, damage variable d and friction.

In such a way the developed model reflects the nonlinear, time-, size- and friction-dependent effect on the macroscopic behaviour of the material, as commonly observed in the experiment.

In the subcritical damage model the damage variable is time dependent, causing its propagation at each time step. Because of this assumption at the current state of development, the same damage evolution law is used in unloading as in loading, i.e. damage still propagates in unloading.

It should be reminded that in the case of quasi-brittle damage model, which is time independent, it is possible to distinguish the state when the crack lips are stick and in consequence the propagation during unloading state is blocked.

This limitation of the subcritical damage model implies the modifications in the formulation of the homogenized stress-strain relations.

Previously, the following phases were determined: stick before sliding, sliding left and right, stick at the beginning of unloading and back sliding. The details can be found in Chapter 2. In this model, because of the continuous propagation in mode II, only sliding regime is present.

The homogenized stress-strain relation for loading and unloading configuration is defined by:

$$\Sigma_{ij}^{(0)} = C_{ijkl}\left(d\right) e_{xkl}\left(\mathbf{u}^{(0)}\right) \tag{4.9}$$

where $C_{ijkl}\left(d\right)$ are homogenized coefficients depending on the domains of linearity in space $\mathbf{R}$ of deformations $e_{x11}, e_{x12}, e_{x22}$, $\mathbf{R}^{+}$, $\mathbf{D}^{R}$ and $\mathbf{D}^{L}$. These different domains are defined by:

$$\mathbf{R}^{+} = \left\{\mathbf{e_x} \mid N_i a_{ijkl} e_{xkl}\left(\mathbf{u}^{(0)}\right) N_j \geq 0\right\} \tag{4.10}$$

$$\mathbf{D}^{R} = \left\{\mathbf{e_x} \mid N_i a_{ijkl} e_{xkl}\left(\mathbf{u}^{(0)}\right) N_j < 0; T_i a_{ijkl} e_{xkl}\left(\mathbf{u}^{(0)}\right) N_j > 0\right\} \tag{4.11}$$

$$\mathbf{D}^{L} = \left\{\mathbf{e_x} \mid N_i a_{ijkl} e_{xkl}\left(\mathbf{u}^{(0)}\right) N_j < 0; T_i a_{ijkl} e_{xkl}\left(\mathbf{u}^{(0)}\right) N_j < 0\right\} \tag{4.12}$$

The negative value of $N_i a_{ijkl} e_{xkl}\left(\mathbf{u}^{(0)}\right) N_j$ indicates the closing of the crack while the positive one indicates opening.

The positive value of $T_i a_{ijkl} e_{xkl}\left(\mathbf{u}^{(0)}\right) N_j$ indicates the right sense of sliding, while negative value indicates the left one.

4.3 Summary of involved parameters

In the following, a review of the parameters and their values will be made. The parameters used in the subcritical damage model are:

- K_{IC} : the fracture toughness. The reported values of K_{IC} of Westerly granite lie between 0.6 and $2.5\,MPa.m^{\frac{1}{2}}$ ([7, 8]). We used $K_{IC} = K_0 = 0.18\,MPa.m^{\frac{1}{2}}$.

- n : the subcritical crack growth index. No data are available for Callovo-Oxfordian argillite whereas values of n for Westerly granite in air at a temperature of $20°C$ range from 31.2 to 39 ([61]). n is a constant parameter which depends on the type of rock and such enviromental conditions as temperature and atmospheric moisture. The argillaceous rocks are soft rocks with the mean Young modulus equal to $9.5GPa$ and mean Poisson ratio $\nu = 0.16$ ([22]), while the reported values for Westerly granite ([18]) are: $E = 57\,GPa$ and $\nu = 0.32$. According to this we assumed the value of n to be 3.

- v_0 : the crack velocity in subcritical crack growth at $K_I = K_0$. Because of the poor reproducibility of laboratory data, reported values of the coefficient v_0 vary considerably from 10^{-3} to $10^{-12}\frac{m}{s}$ for $K_0 = 1.0MPa.m^{\frac{1}{2}}$ under the same experimental conditions ([70]). v_0, like n, depends on type of material and enviromental conditions. For example for Westerly granite $v_0 = 4.5 \times 10^{-9}$to $1.0 \times 10^{-8}\ \frac{m}{s}$ at $K_0 = 1.0\,MPa.m^{\frac{1}{2}}$ ([7]), and $v_0 = 1.0 \times 10^{-7}$to $1.8 \times 10^{-4}\ \frac{m}{s}$ at $K_0 = 1.26\,MPa.m^{\frac{1}{2}}$([79]). We used $v_0 = 5 \times 10^{-6}\frac{m}{s}$.

- ε : size of periodic microscopic structure. Following the method of asymptotic homogenization, the microstrucural length has to be small enough with respect to the macroscopic one (a characteristic dimension of the whole body). For a size specimen of $25\,mm \times 50\,mm$ the value of internal length was set to $\varepsilon = 10^{-3}\,m$. In the case when $n = 2$ (subcritical crack growth index), the internal length ε disapears from the damage equation and the tests involving size effects can not be performed.

- $\dot{e}$: rate of deformation. Reported values used in the experimental test of argillaceous rock (from Eastern France) vary in the range $\dot{e} = 10^{-4} - 10^{-8}\,s^{-1}$ ([35]). In the global macroscopic simulation we used constant strain rate $\dot{e} = 10^{-6}\,s^{-1}$.

The values established above have been used in the global macroscopic computations. In case of local macroscopic computations, we considered a variation around their exact quantity. The next section is dedicated to these parametric studies.

4.4 Formulation of the two-scale damage problem

To summarize, the homogenized damage problem to be solved is defined by the system of following equations:

- **Homogenized equilibrium**

$$\frac{\partial}{\partial x_j}\Sigma_{ij}^{(0)} = 0$$

- **Effective stress-strain laws**

$$\Sigma_{ij}^{(0)} = C_{ijkl}\left(E\,,\nu,d,\mu_f,\theta\right)e_{xkl}\left(\mathbf{u}^{(0)}\right)$$

- **Damage law**

$$\frac{dl}{dt} = v_0\left(\frac{K_{II}\left(\mathbf{e_x},E\,,\nu,d,\mu_f,\theta\right)}{K_0}\right)^n$$

4.5 Local macroscopic behaviour

4.5.1 Introduction

In this part the analysis of the homogenized response in the macroscopic point will be studied. Depending on the problem, the damage equation (4.8) will be solved by applying the macroscopic stress and strain. In the case of uniaxial compression, a constant strain rate loading in the vertical direction will be imposed and horizonal direction will be free of stress, while for biaxial compression a constant lateral stress will be applied.

The problems are highly nonlinear because elastic modulus C_{ijkl} depends on the damage variable d and because of the form of the damage energy release rate (4.7) used to calculate the stress intensity factors. Several tests have been performed (uniaxial, biaxial with different lateral stresses). We will present the macroscopic behaviour and the influence of friction coefficient, strain rate $\dot{e}$, n, ε, v_0 and different lateral stresses Σ_{11}. The set of material parameters used in the simulations are listed in the table 4.1.

$E\,[Pa]$	$\nu\,[-]$	$\dot{e}\left[s^{-1}\right]$	$-\Sigma_{11}\,[Pa]$	$\mu_f\,[-]$	$d_0\,[-]$
2×10^9	0.2	$10^{-6}-10^{-5}$	$0.0-12\times10^6$	$0.0-0.5$	10^{-6}
$v_0\left[\frac{m}{s}\right]$		$\varepsilon\,[m]$	$K_0\left[MPa.m^{\frac{1}{2}}\right]$	$n\,[-]$	$\theta\,[^\circ]$
$10^{-6}-10^{-5}$		$10^{-4}-10^{-3}$	0.2	$2-4$	135

Table 4.1: Parameters used in the simulations at local macroscopic scale

4.5.2 Computation algorithm

For the numerical integration of the model, we present below the computation scheme.

For each time step $n+1$, the stress update algorithm is given by explicit scheme:

1. input at step $(n+1)$ for time t^{n+1}:
   $e_{xkl}(t^n)$, $d(t^n)$
2. verify the state of opening/sliding right/sliding left ($\mathbf{e_x} \in \mathbf{R}^+$or $\mathbf{D}^R$ or $\mathbf{D}^L$, respectively).
3. compute dissipative term I_{ijkl}:
   $I_{ijkl} = I_{ijkl}(d(t^n))$
4. compute the homogenized coefficient C_{ijkl} :
   $C_{ijkl} = C_{ijkl}(d(t^n))$
5. compute the stress intensity factor :
   $K_{II} = K_{II}\left(\frac{\partial C_{ijkl}(d(t^n))}{dd}, I_{ijkl}\left(d\left(t^n\right)\right)\right)$
6. update the damage :
   $\dot{d} = f\left(e_{xij}(t^n), \frac{\partial C_{ijkl}(d(t^n))}{dd}, I_{ijkl}\left(d\left(t^n\right)\right)\right)$, obtained from (4.8).
   $d\left(t^{n+1}\right) = d\left(t^n\right) + \dot{d}\triangle t$
7. update the homogenized coefficient C_{ijkl} :
   $C_{ijkl} = C_{ijkl}(d(t^{n+1}))$
8. calculate the updated strain:
   $e_{xij}(t^{n+1}) = C^{-1}_{ijkl}\left(d\left(t^{n+1}\right)\right)\Sigma^{(0)}_{ij}$
9. calculate the stress:
   $\Sigma^{n+1}_{ij} = C_{ijkl}\left(d_{n+1}\left(t^{n+1}\right)\right)e^{n+1}_{xij}\left(t^{n+1}\right)$

where n is the step number, t^n is the time step number, $\triangle t$ is the size of time step. Similar algorithm can be used for different types of loading.

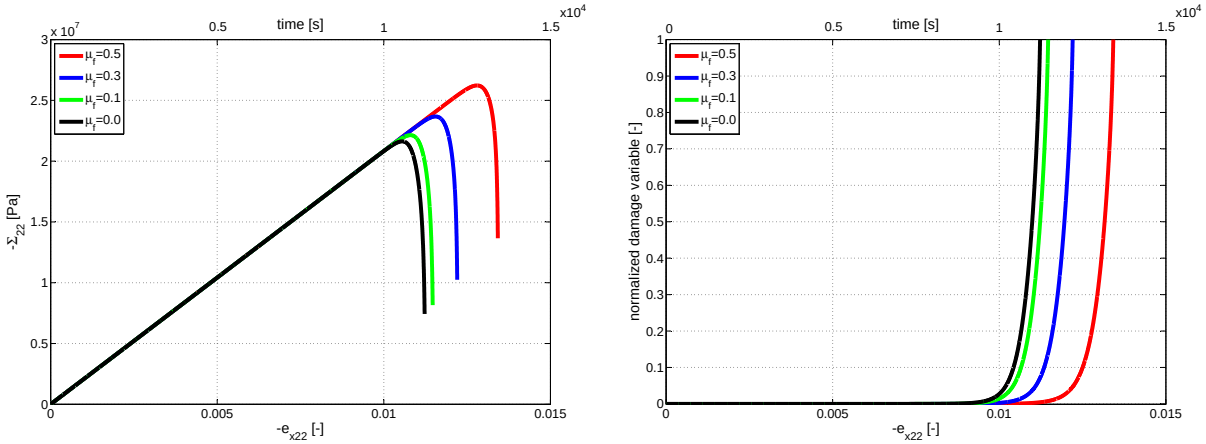

(a) (b)

Figure 4.1: Stress curves (a) and corresponding evolution of normalized damage variable (b) *vs* axial strain and *vs* time under compressive uniaxial loading for different friction coefficients ($\mu_f = 0.0, 0.1, 0.3$ and 0.5, respectively).

4.5.2.1 Uniaxial tests : local macroscopic response in case of different friction coefficients.

In this section the macroscopic behaviour in the local point under uniaxial compression is presented. Different friction coefficients were considered.

The numerical tests were performed under constant vertical strain rate loading of $\dot{e} = 10^{-5}\, s^{-1}$ and model parameters were set to $v_0 = 5 \times 10^{-6}\, \frac{m}{s}$ for crack velocity, $n = 2$ for subcritical crack growth index and $\varepsilon = 10^{-3}\, m$ for internal length.

Figure 4.1 shows the stress curves (on the left) and the damage evolution (on the right) for $\mu_f = 0.0, 0.1, 0.3$ and 0.5, respectively, versus axial strain and versus time. We can observe different responses for different frictional properities of the material. The strength of the material increases together with friction coefficient and time. The passage from friction-free case to frictional one (the difference in responses of $\mu_f = 0.0$ and $\mu_f = 0.1$) is smooth. Significant differences can be observed in the doimain of frictional behaviour for different μ_f.

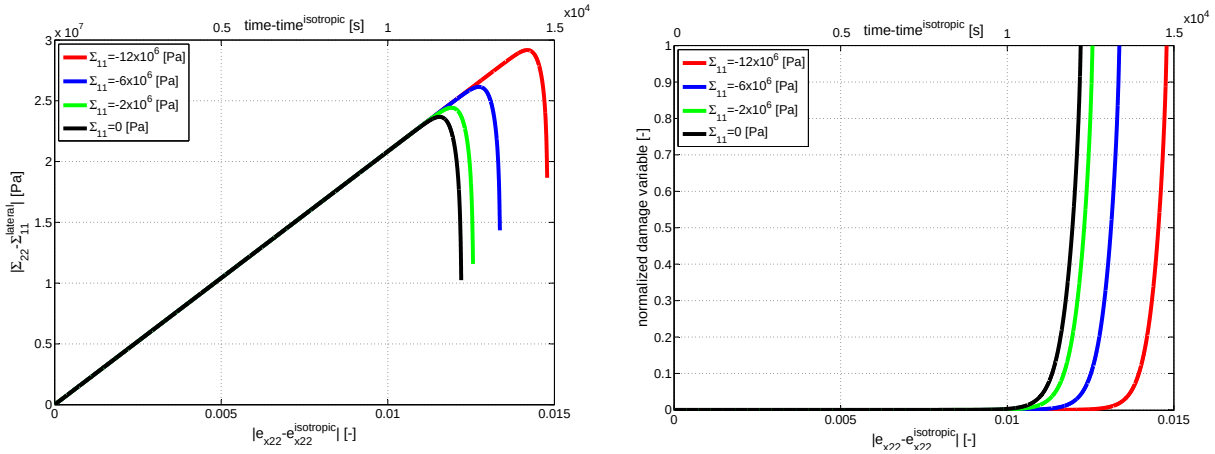

(a) (b)

Figure 4.2: Macroscopic response under biaxial compression: stress curves (a) and damage evolution (b) *vs* axial strain and *vs* time for $\mu_f = 0.3$ and different lateral stresses ($\Sigma_{11} = 0\,Pa, -2\times10^6\,Pa, -6\times10^6\,Pa, -12\times10^6\,Pa$).

4.5.2.2 Biaxial tests : effects of different lateral stresses

The objective of this section is to study the influence of the lateral stress and to verify the presence of friction. We analyse the influence of lateral stresses on individual frictional materials (materials defined by $\mu_f = 0.0, 0.1, 0.3$ and 0.5). The loading is controlled by constant vertical strain rate $\dot{e}$ and by constant lateral stress Σ_{11} in horizontal direction. The values of lateral stress were established to $\Sigma_{11} = 0\,Pa, -2\times10^6\,Pa, -6\times10^6\,Pa, -12\times10^6\,Pa$. We performed the biaxial compression tests with different lateral stresses for each value of μ_f. The model parameters are identical as used in 4.5.2.1.

The macroscopic response of frictional material ($\mu_f = 0.3$) is plotted in the frame defined by strain $e_{x22} - e_{x22}^{isotropic}$, stress $\Sigma_{22} - \Sigma_{11}$ and $time - time^{isotropic}$, where $e_{x22}^{isotropic}$ and $time^{isotropic}$ are the deformation and time corresponding to the isotropic state ($\Sigma_{22} = \Sigma_{11}$), and Σ_{11} is the constant lateral stress (see left-hand side of figure 4.2). In this way we obtained the actual influence of the presence of the friction, which is confirmed by the fact that the peak value of $\mid \Sigma_{22} - \Sigma_{11} \mid$ increases with the value of lateral stress. In the case of non frictional material these curves would overlap. Evolution of damage, which correspond to those stress-strain curves, is presented on the right-hand side of the figure 4.2.

Stress paths for different values of lateral stresses are presented in figure 4.3. The slope, which appears in figure 4.3, confirms that tested material is frictional. If material were non frictional the slope would be zero.

The macroscopic friction coefficient can be deduced from graphical form of Mohr's circles and Coulomb's line, which is presented in figure 4.4. The tangential to the Mohr's circle line is a Coulomb's line and draws an angle of $\phi = 11.5°$. The macroscopic friction coefficient can be computed from the following relation:

$$\mu_f^* = tan\,(\phi) \tag{4.13}$$

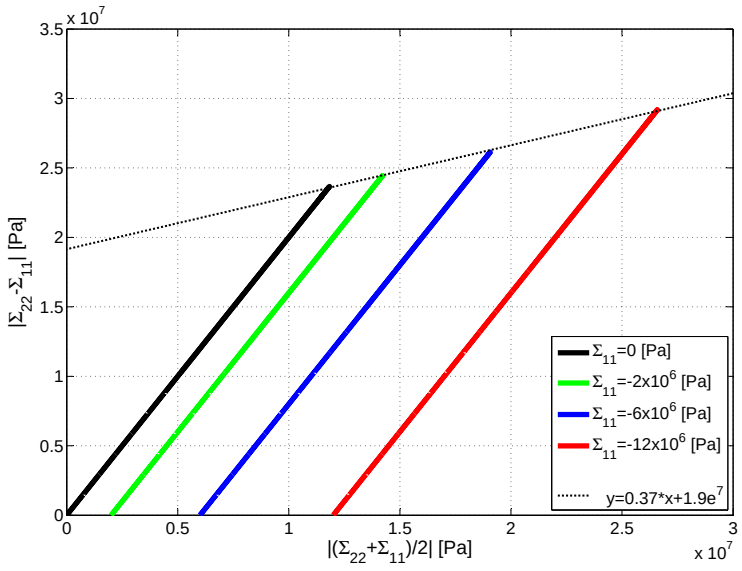

Figure 4.3: Stress path curves for different lateral stresses ($\Sigma_{11} = 0\,Pa, -2\times10^6\,Pa, -6\times10^6\,Pa, -12\times10^6\,Pa$) and friction coefficient $\mu_f = 0.3$

microscopic friction coefficient μ_f [−]:	0.0	0.1	0.3	0.5
slope in the deviatoric and mean stress frame [−]:	0.0	0.081	0.37	0.79

Table 4.2: Values of the slope in the deviatoric and mean stress frame for different friction coefficient

and it is equal to $\mu_f^* = 0.2$, while the microscopic friction coefficient, in this case, was established to $\mu_f = 0.3$. The Coulomb's line crosses the vertical axis in the point corresponding to the value of cohesion equal to $c = 10^7 Pa$.

Figure 4.5 shows a comparison between different stress paths depending on friction coefficient $\mu_f = 0.0, 0.1, 0.3$ and 0.5. It can be observed that the slope of the stress paths changes according to the increase of friction coefficient. The slope is equal to zero for non frictional material and is higher with the increase of friction. The slope values are summarized in table 4.2.

The Mohr's circles and Coulomb's lines in case of different friction coefficients $\mu_f = 0.0, 0.1, 0.3$ and 0.5 are plotted in figure 4.6. We can observe that the angle ϕ grows together with the frictional properties of the material. Summary of obtained values can be found in table 4.3.

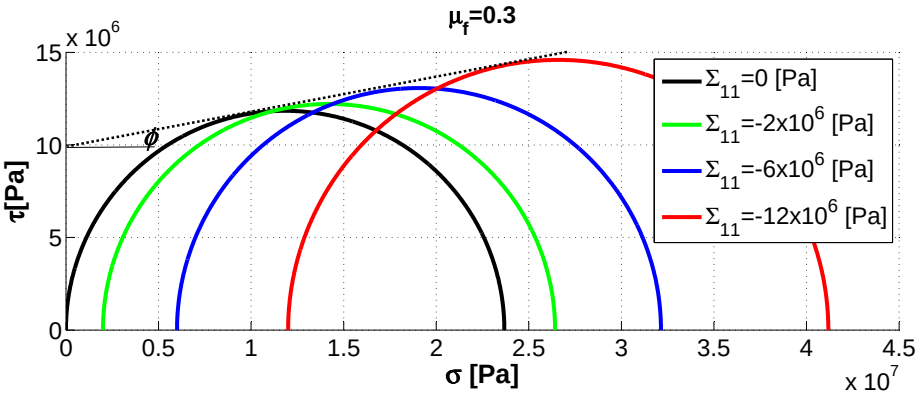

Figure 4.4: Mohr's circles and Coulomb's line for frictional material ($\mu_f = 0.3$).

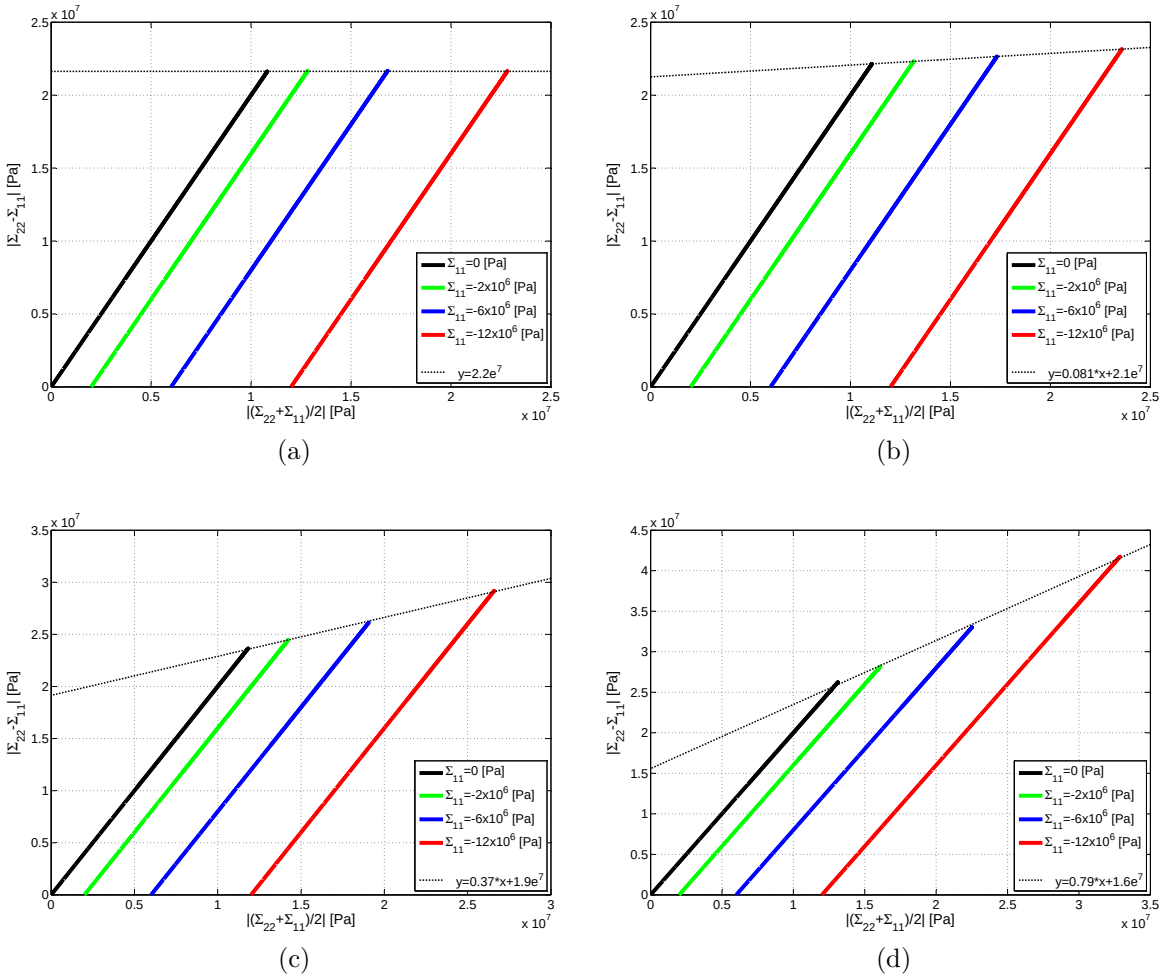

Figure 4.5: Stress path curves for different lateral stresses ($\Sigma_{11} = 0\,Pa, -2 \times 10^6\,Pa, -6 \times 10^6\,Pa, -12 \times 10^6\,Pa$) and friction coefficients: a) $\mu_f = 0.0$, b) $\mu_f = 0.1$, c) $\mu_f = 0.3$, d) $\mu_f = 0.5$.

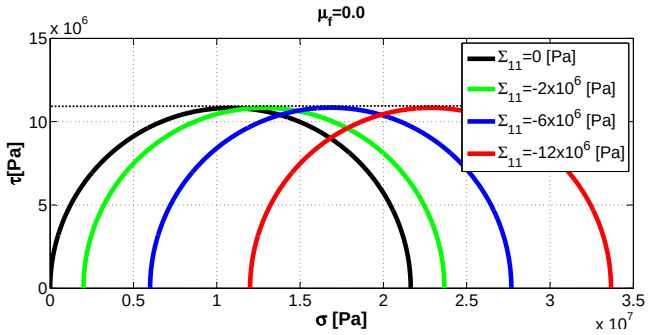

(a)

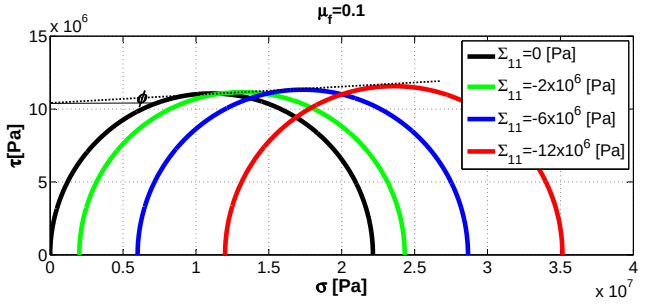

(b)

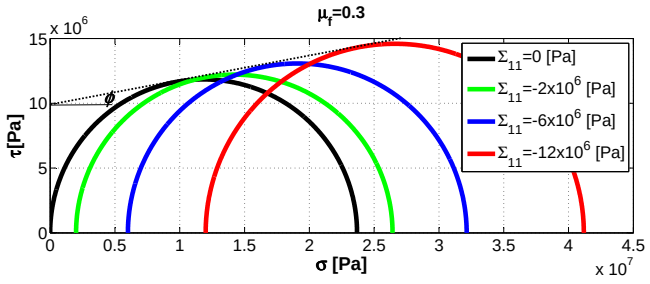

(c)

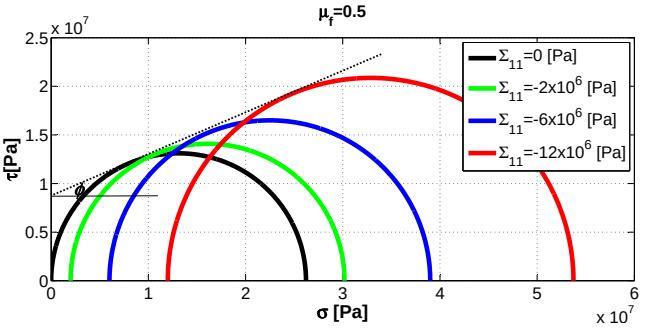

(d)

Figure 4.6: Mohr's circles and Coulomb's lines for different lateral stresses ($\Sigma_{11} = 0\,Pa, -2\times10^6\,Pa, -6\times10^6\,Pa, -12\times10^6\,Pa$) and friction coefficients: a) $\mu_f = 0.0$, b) $\mu_f = 0.1$, c) $\mu_f = 0.3$, d) $\mu_f = 0.5$.

microscopic friction coefficient μ_f $[-]$	0.0	0.1	0.3	0.5
friction angle $\phi[^\circ]$	0.0°	3.5°	11.5°	23.0°
macroscopic friction coefficient $\mu_f^*[-]$	0.0	0.06	0.2	0.42

Table 4.3: Values of friction angle ϕ and macroscopic friction coefficient μ_f^*

4.5.2.3 Influence of subcritical crack growth index n

In this part we will present the influence of subcritical crack growth index n on a macroscopic response of material in local point. We performed the biaxial test under constant strain rate $\dot{e} = 10^{-6}\, s^{-1}$, constant lateral stress $\Sigma_{11} = -6 \times 10^6\, Pa$ and friction coefficient $\mu_f = 0.3$. An increase of sub-critical exponent decreases the rate of crack propagation and postpones the failure of the material, as observed in figure 4.7, where the stress curves versus axial strain and versus time are plotted. In the case of $n = 2$ the behaviour is more controlled, which can be underlined by the soft shape of stress-strain curve and damage evolution along the test. A rapid and immediate progress of damage and lost of ridigity can be observed for $n = 3$ and $n = 4$, which indicates more brittle behaviour.

Figure 4.8 shows evolution of the damage variable versus axial strain and versus time for different values of sub-critical exponent n.

In order to study the influence of subcritical crack growth index n on frictional properties of the material, stress paths curves were plotted. Figure 4.9 shows stress path curves for different values of n. The slopes formed by these curves remain constant and this explains the n independency on frictional properties of the material. It changes only the apparent cohesion of the material.

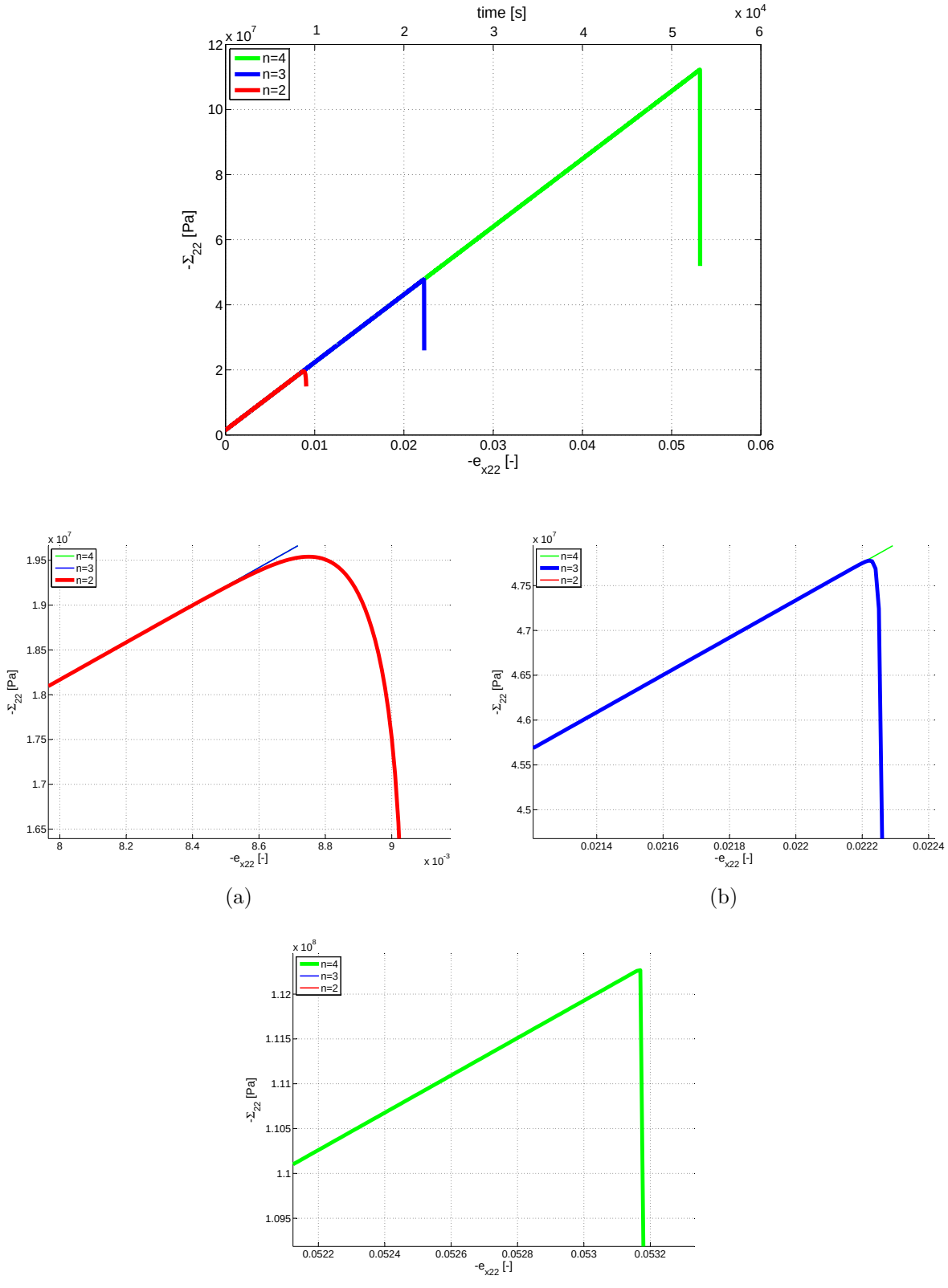

Figure 4.7: Stress curves *vs* axial strain and *vs* time: influence of subcritical index n, under biaxial compression with lateral stress $\Sigma_{11} = -6 \times 10^6\, Pa$ and friction coefficient $\mu_f = 0.3$, with magnification of $n = 2$ (a), $n = 3$ (b), $n = 4$ (c).

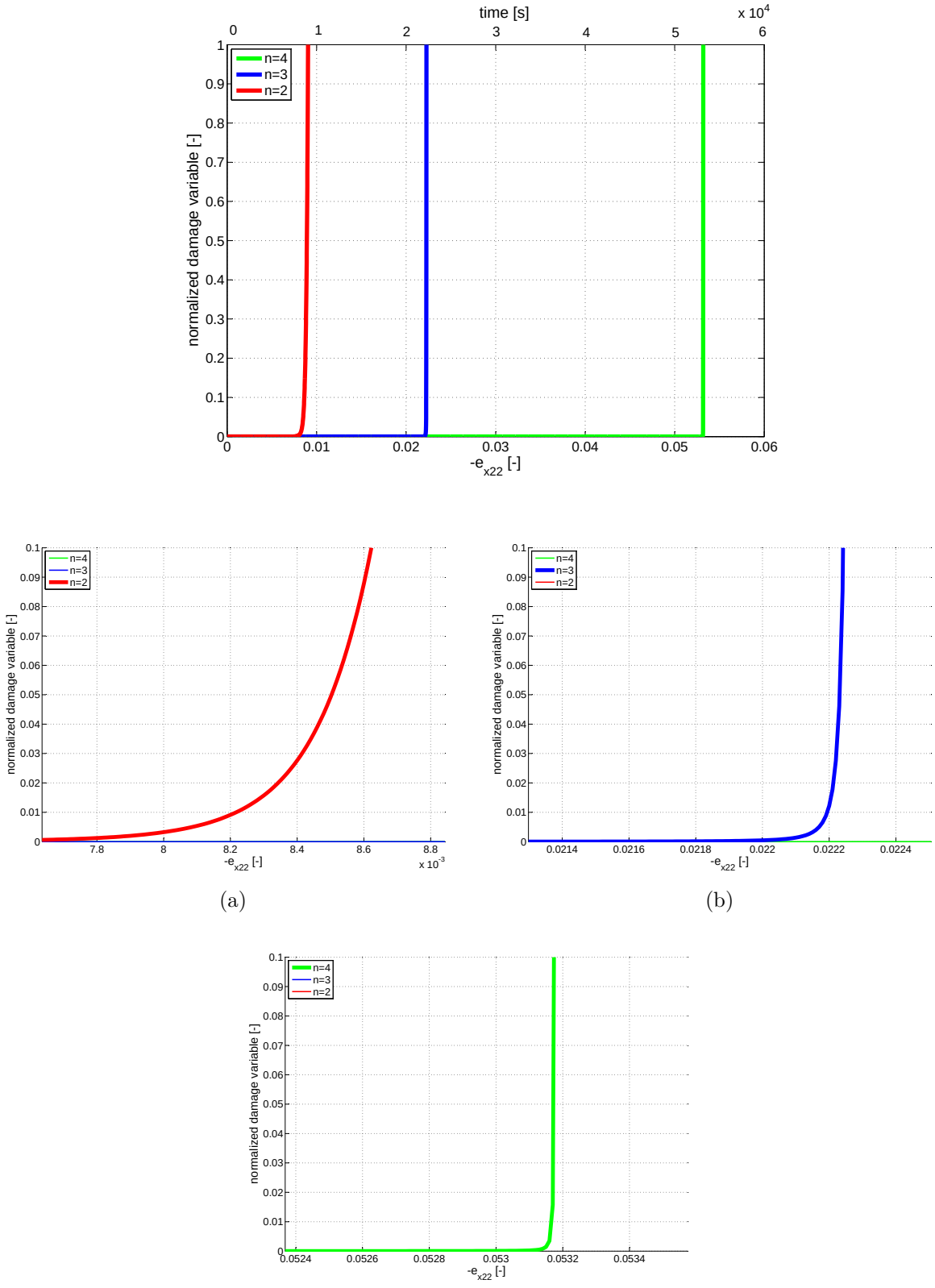

Figure 4.8: Damage variable evolution *vs* axial strain and *vs* time : influence of subcritical index under biaxial compression with lateral stress $\Sigma_{11} = -6 \times 10^6\, Pa$ and friction coefficient $\mu_f = 0.3$, with magnification of $n = 2$ (a), $n = 3$ (b), $n = 4$ (c).

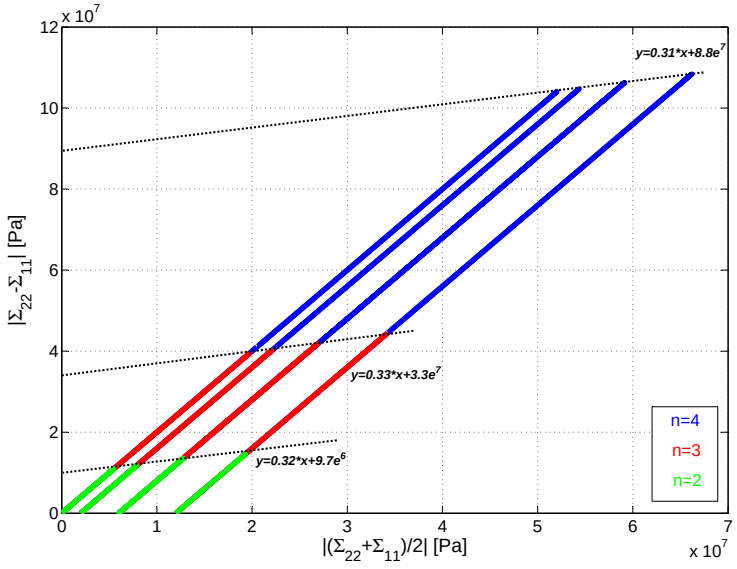

Figure 4.9: Stress path curves: influence of subcritical index n on frictional properties of material

4.5.2.4 Influence of the strain rate

The stress-strain and damage-strain relations under various constant vertical strain rates is presented in figure 4.10. The tests were performed for one lateral stress $\Sigma_{11} = -6 \times 10^6\, Pa$, one friction coefficient $\mu_f = 0.3$, and different constant strain rates established to $\dot{e} = -10^{-5}\, s^{-1}, -5 \times 10^{-6}\, s^{-1}, -10^{-6}\, s^{-1}$. The response of the material depends not only on strain level, which controls the stress intensity factor at the crack lips, but also on time. Under low strain rate, the effect of time becomes predominant and the failure appears for a lower strain level than in the case of faster loading. The micro-cracks have enough time to develop so that it is not necessary to reach high levels of deformation and in consequence the material strength decreases, as observed in figure 4.11, where evolution of vertical stress and damage variable is plotted with respect to time.

The slopes of the curves drawn by the peak stress paths in case of different strain rates remain unchanged, which indicates independency of frictional properties on the strain rate, as shown in figure 4.12. It changes only the apparent cohesion of the material.

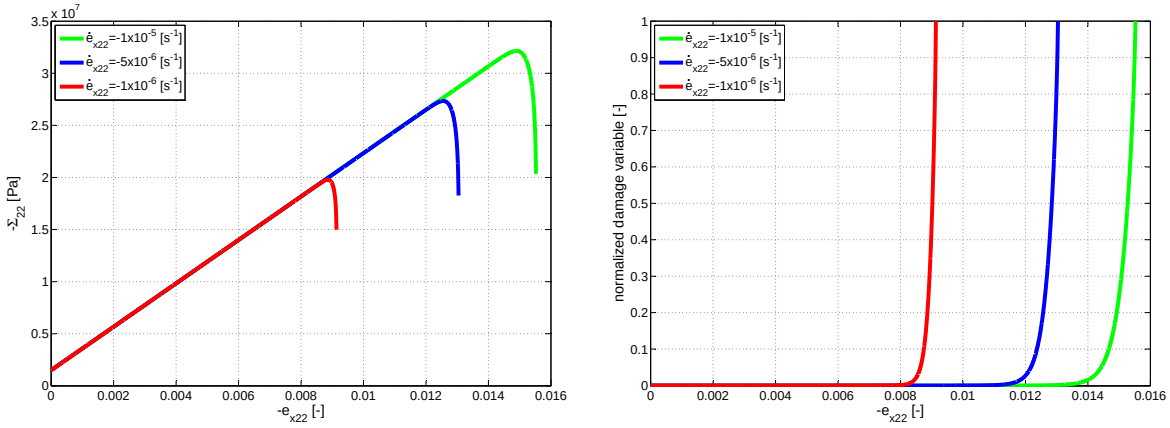

(a) (b)

Figure 4.10: Stress-strain curves (a) and damage variable evolution *vs* axial strain (b): influence of loading rate under biaxial compression with lateral stress $\Sigma_{11} = -6 \times 10^6\, Pa$ and friction coefficient $\mu_f = 0.3$..

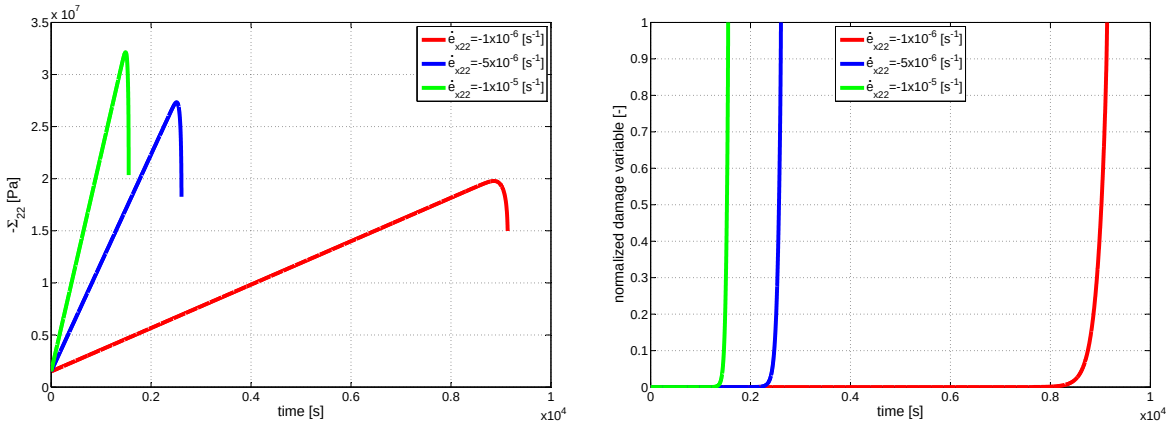

(a) (b)

Figure 4.11: Evolution of stress (a) and damage variable (b) *vs* time : influence of loading rate under biaxial compression with lateral stress $\Sigma_{11} = -6 \times 10^6\, Pa$ and friction coefficient $\mu_f = 0.3$..

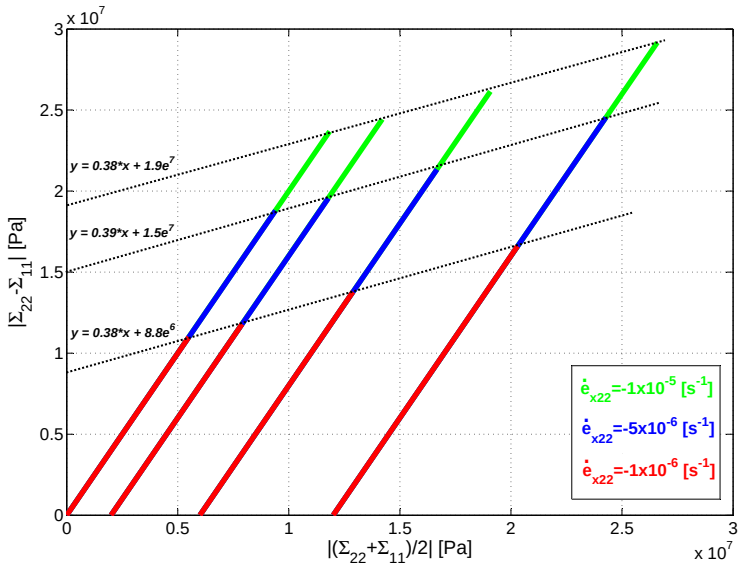

Figure 4.12: Stress path curves : influence of loading rate on frictional properties of material.

4.5.2.5 Influence of the velocity v_0

In this part we will present the influence of the velocity v_0 on macroscopic response of material in local point. For different values we performed the biaxial tests under constant strain rate $\dot{e} = 10^{-5}\, s^{-1}$, constant lateral stress $\Sigma_{11} = -6 \times 10^6\, Pa$ and friction coefficient $\mu_f = 0.3$. Figure 4.13 present the macroscopic results in terms of vertical stress and damage evolution versus axial strain and versus time. For low velocities, v_0, the material attains higher levels of deformation and the failure is also postponed in time.

The influence of the velocity, v_0, on the frictional properties of the material was not observed, as shown in figure 4.14, where the different stress paths under different velocities are plotted. The change of the velocity does not affect the slope of the stress path curves in frame of deviatoric and mean stress. It changes only the apparent cohesion of the material.

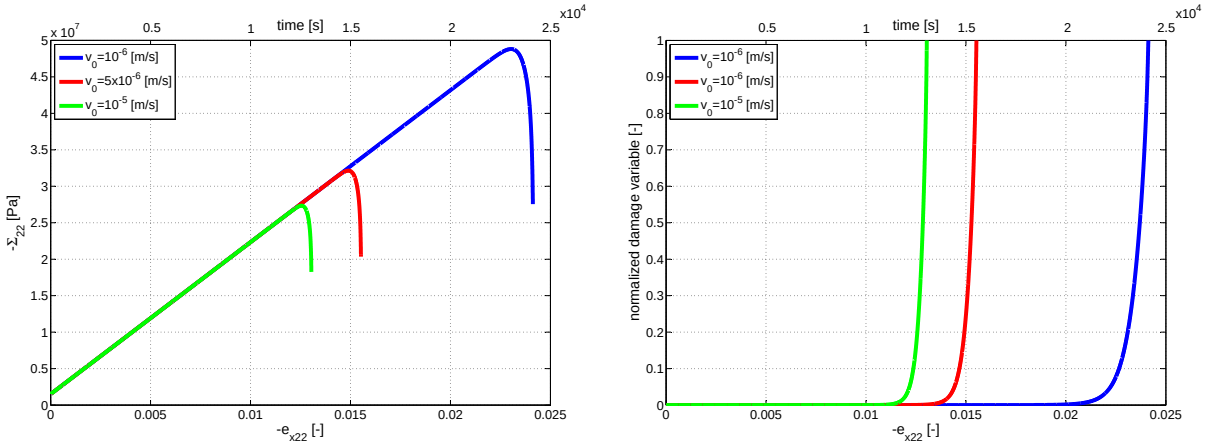

(a) (b)

Figure 4.13: Stress curves (a) and damage variable evolution (b) *vs* axial strain and *vs* time: influence of crack velocity v_0 under biaxial compression with lateral stress $\Sigma_{11} = -6 \times 10^6\, Pa$ and friction coefficient $\mu_f = 0.3$.

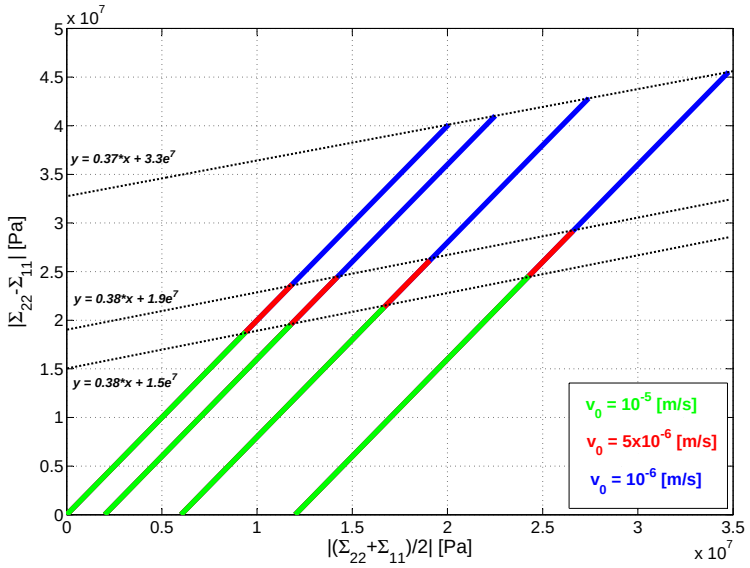

Figure 4.14: Stress path curves : influence of the velocity v_0 on the frictional properties of the material.

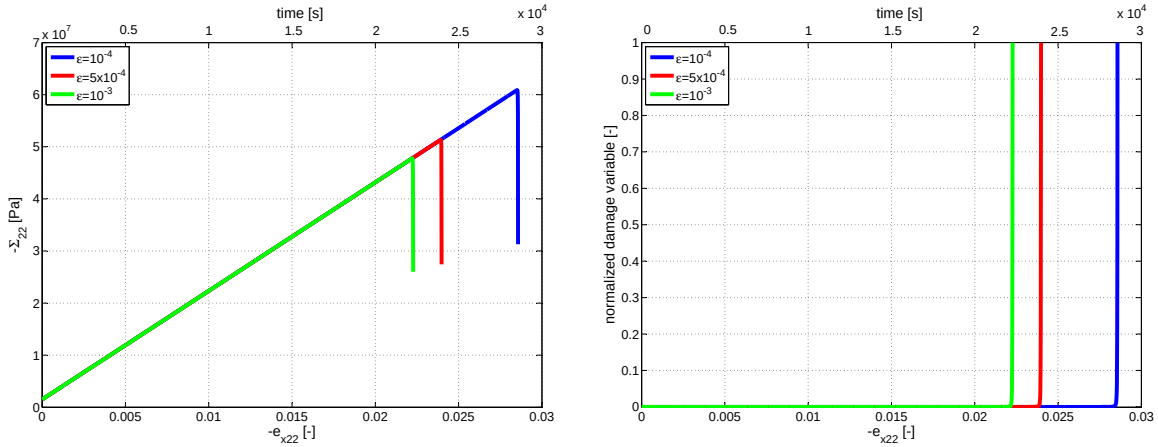

(a) (b)

Figure 4.15: Stress-strain curves (a) and damage variable evolution (b) *vs* axial strain and *vs* time : influence of micro-structural length ε under biaxial compression with lateral stress $\Sigma_{11} = -6 \times 10^6\, Pa$ and friction coefficient $\mu_f = 0.3$.

4.5.2.6 Size effect: influence of internal length ε

Figure 4.15 shows the effect of micro-structural length ε on the response of the material under biaxial compressive test at constant strain rate $\dot{e} = 10^{-6}\, s^{-1}$ with lateral stress $\Sigma_{11} = -6 \times 10^6\, Pa$, friction coefficient $\mu_f = 0.3$ and subcritical crack growth index $n = 3$.

If in these tests Charles' law exponent had been chosen as $n = 2$ (like in previous examples of this section), then the internal length ε would have vanished, therefore no size effect would have been encountered.

We observe that the strength of the material increases with the size of the micro-structure decreasing. In other words, the finer is micro-structure, the more resistant is the material. The same relations are observed in term of time.

As observed in case of previous model parameters, also the micro-structural length does not have any influence on frictional properties of the material. The inclinations of the lines in figure 4.16 were constant while changing the internal length ε. It changes only the apparent cohesion of the material.

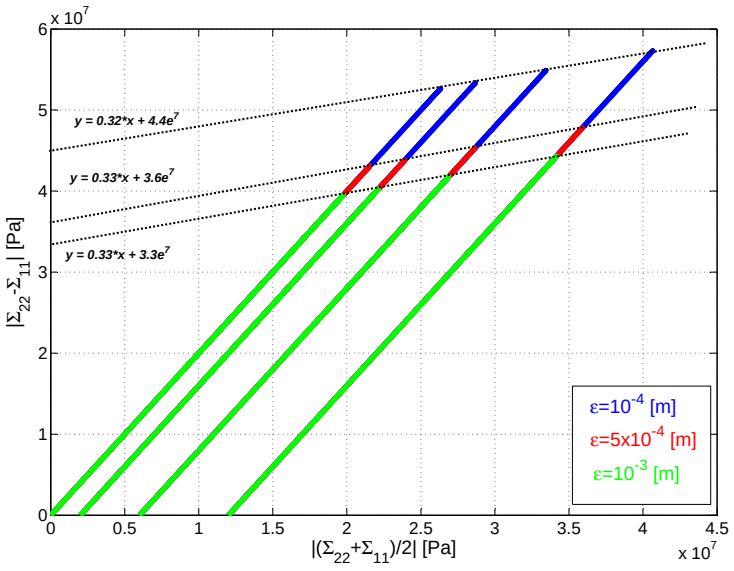

Figure 4.16: Stress path curves : influence of micro-structural length ε on frictional properties of material.

4.6 Global macroscopic behaviour

4.6.1 Introduction

In this part the global macroscopic behaviour will be discussed. We will analyse the response of the sample considered as a structure under different compressive loadings (uniaxial test and biaxial tests with lateral stresses).

We study the effect of friction coefficient, lateral stress and their role in forming the damage localization zone.

We investigate the influence of mesh size and element shape on the results.

The comparison between numerical and experimental results will be presented in the following parts.

At first, the simulations run on a rectangular specimen with regular mesh of 800 elements, each one containing 4 nodes and 4 Gauss points. Then, different meshes are considered.

A lower K_0 was simulated in the elements of one corner, in order to perform the macroscopic response including the localization band. By this way, the band is favored to initiate from the corner.

The damage variable was set to $d_0 = 10^{-6}$, so the material can be considered as initially undamaged.

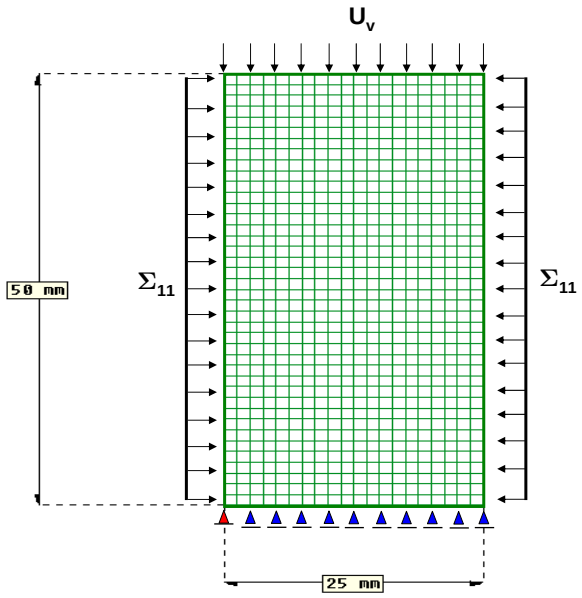

Figure 4.17: Geometry and boundary conditions of the sample.

4.6.2 Geometry and boundary conditions of the sample

Geometry and boundary conditions were based on experimental tests, which were performed in parallel to this studies. In 2D representation the height of the specimen is $50\,mm$ and the width is $25\,mm$.

The axial loading is controlled in displacement by keeping a constant displacement rate. The constant stress is applied on two lateral sides of the specimen.

Dimensions and boundary conditions of the sample are shown in figure 4.17.

4.6.3 Computation algorithm

In every Gauss point, at each time step $n+1$, the damage variable d^{n+1} , stress Σ_{ij}^{n+1} and tangent matrix $\frac{d\Sigma_{ij}^{n+1}}{de_{xkl}^{n+1}}$ are computed using the explicit method as below:

1. input at step $(n+1)$ for time t^{n+1}:
   $e_{xkl}(t^n)$, $d(t^n)$
2. verify the state of opening/sliding right/sliding left ($\mathbf{e_x} \in \mathbf{R}^+$or $\mathbf{D}^R$ or $\mathbf{D}^L$, respectively).
3. compute dissipative term I_{ijkl}:
   $I_{ijkl} = I_{ijkl}(d(t^n))$
4. compute the homogenized coefficient C_{ijkl} :
   $C_{ijkl} = C_{ijkl}(d(t^n))$

5. compute the stress intensity factor :
   $K_{II} = K_{II}\left(\frac{\partial C_{ijkl}(d(t^n))}{dd}, I_{ijkl}\left(d\left(t^n\right)\right)\right)$
6. update the damage :
   $\dot{d} = f\left(e_{xij}(t^n), \frac{\partial C_{ijkl}(d(t^n))}{dd}, I_{ijkl}\left(d\left(t^n\right)\right)\right)$, obtained from (4.8).
   $d\left(t^{n+1}\right) = d\left(t^n\right) + \dot{d}\triangle t$
7. update the homogenized coefficient C_{ijkl} :
   $C_{ijkl} = C_{ijkl}(d(t^{n+1}))$
8. calculate the updated strain:
   $e_{xij}(t^{n+1}) = C^{-1}_{ijkl}\left(d\left(t^{n+1}\right)\right)\Sigma^{(0)}_{ij}$
9. calculate the stress:
   $\Sigma^{n+1}_{ij} = C_{ijkl}\left(d_{n+1}\left(t^{n+1}\right)\right)e^{n+1}_{xij}\left(t^{n+1}\right)$
10. compute tangent matrix:
    $\frac{d\Sigma^{n+1}_{ij}}{de^{n+1}_{xkl}} = C_{ijkl}(d^{n+1})$

where n is the step number, t^n is the time step number, $\triangle t$ is the size of time step.

At time step $n+1$, the damage variable d^{n+1} is obtained by adding to the previous damage variable d^n, the increment $\triangle d$ computed by using the previous deformation e^n_{xkl}. Under such a condition, the tangent matrix has a form :

$$\frac{d\Sigma^{n+1}_{ij}}{de^{n+1}_{xkl}} = C_{ijkl}(d^{n+1}) \tag{4.14}$$

This result is compatible with secant method.

$E\,[Pa]$	$\nu\,[-]$	$K_0\left[MPa.m^{\frac{1}{2}}\right]$	$K_0^1\left[MPa.m^{\frac{1}{2}}\right]$	$v_0\left[\frac{m}{s}\right]$	$\varepsilon\,[m]$
2×10^9	0.2	0.18	0.16	5×10^{-6}	10^{-3}
$d_0\,[-]$	$n\,[-]$	$\dot{e}\left[s^{-1}\right]$	$\theta\,[^\circ]$	$\Sigma_{11}\,[Pa]$	$\mu_f\,[-]$
10^{-6}	3	10^{-6}	135	0	$0.0-0.5$

Table 4.4: Parameters used in the simulations of uniaxial tests at global macroscopic scale.

4.6.4 Uniaxial compression: influence of the friction

After parametric studies in the local frame and refering to experimental results, the following parameters were set (see table 4.4). K_0^1 is the value of critical stress intensity factor related to low-left corner elements in the mesh (in order to initiate the localization band), while K_0 is the value related to rest of elements. θ refers to the orientation of the cracks in the sample and it is kept constant during computation.

Figure 4.18a illustrates the response of the sample defined by the parameters reported in table 4.4 under uniaxial compressive loading. The uniaxial configuration was obtained by applying a constant increment of displacement in the vertical direction and leaving horizontal direction free of stress.

Figure 4.18a shows the evolution of the global vertical stress *vs* axial strain and *vs* time for different values of friction coefficient. As we observed at local macroscopic scale, also at global scale we obtain the increase of material strength together with the increase of friction coefficient. The responses in passing from non frictional example to the lowest friction coefficient one are not significantly different.

Concerning frictional computations, the dependency of peak stress *vs* friction coefficient is not linear. In fact, for a constant increase of friction coefficient (0.1 to 0.3, 0.3 to 0.5), the structural response does not behave in the same way as can be observed in figure 4.18b.

In terms of time, the failure of non frictional material appears as first, while for the material with highest value of friction coefficient, as last. It follows that the time needed to break a sample increases with the friction coefficient. The exact values of critical time for all friction coefficients are presented in the table 4.5.

Concerning the shapes of the presented curves, we can observe that all examples indicate similar behaviour up to peak value, while in post-peak regime the slope of the curve becomes slightly sharper with the increase of friction coefficient. This phenomenon can also be deduced from the plot 4.19, where the damage maps are shown at different time steps.

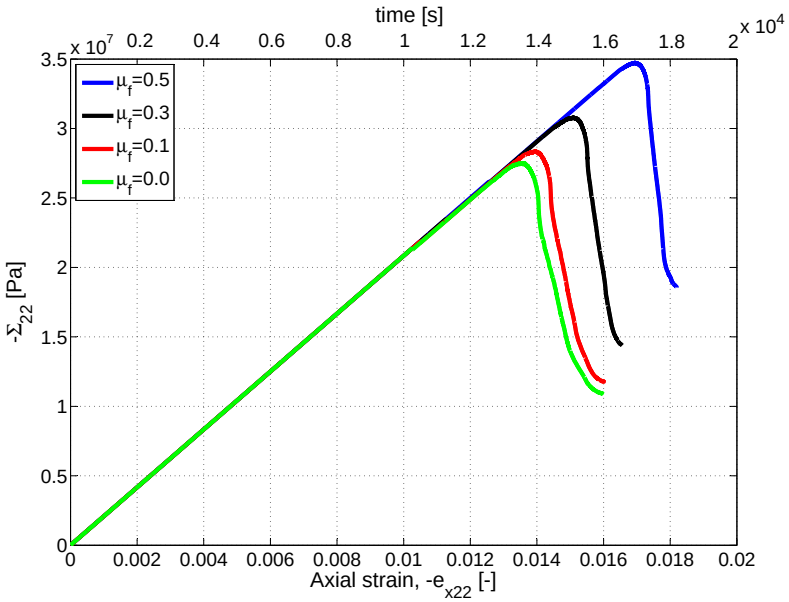

(a)

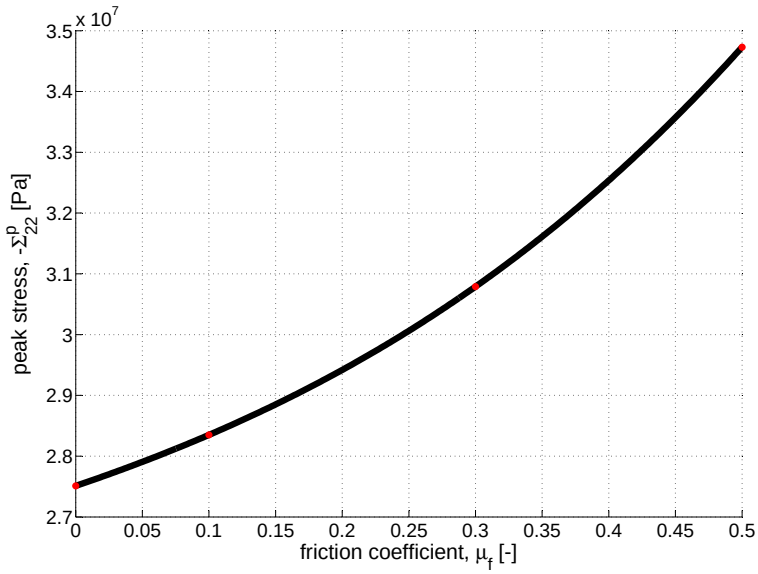

(b)

Figure 4.18: Uniaxial compression for different values of friction coefficient ($\mu_f = 0.0, 0.1, 0.3, 0.5$): (a) stress-strain and stress-time relations (b) stress peak *vs* friction coefficient.

microscopic friction coefficient $\mu_f\,[-]$:	0.0	0.1	0.3	0.5
stress peak time $[s]$:	1.361×10^4	1.396×10^4	1.507×10^4	1.69×10^4

Table 4.5: Uniaxial compression: stress peak time for different friction coefficient ($\mu_f = 0.0, 0.1, 0.3, 0.5$).

In order to compare the response of the sample for different friction coefficients, the results are presented as follows.

Since the time varies between simulations, the appearance of the peak stress is set as "time zero" (time*). The results are plotted at 200 seconds before peak value, at peak value, at 100s, 300s, 400s, 450s, 500s and 550s after peak. In such a way the comparison is possible. We can study the differences in the behaviour along all computations.

The red box in figure 4.19 indicates the state of damage at peak stress and corresponds to time zero. The results placed in the first row from the bottom represent the damage map for non frictional material, the ones in second row the material with friction coefficient equal to $\mu_f = 0.1$, the ones in third row $\mu_f = 0.3$ and in last one $\mu_f = 0.5$.

The presence of friction does not only influence the resistance of the material in time, but also the distribution of damage in the sample. We can observe that depending on the friction coefficient we have different damage distributions. The damage maps for all considered friction coefficients at the "time zero" (at the individual stress-peak) are highlighted in red in figure 4.19.

During the first three considered steps (at the time corresponding to -200s, 0s and 100s) the damage zones tend to similar localized patterns even if the amount of load and time at the analysed steps is not the same. In fact, it grows together with the friction coefficient. Until now, the presence of the friction blocks the propagation of the damage.

The behaviour changes at the state corresponding to 300 seconds, where we observed that the propagation accelerates for higher friction coefficients.

Together with propagation of the damage band, another damage localization appears on the opposite side of the specimen. At first we observed this for the highest friction coefficients ($\mu_f = 0.5$) at the time corresponding to 400 seconds after peak value. These two damage localizations will unify first in case of friction coefficient equal to $\mu_f = 0.5$.

The analysis were stopped at the point where the damage band fully crosses the specimen; this event depends on the friction coefficient. The damage in the sample with the highest friction coefficient ($\mu_f = 0.5$) evolved completly at the time corresponding to 450 seconds, while the rest still needs time to fully cross the specimen. The last two time steps (500 and 550 seconds) show the following stages of damage development for friction coefficient equal to $\mu_f = 0.1$ and $\mu_f = 0.0$. The damage band orientation does not depend on the friction coefficient.

These results confirm the observation presented previously about the sharper shape of the stress-strain and stress-time curves in the post-peak regime (see Fig.4.18a), where stress gradient grows together with friction coefficient.

The horizontal and vertical strain localizations, which correspond to the damage evolution presented in figure 4.19, are shown in figures 4.20 and 4.21, respectively. We can observe that the strain localizations perfectly follow the damage localizations.

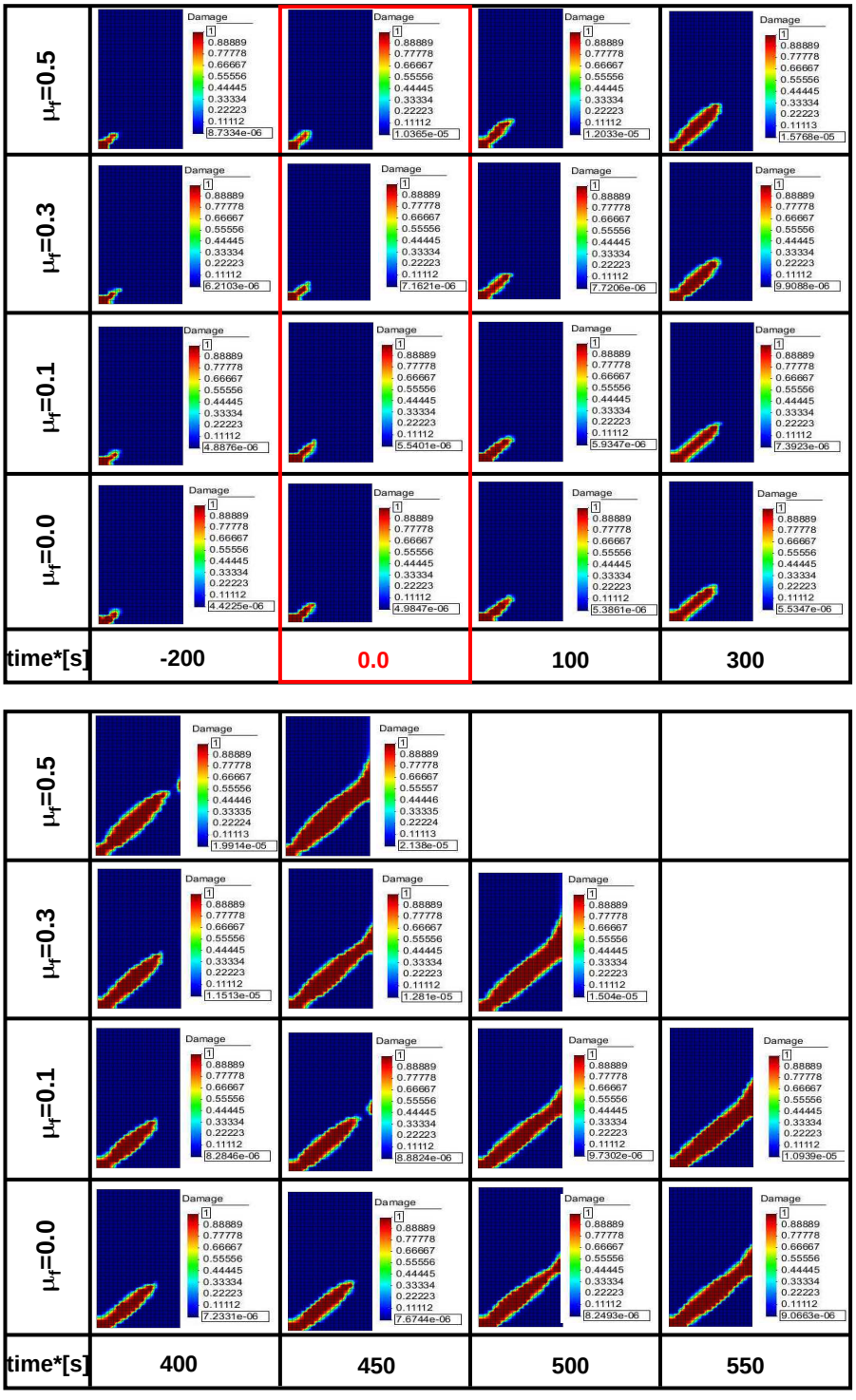

Figure 4.19: Evolution of damage : uniaxial test for different values of friction coefficient ($\mu_f = 0.0, 0.1, 0.3, 0.5$). Time zero corresponds to the stress peak.

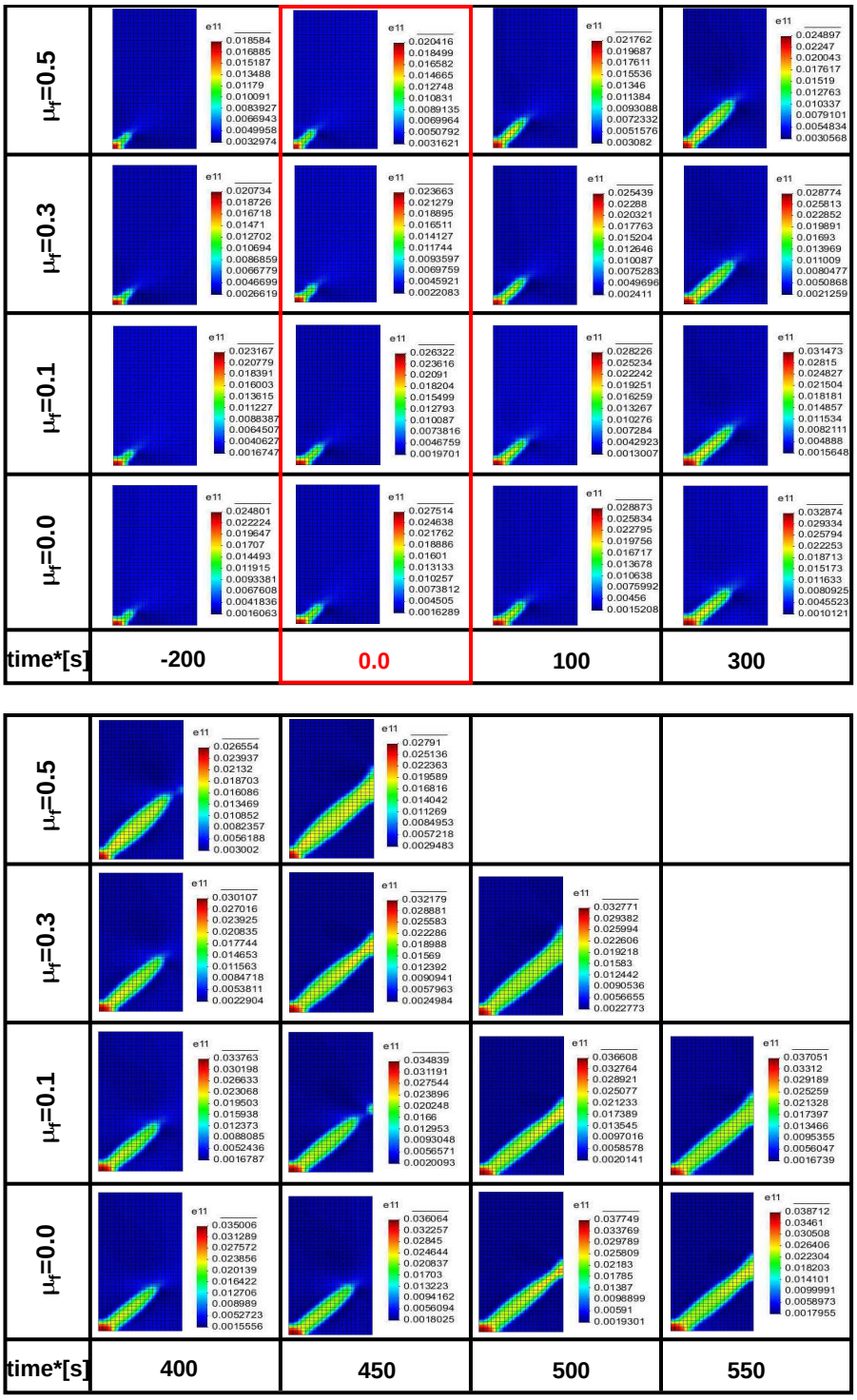

Figure 4.20: Horizontal strain localization: uniaxial test for different values of friction coefficient ($\mu_f = 0.0, 0.1, 0.3, 0.5$). Time zero corresponds to the stress peak.

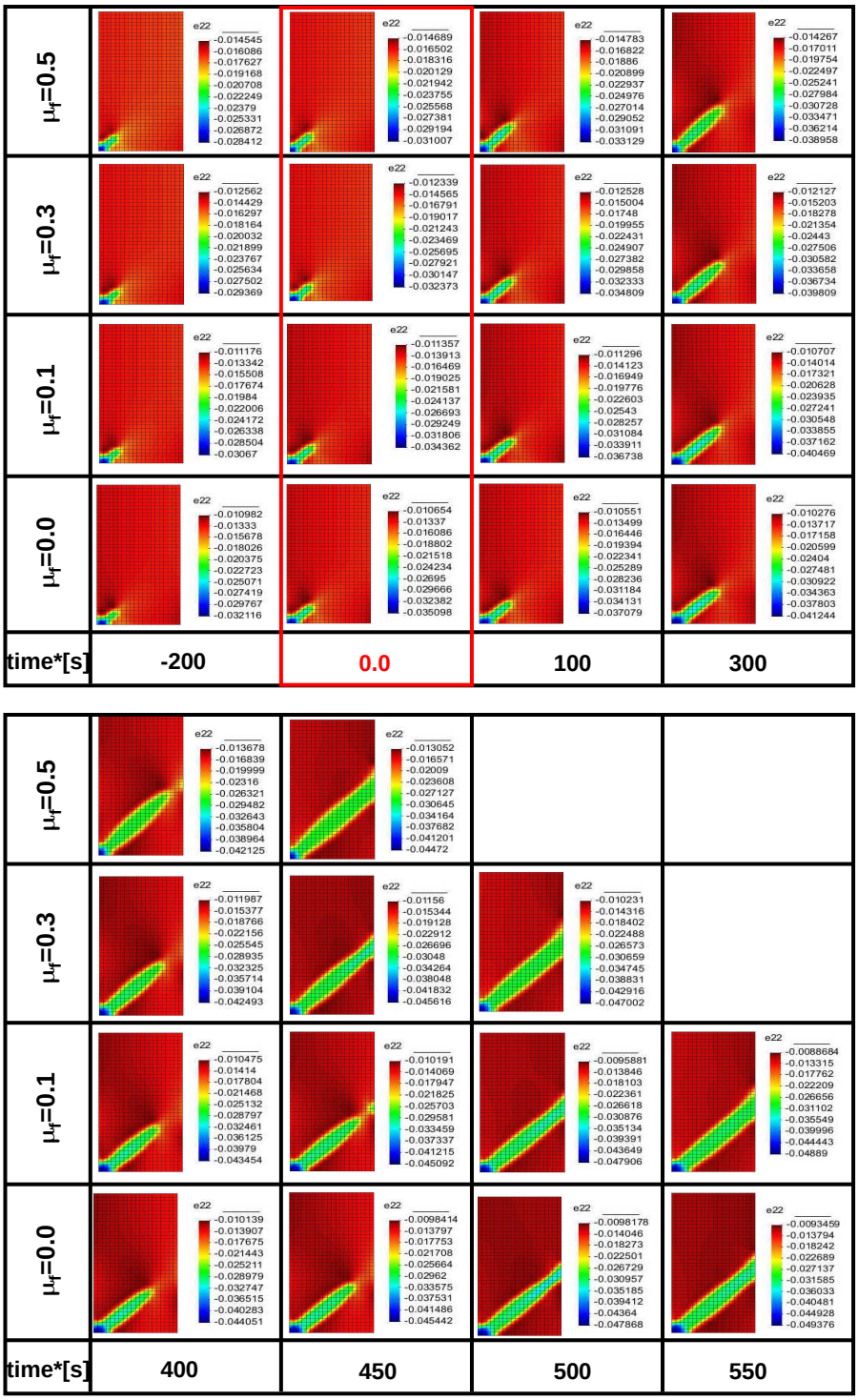

Figure 4.21: Vertical strain localization : uniaxial test for different values of friction coefficient ($\mu_f = 0.0, 0.1, 0.3, 0.5$). Time zero corresponds to the stress peak.

$E\,[Pa]$	$\nu\,[-]$	$K_0\left[MPa.m^{\frac{1}{2}}\right]$	$K_0^1\left[MPa.m^{\frac{1}{2}}\right]$	$v_0\left[\frac{m}{s}\right]$	$\varepsilon\,[m]$
2×10^9	0.2	0.18	0.16	5×10^{-6}	10^{-3}
$d^0\,[-]$	$n\,[-]$	$\dot{e}\left[s^{-1}\right]$	$\mu_f\,[-]$	$\theta\,[^\circ]$	$-\Sigma_{11}\,[Pa]$
10^{-6}	3	10^{-6}	0.5	135	$0-12\times10^6$

Table 4.6: Parameters used in the simulation of biaxial tests at global macroscopic scale.

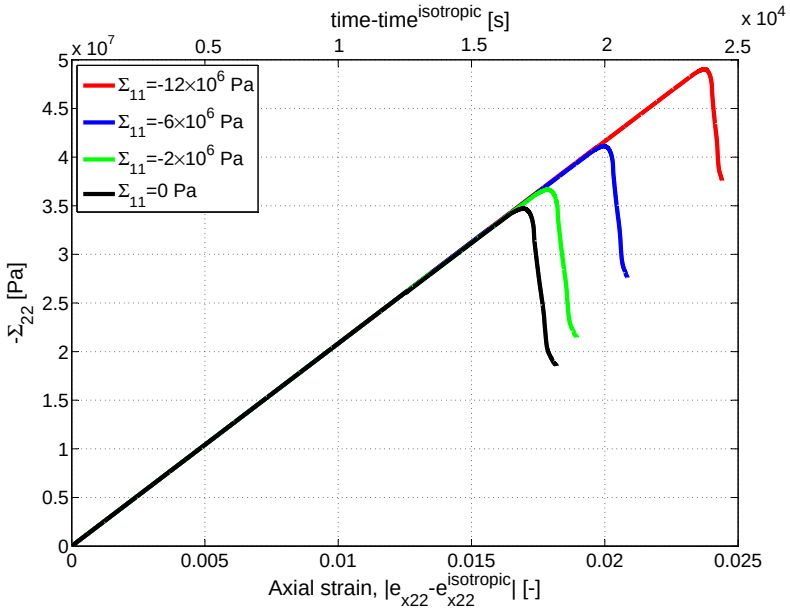

Figure 4.22: Stress curves *vs* axial strain and *vs* time under biaxial compression for $\mu_f = 0.5$ and different lateral stresses ($\Sigma_{11} = 0\,Pa, -2\times10^6\,Pa, -6\times10^6\,Pa, -12\times10^6\,Pa$).

4.6.5 Biaxial compression : influence of lateral stress.

In this section the influence of lateral stress is studied. The geometry and boundary conditions are shown in figure 4.17. The tests were performed for different lateral stresses and for the parameters listed in the table 4.6.

Figure 4.22 presents the macroscopic response of the sample in terms of strain $e_{x22} - e_{x22}^{isotropic}$, stress $\Sigma_{22} - \Sigma_{11}$ and $time - time^{isotropic}$, where $e_{x22}^{isotropic}$ and $time^{isotropic}$ are the deformation and time corresponding to the isotropic state ($\Sigma_{22} = \Sigma_{11}$), and Σ_{11} is the constant lateral stress. Σ_{11} assumes the following values: $0\,Pa, -2\times10^6\,Pa, -6\times10^6\,Pa, -12\times10^6\,Pa$. The fact that the peak stress value increases with the value of the lateral stress confirms the presence of the friction.

Figure 4.23 shows how the lateral stress influences the damage distribution in the sample. The first line of results corresponds to the biaxial compression with lateral stress equal to $-12\times10^6\,Pa$, and the following ones to$-6\times10^6\,Pa$, $-2\times10^6\,Pa$, $0\,Pa$, respectively.

lateral stress $\Sigma_{11}\,[Pa]$:	0.0	-2×10^6	-6×10^6	-12×10^6
stress peak time $[s]$:	1.69×10^4	1.852×10^4	2.21×10^4	2.802×10^4

Table 4.7: Biaxial compression for different lateral stresses: stress peak time.

As mentioned before, the peak stress takes place later for higher values of lateral stress. Peak times are listed in the table 4.7.

In order to perform a better comparison, the results are plotted in a new time scale (as explained in section 4.6.4). The appearance of peak stress was chosen as a referencial point called "time zero". The red box points the results corresponding to the level of damage at the peak stress for different lateral stresses.

We can observe that at "time zero" the damage distributions developed up to similar stage, even if the amount of time and load at the peak is higher for higher lateral stress. The time to reach the peak value grows with the lateral stress, so until now the evolution of damage is slowing down during increasing the lateral stress.

After peak value the damage grows together with the increase of lateral stress value. This tendency is kept during all post-peak regime and accelerates in its final part, i.e. the differences become more significant (300-450 seconds). The post-peak regime becomes shorter for higher values of lateral stress, and this can be underlined by the damage distribution in time and stress-strain relations presented in the figure 4.22.

The horizonal and vertical strain localizations, which correspond to the damage evolution presented in figure 4.23 are shown in figures 4.24 and 4.25, respectively. The strain localizations are direcly linked with the damage localizations.

The stress path corresponding to the previous plots is presented in the figure 4.26. The appearance of the slope indicates the presence of the friction. The graphical interpretation of Mohr's circle and Coulomb line is shown in the figure 4.27. The macroscopic friction coefficient can be deduced from the friction angle ϕ formed by the Coulomb line, which is tangential to the Mohr's circles. Based on this angle, which is about 24.0^o, the friction coefficient can be computed using the following relation (4.15):

$$\mu_f^* = tan\,(\phi) \tag{4.15}$$

where μ_f^* represents the macroscopic friction coefficient. The obtained macroscopic Coulomb coefficient is equal to $\mu_f^* = 0.45$ while the microscopic one was established to $\mu_f = 0.5$.

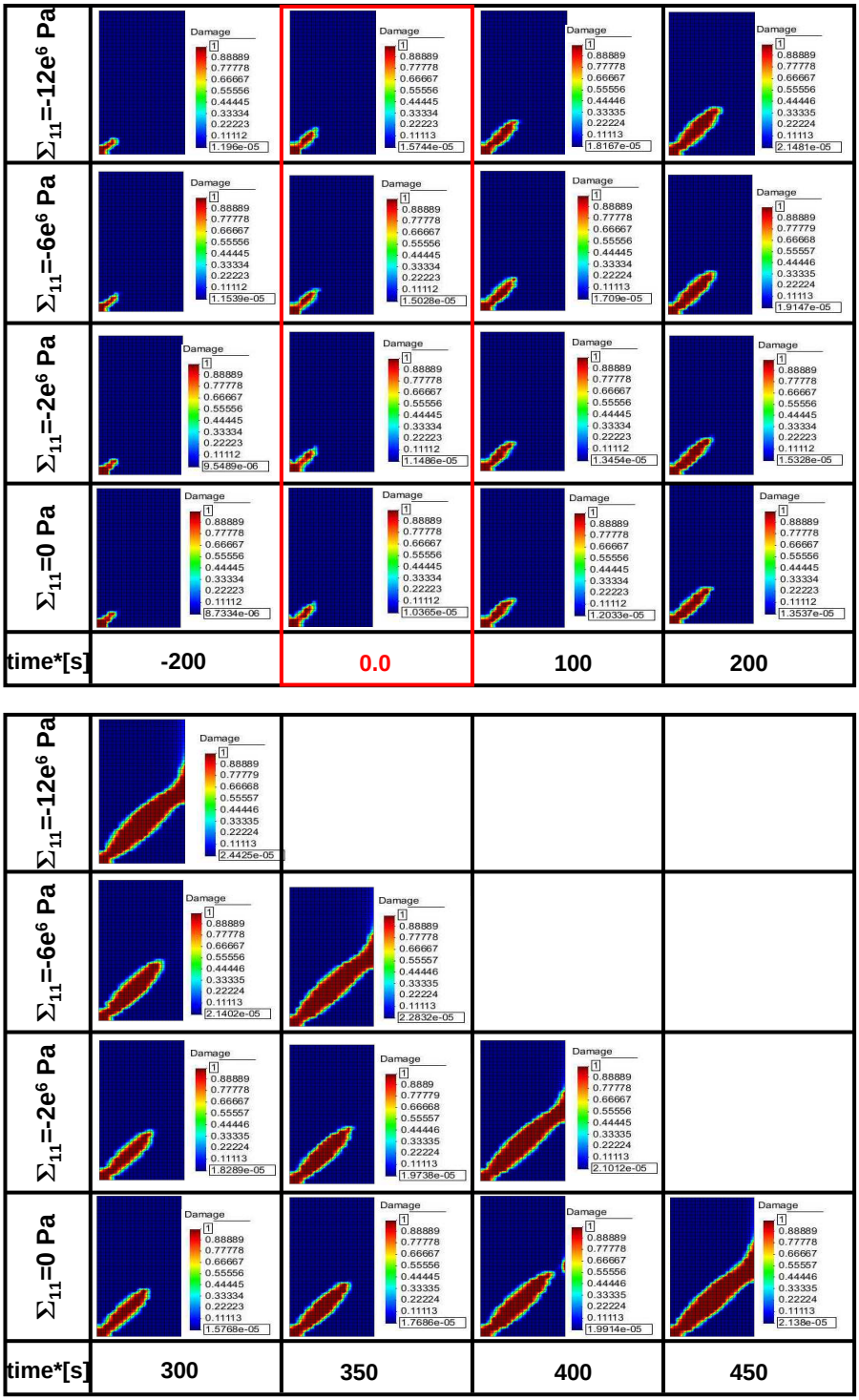

Figure 4.23: Evolution of damage: biaxial compression for $\mu_f = 0.5$ and different lateral stresses ($\Sigma_{11} = 0\,Pa, -2\times10^6\,Pa, -6\times10^6\,Pa, -12\times10^6\,Pa$). Time zero corresponds to the stress peak.

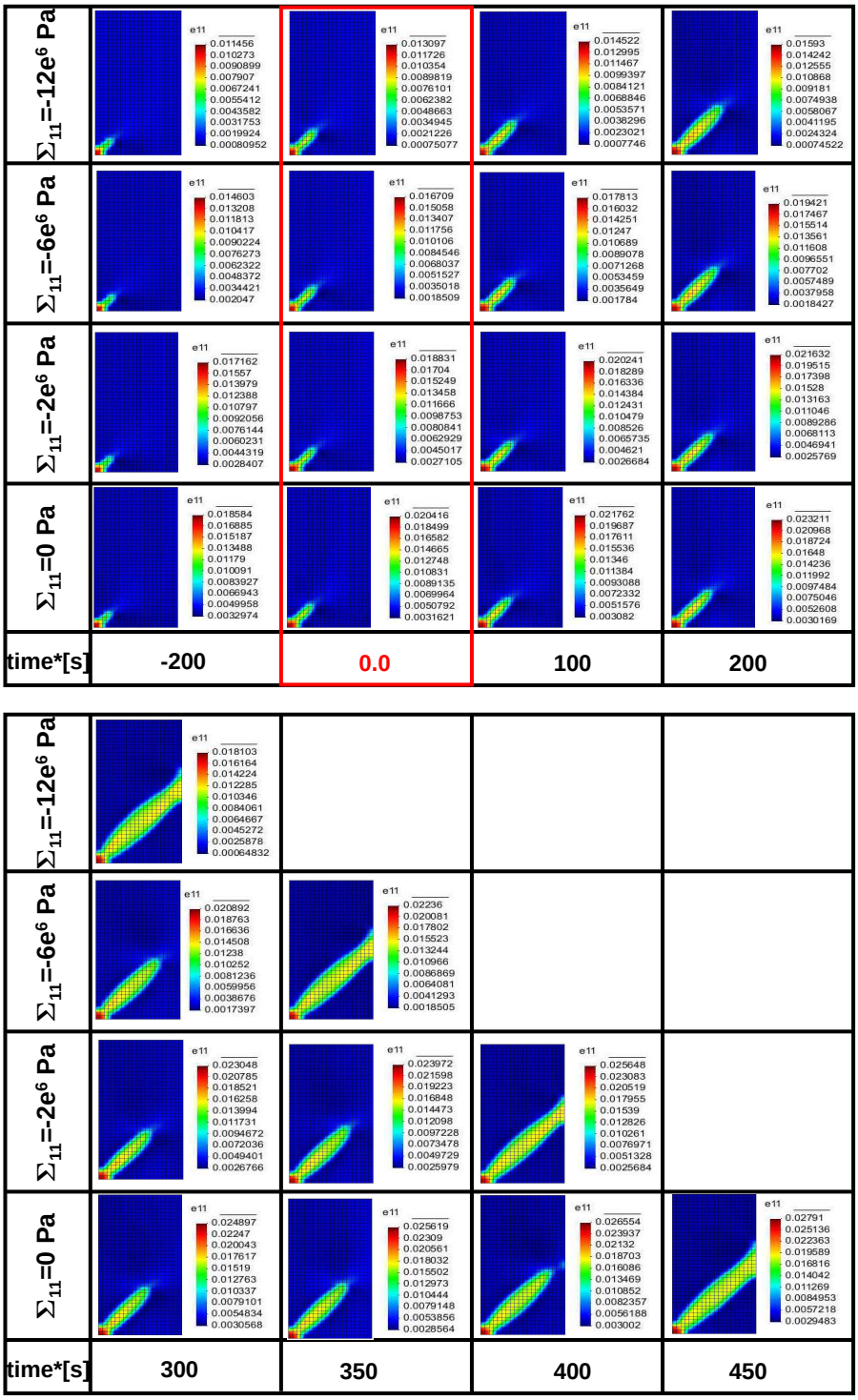

Figure 4.24: Horizontal strain localization: biaxial compression for $\mu_f = 0.5$ and different lateral stresses ($\Sigma_{11} = 0\,Pa, -2 \times 10^6\,Pa, -6 \times 10^6\,Pa, -12 \times 10^6\,Pa$). Time zero corresponds to the stress peak.

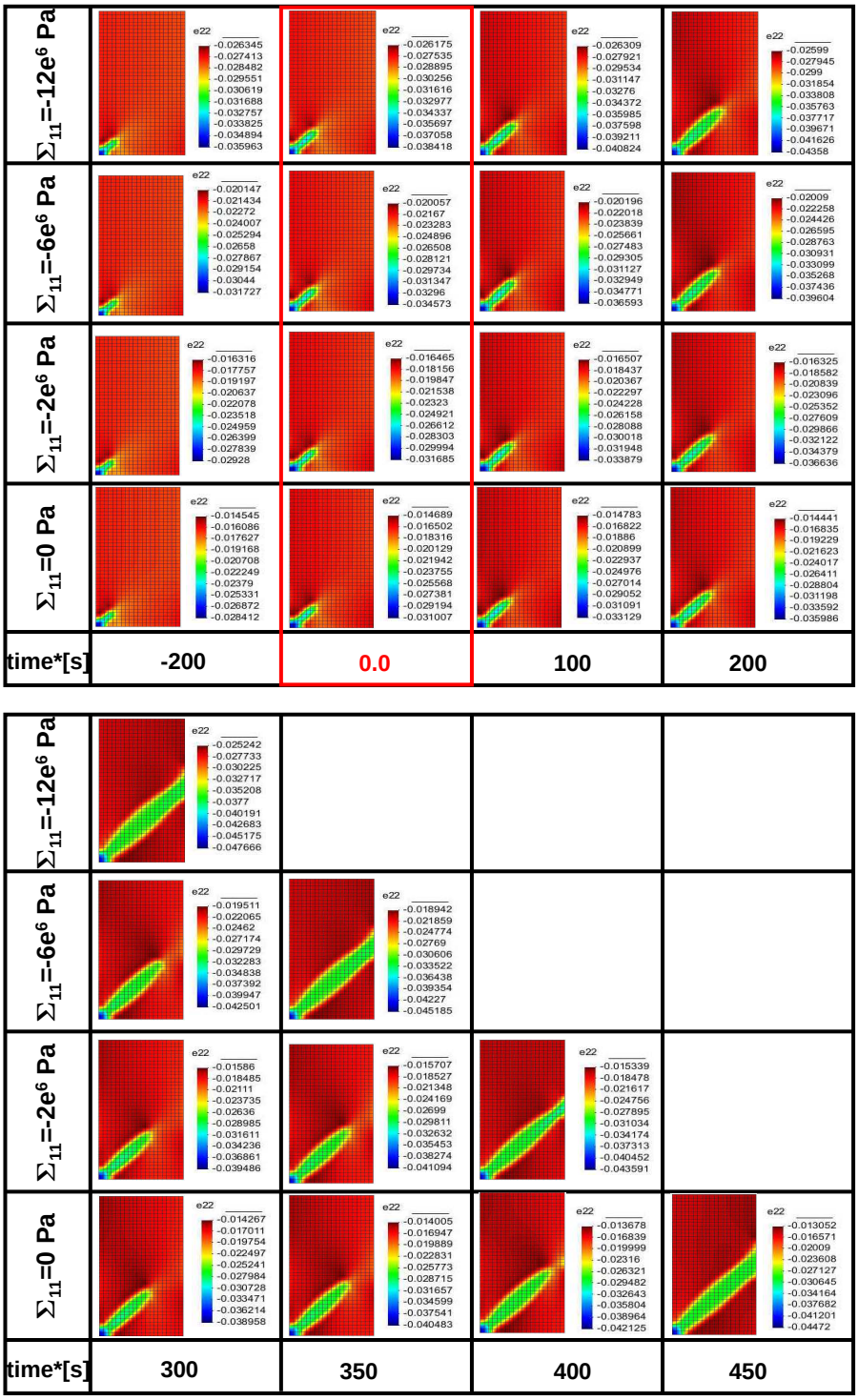

Figure 4.25: Vertical strain localization: biaxial compression for $\mu_f = 0.5$ and different lateral stresses ($\Sigma_{11} = 0\,Pa$, $-2\times10^6\,Pa$, $-6\times10^6\,Pa$, $-12\times10^6\,Pa$). Time zero corresponds to the stress peak.

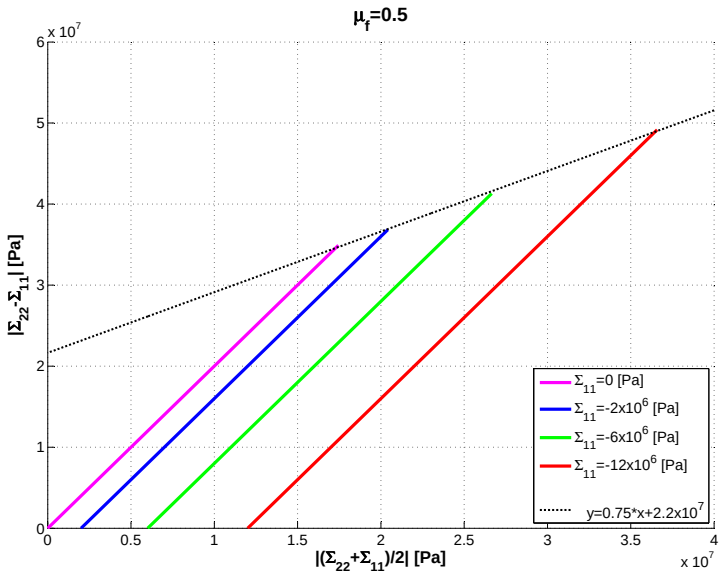

Figure 4.26: Global stress path curves for different lateral stresses and friction coefficient $\mu_f = 0.5$.

microscopic friction coefficient μ_f [−]:	0.0	0.1	0.3	0.5
slope value in the deviatoric and mean stress frame [−]:	0.0	0.085	0.36	0.75

Table 4.8: Values of the slope in the deviatoric and mean stress frame for different microscopic friction coefficients.

The Coulomb's line crosses the vertical axe in the point corresponding to the value of the cohesion equal $c = 1.2 \times 10^7 Pa$.

Figure 4.28 shows the influence of friction coefficient on the stress path curves. It can be observed that the slope of the stress paths changes according to friction coefficient. The slope is equal to zero for non frictional material and increases with friction coefficient. The table 4.8 summarizes these results.

The Mohr's circle with tangential Coulomb's line for different friction coefficients is plotted in the figure 4.29. The obtained friction angle ϕ, the macroscopic friction coefficient μ_f^* and the corresponding microscopic coefficients are listed in the table 4.9:

The microscopic friction coefficient is the value established at the microscale (used in unit cell computations) while friction angle and macroscopic friction coefficient established herein are quantities deduced from global macroscopic computations.

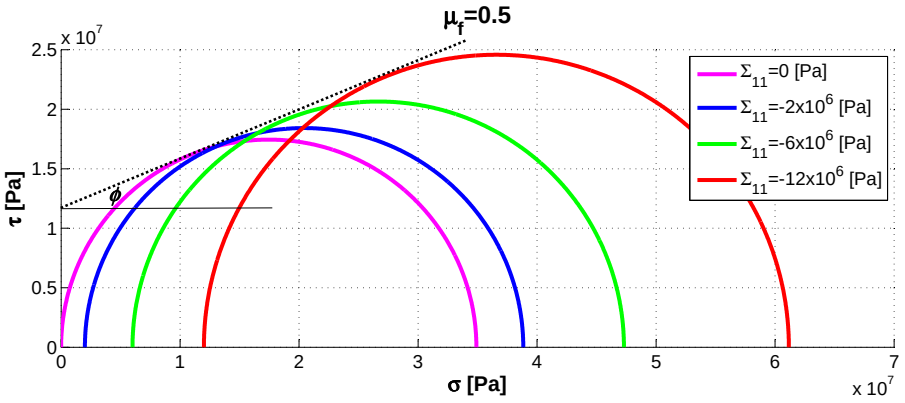

Figure 4.27: Global Mohr's circles and Coulomb's line for frictional material ($\mu_f = 0.5$).

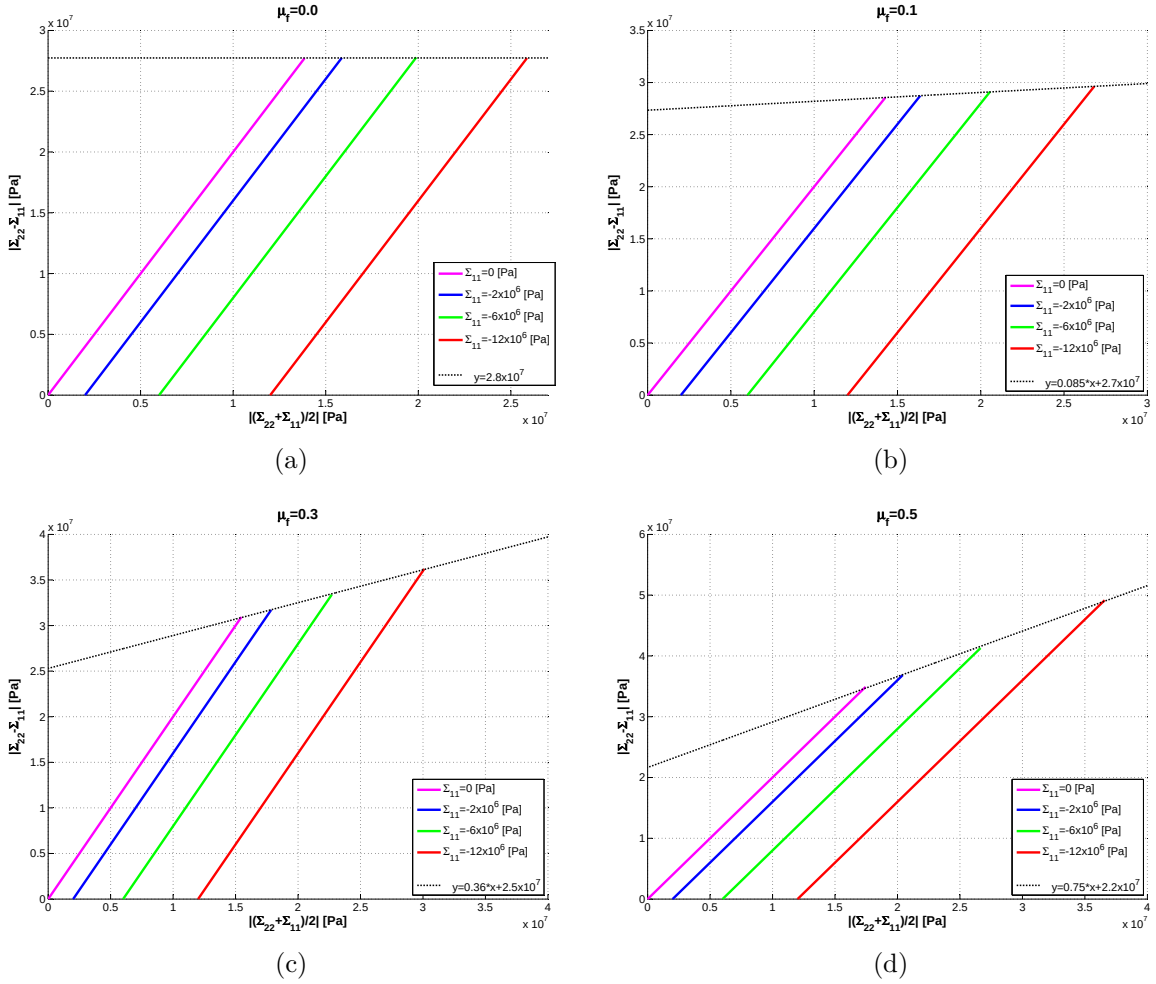

(a) (b) (c) (d)

Figure 4.28: Global stress path curves for different lateral stresses ($\Sigma_{11} = 0\,Pa, -2 \times 10^6\,Pa, -6 \times 10^6\,Pa, -12 \times 10^6\,Pa$) and friction coefficients: a) $\mu_f = 0.0$, b) $\mu_f = 0.1$, c) $\mu_f = 0.3$, d) $\mu_f = 0.5$.

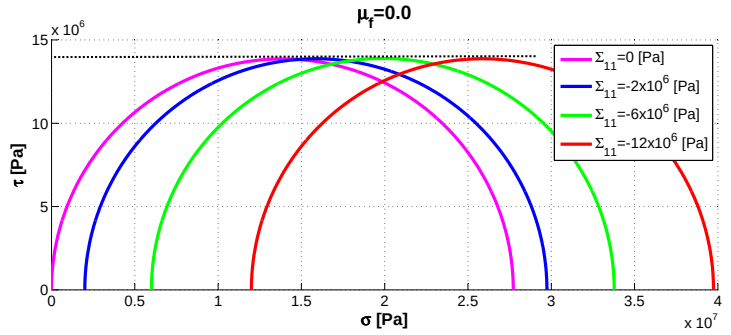

(a)

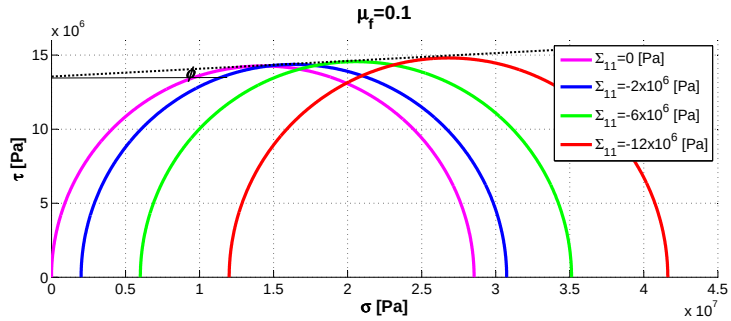

(b)

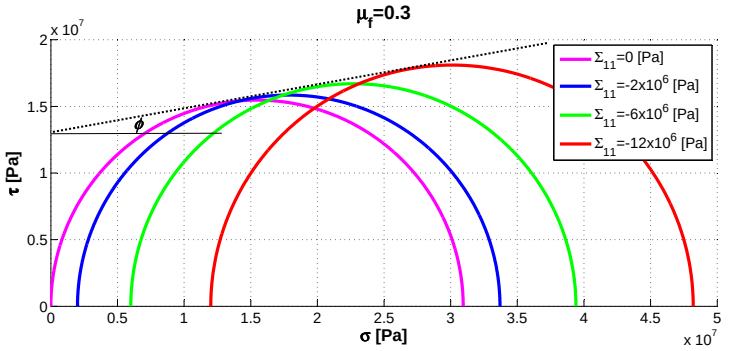

(c)

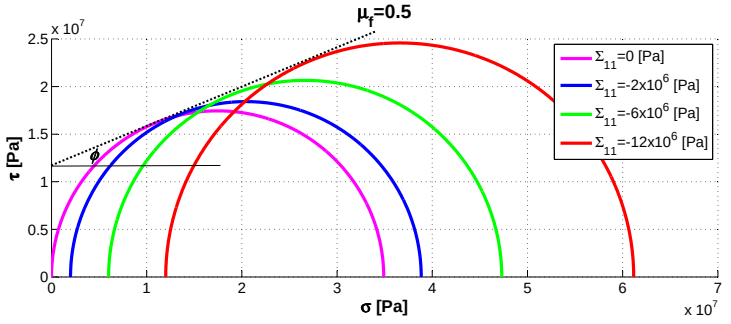

(d)

Figure 4.29: Global Mohr's circles and Coulomb's lines for different lateral stresses ($\Sigma_{11} = 0\,Pa, -2\times10^6\,Pa, -6\times10^6\,Pa, -12\times10^6\,Pa$) and friction coefficients: a) $\mu_f = 0.0$, b) $\mu_f = 0.1$, c) $\mu_f = 0.3$, d) $\mu_f = 0.5$.

microscopic friction coefficient μ_f [−]	0.0	0.1	0.3	0.5
friction angle $\phi[^\circ]$	0.0^o	4.0^o	12^o	24^o
macroscopic friction coefficient $\mu_f^*[-]$	0.0	0.07	0.21	0.45

Table 4.9: The values of friction angle ϕ and macroscopic friction coefficient μ_f^* .

$E\,[Pa]$	$\nu\,[-]$	$K_0\left[MPa.m^{\frac{1}{2}}\right]$	$K_0^1\left[MPa.m^{\frac{1}{2}}\right]$	$v_0\left[\frac{m}{s}\right]$	$\varepsilon\,[m]$
2×10^9	0.2	0.18	0.16	5×10^{-6}	10^{-3}
$d^0\,[-]$	$n\,[-]$	$\dot{e}\left[s^{-1}\right]$	$\Sigma_{11}\,[Pa]$	$\theta\,[^\circ]$	$\mu_f\,[-]$
10^{-6}	3	10^{-6}	0	135	0.1

Table 4.10: Parameters used in the numerical uniaxial compression tests performed for different types of mesh.

4.6.6 Mesh effect

The last step in the development of time dependent damage model is the verification of the results concerning dependency on mesh size and element shape. For each mesh the same uniaxial compression test were perfomed. Geometry, boundary conditions and considered meshes are presented in figure 4.30, and parameters used in the computations are reported in the table 4.10.

The meshes contain 800, 1741 and 3200 elements with 4 nodes and 4 Gauss points each. Two meshes are constructed with square elements and one mesh with unregular shape of elements.

Figure 4.31 presents the evolution of global vertical stress *vs* time and *vs* axial strain obtained for different meshes. We can observe that the curves overlap with very small perturbations in its final part. The results presented in figures 4.32 and 4.33 correspond to the time defined by the points (*t1*, *t2, t3* and *t*4) in figure 4.31.

Damage localization zones (see Fig.4.32), horizontal and vertical strain localizations (see Fig.4.33) are plotted in each point (*t1=13960*, *t2=14110, t3=14310* and *t3=14510* seconds) for every mesh. We can observe that at the same time, the specimen is approximately at the same stage of degradation of the elastic properties. Even if some differences in size and shape of localized zones can be observed, the responses of the material tend to the same result.

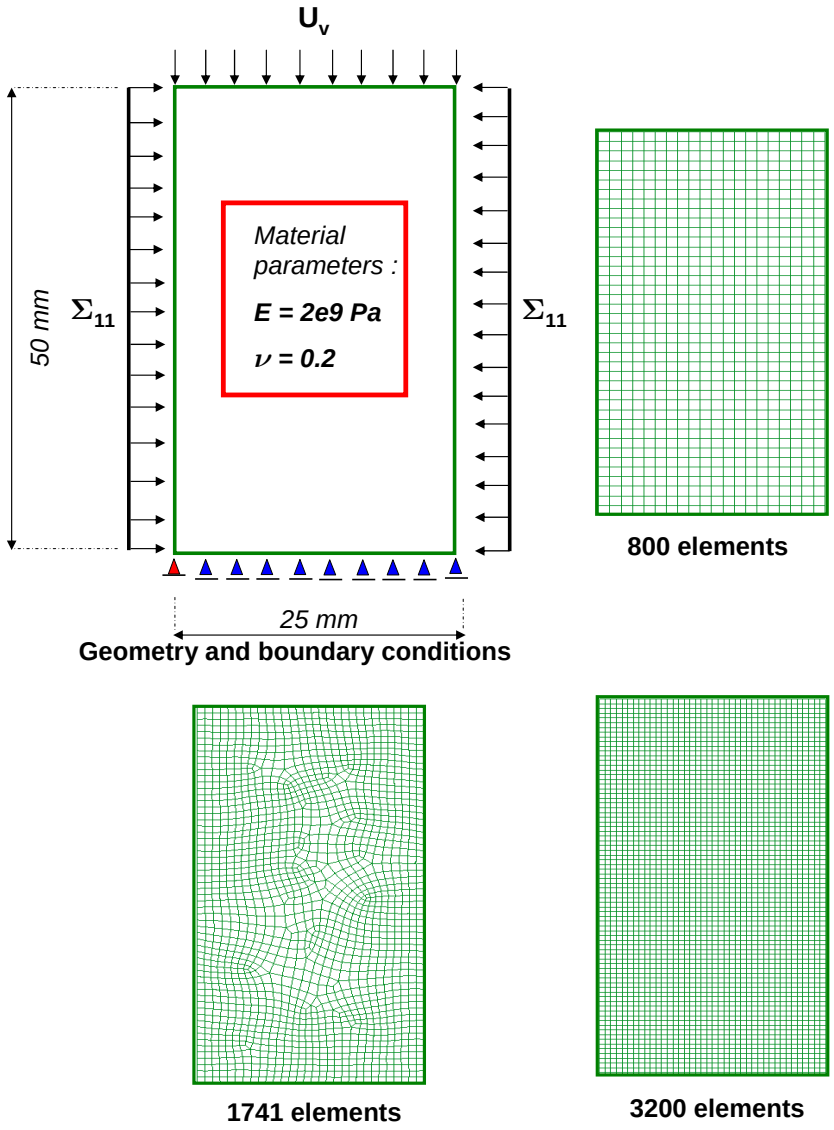

Figure 4.30: Geometry, boundary conditions and three meshes used in uniaxial compression test.

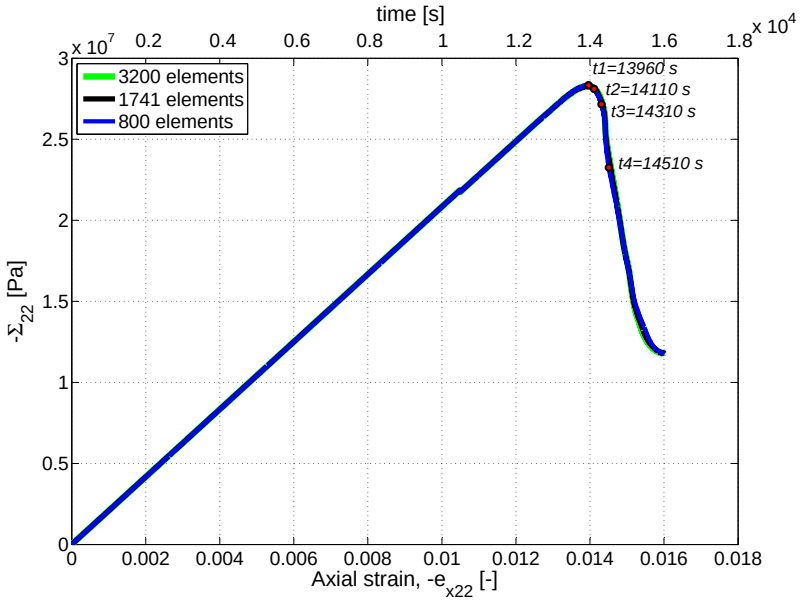

Figure 4.31: Global vertical stress *vs* time and *vs* axial strain curves obtained with the same time dependent damage model and different types of mesh (800, 1741 and 3200 elements).

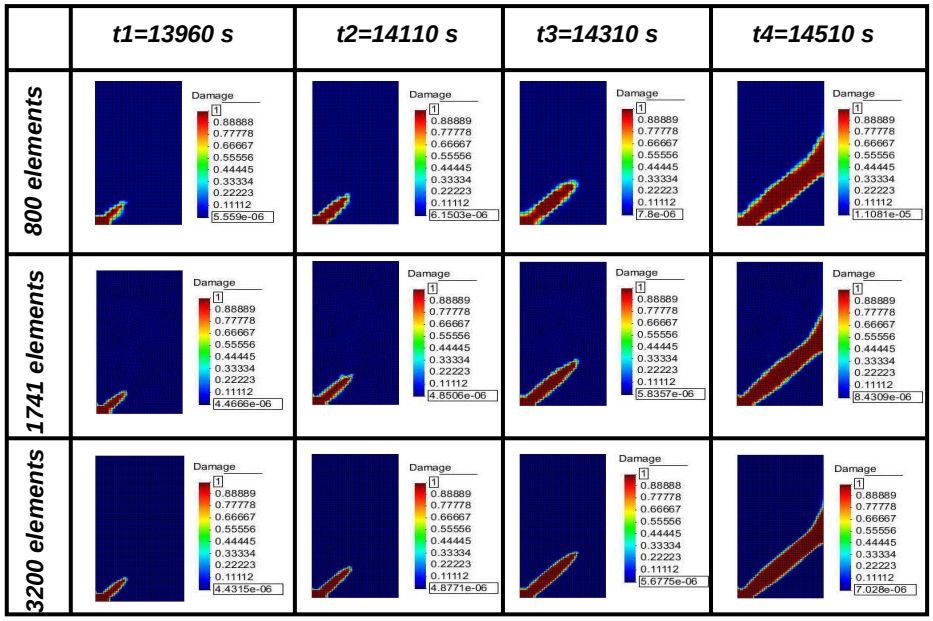

Figure 4.32: Comparison of damage distribution zones obtained with the same time dependent damage model and different types of mesh (800, 1741 and 3200 elements).

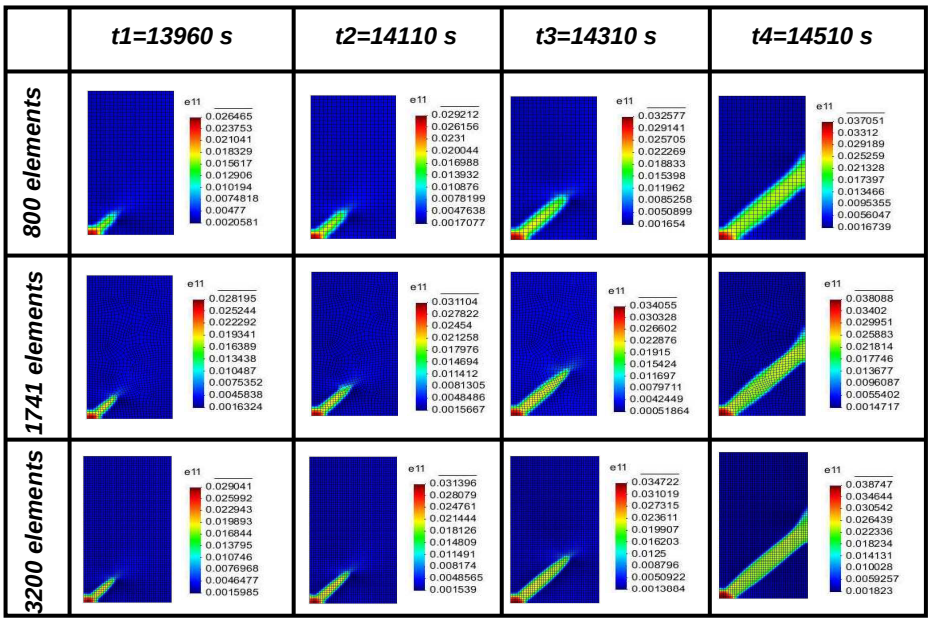

(a)

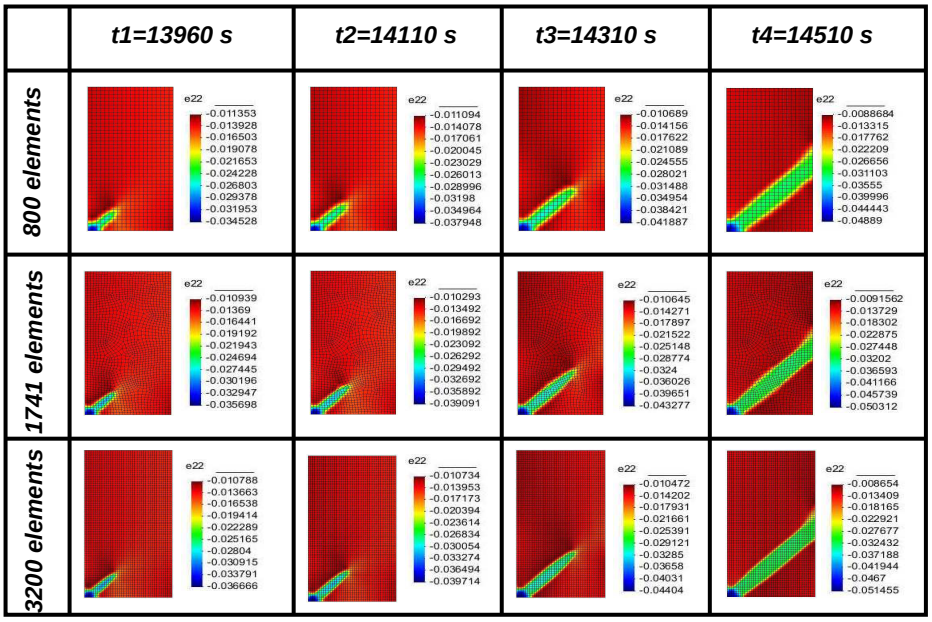

(b)

Figure 4.33: Comparison of horizontal strain localization zones (a) and vertical strain localization zones (b) obtained with the same time dependent damage model and different types of mesh (800, 1741 and 3200 elements).

4.7 Conclusions

The objective of this chapter was to develop a complex time-dependent damage model capable to take into account the propagation of the frictional microcracks. A subcritical propagation criterion has been employed to describe their evolution.

The mathematical formulation of subcritical single mode propagation obtained by homogenization was presented.

The macroscopic response of micro-fractured elastic body involving damage evolution was deduced thanks to asymptotic homogenization technique.

The effective stress-strain and damage responses, depending on time, have been numerically evaluated in macroscopic local point and at global macroscopic sample-scale including localization driven by a heterogeneity in K_0.

In the local frame we studied the influence of the parameters involved in the model, such as velocity v_0, strain rate $\dot{e}$, subcritical growth coefficient n, internal length ε, under different compressive loadings and different friction coefficients. We did not notice any significant influences of those parameters on the frictional properties. The strength of the material grows together with n, strain rate and internal length ε and decreases with v_0.

We found different structural responses depending on frictional properties and applied lateral stresses. In particular, the strength of material increases together with them, and this was observed in both local and global level.

The effects of friction coefficient and lateral stresses can be seen not only in terms of peak stress level, but also in terms of post-peak regime behaviour. The post-peak regime evolves more rapidly for the material with higher friction coefficient and under higher lateral stress.

The damage localization zone forms in the same way. In fact, after peak-stress it evolves faster for the material with higher friction and under higher lateral stress. In pre-peak regime the development of damage zone progresses slower in case of higher friction coefficient. The presence of the friction acts in opposite direction to the propagation of the damage only in pre-peak regime. The band orientation is not inlfluenced by friction coefficient and lateral stress.

In terms of time, the failure of non frictional material appears as first, while for the material with highest value of friction coefficient, as last. The same relation is observed while increasing the lateral stress.

We studied the variations of the frictional properties passing from microscopic scale to macroscopic scale. Values of friction coefficients, obtained at the macroscopic scale, are slightly reduced with respect to assumed one.

Finally, the effect of different meshes was studied. The response of the material for each considered mesh type tends to the same results, verifing the mesh independency. This is a conseqence of regularization by time-dependency.

The numerical simulations presented here showed the ability of the developed model to reproduce time dependent damage response.

Chapter 5

Experimental characterization of the strain localization

Contents

5.1 Introduction

The results presented in this chapter are part of an experimental program for ANDRA (Groupement de Laboratoire "Géomécanique" GM4). The tests were performed using a new experimental device constructed in the 3SR Laboratory [15].

Failure by strain localization is commonly observed in geomaterials. Measurements of strain fields and their evolution in time are particularly useful to study strain localization (initiation of deformation bands) and post-localization regimes. Such tools have been developed for soils (e.g., sand specimens in plane strain conditions [30] or in triaxial conditions using X-ray tomography [44]). Similar developments for rocks are still difficult, especially because the pertinent confining pressure to reproduce in-situ stresses and material stiffnesses are higher than for soils; only a very few devices exist (e.g.[80]).

In this chapter we present the results obtained in a new true-triaxial apparatus that allows observation of rock specimens under loading. Whilst several triaxial apparatuses exist that allow the application of three different principal stresses, they do not allow observation

of specimens under load and such analysis is only possible post-mortem (e.g., [64, 9, 62, 83, 43, 52, 67, 74]). Furthermore, in this new device, as for biaxial apparatuses (e.g., [55] and [71]), failure surfaces can develop and propagate in a sample in an unrestricted manner; this can be under true-triaxial or plane-strain (biaxial) conditions as, if required, the intermediate stress can be controlled (with active control) to impose a plane strain condition during a test. The observation of a specimen under load is possible as one surface of the prismatic specimen, which is orthogonal to the plane strain direction, is in contact with a hard transparent window. The deformation of this surface should be representative of the deformation in the whole specimen (due to the plane-strain condition), up to and beyond strain localization. Therefore the evolution of the strain field in a sample can be measured by digital image correlation (DIC) of photographs taken of this surface.

The next section describes briefly the new apparatus. We present in a third section the results obtained with the Callovo-Oxfordian argillite extracted from the Underground Research Laboratory (URL) at Bure, France. We will focus on strain localization and crack initiation. In the last section of this chapter we compare these experimental results with numerical results and we discuss the abilities of the time-dependent damage model, which has been developed in the previous chapters of this thesis.

5.2 Description of the true triaxial cell

The apparatus has been developped in Laboratoire 3SR (Grenoble) with the aim to charaterize the initiation of localization and the post-localization regime in rocks. With this device three independant stresses can be applied in the three space directions on prismatic rock specimens, with the ability to visualise the specimen under load. The surfaces perpendicular to the major and intermediate stresses (compression) are in contact with rigid platens, which are moved by two perpendicular pistons, while the two surfaces perpendicular to the minor stress are free to deform because the stress is applied by a confining fluid (through a soft membrane). As deformation bands and cracks are generally parallel to the intermediate stress, the specimen has the freedom to deform and fail with no kinematic constraints imposed on the formation of the failure zone. Moreover, one of the two surfaces perpendicular to the intermediate stress is in contact with a hard window to observe the specimen under load. The two pistons can be controlled in stress or displacement. In particular, the intermediate stress can be controlled such that there is no deformation in this direction, which allows application of plane strain loading. In such a case, the kinematics over the surface in contact with the window is representative of the kinematics in the whole specimen up to and beyond strain localization.

A simplified schema of the apparatus is presented in figure 5.1. The hydraulic axial piston (1) applies the axial loading on the specimen (2). This is self-compensated with respect to the confining pressure, i.e., it is in equilibrium whatever the confining pressure. The axial loading is controlled in displacement by an external displacement transducer linked to a pressure generator that adapts the pressure applied to the top of the piston to keep a constant displacement rate. The axial piston moves inside a floating axial frame (3), when the piston moves down, the frame and the bottom loading cap move up by about the same value. In such a way, if the specimen deforms homogeneously, the middle of the specimen does not move (or only very slightly). The weight of the floating frame is compensated by

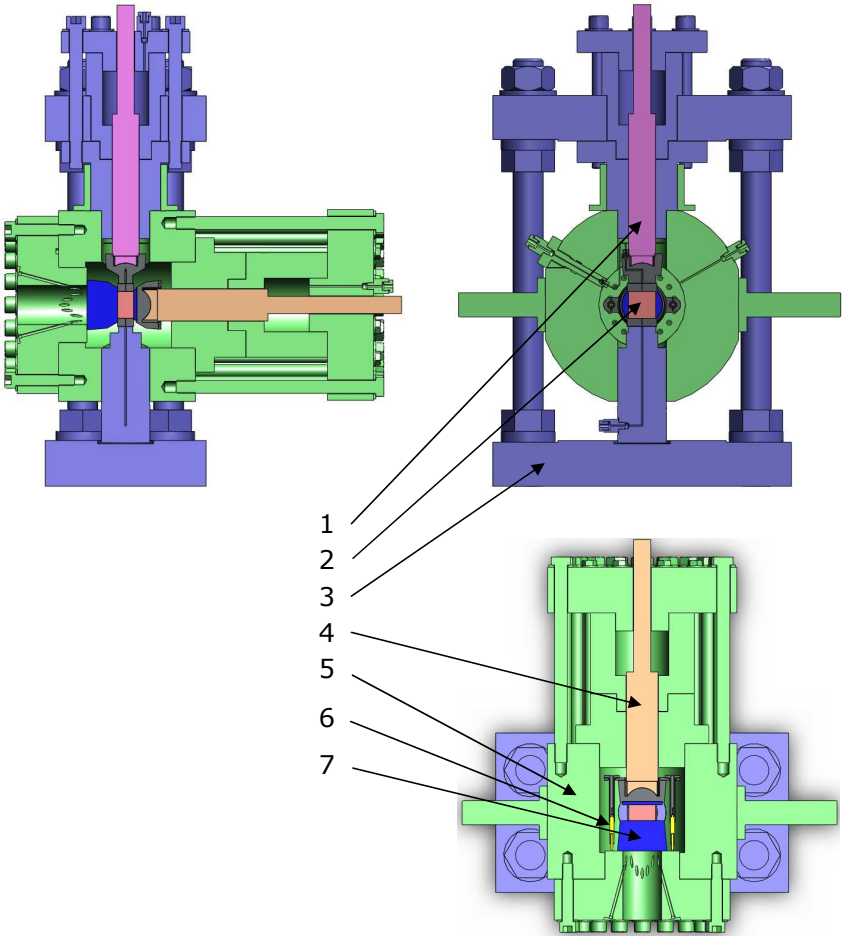

Figure 5.1: Scheme of the true triaxial cell with an observation window: 1) axial piston, 2) specimen, 3) floating axial frame, 4) horizontal piston, 5) confining chamber and fixed frame, 6) internal displacement tranduceres, 7) sapphire window

an external air piston. The horizontal piston (4) applies the intermediate stress. This is also self-compensated with respect to the confining pressure inside the confining chamber (5). The piston can be controlled in displacement by the internal displacement transducers (6). One possible mode of operation is to adapt the pressure sent by its generator pressure to keep a zero displacement, i.e., a plane strain condition on the specimen, although all other controls in displacement or stress are possible. The surface of the specimen, opposed to the horizontal piston, is in contact with a thick, transparent sapphire window. This surface can be observed and photographs of the surface can be taken. For a symmetry of the contact, the surface on the side of the horizontal piston is in contact with a thin sapphire platen, to have the same boundaries conditions.

The minor stress is applied by the confining fluid on the two lateral surfaces of the specimen. The specimen is separated from the fluid by a silicone membrane. The membrane wraps around both the specimen and the four loading caps. In such a way, there is a direct contact between the specimen and the window. Note that in the axial direction, a special device of wedges between the specimen and the loading caps allows to have the same thickness of the specimen in the direction of intermediate stress. If a compression or extension of specimen in this direction occurs, the set of wedges automatically follows this change. This avoids an extrusion of the membrane during the deformation of the specimen.

A set of three pressure generators (syringe pumps with electronic control) is associated with the apparatus, to apply the loading in the three space directions. Further development is a control of the bottom and top pore pressure inside the specimen to impose a fluid flux. Note also that numerous electrical connectors in the cell allow to put several internal transducers, e.g., for acoustic emissions measurement.

The surface of the specimen is illuminated through the sapphire window by light from a set of LEDs focussed onto the sample surface through optical fibers; this provides a good and homogenous luminosity to take photographs. Photographs of the visible surface of the specimen were taken throughout the loading with a high resolution camera (providing images of 6080×4044 pixels). DIC analysis can thus be carried out on the the resultant images to yield displacement and strain fields over the observed surface; for details on the DIC procedure see [45]. However, it is important to note that for the DIC, it is necessary to have a pattern over the surface of the sample that varies such that different parts of the surface can be uniquely distinguished. Depending on the test specimen, this pattern can be natural (as with some sandstones for example) or artificial (in this case it was necessary to add this pattern as discussed later).

The size of the specimen is $50\,mm$ in the axial direction, $30\,mm$ in the direction of intermediate stress, and 25 or $50\,mm$ in the direction of minor stress, which corresponds to slenderness ratios (the ratio of the height to the width) of two and one, respectively. The capacity of the cell for confining pressure is $100\,MPa$, the axial piston can apply a force of $500\,kN$ and the horizontal piston a force of $700\,kN$, which correspond to a differential stress with respect to the confining pressure of $670\,MPa$ and $530\,MPa$, respectively, for a specimen with a slenderness ratio of two, and half that for a $50\,mm$ width specimen.

5.3 Selected results

We present here tests that have been performed on a clay rock specimen, the Callovo-Oxfordian argillite, from the underground research laboratory (URL) at Bure (Eastern France) at approximately $500\,m$ below the ground surface. It is a sedimentary rock composed of particles of calcite and quartz in a clay matrix [59]. The specimen has been prepared with a diamond wire saw and then polished with a fine sandpaper. The surface of the specimen in contact with the window of the triaxial apparatus has been painted with a thin layer of white ink and then a speckle of black ink, using an airbrush. The size of pixels in the photographs correspond to about $10\,\mu m$ on the sample surface. The tests have been performed with an initial isotropic loading to $2\,MPa$, $6\,MPa$ and $12\,MPa$, and then an axial loading in plane strain conditions with a displacement rate of $1.25\,\mu m.s^{-1}$, i.e., a strain rate of $2.5 \times 10^{-5}\,s^{-1}$.

Figure 5.2 shows the evolution of deviatoric stress $(\sigma_1 - \sigma_3)$ with respect to the axial strain (specimen shortening divided by its initial height) under different confining pressure. Each full curve is presented in 5.2a, 5.2b and 5.2c with the indication of the number of steps when the analyzed photographs were taken.

- Test with lateral stress $\sigma_3 = -2 \times 10^6\,Pa$: The beginning of the stress-strain curve (black curve on the figure 5.2) is slightly not linear with a first stress peak at 0.015 axial strain, followed by a strong stress drop. Then a slow stress increase is observed, followed by a second stress drop at 0.04 axial strain. After the stress is quite constant. The two stress drops are associated with major failure in the specimen. The crack that appeared during the second drop is conjugate to the first crack set, which appeared at the first drop. We focus later on strain localization around the first stress peak.

- Test with lateral stress $\sigma_3 = -6 \times 10^6\,Pa$: The beginning of the stress-strain curve (blue curve on the figure 5.2) is also slightly not linear. After the peak stress (at 0.0225 axial strain), there is a controlled softening and then a drop like in the previous test. This indicate a more ductile behaviour of the material than for lower confining pressure, however it is also a matter of the control of the test depending on the experimental parameters (pressure regulation, cell stiffness). The significant stress drop appears at 0.024 axial strain. Then the stress slowly increases.

- Test with lateral stress $\sigma_3 = -12 \times 10^6\,Pa$: From the begining, the stress-strain curve (red curve on the figure 5.2) indicates non linear relationship. The stress peak appears at 0.024 axial strain followed by three regimes of softening. The first regime starts at the peak stress and a strong softening is observed, followed by a quasi horizontal plateau. The second softening starts at the 0.035 axial strain. The third softening step appears at 0.039 axial strain and is followed by an horizontal plateau. Each softening is related with the new crack pattern. The fact that we observed softening in the several steps is a consequence of more ductile behaviour of the material and of the control of the compression after the stress peak.

Figures 5.3, 5.4 and 5.5 present the fields of a few axial displacement increments during the test. The results placed in the figure 5.3 correspond to the test with lateral stress

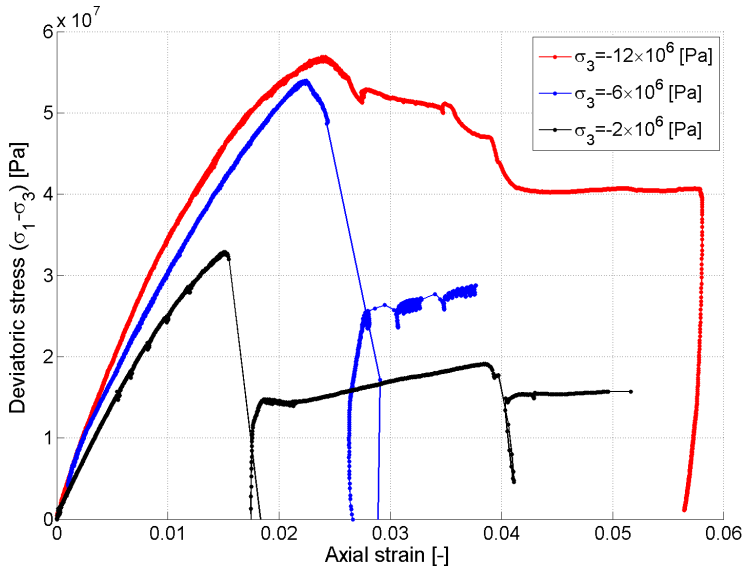

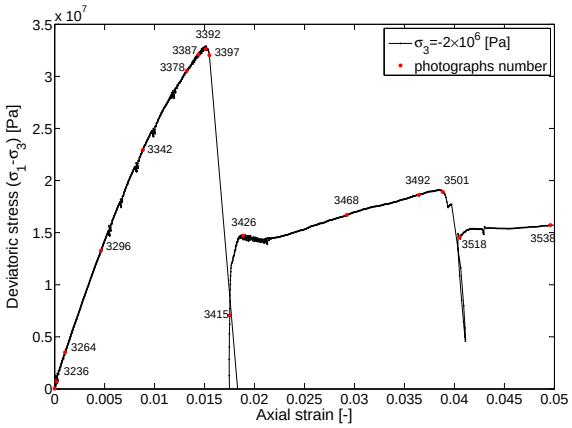

(a) $\sigma_3 = -2 \times 10^6\, Pa$

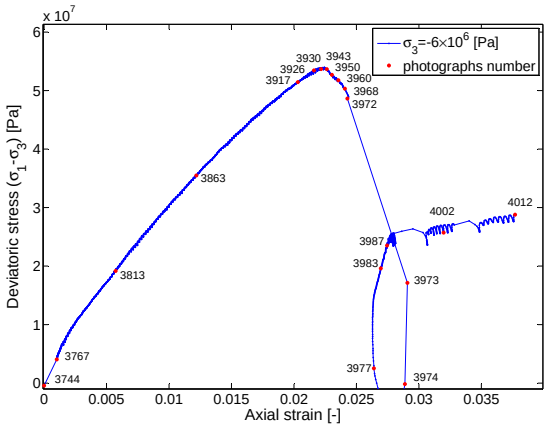

(b) $\sigma_3 = -6 \times 10^6\, Pa$

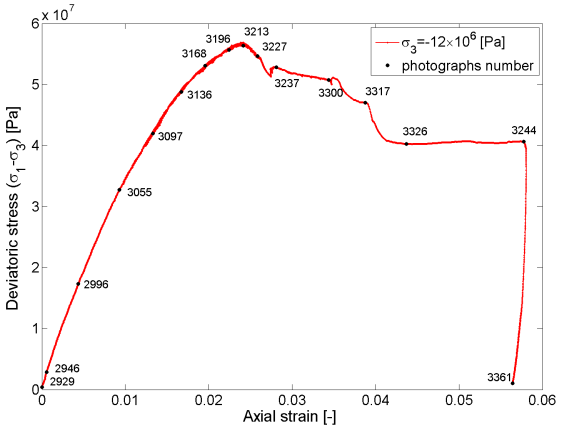

(c) $\sigma_3 = -12 \times 10^6\, Pa$

Figure 5.2: Evoultion of the deviatoric stress $(\sigma_1 - \sigma_3)$ *vs* axial strain with details of the full curves: a) $\sigma_3 = -2 \times 10^6\, Pa$, b) $\sigma_3 = -6 \times 10^6\, Pa$, c) $\sigma_3 = -12 \times 10^6\, Pa$. Numbers correspond to the photographs.

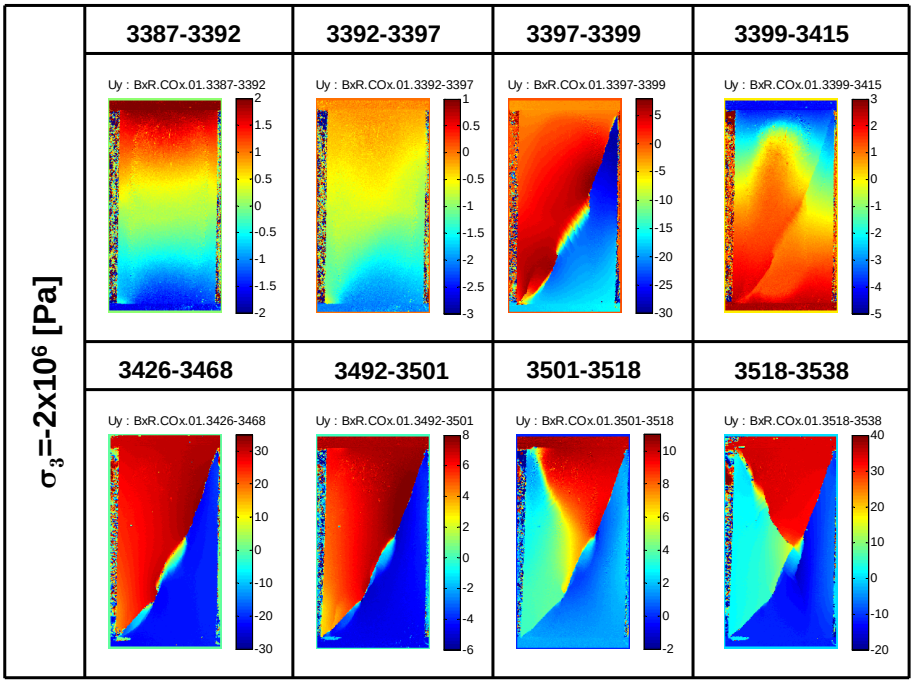

Figure 5.3: Fields of axial displacement increments for the test with lateral stresses $\sigma_3 = -2 \times 10^6\, Pa$. Couples of numbers on the top of each picture correspond to the photographs numbers used for DIC.

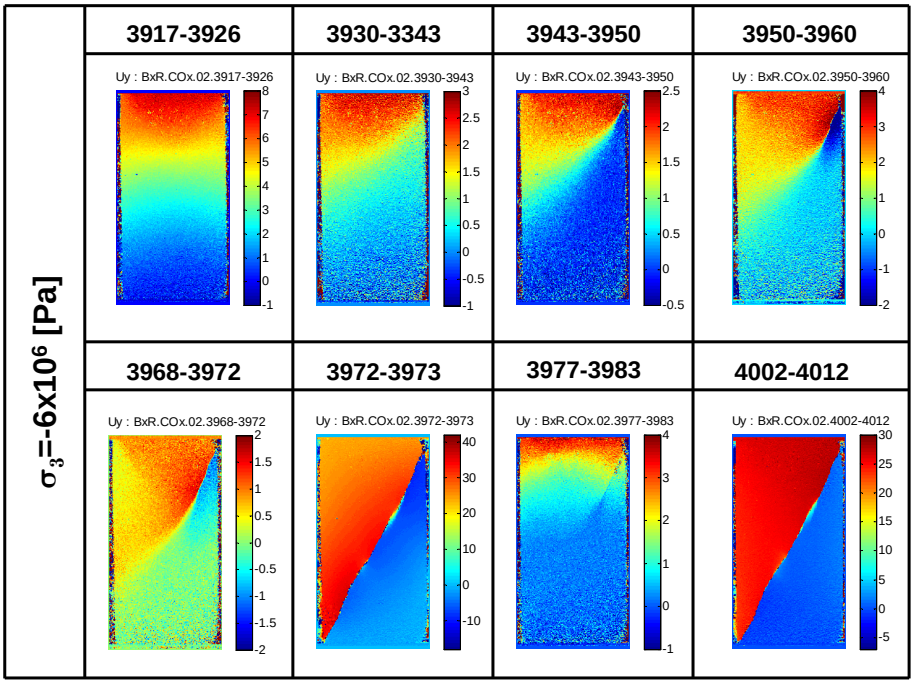

Figure 5.4: Fields of axial displacement increments for the test with lateral stresses $\sigma_3 = -6 \times 10^6\, Pa$. Couples of numbers on the top of each picture correspond to the photographs numbers used for DIC.

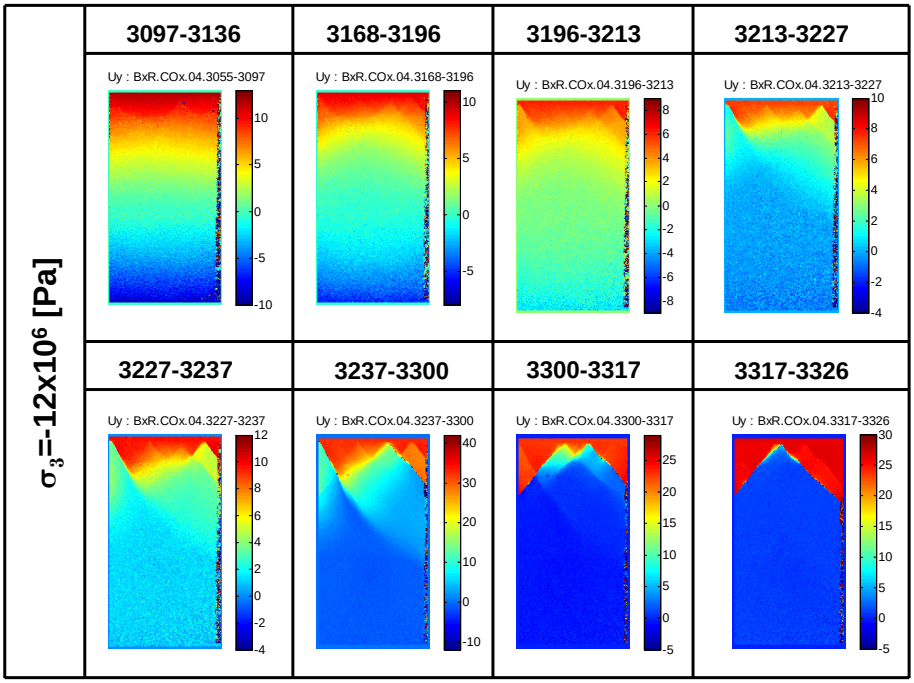

Figure 5.5: Fields of axial displacement increments for the test with lateral stresses $\sigma_3 = -12 \times 10^6\, Pa$. Couples of numbers on the top of each picture correspond to the photographs numbers used for DIC.

$\sigma_3 = -2 \times 10^6\, Pa$, in the figure 5.4 to the test with $\sigma_3 = -6 \times 10^6\, Pa$ and in the figure 5.5 to the test with $\sigma_3 = -12 \times 10^6\, Pa$. Couples of numbers on the top of each picture correspond to the photographs numbers used for DIC. The positions of the photographs are marked on the figures 5.2a, 5.2b and 5.2c.

- Test with lateral stress $\sigma_3 = -2 \times 10^6\, Pa$: The specimen deformation during increment $3387 - 3392$ seems quite homogeneous, and the displacement gradient is primarily vertical. The increment $3392 - 3397$ shows a loss of the homogeneity with gradient of displacement oriented along an inclined line from the bottom left to the top right of the specimen. This corresponds to an incipient strain localization arriving at the stress peak. During increment $3397 - 3399$, a strong discontinuity is observed in the displacement field, which corresponds to a crack initiation in the place of the previous shear band. During increment $3399 - 3415$ the major crack is stick due to unloading and is activated again during reloading as can be observed for increments $3492 - 3501$ and $3501 - 3518$. Another shear band appears during increment $3501 - 3518$ and in the following increment $(3518 - 3538)$, in the place of this shear band, we can observe a new crack oriented from the left top corner to the middle of the specimen. The strain fields of few last increments are shown in figure 5.6, where the volume strain and shear strain are plotted. During increment $3397 - 3399$ a major crack crosses the specimen from the bottom left to the top right. In central zone of the specimen, there is a set of small conjugate cracks (see zoom of the central part), showing two, quite close, preferential orientations. These small cracks are arranged inside an elongated zone parallel to the major crack. In most of cases, the major and small cracks initiation is associated with a dilatancy combined

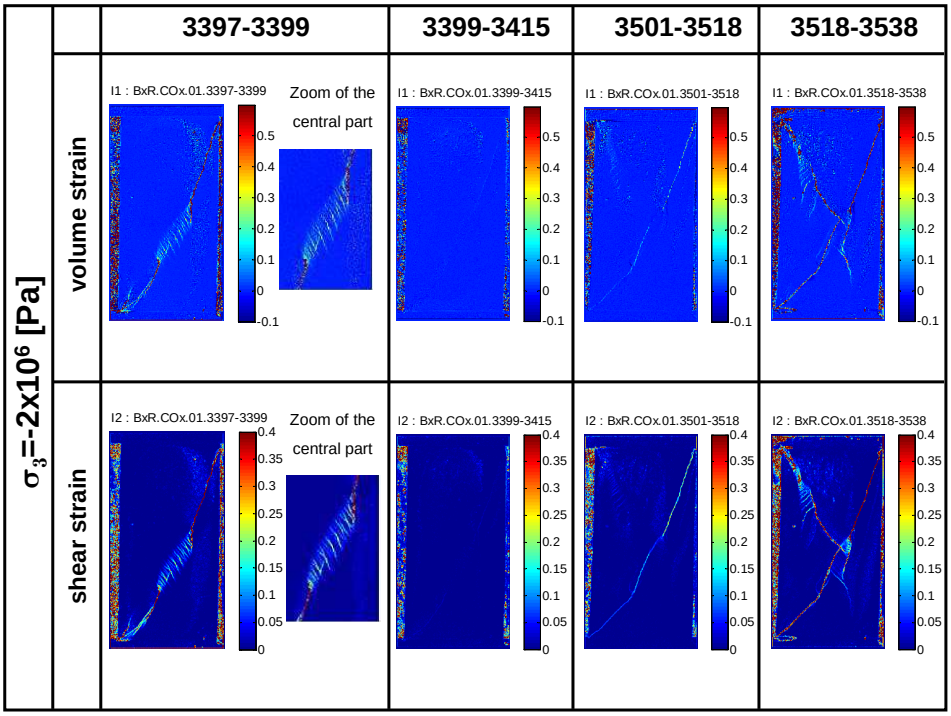

Figure 5.6: Fields of volume and shear strain during increments $3397-3399$, $3399-3415$, $3501-3518$ and $3518-3538$ for the test with lateral stress $\sigma_3 = -2 \times 10^6\, Pa$.

with the shear sliding. The sub-vertical zone of concentration of the volume strain and shear strain on the right of the specimen (increment $3397-3399$) is in fact an artefact of the measure due to change of luminosity of the surface of the specimen in contact with the window (probably a consequence of an initial small default of planarity of the specimen).

- Test with lateral stress $\sigma_3 = -6 \times 10^6\, Pa$: The specimen deformation during increment $3917-3926$ indicates quite homogeneous and primarily vertical gradient of axial displacement. During increment $3930-3934$ we can observe a loss of the homogeneity with gradient of displacement oriented along an inclined line from the top right of the specimen. This is related to an incipient strain localization arriving at the stress peak. During the increment $3943-3950$ a discontinuity in the displacement field is developing from the right top to bottom left of the specimen and we can observe the initiation of a small crack in the top right corner of the specimen. Contrary to the previous test ($\sigma_3 = -2 \times 10^6\, Pa$), where we could not observe such a development of the shear band, because we lost the control of the loading, in this case we can observe a crack propagation. The crack propagates througth the specimen from the increment $3950-3960$ to the increment $3968-3972$. During increment $3972-3973$, a strong discontinuity is observed in the displacement field, which is linked with the propagation of a major crack, across specimen, in the place of the previous shear band. A major crack crosses the specimen from the top right to the bottom left. Due to reloading the major crack is partialy activated and starts to slide from the right top corner of the specimen as can be observed during increment $3977-3983$. A strong discontinuity across specimen is again observed in the

displacement field during the increment $4002-4012$, which is linked with the sliding process along whole crack. The strain fields of the last few increments are shown in figure 5.7, where the volume strain and shear strain are plotted. One observe a shear strain concentration, which is in fact a crack sliding and a dilatancy inside crack (crack opening).

- Test with lateral stress $\sigma_3 = -12 \times 10^6\, Pa$: During increment $3097-3136$ the gradient of axial displacement is quite homogeneous and primarily vertical. A slight loss of the homogeneity is observed during increment $3168-3196$. During following increments ($3196-3213$, $3213-3227$ and $3227-3237$) we observe a development of the discontinuity in the displacement field and an appearance of the small cracks in the two top corners of the specimen. This corresponds to an incipient strain localization arriving at the stress peak and to the first regime of softening (see fig. 5.2c). During increment $3237-3300$ two cracks in the top right corner become stick and a new crack forms near them. During the last two presented increments ($3300-3317$ and $3317-3326$) several cracks become stick and several new cracks are formed. This is related with the second (increment $3300-3317$) and third (increment $3317-3326$) regime of softening. Each softening is related with the new crack pattern and we observe globally that a softening is associated with a reduction of the number of active cracks (cracks which are sliding at the given time). Contrary to the previous tests, where the major crack crosses through the specimen, in this case two major cracks, with a lower angle with respect to the horizontal direction, are located in the top part of the specimen. The strain fields of the few last increments are shown in figure 5.8, where the volume strain and shear strain are plotted.

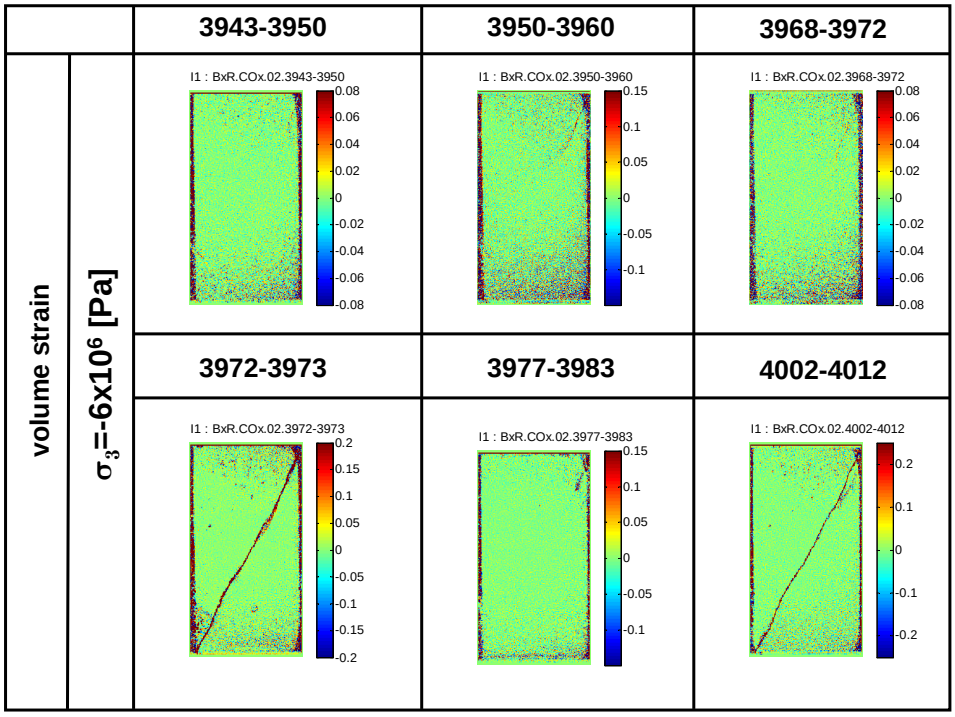

(a)

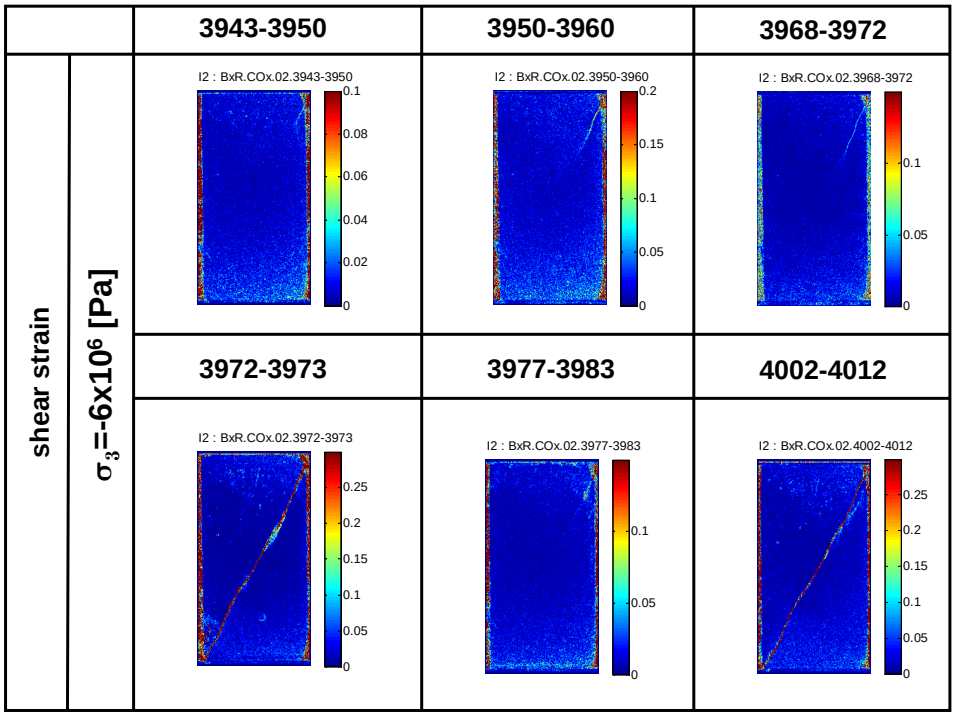

(b)

Figure 5.7: Fields of volume (a) and shear (b) strain during increments $3943-3950$, $3950-3960$, $3968-3972$, $3972-3973$, $3977-3983$ and $4002-4012$ for the test with lateral stress $\sigma_3 = -6 \times 10^6\, Pa$.

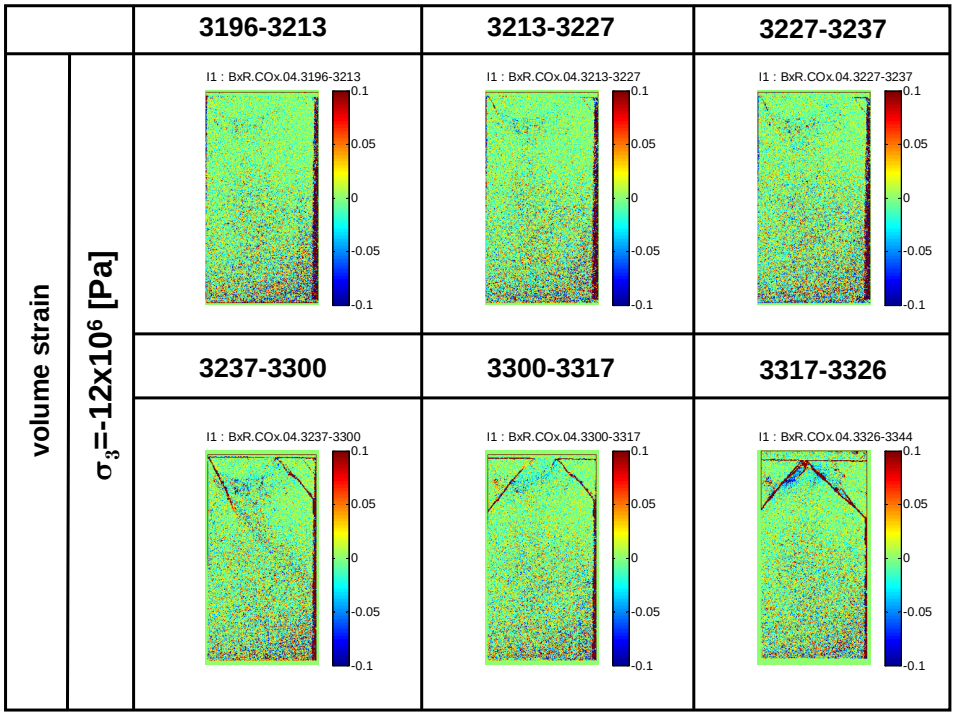

(a)

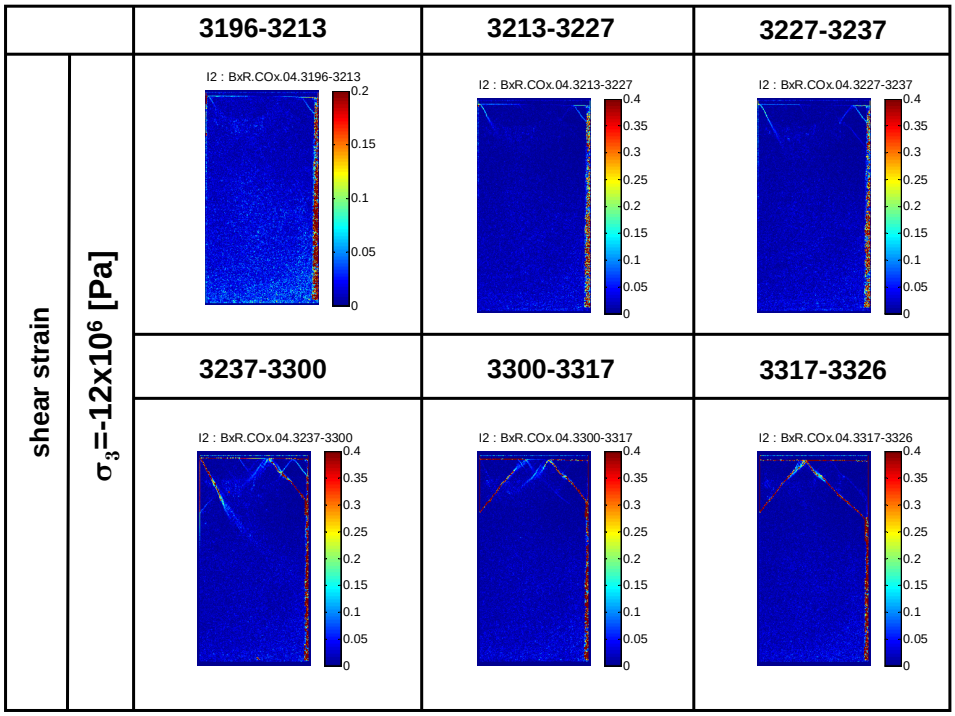

(b)

Figure 5.8: Fields of volume (a) and shear (b) strain during increments $3196-3213$, $3213-3227$, $3227-3237$, $3237-3300$, $3300-3317$ and $3317-3326$ for the test with lateral stress $\sigma_3 = -12 \times 10^6\, Pa$.

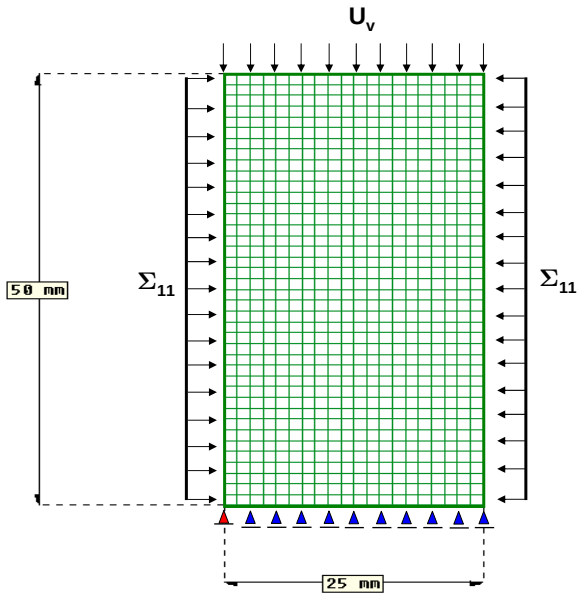

Figure 5.9: Geometry and boundary conditions of the sample.

$E\,[Pa]$	$\nu\,[-]$	$K_0\left[MPa.m^{\frac{1}{2}}\right]$	$K_0^1\left[MPa.m^{\frac{1}{2}}\right]$	$v_0\left[\frac{m}{s}\right]$	$\varepsilon\,[m]$
2×10^9	0.2	0.18	0.16	5×10^{-6}	10^{-3}
$d_0\,[-]$	$n\,[-]$	$\dot{e}\left[s^{-1}\right]$	$\mu_f\,[-]$	$\theta\,[^\circ]$	$-\Sigma_{11}\,[Pa]$
10^{-6}	3	10^{-6}	0.5	135	$2-12\times10^6$

Table 5.1: Parameters used in the simulation of biaxial compression tests at global macroscopic scale

5.4 Numerical *vs* experimental results

Using time dependent damage model including frictional sliding of the micro-cracks we performed the simulations at the laboratory scale which corresponds to the experimental tests presented in this chapter. This choice has been done to avoid mesh-dependency and difficulties related to non-uniqueness of solution, which were observed in the case of quasi-brittle damage model. The present model is regularized by time dependency.

In simulations, the geometry and boundary conditions are based on experimental tests and in 2D representation the height of the specimen is $50mm$ and the width is $25\,mm$. The axial loading is controlled in displacement by keeping a constant displacement rate. The constant stress is applied on two lateral sides of the specimen. The geometry and boundary conditions are presented in the figure 5.9. After parametric studies, the convenient choice of the model parameters with respect to experimental results is listed in the table 5.1.

5.4.1 Friction angle and friction coefficient

Using a stress path method we can compute the friction angle from the following relation ([48]):

$$sin\phi = tg\beta \tag{5.1}$$

where ϕ is a friction angle and β is an angle drawn by the stess path ($\frac{\sigma_1+\sigma_3}{2}$ vs $\frac{\sigma_1-\sigma_3}{2}$).

Next, friction coefficient μ_f^* can be obtained using the relation:

$$\mu_f^* = tg\phi \tag{5.2}$$

According to the experimental results, friction angle and friction coefficient of Callovo-Oxfordian argillite are:

- Chiarelli ([22]): obtained friction angles are $\phi = 27°, 26.3°, 35.5°$ and corresponding friction coefficients are $\mu_f^* = 0.51, 0.49, 0.71$ (see figure 5.10).
- our experiment: obtained friction angle is $\phi = 34.7°$ and corresponding friction coefficient is $\mu_f^* = 0.69$ (see figure 5.10). A possible explanation of such high friction coefficient is that our experiments are not in axisymmertic conditions (as in [22]) but in plane strain conditions.

According to the time-dependent damage model, for microscopic friction coefficient $\mu_f = 0.5$ the resulting macroscopic friction angle is $\phi = 24°$ and corresponding macroscopic friction coefficient is $\mu_f^* = 0.45$. The microscopic friction coefficient $\mu_f = 0.5$ is the maximum value available in our actual model, which is not the theoretical limit of the model. (see figure 5.10).

5.4.2 Experimental and numerical stress-strain response

Using time-dependent damage model and parameters listed in the table 5.1 we obtain the response of the material for three different confining pressures ($\Sigma_{lateral} = -2\times10^6\,Pa, -6\times10^6\,Pa, -12\times10^6\,Pa$). Obtained stress-strain curves are plotted together with corresponding experimental results on the figure 5.11.

In both cases, experimental and numerical, we obtained the increase of the strength of the material together with lateral stress. Obviously, from the modelling point of view, this is a result of including frictional phenomenon in the model. For non frictional material such a behaviour is not possible to observe. In that case the stress-strain curves would overlap. We can also observe similar ranges in the values of stress-strain relations.

We observed that the initial modulus of numerical curves is lower than the experimental one, as a consequence of the elastic parameters chosen at the microscopic scale (which is not the theoretical limit of the model) .

The experimental response is not linear, and this is not reproduced by the actual model, because we assumed the Coulomb friction law, which results into linear global response.

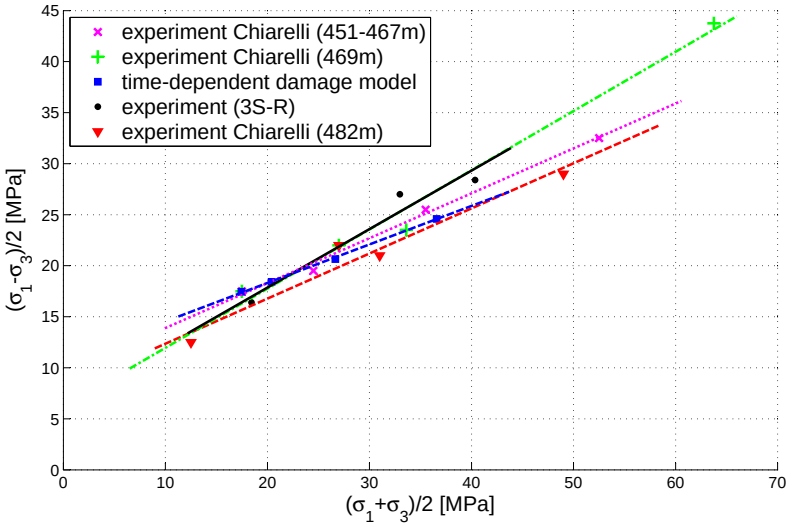

Figure 5.10: Stress paths ($\frac{\sigma_1+\sigma_3}{2}$ *vs* $\frac{\sigma_1-\sigma_3}{2}$): Chiarelli ([22]), our experiment and our time-dependent damage model.

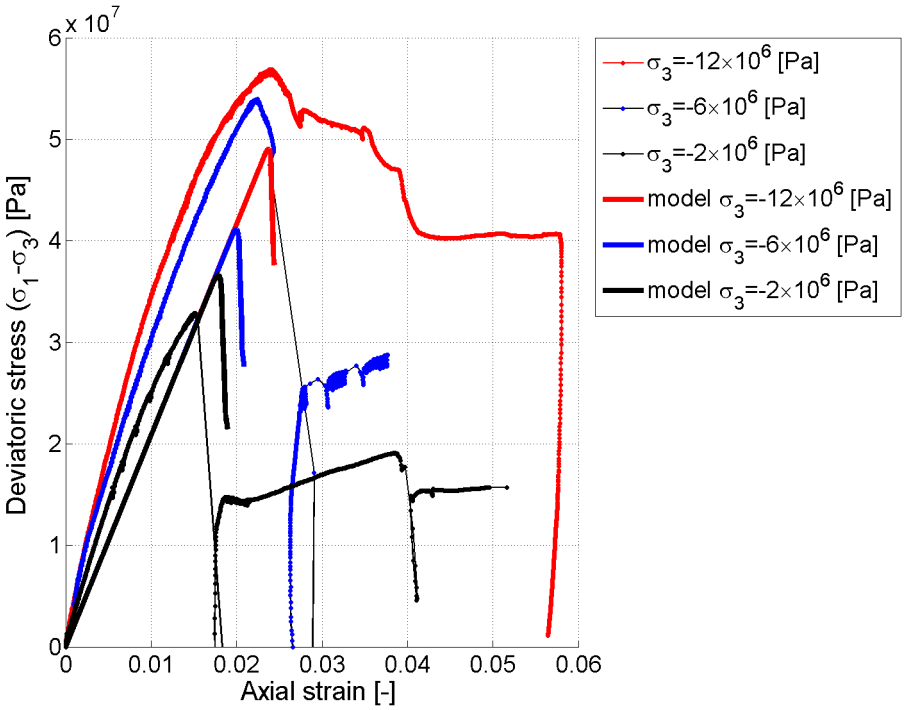

Figure 5.11: Experimental and numerical stress-strain curves in terms of deviatoric stress $(\sigma_1 - \sigma_3)$ and axial strain.

5.4.3 Axial displacement and shear strain fields

Figure 5.12 presents experimental and numerical results obtained under biaxial compression with lateral stress $\Sigma_{lateral} = -2 \times 10^6\, Pa$. Experimental stress-strain response with a few fields of the increment of axial displacement and shear strain before and after the stress peak are shown in figure 5.12a. Couples of numbers on the top of each picture correspond to the photographs numbers used for DIC. The positions of the photographs are marked on the stress-strain curves (see figure 5.12a).

Figure 5.12b presents the numerical stress-strain relation with a few fields of axial displacement and shear strain before and after the stress peak. The points underlined on the stress-strain curve (see figure 5.12b) correspond to the plotted fields.

In both cases, in experiment and numerical simulation, the softening is due to the crack propagation, which can be observed also in the evolution of the axial displacement. For the first analysed step, the displacement fields (experimental and numerical) seem quite homogeneous, while for the following steps, the discontinuity in the displacement fields are observed starting from the bottom left corner of the specimen. The orientation of the major crack in the experiment is influenced by the boundary conditions and links the opposite corners of the specimen.

Figure 5.13 presents the orientation of shear bands in the case of numerical simulations and experimental tests under biaxial comression with different lateral stresses ($\Sigma_{lateral} = -2 \times 10^6\, Pa$, $-6 \times 10^6\, Pa$, $-12 \times 10^6\, Pa$). The orientation of the shear band in the case of numerical simulations, for all lateral stresses, is always oriented at around 43°. In the experimental case, the lateral stress changes a micromechanism, so the shear band is inclined in different way according to the different lateral stress. For low lateral stresses the shear band is inclined at around 60° and links the opposite corners of the specimen. For high lateral stress, the shear band is inclided at 45° as obtained in the numerical simulations.

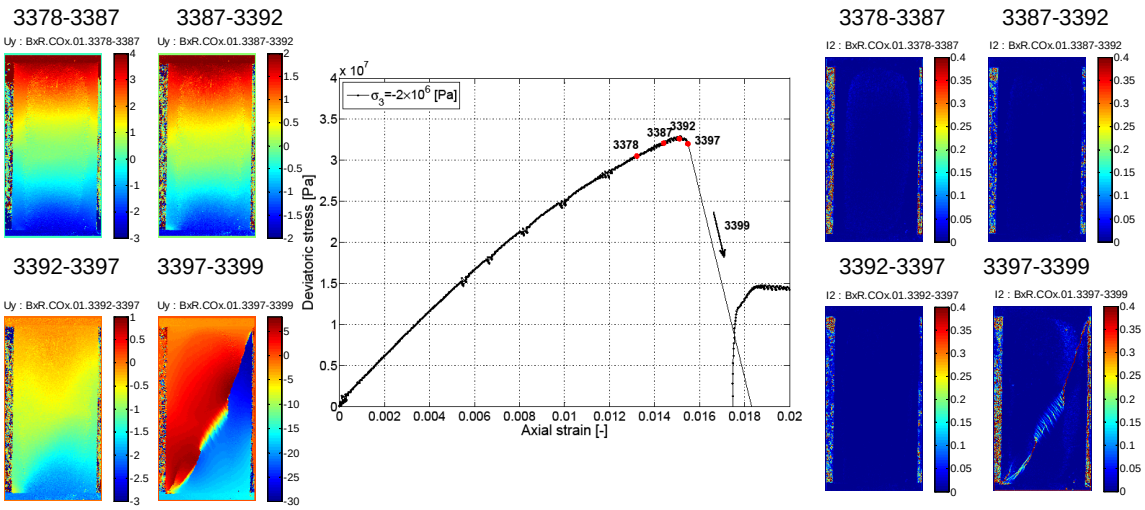

(a) Experimental stress-strain curve with a few fields of the increment of axial displacement (on the left) and shear strain (on the right).

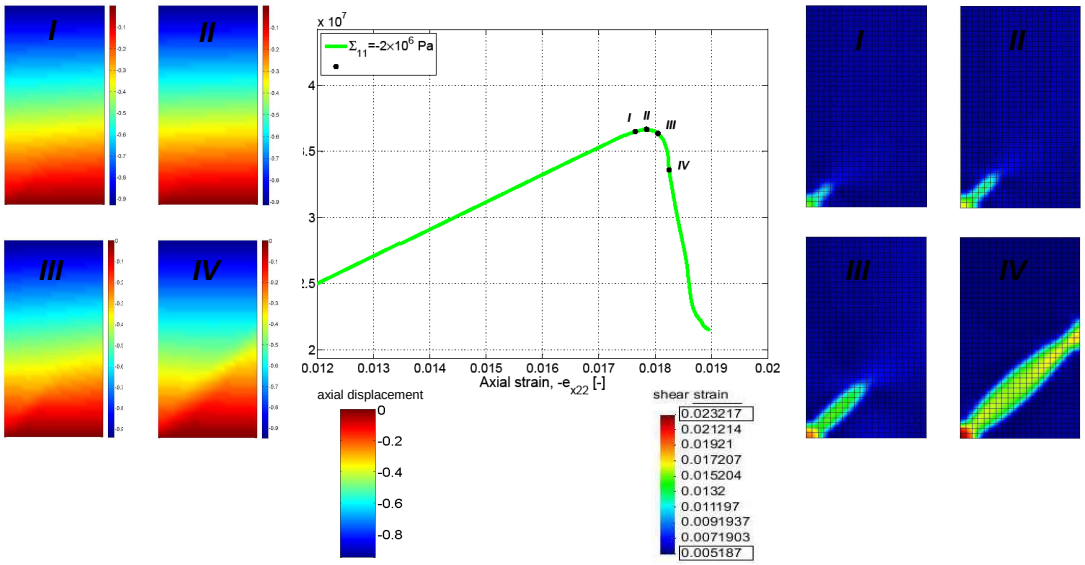

(b) Numerical stress-strain curve with a few fields of axial displacement (on the left) and shear strain (on the right).

Figure 5.12: Experimental and numerical stress-strain relations under biaxial compression with lateral stress $\Sigma_{lateral} = -2 \times 10^6\, Pa$.

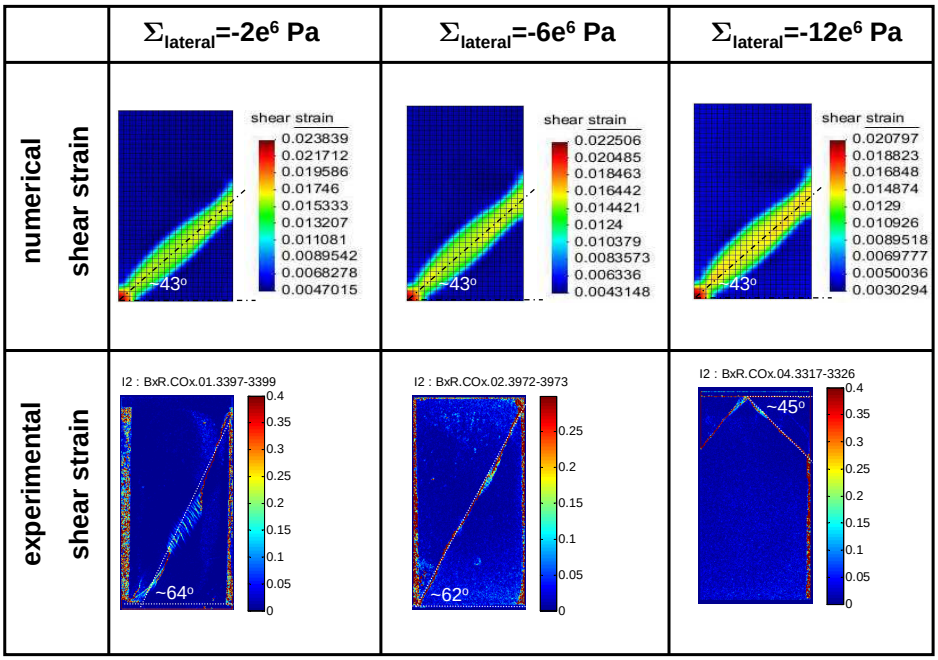

Figure 5.13: Orientation of the numerical and experimental shear bands under biaxial compression with lateral stress $\Sigma_{lateral} = -2 \times 10^6\, Pa$, $-6 \times 10^6\, Pa$, $-12 \times 10^6\, Pa$.

5.5 Conclusions

The ability to characterize localized failure in rocks and, in particular, to follow the strain field evolution inside rock specimens during loading using a new true-triaxial apparatus, has been demonstrated. Displacement and strain field results from a plane-strain loading test on a clay rock, the Callovo-Oxfordian argillite, have been presented, which reveal a complex pattern of localization at failure. Furthermore the evolution of the deformation has been followed, using DIC, from an initially homogeneous deformation through the development of a shear band and subsequent initiation of a set of cracks resulting in major faults and small conjugate cracks arranged inside a band parallel to the major fault. The effect of lateral stress on the processes of failure and localization was underlined.

In the final part of this chapter the numerical model was compared with experimental results. Presented time-dependent damage model is capable to reproduce the mean stress dependency. This is a result of including frictional phenomenon in the model. In order to fit better experimental results, the elastic parameters such as Young's modulus and Poisson ratio should be modified at the microscale. A modification concerns also the friction coefficient of the material, which experimentally obtained is higher than the one used in the numerical simulations. These aspects are not related to theoretical limits of the model but with the choices made at the microscopic scale.

Chapter 6

General conclusions and perspectives

The objective of this study was to develop a two-scale model for micro-cracks capable to take into account not only the propagation of the micro-cracks but also frictional sliding of these micro-cracks. Presented micro-mechanical damage models were obtained by using an upscaling procedure, which combines a periodic homogenization based on asymptotic development and micro-fracture energy analysis. Damage evolution laws are completely deduced from microstructural analysis by homogenization, without phenomological assumptions. The microscopic energy analysis was performed on a periodicity cell of finite size which leads, through homogenization, to a macroscopic evolution equation for damage. In this equation the normalized micro-crack length appears as a damage variable d, and the cell size ε as a material length parameter. Starting from micro-fracture criteria based on fracture resistance curve and power law for subcritical growth, we deduced quasi-brittle and, respectively, time-dependent damage models. The resulting damage models incorporate stiffness degradation, material softening, size effects, unilaterality, induced anisotropy, irreversible strain after unloading and different fracture behaviour depending on frictional properties.

We succeeded to impose the mean stress dependency in the models. This is obviously a result of adding a friction phenomenon. Additionaly, thanks to this fact, in the case of quasi-brittle model, the stress-strain relation contains stick during the first phase of loading, stick during unloading, back sliding and irreversible strain. All these phenomenon are absent in the case of the models with frictionless contact on the crack faces. Abandoning frictional mechanisms in the models we are loosing many interesting informations about micro-structure which may lead to less efficient engineering design.

From the numerical point of view, we had to deal with several difficulties at some points of the implementation. In the case of time independent damage model (quasi-brittle damage model) the linear resistance curve [13] led to snap-back behaviour in overall response. We regularized it by adding to the formulation of the linear R-curve a term consisting in power function of damage. At the level of macro-structure, the deduced model dealt with a mesh-dependency and non-physical representation of the localization phenomenon. Such behaviour is linked to the non-uniqueness of the solution of the boundary-value problems for the damage model involving softening effects. In order to avoid these issues, the model was regularized by time dependency resulting in time-dependent damage model

with subcritical criterion for crack propagation. Using this model we obtained structural response of the material and failure by strain localization.

Summaries were given at the end of each chapter, however we recall now the main conclusions. In Chapter 2 we presented the theoretical aspects concerning asymptotic homogenization and damage evolution law. Due to frictional mechanisms, the numerical implementation of the micro-structure led to different homogenized coefficients and different coefficients related with the dissipation of the energy during frictional sliding. These different coefficients depend on the sense of sliding, on friction coefficients and on the orientation of the crack. Finally, we determined the constitutive relations for each possible state of the crack, i.e. stick, sliding and backsliding. These states are controlled by frictional law and by loading path.

Numerical results for uniaxial and biaxial compression tests in local frame for quasi-brittle damage model have been presented in Chapter 3. In this model, as the crack grows, the resistance of the material increases until a maximum value is achieved. We considered a special fracture criterion for a crack in the elastic material to express the effect of the process zone. The size of FPZ (fracture process zone) enters into the damage equation through the variable c_f. In the presented model, linear resistance curve led to snap-back behaviour in overall response. In order to avoid this phenomenon we looked for an additional term in the resistance curve. We studied the influence of this term in the R-curve and we compared them to the results obtained by using the linear resistance curve like in [13]. We observed that this change allowed us to avoid a snap-back and control the post-peak phase with light drift of material properties. In the same time the influence of the friction was studied. The presence of the friction causes the increase of the material strength and changes the crack propagation characteristics. For non frictional material the crack propagation is rapid while for the frictional material the process of the propagation slows down.

We studied also the influence of the lateral stress on the macroscopic response, which grows together with it, confirming the presence of frictional phenomenon. The increment of damage variable *vs* applied deformation decreases due to growth of lateral stress. The post-peak regime indicates more brittle behaviour for the lower values of lateral stress while for higher values it is more controlled.

Thanks to the additional term in the resistance curve, the loading-unloading cycle was possible to perform. We could study the behaviour related to frictional mechanisms like backsliding and stick case during unloading. All these mechanisms are controlled by Coulomb friction law.

We studied the evolution of the components of the friction law ($\mathbb{N}$ and $\mathbb{T}$) and their influence on the macroscopic behaviour. In the first phase of unloading the crack is locked due to friction, and this phase extends together with increase of friction coefficient and lateral stress. After this phase, the crack is unlocked and starts to slide in reverse sense, and consequently the backsliding regime is reduced.

Concerning the global computations, at the level of macro-structure, the deduced model needs regularization (like adding gradient terms), in order to avoid mesh-dependency and non-physical representation of the localization phenomenon. Such pathological behaviour is linked to the non-uniqueness of the solution of the boundary-value problems for the

damage model involving softening effects. In the next chapter a regularized two-scale model was proposed.

Chapter 4 was dedicated to time-dependent damage model with subcritical criterion of propagation. Numerical results for uniaxial and biaxial compression tests in both, local and global frame, have been presented. In the local frame we studied the influence of the parameters involved in the model, such as velocity v_0, strain rate $\dot{e}$, subcritical growth coefficient n, internal length ε, under different compressive loadings and different friction coefficients. We did not notice any significant influences of those parameters on the frictional properties. The strength of the material grows together with n, strain rate and ε and decreases with v_0. We found different structural responses depending on frictional properties and applied lateral stresses. In particular, the strength of material increases together with them, and this was observed in both local and global level.

The effects of friction coefficient and lateral stresses can be seen not only in terms of peak stress level, but also in terms of post-peak regime behaviour. The post-peak regime evolves more rapidly for the material with higher friction coefficient and under higher lateral stress. At the global level, experimentally known behaviour, like the localization of damage has been reproduced. After peak-stress, the damage zone evolves faster for the material with higher friction and under higher lateral stress. In pre-peak regime the development of damage zone progresses slower in case of higher friction coefficient. The presence of the friction acts in opposite direction to the propagation of the damage.

In terms of time, the failure of nonfrictional material appears as first, while for the material with highest value of friction coeffient, as last. The same relation is observed while increasing the lateral stress.

We studied the variations of the frictional properties passing from microscopic scale to macroscopic scale. Values of friction coefficients, obtained at the macroscopic scale, are slightly reduced with respect to assumed one (friction coefficient at the microscopic scale).

Finally, the effect of different meshes was studied. The response of the material for each considered mesh type tends to the same results, verifying the mesh independency. This is a consequence of regularization by time-dependency. Numerical simulations presented in Chapter 4 showed the ability of the developed model to reproduce time dependent damage response.

In Chapter 5 we presented the experimental results obtained in a new true-triaxial apparatus that allows observation of the rock specimens under loading. Displacement and strain fields results, using DIC (Digital Image Correlation) , from a plane-strain loading test on a Callovo-Oxfordian argillite have been presented, which reveal a complex pattern of localization at failure. Futhermore the evolution of deformation has been followed from an initially homogenous deformation through the development of a shear band and subsequent of a set cracks resulting in major faults and small conjugate cracks arranged inside a band parallel to the major fault. The experiments focused on the effect of confinement on the processes of failure, localization and stress-strain relations. The behaviour of the material indicates more ductile characterizations during increase of the lateral stress. Additionally, in this chapter, the experimental observations were compared with numerical results obtained using time-dependent damage model. All numerical choices, like for example geometry and boundary condition, have an origin in experimental studies.

Presented time-dependent damage model is capable to reproduce the mean stress dependency and failure by strain localization. However, to fit better experimental results, some parameters which were set at microscale should be modified. This concerns the elastic parameters such as Young's modulus and Poisson ratio, and friction coefficient.

In order to complete this work, we propose some short-term perspectives:

- consideration of more orientations of the micro-crack, which may lead to equivalent rotating micro-cracks in the damage models.
- consideration of curvilinear and partially closed micro-crack, which could lead to dilatancy and volume change.
- concerning the global computations in the case of quasi-brittle damage model, the deduced model can be regularized by adding gradient terms, in order to avoid mesh-dependency and non-physical representation of the localization phenomenon.
- in the case of time-dependent damage model we propose to introduce elastic unloading, which may lead to irreversible strain and better representation of the phenomenon experimentally observed (like for instance more ductile behaviour with higher confining pressure).
- application of the model to the engineering problems such as tunneling or excavations.

Chapter 7

Résumé français / French Summary

Contents

7.1 Motivation

La compréhension ainsi qu'une modélisation précise du comportement inélastique et de la rupture des géomatériaux sont nécessaires dans de nombreuses applications d'ingénierie. Toutefois, les géomatériaux sont difficiles à modéliser en raison de leurs microstructures complexes et de leurs hétérogénéités à une échelle donnée. Cette hétérogénéité

a une influence significative sur leur comportement observé à l'échelle macroscopique. Divers phénomènes qui se produisent au niveau macroscopique, comme la réponse inélastique non linéaire, la dégradation de la rigidité et l'anisotropie induite, l'adoucissement du comportement des matériaux, le comportement hystérétique et la deformation irreversibile après le déchargement, proviennent de la physique et de la mécanique de la microstructure sous-jacente. A l'échelle microscopique, les géomatériaux contiennent diverses sources d'hétérogénéités telles que des fissures, des pores, des inclusions ou des interfaces inter-granulaires. Deux mécanismes physiques de base peuvent généralement être identifiés: propagation des microfissures et glissement avec frottement entre les lèvres des microfissures. La détermination des caractéristiques macroscopiques globales des milieux hétérogènes est un problème essentiel dans les applications d'ingénierie. L'analyse de la relation entre les phénomènes microstructuraux et le comportement macroscopique permet de prédire le comportement des matériaux existants et d'avoir une conception plus efficace.

7.2 Modèle d'endommagement deux-échelle par homogénéisation asymptotique

Dans cette thèse, nous considérons une procédure pour obtenir des modèles d'endommagement micromécaniques pour les solides, dans lequel les lois d'évolution d'endommagement sont entièrement déduites d'une analyse microstructurale sans hypothèses phénoménologiques supplémentaires ou idéalisation du modèle. Notre formulation reste dans le cadre de la formulation continue classique, mais introduit un paramètre de longueur interne par la loi d'évolution d'endommagement, en raison de l'équilibre énergétique à l'échelle microscopique et du critère de Griffith sur la propagation de microfissures. L'analyse énergétique est faite sur une cellule de périodicité de dimension finie, contenant une seule microfissure, pour des trajectoires arbitraires, régulières de la microfissure, a priori connues. Les modèles micromécaniques d'endommagement ont été obtenus en utilisant une procédure de mise à l'échelle, qui combine une homogénéisation périodique basée sur des développements asymptotiques et sur l'analyse énergétique de la microfissure. Cette procédure a été initialement développée pour les milieux fragiles, par Dascalu et ses collaborateurs ([25, 29]) avec une loi d'endommagement indépendante du temps. Une extension de ce modèle peut être trouvée dans [31], où une microfissure de type "wing" a été utilisée.

D'autres développements se sont poursuivis dans deux directions: les modèles d'endommagement indépendant du temps et les modèles dépendantes du temps. L'extension du modèle d'endommagement indépendant du temps est donnée par la loi d'endommagement quasi-fragile dans l'espace à deux et trois dimensions ([27, 28]). La deuxième direction de développement est liée aux modèles d'endommagement dépendants du temps avec un critère sous-critique pour décrivant la propagation de microfissures. Dans la première étape, il a été considéré que la propagation se produit dans la direction fixe donnée par l'orientation de la fissure ([26, 27, 31]). Dans ce cas, des calculs macroscopiques locaux et globaux ont été effectués. La deuxième étape concerne le développement d'un modèle avec microfissure équivalente tournante. Ce complexe modèle d'endommagement dépendant du temps est capable de prendre en compte une propagation de la fissure et de son changement d'orientation. Ce modèle a été proposé par François et Dascalu ([36]),

mais seulement au niveau local macroscopique. La mise en œuvre de ce modèle à l'échelle macroscopique global peut être trouvée dans [31].

Tous ces modèles présentés ci-dessus, sont formulés à l'aide de conditions générales aux bords de la microfissure, en tenant compte de l'ouverture ou de la fermeture de la fissure avec contact sans frottement. Cette étude vise à étendre ces modèles, en considérant le cas d'une microfissure frottante. Nous considérons un critère de frottement de Coulomb sur les lèvres de la microfissure. Avec les phénomènes de frottement, le modèle sera étendu pour la loi d'endommagement quasi-fragile, ce qui conduit à la propagation progressive de microfissures, qui est plus en adéquation avec le comportement à la rupture de la roche.

De plus, de nouveau modèle d'endommagement seront introduites, i.e. le modèle d'endommagement dépendant du temps pour les microfissures avec frottement, permettant de surmonter certaines limitations qui se produisent avec le modèle indépendant du temps (snap-back macroscopique). L'évolution de la longueur de la microfissure est décrite par un critère sous-critique contrôlé par la loi de Charles ([21]).

Pour les modèles d'endommagement indépendant et dépendant du temps, l'analyse énergétique est faite sur une cellule périodique de dimension finie, contenant une seule microfissure avec frottement. Une analyse appropriée de l'énergie micro-mécanique est proposé pour formuler une loi d'évolution d'endommagement qui intègre dégradation de la rigidité, l'adoucissement du comportement des matériaux, les effets de taille, unilatéralité, comportement à la rupture différent en contact avec et sans frottement.

Les coefficients différents dans la loi homogénéisée (relation de contrainte-déformation) sont obtenus par des calculs par éléments finis sur la cellule unitaire et des méthodes d'interpolation spécifiques. Ces coefficents dépendent de l'orientation de la fissure, du coefficient de frottement, du sens de glissement et en conséquence ils mènent à une anisotropie induite et à l'hétérogénéité dans la réponse globale du matériau.

En raison de phénomènes de frottement, les différents états de la fissure sont considérés (adhérence, glissement et glissement inverse). Cela conduit à différentes formulations du comportement correspondant à différents états de la fissure. Le comportement macroscopique comprend réponse complexe de contrainte-déformation et déformation irréversible après le déchargement. Ce comportement particulier ne peut pas être observé dans le cas du contact sans frottement.

Les problèmes géomécaniques, dans les deux modèles, sont résolus pour une direction fixe de propagation, déterminée par l'orientation de la fissure. Deux orientations de la fissure sont prises en compte.

7.3 Modèles d'endommagement continus/modèles de frottement

La nucléation et la propagation de microfissures sont des mécanismes d'endommagement typiques dans les solides fragiles et quasi-fragiles comme les roches, le béton, la céramique, le fer et quelques classes de matériaux composites. En raison de leur microstructure

hétérogène et phénomènes dissipatifs tels que la propagation de microfissures et le glissement sur les lèvres de la microfissure, le comportement macroscopique comprend une réponse contrainte-déformation inélastique non linéaire, la dégradation des propriétés élastiques et l'anisotropie induite, le comportement hystérétique, les effets unilatéraux liés à la fermeture des fissures, et la déformation irréversible après le déchargement en raison de phénomènes de frottement.

Depuis la première introduction du concept d'endommagement scalaire par Kachanov (1958, [53]) et Rabotnov (1963, [76]) pour le fluage des métaux, la mécanique des milieux continus est devenue un nouveau domaine de recherche actif. De nombreuses recherches ont adopté cette théorie à leurs problèmes. Du point de vue de la procédure de construction, on peut classer les modèles d'endommagement dans: modèles macroscopiques (généralement basée sur des observations phénoménologiques) et approches micromécaniques (à deux échelle et à modèles micromécaniques).

Dans l'approche phénoménologique, une formulation du modèle peut être soit basée sur les mécanismes motivés par la micromécanique, ou alors le tenseur d'endommagement peut être considérés comme une variable interne affectant la réponse contrainte-déformation sans fond micromécanique. Les modèles phénoménologiques utilisent des variables internes pour représenter la densité et l'orientation des microfissures, par exemple des variables scalaires en cas d'endommagement isotrope, ou des tenseurs du deuxième et quatrième rang pour décrire l'endommagement anisotrope. Les équations constitutives sont généralement dériveés par la notion de contrainte effective ou par la formulation d'un potentiel d'énergie libre. La loi évolution de l'endommagement est déterminée selon les principes de la thermodynamique irréversible. Le principal avantage de ces modèles est qu'ils fournissent des équations macroscopiques constitutives qui peuvent être facilement mises en œuvre et appliquées aux analyses techniques. La principale faiblesse est que certains des concepts et paramètres impliqués dans ces modèles ne sont pas clairement liées aux mécanismes physiques. Parmi les différents modèles trouvés dans la littérature, nous allons parler de quelques-uns, qui traitent des microfissures avec frottement, comme par exemple Halm et Dragon ([46]), Dragon et al.([33]), Lawn et Marshall ([56]), Bargellini et al. ([11]) et Poon et al. ([73]).

Au cours des dernières années, des efforts considérables ont été faits pour établir un lien entre les phénomènes de microfissurations structurelles et les comportements macroscopiques correspondants. Beaucoup de chercheurs se sont concentrés sur le développement de modèles macroscopiques déduits d'une analyse micromécanique d'un milieu fissuré par des procédures d'homogénéisation. Avec cette approche, les arguments micromécaniques, peuvent conduire à une meilleure compréhension des phénomènes observés au niveau macroscopique dans les expériences. Les modèles homogénéisés peuvent être divisés en modèles micromécaniques et modèles à deux échelles.

Diverses études micromécaniques ont été proposées afin de modéliser l'évolution de microfissures avec frottement comme par exemple Kachanov ([54]). Cette approche a été plus développée pour des microfissures sans interactions, par des auteurs, tels que Nemat-Nasser et Obata ([68]), Gambarotta et Lagomarsino ([38]). Pour les microfissures avec interactions et microfissures "penny-shaped" qui se propagent, dans le cadre de la méthode auto-cohérente nous pouvons nous référer à Lee et Ju ([57]). En outre, ces modèles sont basés sur une formulation en contraintes et sont limités à des chemins de contraintes particuliers.

Une approche intéressante est proposée par Andrieux et al. ([5]). Une hypothèse importante faite par ces auteurs : pour un problème local une fissure est rectiligne et petite par rapport aux dimensions de la cellule de base. Dans ce cas, une approximation de milieu infini est acceptable.

Une analyse micromécanique a trois dimensions formulée en déformation (basé sur Andrieux et al. ([5])) d'endommagement fragile intégrant la microfissure de fermeture et frottement peut être trouvée dans les travaux de Pensée et al. ([72]). Ce modèle montre une capacité a prédire plusieurs aspects importants de l'endommagement anisotrope fragile et du comportement hystérétique en raison de phénomènes de frottement.

Une modélisation micromécanique des fissures fermées avec frottement comme des inhomogénéités ellipsoïdales est proposé par Barthélémy et al. ([12]). Trois lois de frottement de l'interface ont été prises en compte dans le présent document: von Mises, Coulomb et Drucker-Prager. Le comportement macroscopique d'un tel milieu fissuré a été obtenu par la technique d'homogénéisation basé sur les résultats Eshelby.

Le comportement des fissures fermées avec frottement est étudié également dans Zhu et al. ([84]) dans le cadre d'homogénéisation basée sur sur les solutions d'Eshelby. Ils considèrent une famille de microfissures fermés avec frottement obéissant à la loi de Coulomb classique. Dans cet article, trois schémas d'homogénéisation sont utilisés: le "dilute scheme", le schéma de Mori-Tanaka (MT) et l'estimation de Ponte Castaneda et Willis (PCW). La loi d'évolution d'endommagement et glissement avec frottement a été déterminé dans le cadre de la thermodynamique classique.

Dans le contexte de l'approche asymptotique, Leguillon et Sanchez-Palencia ([58]) a effectué l'homogénéisation d'un milieu bidimensionnelle élastique linéaire en présence de conditions de Signorini avec frottement de Coulomb, à condition que les fissures soient rectilignes. Le problème quasi-statique a été étudié.

Telega ([81]) a proposé un modèle qui traite de l'homogénéisation d'un solide hyperélastique, contenant des microfissures avec frottement à distributions périodiques, en présence de conditions de Signorini.

7.4 Portée et aperçu

L'objectif de cette thèse est de développer, avec la technique d'homogénéisation, un modèle d'endommagement à deux échelles basé sur la description explicite du niveau microscopique, incluant les phénomènes de frottement, ce qui pourrait décrire la rupture des géomatériaux .

La structure de la thèse, en considérant ce chapitre introductif, est construite comme suit:

Dans le chapitre 2, les aspects théoriques concernant l'homogénéisation asymptotique et la construction de la loi d'endommagement pour le glissement des microfissures avec frottement sont présentés. Les développements déjà réalisés sont soulignés. L'implémentation numérique de la microstructure est réalisée, conduisant à la détermination des différents coefficients homogénéisés, coefficients liés à la dissipation de l'énergie due au mécanisme

de frottement et aux composantes de la loi de frottement de Coulomb. Enfin, les relations constitutives pour chaque état possible de la fissure (adhérence, glissement et glissement inversé) sont déterminées. Ces états sont contrôlés par la loi de frottement et par le chargement.

Dans le chapitre 3 la loi d'endommagement quasi-fragile est considérée et les résultats concernant le comportement local (en un point macroscopique) sont présentés. La loi d'endommagement est déduite de critères de propagation quasi-fragiles pour les microfissures. L'influence du frottement sur les microfissures et sur le comportement macroscopique est analysée. Dans la première étape une relation linéaire pour la courbe de résistance, R-curve, est utilisée, ce qui conduit à un snap-back dans la réponse globale. Dans la deuxième étape, la R-curve linéaire est étendue par l'ajout d'une fonction en puissance de d, pour surmonter les difficultés liées au snap-back. La comparaison des résultats obtenus pour ces deux courbes de résistance est présentée. Dans la dernière partie de ce chapitre, un cycle de charge-décharge est effectué. Les comportements liés aux phénomènes de frottement comme glissement inversé et adhérence pendant la phase de décharge sont obtenus et analysés.

Le chapitre 4 est consacré au modèle d'endommagement dependent du temps. Dans ce chapitre, un modèle alternatif à deux échelles est présenté. Ce modèle est capable de surmonter les difficultés liées à la non-unicité de solution et dépendance de maillage, observés dans le cas du modèle d'endommagement quasi-fragile. Ce modèle est régularisé par la dépendance du temps et est déduit par homogénéisation pour les microfissures qui se propagent en régime sous-critique. L'évolution de la longueur de la microfissure est décrite par un critère sous-critique régie par la loi de Charles. Les réponses effectives contrainte-déformation et endommagement, dépendent du temps, elles sont évaluées numériquement au point local macroscopique et à l'échelle macroscopique globale. A l'échelle locale, l'influence des paramètres intervenant dans le modèle, comme la vitesse v_0 , la vitesse de déformation $\dot{e}$, le coefficient sous-critique n, et la longueur interne ε, est étudiée sous différentes charges de compression et de coefficients de frottement différents. L'influence du coefficient de frottement et de la contrainte latérale est également présentée. Dans ce chapitre, le comportement global macroscopique est discutée. La réponse du matériau sous différentes charges de compression (test uniaxial et tests biaxiaux avec des contraintes latérales) est analysée. Géométrie et conditions aux limites sont basées sur des tests expérimentaux, qui ont été réalisées en parallèle à cette étude. L'effet du coefficient de frottement, de la contrainte latérale et leur rôle dans la formation de la zone de localisation d'endommagement est étudié. Dans la dernière partie de ce chapitre l'influence du maillage sur les résultats est analysée.

Dans le chapitre 5, nous démontrons la capacité à caractériser les ruptures localisées dans les roches et, en particulier, à suivre l'évolution du champ de contrainte à l'intérieur de l'échantillon de roche pendant le chargement avec un nouvel appareil triaxial. Le dispositif expérimental et la caractérisation des tests sont présentés. L'effet du confinement sur le processus de rupture et de localisation est étudié. Dans la dernière partie du chapitre 5, les résultats numériques sont comparés avec les résultats expérimentaux. Les capacités du modèle d'endommagement à deux échelles dependent du temps sont discutées.

Finalement, le chapitre 6 résume les différentes conclusions de notre étude. Puis les perspectives d'évolutions de ces travaux sont discutées.

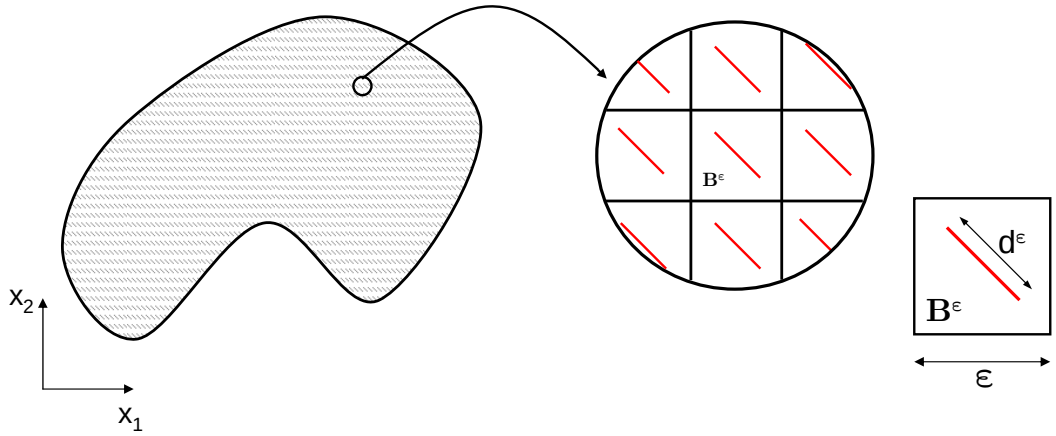

Figure 7.1: Milieu fissuré avec une microstructure locale périodique

7.5 Cadre de modélisation double-échelle

7.5.1 Position du problème

Nous donnons dans ce chapitre introductif quelques rappels du cadre de modélisation double échelle du comportement des roches argileuses.

Nous considérons un milieu élastique isotrope comprenant un grand nombre de microfissures. On suppose que cette structure présente une distribution de fissures localement périodique. Le domaine peut donc être recouvert par un ensemble de cellules périodiques, contenant une fissure (voir Fig.7.1). Chaque fissures est considérée droite et de longueur d^ε. La longueur d^ε est dépendante du temps t et elle peut être différente d'une fissure à l'autre.

Dans la partie solide $B_s = B/C$, ou B est le corps et C l'ensemble de toutes les microfissures dans B , les équations d'équilibre sont:

$$\frac{\partial \sigma_{ij}^\varepsilon}{\partial x_j} = 0 \tag{7.1}$$

et les relations constitutives de l'élasticité linéaire anisotrope sont:

$$\sigma_{ij}^\varepsilon = a_{ijkl} e_{xkl}\left(\mathbf{u}^\varepsilon\right) \tag{7.2}$$

où a_{ijkl} est le tenseur d'élasticité. σ_{ij}^ε est le champs des contraintes et u^ε le champ de déplacement à partir duquel le tenseur des déformations est calculé par rapport aux variables x_i :

$$e_{xij} = \frac{1}{2}\left(\frac{\partial u_i}{\partial x_j} + \frac{\partial u_j}{\partial x_i}\right) \tag{7.3}$$

On suppose que les bords de la fissure sont soit libres de contraintes si la fissure est ouverte soit en contact unilatéral si la fissure est fermée. Ces deux solutions sont exprimées par les deux jeux de formules:

$$\boldsymbol{\sigma}^{\varepsilon}\mathbf{N} = 0;\ [\mathbf{u}^{\varepsilon} \cdot \mathbf{N}] > 0, \tag{7.4}$$

$$[\boldsymbol{\sigma}^{\varepsilon}\mathbf{N}] = 0;\ \mathbf{N}\boldsymbol{\sigma}^{\varepsilon}\mathbf{N} < 0;\ \mathbf{T}\boldsymbol{\sigma}^{\varepsilon}\mathbf{N} = 0;\ [\mathbf{u}^{\varepsilon} \cdot \mathbf{N}] = 0 \tag{7.5}$$

Dans le cas de frottement, nous réécrivons la condition de contact unilatéral:

$$[\boldsymbol{\sigma}^{\varepsilon}\mathbf{N}] = 0;\ \mathbf{N}\boldsymbol{\sigma}^{\varepsilon}\mathbf{N} < 0;\ [\mathbf{u}^{\varepsilon} \cdot \mathbf{N}] = 0 \tag{7.6}$$

En notant μ_f le coefficient du frottement, les conditions de frottement de Coulomb sont:

Si

$$|\mathbf{T}\boldsymbol{\sigma}^{\varepsilon}\mathbf{N}| < -\mu_f \mathbf{N}\boldsymbol{\sigma}^{\varepsilon}\mathbf{N} \tag{7.7}$$

alors l'adhérence

Si

$$|\mathbf{T}\boldsymbol{\sigma}^{\varepsilon}\mathbf{N}| = -\mu_f \mathbf{N}\boldsymbol{\sigma}^{\varepsilon}\mathbf{N} \tag{7.8}$$

alors le glissement.

où $\mathbf{N}$ et le vecteur normal unitaire, $\mathbf{T}$ le vecteur tangent unitaire à la fissure et $[\cdot]$ le saut à travers les lèvres de la fissures. On suppose que chaque microfissure est caractérisée en totalité par une des conditions (7.4-7.8). Le fait que chaque microfissure soit complètement ouverte ou fermée est une hypothèse raisonable pour de petites longueurs de fissures. Le passage d'une état à l'autre sera décrit ultérieurement, au niveau des solutions homogénéisées.

La propagation d'une microfissure est décrite par la théorie de Griffith ([40]), où toute fissure a une énergie proportionnelle à sa longueur. Il postule qu'il y aura propagation et donc augmentation de l'énergie, si cette dernière est parfaitement compensée par la restitution de l'énergie élastique causée par l'avancée de la fissure. Dans le cas des problèmes quasi-statiques, ce critère peut se formuler en terme de taux de restitution d'énergie élastique exprimé comme :

$$\mathcal{G}^{\varepsilon} = \lim_{r \to 0} \int_{\Gamma_r} \mathbf{e} \cdot \mathbf{b}\left(\mathbf{u}^{\varepsilon}\right) \mathbf{n}\, ds \tag{7.9}$$

où Γ_r est le cercle d'un rayon infinitésimal, entourant l'extrémité de la fissure, $\mathbf{n}$ est le vecteur normal au cercle Γ_r, $\mathbf{e}$ est le vecteur unitaire dans la direction de propagation et

$$b_{ij}\left(\mathbf{u}^{\varepsilon}\right) = \frac{1}{2} a_{mnkl} e_{xkl}\left(\mathbf{u}^{\varepsilon}\right) e_{xmn}\left(\mathbf{u}^{\varepsilon}\right) \delta_{ij} - \sigma^{\varepsilon}_{jk} u^{\varepsilon}_{k,i} \tag{7.10}$$

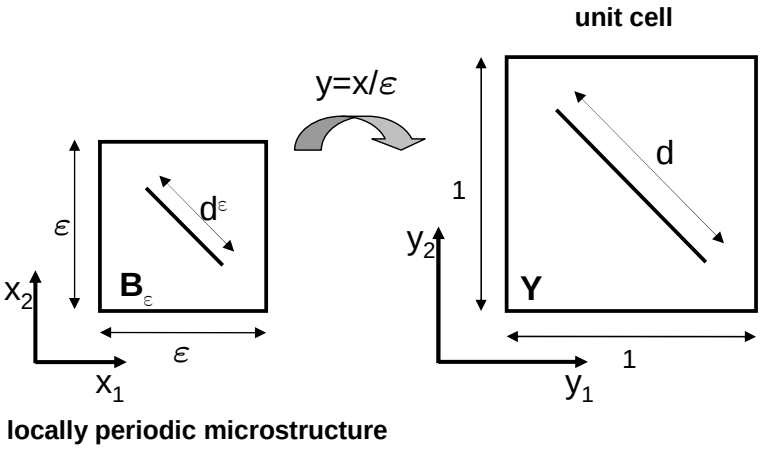

Figure 7.2: Mise à l'échelle de la cellule unitaire à la période spaciale microstructuralle du matériau.

est le tenseur de contrainte Eshelby.

Le critère de Griffith stipule que la propagation a lieu quand une limite critique d'énergie, $\mathcal{G}_{cr}$, est attendue

$$\mathcal{G}^{\varepsilon} = \mathcal{G}_{cr} \tag{7.11}$$

tandis qu'il n'y a aucune évolution de la fissure $\mathcal{G}^{\varepsilon} < \mathcal{G}_{cr}$, où $\mathcal{G}_{cr}$ désigne le taux de restitution d'énergie critique et correspond à la ténacité du matériau.

7.5.2 Homogénéisation

La microstructure locale périodique est construite à partir d'une cellule unitaire $Y = [0,1] \times [1,0]$ mise à l'échelle par un petit paramètre ε, afin que la période du matériau soit εY , comme dans la Fig.7.2. De cette façon, le paramètre ε apparaît, naturellement, comme une longueur caractéristique de la microstructure. Nous supposons que cette longueur est assez petite par rapport aux dimensions du milieu, afin que l'on puisse distinguer deux variables d'espace physique, macro- et microscopique, notées respectivement $\mathbf{x}$ et $\mathbf{y}$. La variable $\mathbf{x}$ est la variable macroscopique et $\mathbf{y}$, la variable microscopique. Dans ce cadre, les deux échelles distinctes sont représentées par les variables $\mathbf{x}$, variables macroscopiques, et $\mathbf{y} = {}^{\mathbf{x}}/_{\varepsilon}$, variables microscopiques (e.g. Sanchez-Palencia [77], Leguillon et Sanchez-Palencia [58]).

La cellule unitaire Y contient une fissure CY et on note la partie solide par $Y_s = {}^{Y}/_{CY}$. La longueur CY est $d = \frac{d^{\varepsilon}}{\varepsilon}$ (voir Fig.7.3).

Suivant la méthode d'homogénéisation basée sur des développements asymptotiques (e.g. Benssousan et al. [14], Sanchez-Palencia [77]), on cherche l'expansion de u^{ε} sous la forme :

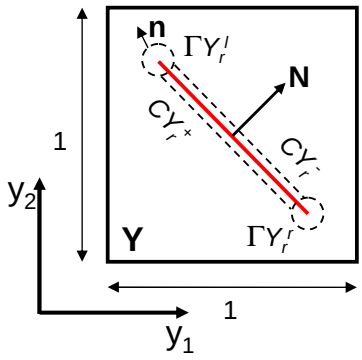

Figure 7.3: Cellule unitaire avec une fissure.

$$\mathbf{u}^{\varepsilon}(\mathbf{x},t) = \mathbf{u}^{(0)}(\mathbf{x},\mathbf{y},t) + \varepsilon\mathbf{u}^{(1)}(\mathbf{x},\mathbf{y},t) + \varepsilon^2\mathbf{u}^{(2)}(\mathbf{x},\mathbf{y},t) + \dots \tag{7.12}$$

Il peut être prouvé que $\mathbf{u}^{(0)} = \mathbf{u}^{(0)}(\mathbf{x},t)$ est indépendant de $\mathbf{y}$; il représente un vrai champ de déplacement macroscopique.

Si nous considérons que la géométrie de la fissure est donnée par une ligne droite, nous proposons une méthode pour faire la distinction entre les états microscopiques d'ouverture et de contact. La relation (2.29) indique que sur les bords de la fissure, dans la cellule unitaire, la solution macroscopique peut être considérée comme une "*force superficielle* - **f**", appliquées sur les lèvres de la fissure. L'orientation de ce vecteur force par rapport à la direction normale la fissure, c'est-à-dire la tendance de cette force à ouvrir ou fermer la fissure, peut être considérée comme un indicateur de l'état d'ouverture ou de fermeture. Au niveau macroscopique, ces deux états induisent une séparation de l'espace $\mathbf{R}$ des variables $e_{x11}, e_{x12}, e_{x22}$ en deux sous-domaines $\mathbf{R}^{\pm}$ définies par: $\mathbf{R}^{\pm} = \left\{\mathbf{e_x} \mid N_i a_{ijkl} e_{xkl}\left(\mathbf{u}^{(0)}\right) N_j \gtrless 0\right\}$, où les signes $+$ et $-$ correspondent respectivement à la traction et la compression. De cette façon, le passage entre les deux comportements homogénéisées élémentaires, correspondant à la traction et la compression, est réalisé au niveau macroscopique, en fonction du champ global de déformation.

Sur chaque sous-domaine, la solution de ce problème est une fonction vectorielle linéaire de $\mathbf{e_x}\left(\mathbf{u}^{(0)}\right)$. Si nous choisissons un système de générateurs $\mathbf{E}^{pq}$ des déformations macroscopiques fondamentales dans chaque sous-domaine, nous écrivons la déformation macroscopique $e_{xij}\left(\mathbf{u}^{(0)}\right)$ comme une combinaison linéaire de ces éléments. Un choix élémentaire est de considérer: $E_{ij}^{pq} = \delta_{ip}\delta_{jq}$ dans $\mathbf{R}^{+}$ et $E_{ij}^{pq} = -\delta_{ip}\delta_{jq}$ dans $\mathbf{R}^{-}$.

Ainsi, si le vecteur $\boldsymbol{\xi}^{pq}$ est la solution particulière, correspondant à $e_{xij}\left(\mathbf{u}^{(0)}\right) = E_{ij}^{pq}$, le correcteur de premier ordre $\mathbf{u}^{(1)}$ peut s'exprimer:

$$u_{\pm}^{(1)} = \xi_{\pm}^{pq} e_{xpq}\left(\mathbf{u}^{(0)}\right) \tag{7.13}$$

où $\xi_{\pm}^{pq}$ sont les fonctions caractéristiques représentant des modes de déformation élémentaires de la cellule unitaire.

En cas de frottement, la sous-région $\mathbf{R}^-$ (correspondant aux fissures fermées) est divisé en trois sous-régions, où les fissures peuvent glisser de deux manières différentes (gauche et droite) ou les lèvres des fissures sont adhérence. Ces régions sont définies par:

$$\mathbf{D}^R = \{\mathbf{e_x} \mid N_i a_{ijkl} e_{xkl}\left(\mathbf{u}^{(0)}\right) N_j < 0; T_i a_{ijkl} e_{xkl}\left(\mathbf{u}^{(0)}\right) N_j > 0 \text{ and } |T_i a_{ijkl} e_{xkl}\left(\mathbf{u}^{(0)}\right) N_j| \geq -\mu_f N_i a_{ijkl} e_{xkl}\left(\mathbf{u}^{(\mathbf{0})}\right) N_j\} \tag{7.14}$$

$$\mathbf{D}^L = \{\mathbf{e_x} \mid N_i a_{ijkl} e_{xkl}\left(\mathbf{u}^{(0)}\right) N_j < 0; T_i a_{ijkl} e_{xkl}\left(\mathbf{u}^{(0)}\right) N_j < 0 \text{ and } |T_i a_{ijkl} e_{xkl}\left(\mathbf{u}^{(0)}\right) N_j| \geq -\mu_f N_i a_{ijkl} e_{xkl}\left(\mathbf{u}^{(0)}\right) N_j\} \tag{7.15}$$

$$\mathbf{S} = \{\mathbf{e_x} \mid N_i a_{ijkl} e_{xkl}\left(\mathbf{u}^{(0)}\right) N_j < 0; \text{ and } |T_i a_{ijkl} e_{xkl}\left(\mathbf{u}^{(0)}\right) N_j| < -\mu_f N_i a_{ijkl} e_{xkl}\left(\mathbf{u}^{(0)}\right) N_j\} \tag{7.16}$$

où $\mathbf{T}$ et $\mathbf{N}$ sont vecteur unitaire tangent et normal, respectivement. $\mathbf{D}^R$, $\mathbf{D}^L$sont les domaines linéaires de glissement à droite et à gauche, $\mathbf{S}$ est le domaine de adhérence et μ_f est le coefficient de frottement.

Dans chaque domaine, la solution $\mathbf{u}^{(1)}$ peut être écrite comme une fonction linéaire de $\mathbf{e_x}\left(\mathbf{u}^{(0)}\right)$. On peut remarquer que les quatre domaines, ainsi définis, ne font intervenir que des grandeurs macroscopiques. Ce qui nous permet de décrire le comportement sur une microfissure, seulement, par la déformation macroscopique $\mathbf{e_x}\left(\mathbf{u}^{(0)}\right)$. Si on choisit un système de générateurs $\mathbf{E}^{pq}$ des déformations macroscopiques fondamentales pour chaque domaine, alors la déformation macroscopique $\mathbf{e_x}\left(\mathbf{u}^{(0)}\right)$ s'écrit comme une combinaison linéaire de ces éléments sous la forme:

$$e_{xij}\left(\mathbf{u}^{(0)}\right) = \alpha_{pq}\left(\mathbf{u}^{(0)}\right) \bar{E}^{pq}_{ij} \tag{7.17}$$

où α_{pq} sont fonctions linéaires de $\mathbf{u}^{(0)}$ et $\bar{E}^{pq}_{ij}$ sont différentes par rapport à E^{pq}_{ij}. Si le vecteur $\boldsymbol{\eta}^{pq}$ est la solution particulière, correspondant à $e_{xij}\left(\mathbf{u}^{(0)}\right) = \bar{E}^{pq}_{ij}$, le correcteur de premier ordre $\mathbf{u}^{(1)}$ peut s'exprimer:

$$\mathbf{u}^{(1)}(\mathbf{x}, \mathbf{y}, t) = \boldsymbol{\eta}^{pq}(\mathbf{y})\, \alpha_{pq}(\mathbf{x}, t) \tag{7.18}$$

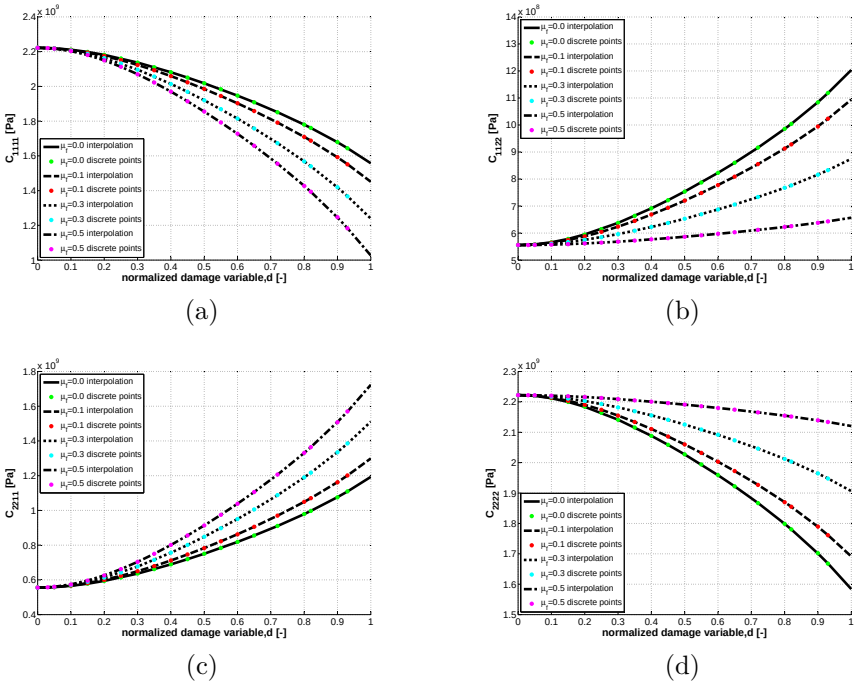

Figure 7.4: Coefficients homogénéisés en fonction de la variable d'endommagement pour différents coefficients de frottement $\mu_f = 0.0, 0.1, 0.3, 0.5$, une orientation de fissure de 135° et glissement à droite: a) C^R_{1111}, b) C^R_{1122}, c) C^R_{2211}, d) C^R_{2222}.

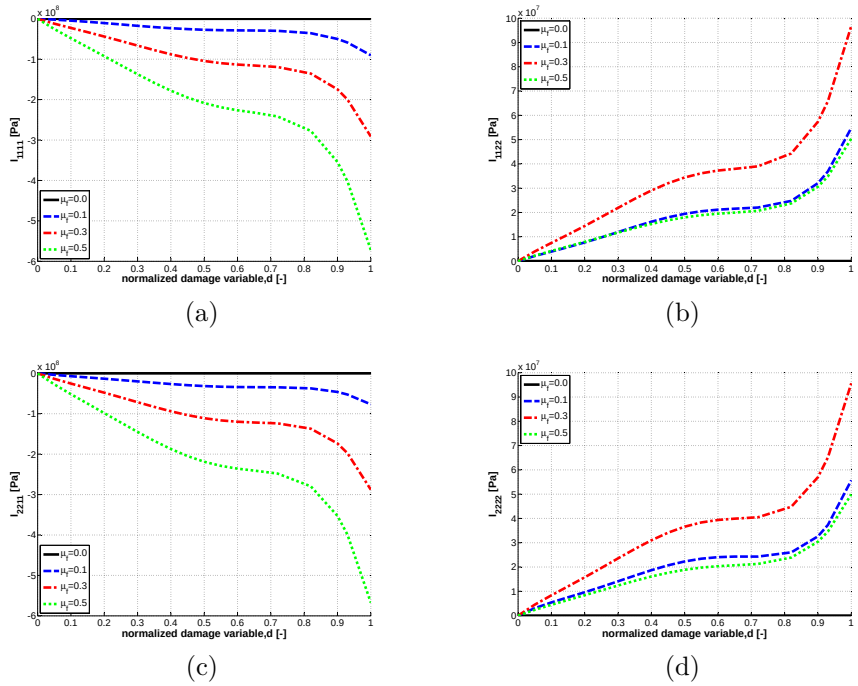

Figure 7.5: Intégrales I_{mnpq} en fonction de la variable d'endommagement pour différents coefficients de frottement $\mu_f = 0.0, 0.1, 0.3, 0.5$, une orientation de fissure de 135° et glissement à droite: a) I^R_{1111}, b) I^R_{1122}, c) I^R_{2211}, d) I^R_{2222}.

7.5.3 Le modèle constitutif utilisé

1. l'équation d'équilibre:

$$div\,\Sigma_{ij} = 0 \tag{7.19}$$

2. a loi de comportement homogénéisé:

   - si on se trouve dans le domaine de la fissure ouverte ou dans le cas de glissement de la fissure

$$\Sigma_{ij} = C^{\alpha}_{ijmn}\alpha_{mn} \tag{7.20}$$

avec

$$C^{\alpha}_{ijmn} = \int_{Y_s}\left(a_{ijkl}E^{mn}_{kl} + a_{ijkl}e_{ykl}\left(\boldsymbol{\eta}^{mn}\right)\right)dy \tag{7.21}$$

ou, en regroupant les termes, on a :

$$\Sigma_{ij} = C_{ijmn}e_{xmn} \tag{7.22}$$

avec

$$C_{ijmn} = \int_{Y_s}\left(a_{ijmn} + a_{ijkl}e_{ykl}\left(\boldsymbol{\xi}^{mn}\right)\right)dy \tag{7.23}$$

ou $\boldsymbol{\xi}^{mn}$ sont déterminés en fonction de $\boldsymbol{\eta}^{mn}$. Les valeurs de C_{ijmn} dépendent de la longueur des fissures, l'orientation des fissures et coefficient de frottement, et ils sont obtenus avec la solution de cellules. Figure 7.4 montre coefficients homogénéisés, C_{ijmn}, en fonction de la variable d'endommagement pour différents coefficients de frottement $\mu_f = 0.0, 0.1, 0.3, 0.5$, une orientation de fissure de 135° et glissement à droite.

- si la fissure est dans le domaine d'adhérence

$$\Sigma_{ij} = a_{ijkl}\left(e_{xkl}\left(\mathbf{u}^{(0)}\right) + e^{p}_{kl}\left(\mathbf{u}^{(1)}\right)\right) \tag{7.24}$$

avec

$$e^{p}_{kl}\left(\mathbf{u}^{(1)}\right) = \frac{1}{2}\left(T_kN_l + T_lN_k\right)\int_{CY}\left[u^{(1)}_m T_m\right]ds_y \tag{7.25}$$

1. loi d'évolution d'endommagement

$$\dot{d}\left(\left(\frac{1}{2}\frac{dC^{\alpha}_{klpq}}{dd}E^{mn}_{kl} + I^{\alpha}_{mnpq}\right)\alpha_{mn}\left(\mathbf{u}^{(0)}\right)\alpha_{pq}\left(\mathbf{u}^{(0)}\right) + \frac{\mathcal{G}_{cr}}{\varepsilon}\right) = 0 \tag{7.26}$$

avec

$$I^{\alpha}_{mnpq} = \frac{1}{2}\frac{d}{dd}\int_{CY}\left(a_{ijkl}E^{mn}_{kl} + a_{ijkl}e_{ykl}\left(\boldsymbol{\eta}^{mn}\right)\right)N_j\left[\eta^{pq}_i\right]ds_y -$$

$$\int_{CY}\left(a_{ijkl}E^{mn}_{kl} + a_{ijkl}e_{ykl}\left(\boldsymbol{\eta}^{mn}\right)\right)N_j\left[\dot{\eta}^{pq}_i\right]ds_y \tag{7.27}$$

sous une forme équivalente, en regroupant les termes, nous avons:

$$\dot{d}\left(\left(\frac{1}{2}\frac{dC_{mnpq}}{dd}+I_{mnpq}\right)e_{xmn}\left(\mathbf{u}^{(0)}\right)e_{xpq}\left(\mathbf{u}^{(0)}\right)+\frac{\mathcal{G}_{cr}}{\varepsilon}\right)=0 \tag{7.28}$$

avec

$$I_{mnpq}=\frac{1}{2}\frac{d}{dd}\int_{CY}\left(a_{ijmn}+a_{ijkl}e_{ykl}\left(\boldsymbol{\xi}^{mn}\right)\right)N_j\left[\xi_i^{pq}\right]ds_y-$$

$$\int_{CY}\left(a_{ijmn}+a_{ijkl}e_{ykl}\left(\boldsymbol{\xi}^{pq}\right)\right)N_j\left[\dot{\xi}_i^{pq}\right]ds_y \tag{7.29}$$

ou $\boldsymbol{\xi}^{mn}$ sont déterminés en fonction de $\boldsymbol{\eta}^{mn}$. Les valeurs de I_{mnpq} dépendent de la longueur des fissures, l'orientation des fissures et coefficient de frottement, et ils sont obtenus avec la solution de cellules. Figure 7.5 montre intégrales, I_{mnpq}, en fonction de la variable d'endommagement pour différents coefficients de frottement $\mu_f = 0.0, 0.1, 0.3, 0.5$, une orientation de fissure de 135° et glissement à droite.

2. condition d'irréversibilité par endommagement

$$\frac{dd}{dt}\geq 0 \tag{7.30}$$

7.6 Modèle quasi-fragile pour des microfissures frottantes.

Cette section est dédié aux modèls d'endommagement indépendents du temps. Nous décrivons un modèle à l'échelle microscopique, dans lequel l'évolution des microfissures induit une augmentation de la résistance du matériau jusqu'à atteindre une valeur maximale. Un tel comportement est possible grâce au développement de la zone d'élaboration de l'endommagement en pointe de fissure. La valeur maximale de résistance du matériau est atteinte quand cette zone est complètement développée. La courbe décrivant ce comportement est appelé R-curve (resistance curve). Le paramètre c_f représente la taille de la zone d'élaboration de l'endommagement propre à chaque matériau. Nous considérons le modèle d'endommagement quasifragile suivant :

$$\left(\frac{1}{2}\frac{dC_{ijkl}(d)}{dd}e_{xkl}\left(\mathbf{u}^{(0)}\right)e_{xij}\left(\mathbf{u}^{(0)}\right)+\frac{\mathcal{G}^{\varepsilon}}{\varepsilon}+I_{mnpq}e_{xmn}\left(\mathbf{u}^{(0)}\right)e_{xpq}\left(\mathbf{u}^{(0)}\right)\right)\dot{d}=0 \tag{7.31}$$

où

$$\mathcal{G}^{\varepsilon}=\mathcal{G}_{cr}(d,\varepsilon,c_f) \tag{7.32}$$

est la courbe de resistance R-curve utilisée dans la loi d'endommagement, qui peut être une fonction linéaire de d (Bazant et Planas [13]). Le premier terme de cette équation est

l'opposé du taux restitution d'énergie de rupture pour une cellule, le second représente la dissipation d'énergie liée au phénomène de microfissuration, et le dernier la dissipation d'énergie par frottement des lèvres des microfissures. Quand l'énergie disponible dans le solide élastique devient égale à l'énergie nécessaire de rupture, les microfissures se propagent. Pour résoudre l'équation d'endommagement, nous utilisons les valeurs calculées sur une cellule élémentaire des intégrales $I_{mnpq}(d)$ et des coefficients homogénéisés $C_{ijkl}(d)$.

7.6.1 Résultats numériques

Au niveau local macroscopique, nous étudions le comportement macroscopique de compression, y compris contact et frottement pour une orientation de la fissure et glissement à droit, coefficients de Coulomb différents et différentes contraintes latérales.

Les tests numériques, tels que les compressions uniaxiaux et biaxiaux, seront effectuée. Dans ces simulations numériques les paramètres suivants sont utilisés : orientation des microfissures de 135°, matériau sain élastique isotrope avec module d'Young $E = 2GPa$, et coefficient de Poisson $\nu = 0.2$, énergie critique de rupture $\mathcal{G}_{cr} = 20^{J}/_{m^2}$, paramètre de longueur microstructurelle $c_f = 10^{-3}m$.

Nous présenterons la inflence du coefficient de frottement ($\mu_f = 0.0, 0.1, 0.3$ and 0.5) sous compression uniaxiale. Les effets des contraintes latérales ($\Sigma_{11} = 0\,Pa, -2 \times 10^6\,Pa, -6 \times 10^6\,Pa$ and $-12 \times 10^6\,Pa$) est effectuée sur le matériau défini par le coefficient de frottement $\mu_f = 0.3$.

7.6.1.1 Courbe de résistance R-curve linéaire

Dans un premier cas, nous utilisons une courbe de résistance linéaire (utilisée par Z.P. Bazant et J.Planas [13]) et nous analysons la réponse macroscopique du modèle. La R-curve est de la forme suivante :

$$\frac{\mathcal{G}^{\varepsilon}(d)}{\varepsilon} = \frac{2\sqrt{2}\mathcal{G}_{cr}d}{c_f} \tag{7.33}$$

Pour une zone d'endommagement complètement développée, le paramètre d'endommagement d est égal à 1. Nous observons que le seul moyen d'atteindre cet état d'endommagement, du fait d'une réponse de type snap-back, est d'abord de charger puis de décharger (i.e de diminuer la déformation imposée tout en ayant un endommagement qui progresse).

Les résultats numériques concernant cette section peuvent être trouvés dans 3.4.2 où l'influence du coefficient de frottement sous compressions uniaxiaux sont présentés dans 3.4.2.1 et compressions biaxiaux sont présentés dans 3.4.2.2.

7.6.1.2 Courbe de résistance modifiée.

Nous considérons que le snap-back observé sur les simulations précédentes n'est pas correct d'un point de vue physique pour une loi quasi-statique où les termes d'inerties ne sont pas pris en compte. Pour éviter ce type de réponse, nous allons chercher à modifier l'expression de la courbe de résistance (R-curve). Nous ajoutons à la relation linéaire précédemment introduite, une fonction polynomiale dépendant de la variable d'endommagement d. Une étude paramétrique nous a montré qu'une fonction en puissance de 5 est le minimum nécessaire pour obtenir une réponse sans snap-back. La fonction R-curve utilisée dans cette section est la suivante :

$$\frac{\mathcal{G}^{\varepsilon}(d)}{\varepsilon} = \frac{\mathcal{G}_{cr}}{c_f}\left(2\sqrt{2}d + \left(\sqrt{2}d\right)^5\right) \tag{7.34}$$

En utilisant la fonction R-curve modifiée, nous réalisons les mêmes simulations que dans la section précédente afin de pouvoir comparer les résultats ainsi obtenus aux résultats précédents et en déduire l'influence de la forme de la courbe de résistance sur la réponse macroscopique.

Les résultats numériques concernant cette section peuvent être trouvés dans 3.4.3 où l'influence du coefficient de frottement sous compressions uniaxiaux sont présentés dans 3.4.3.1 et compressions biaxiaux sont présentés dans 3.4.3.2.

7.6.1.3 Chargement-déchargement en utilisant courbe de résistance modifiée.

Dans ce paragraphe nous allons effectuer des tests uniaxiaux et biaxiaux avec régimes de déchargement. Dans les modèles qui couple friction et endommagement, la réponse à la phase de déchargement contient comportement non élastique, qui ne peut être observée pour des matériaux nonfrictional.

En raison du glissement avec frottement des microfissures, on peut distinguer plusieurs états de fissure, qui sont contrôlées par la loi de Coulomb classique dans la forme générale:

$$|\,\mathbb{T}\,| < -\mu_f \mathbb{N} \tag{7.35}$$

lors d'un contact stationnaire et

$$|\,\mathbb{T}\,| = -\mu_f \mathbb{N} \tag{7.36}$$

au cours de glissement.

$\mathbb{N}$ et $\mathbb{T}$ sont des composantes normale et tangentielle de la contrainte à les lèvres et ils ont été déduites de la forme:

	Linear R-curve	Modified R-curve
slope in the deviatoric and mean stress frame[-]	0.48	0.5
friction angle ϕ [°]	14.1	14.5
macroscopic friction coefficient μ_f^*[-]	0.25	0.26
cohesion c [MPa]	7.69	7.79

Table 7.1: Influence R-curve linéaire et R-curve modifié sur les paramètres du matériau.

$$\mathbb{N}^{pq} \equiv N_i a_{ijkl} \bar{E}^{pq}_{kl} N_j \int_{CY} ds_y + \int_{CY} \left(N_i a_{ijkl} e_{ykl} \left(\boldsymbol{\eta}^{pq} \right) N_j \right) ds_y \tag{7.37}$$

$$\mathbb{T}^{pq} \equiv T_i a_{ijkl} \bar{E}^{pq}_{kl} N_j \int_{CY} ds_y + \int_{CY} \left(T_i a_{ijkl} e_{ykl} \left(\boldsymbol{\eta}^{pq} \right) N_j \right) ds_y \tag{7.38}$$

Ces quantités proviennent des computions sur la cellule unitaire et ils sont stockés dans les fonctions polynomiales de d.

À la suite de nombreux auteurs ([5, 46, 56, 72, 84]), qui ont observé que lors de la phase initiale de décharger les lèvres des fissures restent immobile jusqu'à ce que le glissement inverse se produit, nous réécrivons la formulation pour $\mathbb{N}$ (7.37) et $\mathbb{T}$ (7.38) pour le déchargement par définir les termes inélastiques. Ces termes restent constants pendant le déchargement et ils ont des formes:

$$\mathbb{N}^{pq}_{un} = \int_{CY} \left(N_i a_{ijkl} e_{ykl} \left(\boldsymbol{\eta}^{pq} \right) N_j \right) ds_y \tag{7.39}$$

$$\mathbb{T}^{pq}_{un} = \int_{CY} \left(T_i a_{ijkl} e_{ykl} \left(\boldsymbol{\eta}^{pq} \right) N_j \right) ds_y \tag{7.40}$$

Les termes (7.39) et (7.40) sont calculées pour la dernière configuration de chargement et sont maintenus constants pendant le déchargement jusqu'à ce que le retour en arrière se produit.

Dans les tests suivants nous ne serons uniquement concentreé sur la réponse du matériau sous des charges de compression, mais aussi sur les évolutions et les relations des composantes particulières de la loi de Coulomb (Eqs.7.35 et 7.36).

Les résultats numériques obtenus par compression uniaxiale et biaxiale dans le cas de cycle de chargement-déchargement sont présentés dans 3.4.5.1 et 3.4.5.2, respectivement.

7.6.1.4 Comparaison entre R-curve linéaire et R-curve modifié

Le Tableau 7.1, présente l'influence de la fonction R-curve sur les paramètres matériau tel que : la pente du chemin de contrainte, l'angle de frottement, le coefficient de frottement

macroscopique, et la cohésion. En comparant les résultats des simulations (avec coefficient de frottement microscopique $\mu_f = 0.3$) R-curve linéaire au R-curve modifié, on constate que le terme supplémentaire utilisé dans la fonction R-curve modifiée n'a pas de forte influence sur les paramètres matériau. La fonction R-curve modifiée nous permet donc d'éviter les problèmes de snap back et de contrôler la phase post-pic sans influencer significativement les paramètres matériau déduits des simulations.

7.7 Modèle dépendant du temps

Dans ce chapitre, un modèle alternatif à deux échelles est présenté. Ce modèle est capable de surmonter les difficultés liées à la non-unicité de solution et dépendance de maillage, observés dans le cas du modèle d'endommagement quasi-fragile. Ce modèle est régularisé par la dépendance du temps. Ce modèle d'endommagement est obtenu par homogénéisation à partir d'une loi de propagation sous-critique des microfissures. Ce modèle va être employé pour la description de l'endommagement à des échelles courtes ou longues de temps, par un choix approprié des paramètres du modèle (temps caractéristique). Dans cette section nous considérons le cas de la propagation en mode II, décrite par une loi de type Charles [21]:

$$\frac{dl}{dt} = v_0 \left(\frac{K_{II}}{K_0} \right)^n \tag{7.41}$$

Dans cette formule v_0 est la vitesse de référence, n est le coefficient souscritique et K_{II} représente le facteur d'intensité des contrainte en mode II . K_0 est une valeur particulière du facteur d'intensité des contraintes pour laquelle la vitesse de propagation de la fissure est v_0. K_0, v_0 et n sont les paramètres de matériau. K_{II} depend de l'état de contrainte, de la longueur interne ε et de la geometrie de la microfissure.

En employant la méthode d'homogénéisation basée sur des développements asymptotiques, nous obtenons la loi d'endommagement sous la forme:

$$\dot{d} = \frac{v_0}{\sqrt{2}\varepsilon} \left(\frac{\sqrt{\frac{E\varepsilon}{1-\nu^2} \left(\left(-\frac{1}{2} \frac{dC_{ijkl}(d)}{dd} + I_{ijkl}(d) \right) e_{xkl}\left(u^{(0)}\right) e_{xij}\left(u^{(0)}\right) \right)}}{K_0} \right)^n \tag{7.42}$$

7.7.1 Formulation du problème d'endommagement à deux échelles

Pour résumer, le problème d'endommagement homogénéisé à résoudre est défini par le système d'équations suivantes:

- **l'équation d'équilibre**

$$\frac{\partial}{\partial x_j}\Sigma_{ij}^{(0)} = 0$$

- **loi de contrainte-déformation effective**

$$\Sigma_{ij}^{(0)} = C_{ijkl}\left(E\,,\nu,d,\mu_f,\theta\right)e_{xkl}\left(\mathbf{u}^{(0)}\right)$$

- **loi d'évolution d'endommagement**

$$\frac{dl}{dt} = v_0\left(\frac{K_{II}\left(\mathbf{e_x},E\,,\nu,d,\mu_f,\theta\right)}{K_0}\right)^n$$

7.7.2 Résultats numériques : comportement local

Dans cette partie l'analyse de la réponse homogénéisé au point macroscopique sera étudiés.

Selon le problème, l'équation d'endommagement (7.42) sera résolu par l'application de la contrainte et déformation macroscopique. Dans le cas de la compression uniaxiale, une taux de déformation constante est imposée dans la direction verticale et la direction horizontale est libre de contrainte, tandis que pour la compression biaxiale une contrainte constante latérale sera appliquée.

Tous les tests sont effectués pour différents coefficients de frottement ($\mu_f = 0.0, 0.1, 0.3$ and 0.5) ou différentes contraintes latérales ($\Sigma_{11} = 0\,Pa, -2\times10^6\,Pa, -6\times10^6\,Pa, -12\times10^6\,Pa$). Dans le cadre local, nous avons étudié l'influence des paramètres du modèle (comment la vitesse de référence v_0, le taux de déformation $\dot{e}_{xkl}$, le temps t, le coefficient souscritique n, la longueur interne ε) afin de définir les valeurs correctes pour les calculs macroscopiques globales.

Tous les résultats numériques impliquées de cette analyse sont présentés dans les sections suivantes: la section4.5.2.1 pour l'influence du coefficient de frottement sous compression uniaxiale, la section 4.5.2.2 pour compression biaxiale, la section 4.5.2.3 pour l'influence du coefficient souscritique n , la section 4.5.2.4 pour l'effet du taux de déformation, la section 4.5.2.5 pour l'influence de la vitesse v_0 et la section 4.5.2.6 pour l'influence de la longueur interne ε.

7.7.3 Résultats numériques: comportement globale

Dans cette partie, le comportement global macroscopique sera discutés. Nous allons analyser la réponse de l'échantillon considéré comme une structure sous différentes charges de compression (tests uniaxiaux et biaxiaux avec des contraintes latérales).

Nous étudions l'effet du coefficient de frottement ($\mu_f = 0.0, 0.1, 0.3, 0.5$), contrainte latérale ($\Sigma_{11} = 0\,Pa, -2\times10^6\,Pa, -6\times10^6\,Pa, -12\times10^6\,Pa$) et leur rôle dans la formation de la zone de localisation de l'endommagement. Nous étudions l'influence du maillage et de la forme des éléments sur les résultats.

Au début, les simulations effectuées sur un échantillon rectangulaire de $50\,mm$ de hauteur et de $25\,mm$ de largeur avec maillage régulier de 800 éléments, chacun contenant 4 nœuds et 4 points de Gauss.

Ensuite, afin d'étudier l'effet de maillages, des maillages différentes sont envisagées. Les maillages comportent des éléments 800, 1741 et 3200 avec le même nombre de noeuds et de points de Gauss comme précédemment.

Deux maillages sont construits avec des éléments carrés et un maillage avec la forme unregular d'éléments. La charge axiale est commandée en déplacement en maintenant une vitesse de déplacement constante.

La contrainte constante est appliquée sur les deux faces latérales de l'échantillon. Géométrie, conditions limites et maillages considérés sont présentés dans la figure7.6.

Une inférieur K_0 a été introduit dans les éléments de l'un des coins, de manière à effectuer la réponse macroscopique comprenant la bande de localisation. De cette manière, la bande est favorisée pour lancer à partir du coin.

Les résultats numériques concernant l'effet du coefficient de frottement sous compression uniaxiale sont présentés dans 4.6.4, concernant des tests biaxiaux et l'influence de la contrainte latérale sont présentés dans 4.6.5 et concernant l'effet du maillage sont présentés dans 4.6.6.

7.7.4 Résultats numériques vs expérimentales

En utilisant le modèle dépendent du temps avec glissement de frottement de la microfissures nous avons effectué des simulations au niveau du laboratoire, qui correspond aux tests expérimentaux présentés dans le chapitre 5.

Ce choix a été fait pour éviter les difficultés liées à la non-unicité de solution et dépendance de maillage, observés dans le cas du modèle d'endommagement quasi-fragile. Ce modèle est régularisé par la dépendance du temps. Nous comparons les résultats expérimentaux avec les résultats numériques et nous discutons les capacités du modèle d'endommagement en fonction du temps, qui a été développé dans les chapitres précédents de cette thèse.

Dans les simulations, la géométrie et les conditions aux limites sont basées sur des essais expérimentaux et dans la représentation 2D de la hauteur de l'échantillon est de $50mm$ et la largeur est de $25\,mm$.

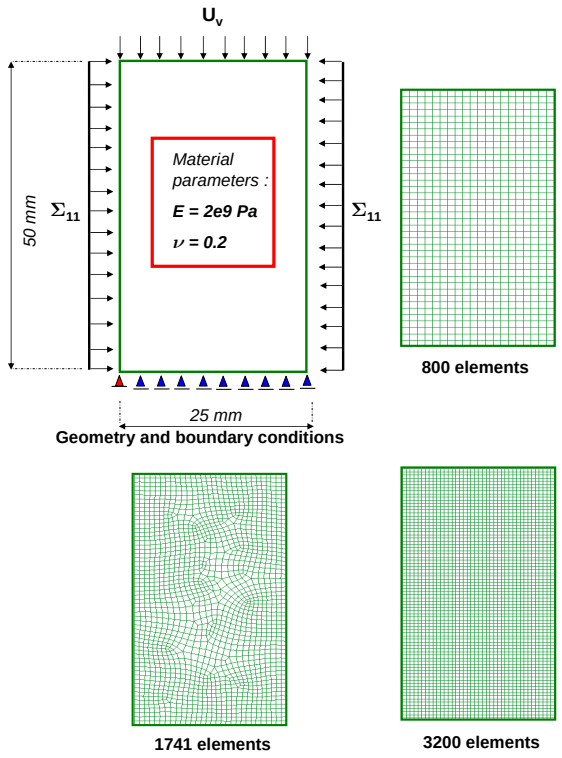

Figure 7.6: Géométrie, conditions limites et maillages considérés dans les simulations numériques

La charge axiale est commandée en déplacement en maintenant une vitesse de déplacement constante.

La contrainte constante est appliquée sur les deux faces latérales de l'échantillon.

Les tests numériques avec différentes contraintes latérales ($\Sigma_{lateral} = -2 \times 10^6\, Pa$, $-6 \times 10^6\, Pa$, $-12 \times 10^6\, Pa$) et le coefficient de frottement $\mu_f = 0.5$ ont été effectuées et comparées avec les résultats expérimentaux correspondants.

La figure 7.7bprésente la relation numérique de contrainte-déformation avec champs de déplacement axial et de déformation de cisaillement avant et après le pic de contrainte. Les points soulignés sur la courbe contrainte-déformation (voir figure 7.7b) correspondent aux champs tracés.

Dans les deux cas, la simulation expérimentale et numérique, l'adoucissement est due à la propagation de la fissure, ce qui peut être observée également dans l'évolution du déplacement axial.

Pour la première étape analysés, les champs de déplacement (expérimentale et numérique) semblent tout à fait homogène, tandis que pour les étapes suivantes, la discontinuité dans les champs de déplacement sont observés à partir du coin inférieur gauche de l'échantillon. L'orientation de la fissure majeur dans l'expérience est influencée par les conditions aux limites et il relie les coins opposés de l'échantillon.

Le dispositif expérimental et la caractérisation des tests expérimentaux sont présentés dans 5.2 et 5.3, respectivement.

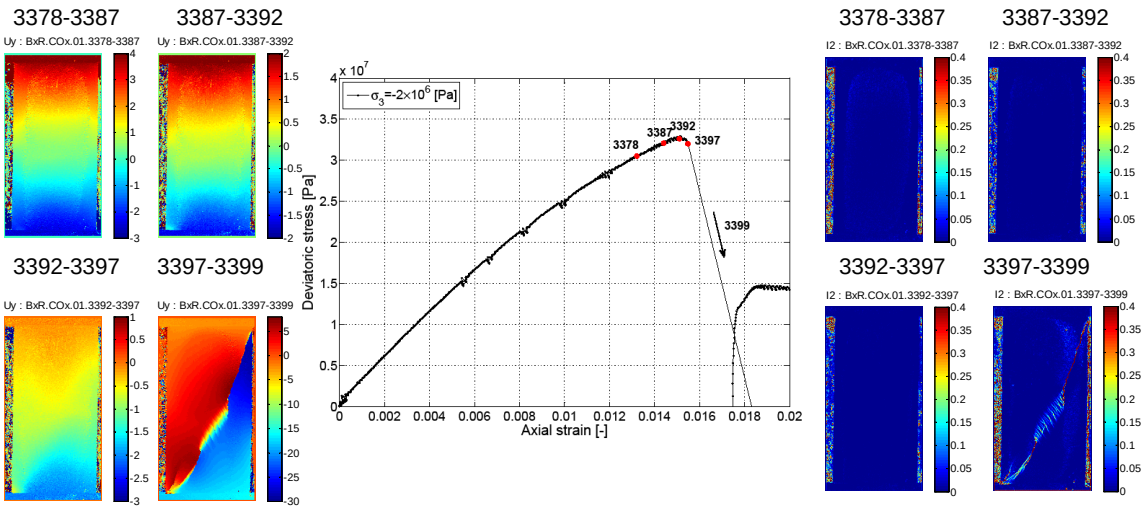

(a) Courbe expérimentale de contrainte-déformation avec champs de l'incrément de déplacement axial (à gauche) et de contrainte de cisaillement (à droite).

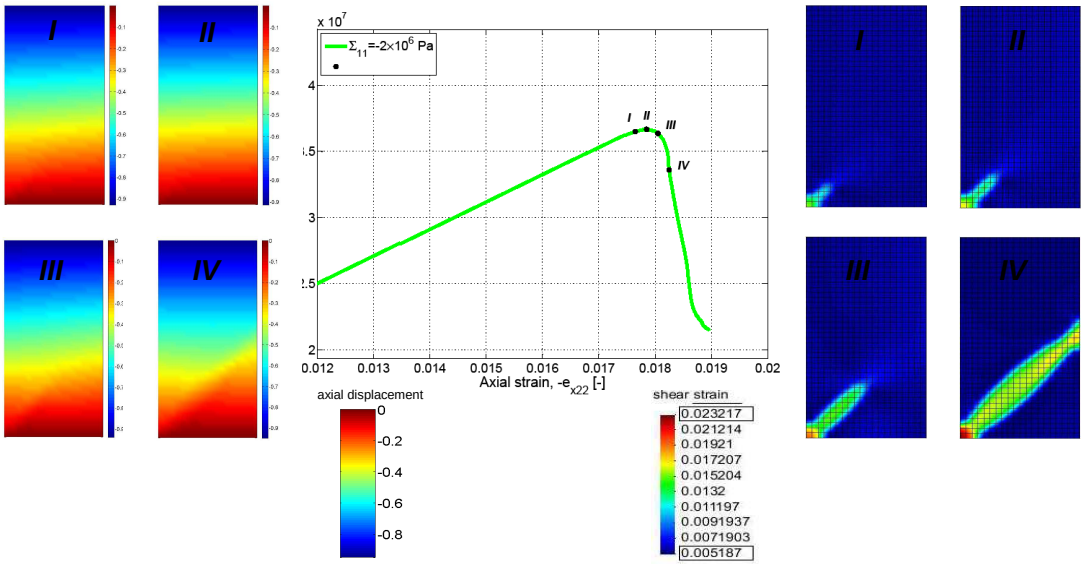

(b) Courbe numérique de contrainte-déformation avec champs de déplacement axial (à gauche) et de contrainte de cisaillement (à droite).

Figure 7.7: Relations de contrainte-déformation expérimentales et numériques sous compression biaxiale avec contrainte latérale $\Sigma_{lateral} = -2 \times 10^6\, Pa$.

7.8 Conclusions générales et perspectives

L'objectif de cette étude était de développer un modèle à deux échelles pour les microfissures, capable de prendre en compte non seulement la propagation des microfissures, mais aussi le frottement de glissement de ces microfissures. Les modèles micromécaniques présentés ont été obtenus en utilisant une procédure de mise à l'échelle, qui combine une homogénéisation périodique basée sur le développement asymptotique et sur l'analyse énergétique de la microfissure. Les lois d'évolution d'endommagement sont entièrement déduites de l'analyse microstructurale par homogénéisation, sans hypothèses phénoménologiques. L'analyse microscopique de l'énergie a été réalisée sur une cellule de périodicité de dimension finie qui conduit, par homogénéisation, à une équation macroscopique d'évolution d'endommagement. Dans cette équation, la longueur des microfissures apparaît comme variable d'endommagement d, et la taille de la cellule de périodicité ε, represente un paramètre de longueur interne du matériau. A partir de critères de microfracture basées sur la courbe de résistance de fracture et basée sur une loi de propagation de type Charles, on déduit le modèle quasi-fragile et, respectivement, le modèle dépendant du temps. Les modèles d'endommagement résultants intègrent une dégradation de la rigidité, un adoucissement du comportement du matériau, de effets de taille, d'unilatéralité, d'anisotropie induite, la déformation irréversible après le déchargement et le comportement de rupture différent qui dépendent des propriétés de frottement.

Nous avons réussi à imposer la dépendance de la contrainte moyenne dans les modèles. C'est évidemment un résultat de l'ajout d'un phénomène de frottement. Additionnellement, dans le cas du modèle quasi-fragile, la relation contrainte-déformation contient l'adhérence pendant la premiere phase de chargement, l'adhérence pendant le déchargement, le glissement inverse et la déformation irréversible. Tous ces phénomènes sont absents dans le cas des modèles avec contact sans frottement sur les lèvres des microfissures. Avec l'abandon des mécanismes de frottement dans les modèles nous perdons beaucoup d'informations intéressantes sur la microstructure qui peut conduire à la conception technique moins efficace.

Du point de vue numérique, nous avons dû faire face à plusieurs difficultés sur certains points de la mise en œuvre. Dans le cas du modèle d'endommagement indépendant du temps (modèle d'endommagement quasi-fragile) la courbe de résistance linéaire ([13]) conduit à un snap-back dans la réponse globale. Nous l'avons régularisé par addition à la formulation de la R-curve linéaire d'un terme consistant dans la fonction de la puissance d'endommagement d. Au niveau de la macrostructure, le modèle déduit traite avec dépendance de maillage et représentation non physique des phénomènes de localisation. Ce comportement est lié à la non-unicité de la solution des problèmes aux limites pour le modèle d'endommagement impliquant des effets adoucissants. Afin d'éviter ces problèmes, le modèle a été régularisée par la dépendance du temps résultant en modèle d'endommagement dépendant du temps avec le critère sous-critique pour la propagation des microfissures. En utilisant ce modèle, nous avons obtenu la réponse structurelle et de la rupture causés par localisation de la déformation.

Résumés ont été donnés à la fin de chaque chapitre, mais nous rappelons maintenant les conclusions principales.

Dans le chapitre 2, nous avons présenté les aspects théoriques concernant l'homogénéisation

asymptotique et la loi évolution d'endommagement. En raison des mécanismes de frottement, la mise en œuvre numérique de la microstructure conduit à differentes coefficients homogénéisé et differentes coefficients liés à la dissipation de l'énergie pendant glissement avec frottement. Ces différents coefficients dépendent du sens de glissement, du coefficients de frottement et de l'orientation de la fissure. Enfin, nous avons déterminé les relations constitutives pour chaque état possible de la fissure, i.e. l'adhérence, le glissement et le glissement inverse. Ces états sont contrôlés par la loi de frottement et le chemin de chargement.

Des résultats numériques pour des tests de compression uniaxiale et biaxiale au niveau macroscopique local pour modèle d'endommagement quasi-fragile ont été présentés dans le Chapitre 3. Dans ce modèle, comme la fissure se propage, la résistance du matériau augmente jusqu'à une valeur maximale soit atteinte. Nous avons considéré un critère de rupture particulière pour une fissure dans le matériau élastique pour exprimer l'effect de la zone de microfissuration. La taille de la zone de microfissuration entre dans l'équation d'endommagement par la variable c_f. Dans le modèle présenté, la courbe de résistance linéaire conduit à un snap-back dans la réponse globale. Afin d'éviter ce phénomène, nous avons cherché un terme supplémentaire dans la courbe de résistance linéaire. Nous avons étudié l'influence de ce terme dans la R-curve et nous l'avons comparé avec les résultats obtenus avec la courbe de résistance linéaire comme dans [13]. Nous avons observé que ce changement nous a permis d'éviter un snap-back et de contrôler la phase post-pic avec une petite dérive des propriétés des matériaux. Parallèlement, l'influence du frottement a été étudiée. La présence de frottement provoque l'augmentation de la résistance du matériau et modifie les caractéristiques de propagation des fissures. Pour un matériau sans frottement la propagation de la fissure est rapide, alors que pour le matériau avec frottement le procédé de la propagation ralentit.

Nous avons étudié également l'influence de la contrainte latérale sur la réponse macroscopique. La réponse augmente avec la contrainte latérale, ce qui confirme la présence du phénomène de frottement. L'incrément de variable d'endommagement *vs* déformation appliquée diminue en raison de l'augmentation de la contrainte latérale. Le régime post-pic indique un comportement plus fragile pour les valeurs inférieures de contrainte latérale tandis que pour des valeurs plus élevées, il est plus contrôlée.

En raison de l'ajout du terme supplémentaire dans la courbe de résistance, le cycle de chargement-déchargement a été possible de réaliser. Nous pourrions étudier le comportement lié à des mécanismes de frottement comme le glissement inverse et l'adhérence pendant le déchargement. Tous ces mécanismes sont contrôlés par la loi de frottement de Coulomb.

Nous avons étudié les évolutions des composantes de la loi de frottement ($\mathbb{N}$ et $\mathbb{T}$) et leur influence sur le comportement macroscopique. Dans la première phase de déchargement, la fissure est bloquée en raison du frottement, et cette phase s'étend conjointement avec une augmentation du coefficient de frottement et de la contrainte latérale. Après cette phase, la fissure est débloqué et se met à glisser dans le sens inverse, et par conséquent le régime de glissement inverse est réduite.

En ce qui concerne les calculs globaux, au niveau de la macrostructure, nous devons regularizer le modèle déduit (avec l'ajout de termes de gradient), afin d'éviter la dépendance de maillage et la représentation non physique du phénomène de localisation. Ce

comportement est lié à la non-unicité de solution des problèmes aux limites pour le modèle d'endommagement impliquant des effets adoucissants. Dans le chapitre suivant une modèle à deux échelles régularisé a été proposé.

Le chapitre 4 a été dédié au modèle d'endommagement dependant du temps avec le critère de propagation sous-critique. Des résultats numériques pour des tests de compression uniaxiale et biaxiale dans le cadre local et global, ont été présentés. Au niveau local, nous avons étudié l'influence des paramètres du modèle, comme la vitesse v_0, le taux de déformation $\dot{e}_{xkl}$, le coefficient souscritique n, la longueur interne ε, sous chargements de compression différentes et coefficients de frottement différentes. Nous n'avons pas remarqué des influences significantes de ces paramètres sur les propriétés de frottement.

La résistance du matériau augmente avec le coefficient souscritique n, le taux de déformation $\dot{e}_{xkl}$ et la longueur interne ε, mais il diminue avec la vitesse v_0. Nous avons trouvé réponses structurelles différentes, qui dépendent des propriétés de frottement et des contraintes latérales appliquées. En particulier, la résistance du matériau augmente avec eux, et cela a été observé au niveau local et global.

Les effets du coefficient de frottement et des contraintes latérales peut être vu non seulement en termes du niveau de pic de contrainte, mais aussi en termes de comportement en régime post-pic. Le régime post-pic évolue plus rapidement pour le matériau avec coefficient de frottement plus élevé et sous contrainte latérale supérieure. Au niveau global, le comportement connue expérimentalement, comme la localisation d'endommagement a été reproduite. Après le pic de contrainte, la zone d'endommagement évolue plus rapidement pour le matériau avec coefficient de frottement plus élevé et sous contrainte latérale supérieure. En pré-pic régime la zone d'endommagement évolue plus lentement en cas de coefficient de frottement plus élevé. La présence de la frottement agit en sens inverse de la propagation de l'endommagement.

En termes de temps, la rupture du matériau sans frottement apparaît comme premiere, tandis que pour le matériau avec la plus haute valeur de coeffient de frottement, en dernier. La même relation a été observée en augmentant la contrainte latérale.

Nous avons étudié les variations des propriétés de frottement passant de l'échelle microscopique à l'échelle macroscopique. Les valeurs des coefficients de frottement obtenus, à l'échelle macroscopique, sont légèrement réduite par rapport à le coefficient de frottement fixé à l'échelle microscopique.

Enfin, les effects de maillages différents a été étudiée. La réponse du matériau pour chaque type de maillage considéré tend aux mêmes résultats. Ce fait vérifie l'indépendance de maille sur les résultats.

C'est une conséquence de la régularisation par le dépendance du temps. Les simulations numériques présentées dans le chapitre 4 ont montré la capacité du modèle développé de reproduire une réponse dépendant du temps.

Dans le chapitre 5, nous avons présenté les résultats expérimentaux obtenus en utilisant un nouvel appareil triaxial qui permet l'observation des échantillons de roches sous chargement. Les expérimentations sont concentré sur l'effet du confinement sur le processus de la rupture, la localisation et les relations contrainte-déformation. Le comportement du

matériau indique caractérisations plus ductile pendant l'augmentation de la contrainte latérale. De plus, dans ce chapitre, les observations expérimentales ont été comparées avec les résultats numériques obtenus en utilisant le modèle d'endommagement dépendant du temps. Ce modèle d'endommagement dépendant du temps peut reproduire la dépendance de la contrainte moyenne et la rupture par localisation de la déformation. Cependant, pour mieux adapter les résultats expérimentaux, certains paramètres qui ont été fixés au échelle microscopique doit être modifiée. Il s'agit des paramètres élastiques tels que le module de Young, le coefficient de Poisson, et le coefficient de frottement.

Pour mener à bien ce travail, nous proposons quelques perspectives à court terme:

- Au niveau de la cellule unitaire d'autres formes et orientations des microfissures peuvent être considéré (i.e. des courbes au lieu des microfissures droites).
- Concernant les calculs globaux, dans le cas du modèle d'endommagement quasi-fragile, le modèle déduit peut être régularisé par l'ajout de termes de gradient, afin d'éviter dépendance de maillage et représentation non physique des phénomènes de localisation.
- Dans le cas du modèle d'endommagement dependant du temps, nous proposons d'introduire un déchargement élastique, ce qui peut conduire à une déformation irréversible et une meilleure représentation des phénomènes observés expérimentalement (comme par exemple un comportement plus ductile avec la pression de confinement plus élevé).
- L'application du modèle à des problèmes d'ingénierie tels que les tunnels ou les excavations.

Appendix A

Bisection method

The damage equation (3.1) is solved using the following procedure:

1. input at step $n+1$: d^n, e_{xkl}^{n+1},$delta$
2. initialization: $a \leftarrow d^n$, $b \leftarrow 1$
3. division of $< a, b >$into i-intervals
4. check in each i-interval (if any of the i-intervals satisfies the condition, go to next n step)
   if $E_c(i) * E_c(i+1) < 0$
   - $a \leftarrow a(i)$, $b \leftarrow b(i+1)$
   - $y_a = E_c(a)$, $y_b = E_c(b)$
   - computation of the number of iterations needed, k_{max}, to achieve a given error, $delta$:
     $k_{max} = \frac{\log(b-a)-\log(delta)}{\log 2}$
   - for $k = 1 : k_{max}$:
     $c = \frac{a+b}{2}$
     $y_c = E_c(c)$
     if $y_c = 0$ the solution is c
     $a, b \leftarrow c$
     elseif $y_b * y_c > 0$
     $b \leftarrow c$
     $y_b \leftarrow y_c$
     else
     $a \leftarrow c$
     $y_a \leftarrow y_c$
     if $b - a < delta$ the solution is : $c = \frac{a+b}{2}$

where $E_c(d) = \frac{1}{2}\frac{dC_{ijkl}(d)}{dd} e_{xkl}\left(\mathbf{u}^{(0)}\right) e_{xij}\left(\mathbf{u}^{(0)}\right) + \frac{\mathcal{G}^{\varepsilon}}{\varepsilon} + I_{mnpq}(d)\, e_{xmn}\left(\mathbf{u}^{(0)}\right) e_{xpq}\left(\mathbf{u}^{(0)}\right)$, and d is assigned to $d \leftarrow a, b, c$.

Bibliography

[1] Anderson, T.L., 2005. [Third Edition] Fracture Mechanics, Fundamentals and Applications. Taylor & Francis Group.

[2] ANDRA, 2007, 182/D/VA. The Meuse/Haute-Marne Underground Research Laboratory.

[3] ANDRA, 2007, 208/D/VA. The Disposal Facility For Low- And Intermediate-Level Short-Lived Radioactive Waste.

[4] ANDRA, 2007, 209/D/VA. Managing Diffuse Nuclear Waste.

[5] Andrieux, S., Bamberger, Y., Marigo, J-J., 1986. Un modele de materiau microfissure pour les betons et les roches. Journal de Mecanique theorique et appliquee, volume:5, issue:3, p.471-513

[6] Atkinson, B.K., Meredith, P.G., 1987. The theory of subcritical crack growth with applications to minerals and rocks. Fracture Mechanics of Rocks. Academic Press, New York, 111-166.

[7] Atkinson, B.K., 1984. Subcritical crack growth in geological materials. J. Geophys. Res. 89(B6), 4077-4114.

[8] Atkinson, B.K., Meredith P.G., 1987a. Experimental fracture mechanics data for rocks and minerals. Fracture Mechanics of Rocks, Academic, San Diego, Calif.,chap.11, 477-525.

[9] Atkinson, R.H., Ko, H-Y., 1973. A fluid cushion, multiaxial cell for testing rock specimens. Int J Rock Mech Mining Sci Geomech Abstr 10,351-361.

[10] Bakhvalov, N., Panasenko, G., 1989. Homogenisation: Averaging Processes in Periodic Media. Kluwer Academic Publisher Group, Dordrecht.

[11] Bargellini, R., Halm, D., Dragon, A., 2008. Modelling of quasi-brittle behaviour: a discrete approach coupling anisotropic damage growth and frictional sliding. European Journal of Mechanics A/Solids 27, 564-581

[12] Barthélémy, J-F., Dormieux, L., Kondo D., 2003. Determination of the macroscopic behaviour of a medium with frictional cracks. C.R. Mecanique 331, 77-84.

[13] Bazant, Z.P., Planas, J.,1997. Fracture and Size Effect in Concrete and Other Quasibrittle Materials. CRC Press, Boca Raton, FL.

[14] Benssousan, A., Lions, J.L., Papanicolaou, G., 1978. Asymptotic Analysis for Periodic Structures. North-Holland, Amsterdam.

[15] Bésuelle, P., Hall, S.A., 2011. Characterization of the strain localization in a porous rock in plane strain condition using a new true-triaxial apparatus. Advances in Bifurcation and Degradation in Geomaterials. Proceeding of the 9th International Workshop on Bifurcation and Degradation in Geomaterials. Springer. Editors: Bonelli S, Dascalu C, Nicot F.

[16] Bésuelle, P., Desrues, J., Raynaud, S., 2000. Experimental characterisation of the localisation phenomenon inside a Vosges sandstone in a triaxial cell. Int J Rock Mech Mining Sci 37,1223-1237.

[17] Bilbie, G., 2007. Modélisation multi-échelle de l'endommagement et de la rupture dans les milieux (quasi-) fragiles, PhD Thesis, Université Joseph Fourier.

[18] Brace, W.F., Jr., Paulding B.W., Scholz, C., 1966. Dilatancy in the fracture of crystalline rocks. J. Geophys. Res., 71, 3939-3953.

[19] Caiazzo, A.A., and Constanzo, F., 2000. On the constitutive relations of materials with evolving microstructure due to microcracking. Int. J. Solids Struct. 37, 3375-3398.

[20] Caillerie, D., Dascalu, C., 2011. One-dimensional Localization Solutions for Time-dependent Damage. International Journal of Damage Mechanics, vol. 20 no. 8, 1178-1197 .

[21] Charles, R., 1958. Dynamic fatigue of glass. J. Appl. Phys., 29, 1657-1662.

[22] Chiarelli A-S., 2000. Etude experimentale et modelisation du comportement mécanique de l'argilite de l'Est. PhD Thesis. Université des Sciences et Technologies de Lille.

[23] Christensen, R.M. and Lo, K.H., 1979. Solutions for effective shear properties in three phase sphere and cylinder models. J. Mech. Phys. Solids, 27, 315-330.

[24] COMSOL Multiphysics, 2006, Version 3.3.

[25] Dascalu, C., Bilbie, G., Agiasofitou, E.K., 2008. Damage and size effects in elastic solids: A homogenization approach. Int. J. Solids Struct., 45, 2, 409-430.

[26] Dascalu, C., Francois, B., Keita, O., 2010. A two-scale model for subcritical damage propagation. Int. J. Solid Struct. 47, 493-502.

[27] Dascalu, C., 2009. A two-scale damage model with material length. C.R. Mecanique, 337, 645-652.

[28] Dascalu, C., Dobrovat A.M., Tricarico M., 2010. On a 3D micromechanical damage model. Int. J. Fract., 166,153–162.

[29] Dascalu, C., Bilbie, G., 2007. A multiscale approach to damage configurational forces. Int. J. of Fract.,147, 285-293.

[30] Desrues, J., Viggiani, G., 2004. Strain localization in sand: an overview of the experimental results obtained in Grenoble using stereophotogrammetry. Int J Num Anal Meth Geomech 28,279-321.

[31] Dobrovat, A-M., 2011. Modelisation multi-echelle de l'endommagement et de l'emission acoustique dans les roches. PhD Thesis. Université de Grenoble.

[32] Dormieux, L., Kondo, D., Ulm, F.-J., 2006. Microporomechanics, John Wiley & Sons, Inc.

[33] Dragon, A., Halm, D., Désoyer, Th., 2000. Anisotropic damage in quasi-brittle solids: modelling, computational issues and applications. Comput. Methods Appl. Mech. Engrg., 183, 331-352.

[34] Eshelby, J.D., 1957. The determination of the field of an ellipsoidal inclusion and related problems. Proc. R. Soc. Lond A, 241, 376-396.

[35] Fabre, G., 2005. Fluage et endommagement des roches argileuses. Evolution de la microstructure et modélisation phénoménologique. PhD Thesis. Université Joseph Fourier, Grenoble.

[36] Francois, B., Dascalu, C., 2010. A two-scale time-dependent damage model based on non-planar growth of micro-cracks. Journal of the Mechanics and Physics of Solids, 58, 1928-1946.

[37] Freund, L.B., 1998. Dynamic Fracture Mechanics. Cambridge University Press.

[38] Gambarotta, L., Lagomarsino S., 1993. A microcrack damage model for brittle materials. Int. J. Solids Structures, 30(2), 177-198.

[39] Ghosh S., Lee, K., and Moorthy, S., 1995. Multiple scale analysis of heterogeneous elastic structures using homogenization theory and Voronoi cell finite element method. Int. J. Solids Structures, 32(1), 27-62.

[40] Griffith, A., 1920. The phenomena of rupture and flow in solids. Phil.Trans.Roy.Soc. London CCXXI-A,163-198

[41] Guedes, J.M. and Kikuchi, N., 1990. Preprocessing and postprocessing for materials based on the homogenization methods with adaptive finite element methods. Comput. Methods Appl. Mech. Engrg., 83, 143-198.

[42] Habib, P., 1990. An introduction to the rheology of geomaterials, in: Geomaterials: Constitutive equations and modelling, F. Darve (ed.), 1–5.

[43] Haimson, B., Chang, C., 2000. A new true triaxial cell for testing mechanical properties of rock, and its use to determine rock strength and deformability of Westerly granite. Int J Rock Mech Mining Sci 37,285-296.

[44] Hall, S.A., Bornert, M., Desrues, J., Pannier, Y., Lenoir, N., Viggiani, G., Bésuelle, P., 2010. Discrete and Continuum analysis of localised deformation in sand using X-ray micro CT and Volumetric Digital Image Correlation. Geotechnique 60,315-322.

[45] Hall, S.A., Muir Wood, D., Ibraim, E., Viggiani, G., 2000. Localised deformation patterning in 2D granular materials revealed by digital image correlation. Granular Matter, DOI: 10.1007/s10035-009-0155-1.

[46] Halm, D., Dragon, A., 1998. An anisotropic model of damage and frictional sliding for brittle materials, European Journal of Mechanics ASolids, Volume: 17, Issue: 3, 439-460

[47] Hill, R., 1965. A self-consistent mechanics of composite materials. J. Mech. Phys. Solids, 13, 213-222.

[48] Jaeger, J.C., Cook, N.G.W., Zimmerman, R.W., 2007. Fundamentals of rock mechanics, 4th Edition.

[49] Kemeny, J. M.,1993. The micromechanics of deformation and failure in rocks. Proc., Int. Symposium on Assessment and Prevention of Failure Phenomena in Rock Engineering, Istambul, Turkey. A.A. Balkema, Rotterdam, pp. 23-33.

[50] Kemeny, J.M., 2003. The time-dependent reduction of sliding cohesion due to rock bridges alonf discontinuities: a fracture mechanics approch. Rock. Mech. Rock Engng. 36(1), 27-38.

[51] Kemeny, J.M., 2005. Time-dependent drift degradation due to progressive failure of rock bridges along discontinuities. Int. J. Rock Mech. Min. Sci. 42, 35-46.

[52] King, M.S., 2002. Elastic wave propagation in and permeability for rocks with multiple parallel fracture. Int J Rock Mech Mining Sci 39,1033-1043.

[53] Kachanov, L.M., 1958. Time of the rupture process under creep conditions. Inv. Akad. Nauk. SSR. Otd Tekh. Nauk., 8, 26-31.

[54] Kachanov, L.M., 1982. A microcrack model of rock inelasticity - Part I: frictional sliding on microcracks; Part II: propagation of microcracks. Mechanics of Materials 1, 19-41.

[55] Labuz, J.F., Dai, S-T., Papamichos, E., 1996. Plane-strain compression of rock-like materials. Int J Rock Mech Mining Sci Geomech Abstr 33,573-578.

[56] Lawn, B.R., Marshall D.B., 1998. Nonlinear stress-strain curves for solids containing closed cracks with friction. J. Mech. Phys. Vol.46, No. 1, 85-113.

[57] Lee, X., Ju, J.W., 1991. Micromechanical Damage Model for Brittle solids - II : Compressive Loadings, J. Engrg. Mech., ASCE, 117, 1515-1536.

[58] Leguillon, D., Sanchez-Palencia, E.,1982. On the behaviour of a cracked elastic body with (or without) friction. J. Mech. Theor. Appl. 1, 195-209.

[59] Lenoir, N., Bornert, M., Desrues, J., Bésuelle, P., Viggiani, G., 2007. Volumetric Digital Image Correlation Applied to X-ray Microtomography Images from Triaxial Compression Tests on Argillaceous Rock. Strain 43,193-205.

[60] Main, I., 2000. A damage mechanics model for power-law creep and earthquake aftershock and foreshock sequences. Geophys. J. Int. 142, 151-161.

[61] Meredith, P.G., Atkinson, B.K., 1985. Fracture toughness and subcritical crack growth during high-temperature tensile deformation of Westerly granite and black gabbro. Phys. Earth Planet. Interior. 39, 33-51.

[62] Michelis, P., 1985. A true triaxial cell for low and high pressure experiments. Int J Rock Mech Mining Sci Geomech abstr 22,193-188.

[63] Miura, K., Okui, Y.,Horii, H., 2003. Micromechanics-based predition of creep failure of hard rocks for long-term safety of high-level radioactive waste disposal system. Mech. Mater. 35, 587-601.

[64] Mogi, K.,1967. Effect of the intermediate principal stress on rock failure. J Geophys Res 72,5117-5131.

[65] Mori, T., Tanaka, K., 1973. Average stress in the matrix and average elastic energy of materials with misfitting inclusions. Acta. Metall., 21, 571-574.

[66] Nasseri, M.H.B., Mohanty, B., and Young, R.P., 2006. Fracture Toughness Measurements and Acoustic Emission Activity in Brittle Rocks. Pure Appl. Geophys., 163, 917–945.

[67] Naumann, M., Hunsche, U., Schulze, O., 2007. Experimental investigations on anisotropy in dilatancy, failure and creep of Opalinus Clay. Phys Chemistry Earth 32,889-895.

[68] Nemat-Nasser, S., and Obata M., 1988. A microcrack model of dilatancy in brittle material. J. of Applied Mechanics, 55, 24-35.

[69] Nemat-Nasser, S., Hori, M., 1999. Micromechanics: Overall Properties of Heterogeneous Materials. Elsevier, Amsterdam, Lausann, New York.

[70] Okui, Y., Horii, H., 1997. Stress and time-dependent failure of brittle rocks under compression: a theoretical prediction. J. Geophys. Res. 102(B7), 14869-14881.

[71] Ord, A., Vardoulakis, I., Kajewski, R., 1991. Shear band formation in Gosford sandstone. Int J Rock Mech Mining Sci Geomech Abstr 28,397-409.

[72] Pensée, V., Kondo, D., Dormieux, L., 2002. Micromechanical Analysis of Anisotropic Damage in Brittle Materials. Journal of Engineering Mechanics, Volume: 128, Issue: 8, Publisher: ASCE, 889-897

[73] Poon, B., Ponson, L., Zhao, J., Ravichandran, G., 2011. Damage accumulation and hysteretic behavior of MAX phase materials. Journal of the Mechanics and Physics of Solids, 59, 2238-2257.

[74] Popp, T., Salzer, K., 2007. Anisotropy of seismic and mechanical properties of Opalinus clay during triaxial deformation in a multi-anvil apparatus. Phys Chemistry Earth 32,879-888.

[75] Prat, P.C., Bazant, Z.P.,1997. Tangential stiffness of elastic materials with systems of growing and closing cracks. J. Mech. Phys. Solids 45, 611-636.

[76] Rabotnov, Y.N., 1963. Creep problems in structural members, North-Holland.

[77] Sanchez-Palencia, E., 1980. Non-homogeneous Media and Vibration Theory, Lecture Notes in Physics, 127, Springer, Berlin.

[78] Suquet, P.M., 1985. Local and global aspects in the mathematical theory of plasticity. In Sawczuk, A. and Bianchi, G., editors, Plasticity today : modelling, methods and applications, London. Elsevier Applied Science Publishers., 279-310.

[79] Swanson, P.L., 1984. Subcritical crack growth and other time- and environment-dependent behaviour in crustal rocks. J. Geophys. Res. 89, 4137-4152.

[80] Takemura, T., Oda, M., Takahashi, M., 2004. Microstructure observation in deformed geomaterials using microfocus X-ray computed tomography. In: Otani J, Obara Y (eds) X-ray CT for Geomaterials, GeoX2004. Balkema.

[81] Telega, J.J., 1990. Homogenization of fissured elastic solids in the presence of unilateral conditions and friction. Comput. Mech., 6, 109-127.

[82] Terada, K., Kikuchi, N., 1995. Nonlinear homogenization method for practical applications. In Ghosh, S. and Ostoja-Starzewski, M., editors, Computational Methods in Micromechanics, AMD-Vol. 212/MD-Vol. 62, 1-16. ASME.

[83] Wawersik, W.R., Carlson, L.W., Holcomb, D.J., Williams, R.J., 1997. New method for true-triaxial rock testing. Int J Rock Mech Mining Sci 34,330.

[84] Zhu, Q.Z., Kondo, D., Shao, J.F., 2007. Micromechanical analysis of coupling between anisotropic damage and friction in quasi brittle materials: Role of the homogenization scheme, International Journal of Solids and Structures 45, 1385–1405.